GEOLOGY AND AGE OF MINERALIZATION AROUND NALDÖKEN VILLAGE (AYVACIK-ÇANAKKALE) IN BIGA PENINSULA

A THESIS SUBMITTED TO
THE GRADUATE SCHOOL OF NATURAL AND APPLIED SCIENCES
OF
MIDDLE EAST TECHNICAL UNIVERSITY

GÖKHAN OKAN YILDIZ

IN PARTIAL FULFILLMENT OF THE REQUIREMENTS
FOR
THE DEGREE OF MASTER OF SCIENCE
IN
GEOLOGICAL ENGINEERING

FEBRUARY 2016

Approval of the thesis:

GEOLOGY AND AGE OF MINERALIZATION AROUND NALDÖKEN VILLAGE (AYVACIK-ÇANAKKALE) IN BIGA PENINSULA

submitted by **GÖKHAN OKAN YILDIZ** in partial fulfillment of the requirements for the degree of **Master of Science in Geological Engineering Department, Middle East Technical University** by,

Prof. Dr. Gülbin Dural Ünver ____________________
Dean, Graduate School of **Natural and Applied Sciences**

Prof. Dr. Erdin Bozkurt ____________________
Head of Department, **Geological Engineering**

Prof. Dr. Erdin Bozkurt ____________________
Supervisor, **Geological Engineering Dept., METU**

Examining Committee Members:

Prof. Dr. Nurettin Kaymakçı ____________________
Geological Engineering Dept., METU

Prof. Dr. Kadir Dirik ____________________
Geological Engineering Dept., Hacettepe University

Prof. Dr. Erdin Bozkurt ____________________
Geological Engineering Dept., METU

Assist. Prof. Dr. Erman Özsayın ____________________
Geological Engineering Dept., Hacettepe University

Assist. Prof. Dr. A. Arda Özacar ____________________
Geological Engineering Dept., METU

Date: February 5, 2016

I hereby declare that all information in this document has been obtained and presented in accordance with academic rules and ethical conduct. I also declare that, as required by these rules and conduct, I have fully cited and referenced all material and results that are not original to this work.

Name, Last name : Gökhan Okan Yıldız

Signature :

ABSTRACT

GEOLOGY AND AGE OF MINERALIZATION AROUND NALDÖKEN VILLAGE (AYVACIK-ÇANAKKALE) IN BIGA PENINSULA

Yıldız, Gökhan Okan
M.S., Department of Geological Engineering
Supervisor: Prof. Dr. Erdin Bozkurt

February 2016, 174 pages

Kestanbol pluton (Biga Peninsula) NW Turkey and its volcanic assemblages hosts magmatic and hydrothermal mineralization around Naldöken village, Ayvacık-Çanakkale. Various rocks assemblages and their spatial with temporal relations was studied to identify their alteration-mineralization characteristics of the study area. By means of this study, Naldöken mineralization is attributed to emplacement of quartz monzodiorite (20.1 Ma), creating potassic alterations on proximal and lithocap with chalcedonic quartz veins and silica cemented breccia dominated mineralization on distal zones. Proposed model for formation of quartz veins and breccia is attributed to NNE-SSW trending dextral coeval faulting creating transtensional stress conditions. Moreover, geochronological and geochemical investigations resulted the emplaced rock bodies and coeval alteration assemblages proved that Naldöken mineralization was occurred during early Miocene (22-19 Ma) in volcanic-arc settings. Investigations also identified the Naldöken mineralization is a typical low-sulfidation mineralization with a porphyry type of root.

Key words: U-Pb dating, Ar-Ar dating, Structural modelling, Naldöken, Mineralization, Biga Peninsula

ÖZ

BİGA YARIMADASI, NALDÖKEN KÖYÜ (AYVACIK-ÇANAKKALE) CIVARINDAKİ CEVHERLEŞMENİN JEOLOJİSİ VE YAŞLANDIRILMASI

Yıldız, Gökhan Okan
Yüksek Lisans, Jeoloji Mühendisliği Bölümü
Tez Danışmanı: Prof. Dr. Erdin Bozkurt

Şubat 2016, 174 Sayfa

Kestanbol Plütonu (Biga Yarımadası) KB Türkiye ve onun volkanik birlikleri Naldöken köyü, Ayvacık-Çanakkale cevresinde magmatik ve hidrotermal mineralizasyonlar içermektedir. Çeşitli kaya toplulukları ve bunların zaman ve mekan ilişkileri, alterasyon ve cevherleşme özelliklerini tanımlamak için çalışılmıştır. Bu çalışma aracılığıyla, Naldöken cevherleşmesi proksimalde potasik alterasyonu ve distalde kil şapka ile kalsedonik kuvars damarları ve silica çimentolu breş baskın cevherleşme, kuvars monzodiyorit'in (20.1 My) yerleşimine dayandırılmıştır. Kuvars damarları ve breş oluşumu için önerilen model KKD-GGB yönelimli sağ atımlı, eş zamanlı faylanmanın yarattığı transtensiyonel sitres koşuluyla ilişkilendirilmiştir. Ayrıca, jeokronolojik ve jeokimyasal incelemelerle sokulan kaya kütleleri ve eş zamanlı alterasyon birlikleri açıklamıştır ki Naldöken cevherleşmesi erken Miyosen'deki (22-19 My) volkanik yay ortamında oluştuğu sonuçlandırılmıştır. Çalışmalarda Naldöken cevherleşmesinin tipik bir düşük-sülfidasyon cevherleşmesiyle birlikte porfiri tipte bir kök ile tanımlamıştır.

Anahtar kelimeler: U-Pb yaşlandırmacı, Ar-Ar yaşlandırması, Yapısal modelleme Naldöken, Cevherleşme, Biga Yarımadası

To My Parents and Siblings

Şeref Yıldız, Münire Yıldız
Ayşe Selda Enez, Betül Emine Derinkuyu and Onur Yıldız

ACKNOWLEDGEMENTS

I would first like to thank my thesis advisor Prof. Dr. Erdin Bozkurt for his endless support and being a great mentor. The door to Prof. Bozkurt office was always open whenever I had a question about my research or writing. He consistently allowed this paper to be my own work, but steered me in the right the direction whenever he thought I needed it. I am also thankful to him for his great effort and teaching during data processing and writing of this thesis. He also processed raw U-Pb data and prepared concordia and probability/density diagrams. Additionally, he is not only a supervisor for me, he is also touched my carrier and life in a magnificent way that I will never forget to say my special thanks to him.

I am grateful to Zehra Deveci for help and guidance during sample preparation and mineral separation. I was involved in crushing and separation of some samples by continuous guidance and self-devotion of Zehra for completion of works even while I am away for fieldwork. With her generous help, we completed separation of heavy minerals using Wilfley water-shaking table, removal of magnetic minerals by hand magnet, passing the heavy fraction through the Frantz electro-magnetic separator. Moreover, she has completed all of the following processes: passing the heavy fraction through heavy liquid Bromoform ($CHBr_3$) to sink zircon-rich fraction, hand picking of zircons directly from the final heavy mineral separate under the stereo microscope at Middle East Technical University, moulding of zircon grains into epoxy, polishing of moulds to expose internal structure of zircon grains, gold-coating of moulds, cathodoluminescence imaging of zircon crystals using electron microscope, performance of U-Pb isotope analysis by laser ablation induced couple mass spectrometer (LA-ICPMS) in Geochronology and Radiogenic Isotope Laboratory, Institute of Geoscience, Goethe University of Frankfurt. In short, without her involvement and contribution, U-Pb analyses would not come through.

I would also like to thank Orhan Karaman for petrographical thin section preparation.

I wish to express my special thanks to my friends Bülent Tokay for his technical support and Merve Taga for her moral support and punctual suggestions that led myself to improve.

I am thankful to Mustafa Kaplan, Faruk Berber, Alican Aktağ, Çiğdem Argunhan and Arzu Arslan who were always helpful and kind to me.

This research was supported by Teck Madencilik Sanayi Ticaret Anonim Şirketi. They supplied analysis support and logistics that greatly assisted the research, although they may not agree with all of the conclusions of this paper. Specially, I am thankful to company individuals Uğur Kızıltepe, Bayram Artun, Ramazan Sarı, Aykut Saygılı, Gökhan Bağcivan and many others for giving me an opportunity to study on enjoyable environment during both course work, data gathering and writing.

I would like to extent my thanks to Naldöken Village locals for their sincere hospitality. Drinking their well-brewed tea after daylong field work and watching one of the best sunset view over Aegean Sea was totally taking away my tiredness.

Last, but not least, I would like to thank my former instructors and idols, Prof. Dr. Ali Koçyiğit who teach me and admires me while I was taking the first step in geology, Assoc. Prof. Dr. Elizabeth J. Catlos from Jackson School of Geosciences, UT Austin for giving me insights about scientific studies, Dr. Cengiz Y. Demirci, SAIMM from Asia Minor Minning for spiriting up my geological enthusiasm, Lions Clubs International (especially the members Emiran Dağlı, Nural Sonbudak and Özgür Abacı) for giving me opportunity to have experience on leadership, that would be a candle thought my story.

Science First. Önce Bilim.

TABLE OF CONTENTS

LIST OF TABLES

TABLES

LIST OF FIGURES

FIGURES

Weathering has occurred due to atmospheric activities, collectively resulting supergene assemblages. Supergene activity can initiate low temperature alteration during which, depending of created pH value, a broad range of clay minerals may form (Corbett & Leach 1998). The alteration products may be illite, halloysite, kaolinite, chlorite, smectite, carbonate, calcite and etc… Moreover, some iron-oxides, like hematite, jarosite, goethite, may also also form during supergene activities (Figure 3.41). In some cases, iron-oxide leakeage and corresponding acidity may result in ferrocrete formation where low pH iron oxide-rich solution meets with the running waters (Figure 3.42). In addition to the weathering, the proximity of Tuzla Geothermal field is critical and continuously causing alteration around geothermal fumaroles, that is a few km southwest of the study area; it is quite significant because it may produce a low temperature extensive halo with overprinting alteration assemblages, like smectite, chlorite, carbonate and calcite. Along pathways of fumaroles or geothermal waters, talc or serpentine occurrences are common. Rhyodacite and some portion of the latite porphyry exposed in the

CHAPTER 1

INTRODUCTION

“There are many arts and sciences of which a miner should not be ignorant.”

(Agricola, 1556)

Likewise the historic times, mine industry has to be aware of multidisciplinary sight of mining activities starting from targeting to production, including safety, economy, politics, machinery, and construction. These diverse major disciplines are the combination of many minor subjects and a great deal of related significant subtopics. Consequently, collaborative working of disciplines is indispensable.

Application of basic geological principles and proposing of a geodynamic model form the first step in any exploration project. For sound geodynamic models, spatial and temporal relations of rock units and geological structures, as well as effects of one unit to another unit should be investigated in detail.

1.1. Rationale for Study

Tethyan Eurasian Metallogenic Belt is currently one of the world’s major metal producing belts considering its diverse mineralization styles (Yiğit, 2012). In this belt, Biga Peninsula, northwestern Turkey, is one of the well-known precious base metal fertile tract and historically it is also active since 3000 B.C., the earlier era of the Bronze Age (Yiğit, 2012).

The recent mining activity in the Biga Peninsula began with the reestablishment of Turkish Mining Law in late 1980s, during which Biga Peninsula gained its attention for precious metal exploration, carried out mostly by the foreign companies. There are several targets in the region and therefore several exploration projects are ongoing.

Naldöken mineralization, located close to Tuzla geothermal site, is one of those untested gold mineralization targets in southwest Biga Peninsula; the prospect is owned by Teck Madencilik Sanayi Ticaret Anonim Şirketi (here after; Teck). The exploration program has been continuing over a couple of years now; there are, however, several questions awaiting for clarification. Most are concerned with the better understanding the geology of the prospect, and controls on mineralization in the concession. They include;

i. establishment of the stratigraphic scheme in the prospect and, spatial and temporal relationships among different lithologies;
ii. mineralizing mechanism(s) in and around the prospect;
iii. emplacement age of mineralization-related intrusion(s);
iv. trend(s) of mineralization, and mineralization-related veining;
v. presence of overprinting mineralization;
vi. presence and trend of un-mineralized structures;
vii. orientation of mineralization related or unrelated structures;
viii. Is there any emplacement that have been eaten the mineralization, if there had a mineralization?
ix. Is there any mineralization at depth? What are the evidences for stating yes/no?

1.2. Purpose and Scope

Biga Peninsula forms the westernmost part of the Sakarya Zone and illustrates a complex geological history recording (i) subduction-accretion process, (ii) opening-closure of oceans, and (iii) collision-amalgamation of continental fragments. It comprises Permian-Cenozoic sedimentary, Tertiary plutonic-volcanic, ophiolitic (Çetmi ophiolitic mélange and Denizgören ophiolite) and amphibolite to granulite facies metamorphic rocks (Kazdağ and Çamlıca massifs, and Karakaya Complex). The region is dominated by the widespread occurrence of Tertiary plutonic

(Kestanbol, Kuşçayır, Evciler, Dikmen, Yenice, Eybek, Sarıoluk, Karabiga and Kapıdağ plutons) and associated volcanic rocks of different age, composition and origin. In addition to those, Biga Peninsula exemplifies complex geology of Aegean extension. The region is also dissected by several branches of the North Anatolian Fault Zone. There are, off course, several contentious about: timing and location of suture zones, exhumation process of metamorphic assemblages, intrusion distributions and Cenozoic volcanic activity, tectonic setting of unconformable clastic sediments and multiphase structures consequent to regional extension.

Biga Peninsula host several porphyry copper-gold and high- to low-sulphidation epithermal vein type gold-silver and magnetite (copper) skarn deposits, etc. (Yiğit, 2009) Most of the porphyry systems are placed around magmatic emplacements. The epithermal systems are, however, distributed across the Biga Peninsula, as illustrated by vein-type epithermal systems of low-sulfidation and high-sulfidation, off and on co-exist with porphyry systems. Naldöken prospect is one of those deposits and form the subject of the present thesis.

Through geological mapping, geochronological and whole-rock geochemical work, a geological model of Naldöken mineralization will be proposed to address some of the questions listed in the preceding section. Additionally, this thesis aims to give a hint about timing of mineralization and discuss the structural control on mineralization.

1.3. Geographic Setting

Study area is located about 60 km southsoutheast of Çanakkale between the villages Babadere, Karbastı, Küçük Kestanelik, Taşboğaz, Çamköy, Tuzla and Naldöken in the Biga Peninsula in northwestern Turkey (Figure 1.1).

Quantitatively, study area lies within I16-d3 of 1/25000 scale Turkish topographic map sheet of Çanakkale; center of the area is located on Easting 432000, Northing 4383000 of European Datum 1950 UTM Zone 35N. Study area has fairly well road networks with all year round accessible surface. All the highways from Çanakkale or Edremit are hard surface highways with more than two lanes whereas roads between highways to villages or inter-village roads have loose surface with one or two lanes. There are also unimproved roads on the forest, animal grazing lands and farm site but those can be used on suitable weather conditions.

1.4. Method of Study

There are three main stages conducted before submitting this thesis; those are preliminary and evolutionary desktop works, field studies and laboratory works.

One of the stages is desktop works on literature research, data compilation and management and data evaluation. During desktop work stage, 64 bit computers and related computer software programs are used. Literature reviews was carried out through Middle East Technical University Library Services to confer previous studies upon both regional and local geology of the study area and conceptual information on topical subjects. The analysis and evaluation of the field and laboratory data was acquired through Esri ArcGIS 10.3.1, Microsoft Office Professional Plus 2013, T-Tecto (Zalohar), Allmendinger-Stereonet, Reflex ioGAS. Additional details about kinematic and geochemical analyses are presented in relevant chapters.

Field work is another stage and carried out in two separate periods during summer seasons of 2014 and 2015. During 13 days in the field, geological mapping of the study areas was completed and samples collected for petrographic and geochronological analyses. Daily field tracks and marks were recorded by Garmin GPSMAP 62s, which works with Garmin Basecamp version 4 series and Microsoft Office programs. Additionally, Brunton 15TDCL with around 4.75^{o} magnetic declination towards east (positive) was used to measure geological structures.

The last stage consists of thin-section preparation, sample separation for geochronological analyses, petrographic analyses of different rock units and they were carried out in laboratories of Geological Engineering Department at METU, Institut für Geowissenschaften at Frankfurt Göethe Universität (Germany) and

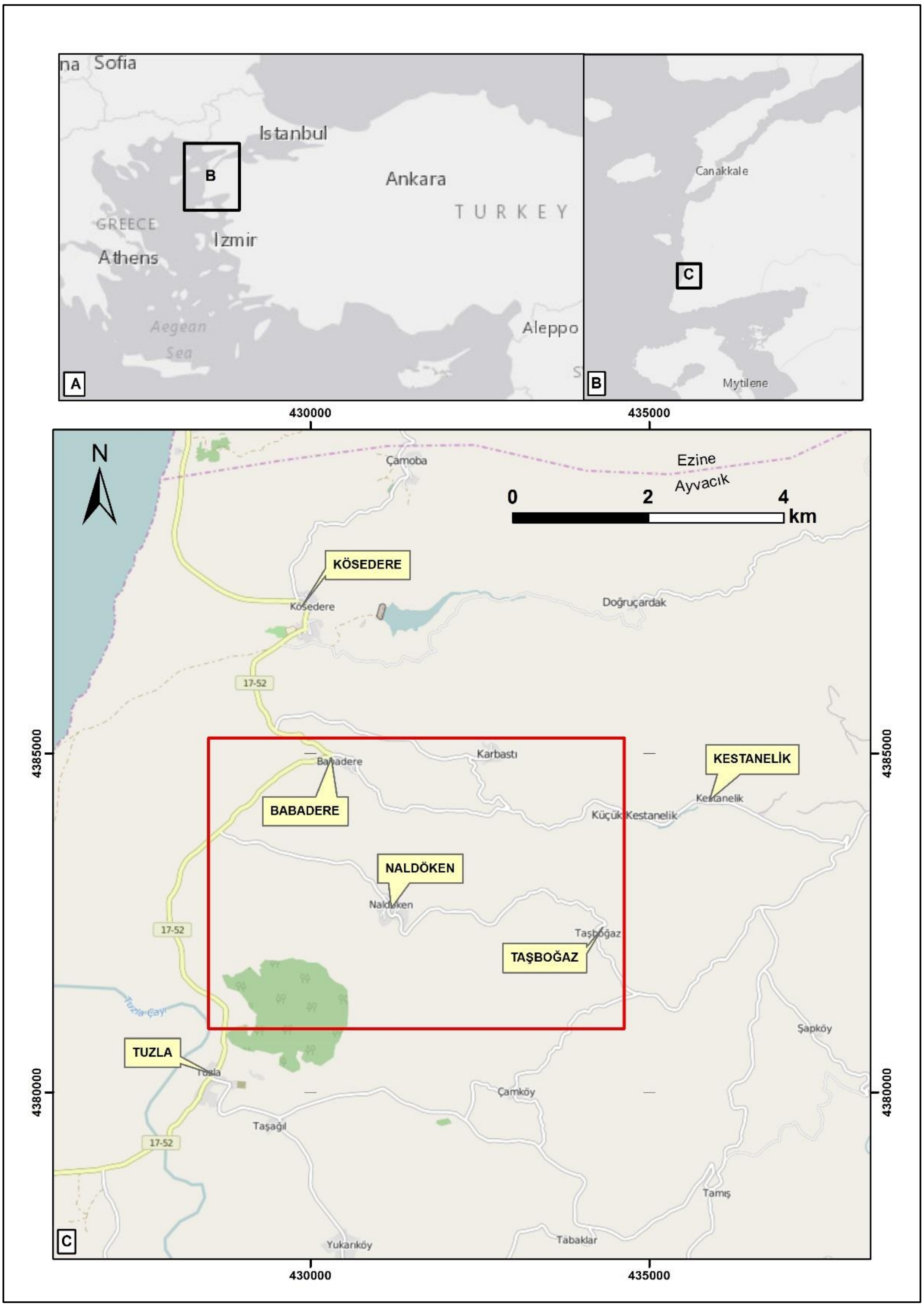

Figure 1.1: Location and access of the study area (rectangle with label 'a' represents the location of the study area). (ArcGIS basemaps; Canvas and OpenStreetMap).

Géosciences Rennes at Université de Rennes1 (France). Geochemical analysis was done in a commercial laboratory. Additional details about method of laboratory works is presented in germane chapters.

1.5. Layout of Thesis

This thesis was organized into eight chapters. The first Chapter introduces rationale, purpose and scope, accessibility, method of study and sponsors of the thesis. Chapter 2 summarizes previous studies about porphyry and epithermal type deposits' main characteristics and gives an overview on both regional and local geological background studies. Stratigraphic scheme of the study area and its mineralization is stated and discussed in Chapter 3. Chapter 4 is concerned with structural features and their kinematic analysis and possible control of these structural features on mineralization. Chapter 5 documents the results of U-Pb and Ar-Ar analysis. In Chapter 7, whole rock geochemistry data is presented and interpreted. Data evaluation and evolutional history of the study area are presented in Chapter 7 where temporal concerns of mineralization is also utilized. Concluding remarks about the thesis and future work recommendations are stated in Chapter 8.

1.6. Thesis Support

The cost of geochronological and geochemical analyses and fieldwork logistics including accommodation, meals and daily transportation was supported by Teck. They also gave me an opportunity to use some licensed computer software programs.

CHAPTER 2

BACKGROUND STUDIES

"…more modern work needs to be done to determine ages more precisely to understand the tectonic history of the Biga Peninsula and its links to the geology of Bulgaria and Greece…"

(Burchfiel, et al., 2008)

Above quotes is drawing a safe path for scientists who are working in the Biga Peninsula. Therefore, importance of working in a rigorous way on the specified time range or rock units are necessary to understand the geological complex history. And, this understanding starts with a well-documented broad literature survey.

2.1. Introduction

In this chapter, previous studies was overviewed at different scale of geological domains as zooming in from Eastern Mediterranean to Western Anatolia to Biga Peninsula to the scoped area. One of the chapter topics was giving an introductory idea about what the porphyry and epithermal deposit is. At the end of this chapter, a summary section will be emplaced to give a serviceable literature information for exploration purposes about the region.

2.2. Overview on Porphyry and Epithermal Deposits

Porphyry and epithermal deposits are sources of gold with a good proportion among gold-bearing systems (Simmons & Brown, 2006). These deposits are closely associated with magmatism (Figure 2.1) that mostly, although not exclusively, is associated with magmatic arcs within convergent geodynamic settings. They involve mainly magmatic-hydrothermal and meteoric fluids that form porphyry Cu-Au-Mo deposits, epithermal Au-Ag, Ag-Zn-Pb and Au-Cu deposits, and Cu-Au and Zn-Pb-Ag skarn deposits (Seedorff, et al., 2005). Some of the largest examples from different metallogenic belts are;

- the Late Cretaceous, calc-alkaline, Pebble porphyry Cu-Au-Mo deposit, Alaska, USA, ~107 Moz Au (Gregory, et al., 2013)
- the Pliocene, high K, calc-alkaline Grasberg Cu-Au-Ag porphyry deposit, Indonesia, ~83 Moz Au (Cooke, et al., 2005)
- the Pleistocene, alkaline, low-sulfidation epithermal Ladolam Au deposit, Papua New Guinea, ~46 Moz Au (Blackwell, et al., 2014)
- the Early Cretaceous, calc-alkaline, high-sulfidation, epithermal Pueblo Viejo Au-Ag-Cu deposit, Dominican Republic, ~25 Moz Au (Richards, 2013)
- the Miocene, alkaline, Au porphyry deposits, Turkey, ~17Moz Au (Juras, et al., 2010)

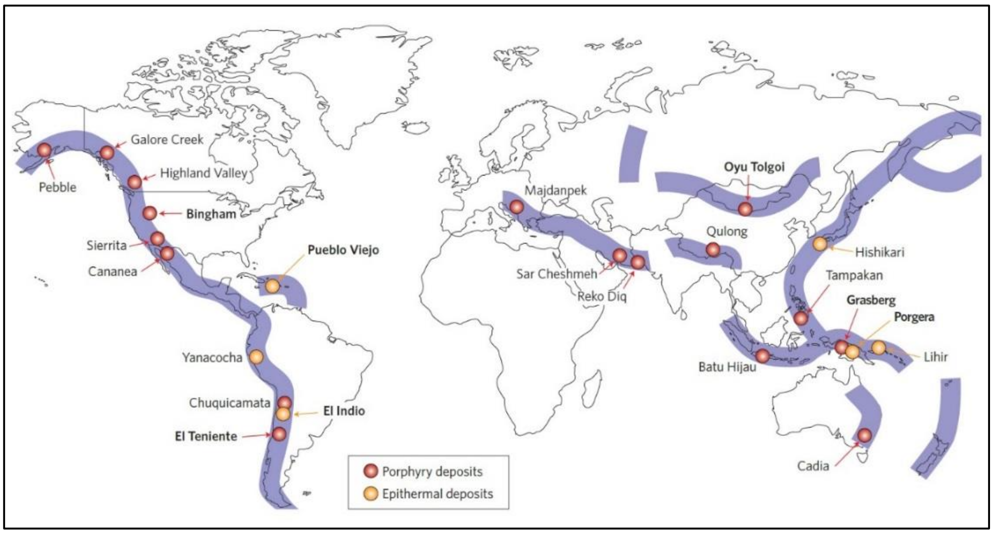

Figure 2.1: Giant ore deposits and significant arc-related metallogenic belts (purple lines) (Richards, 2013).

Most Au-bearing porphyry Cu and epithermal deposits are associated with the emplacement of upper-crustal magma chambers (Tosdal, et al., 2009) (Figure 2.2) at shallow crustal levels. Approximate depth of these deposits are thought to be at <1.5 km for epithermal and <6 km for porphyry deposits (Seedorff, et al., 2005). Due to the shallow depth of emplacement, it is uncommon to discover geologically old (Palaeozoic or older) deposits since low preservation potential (Simmons, et al., 2005).

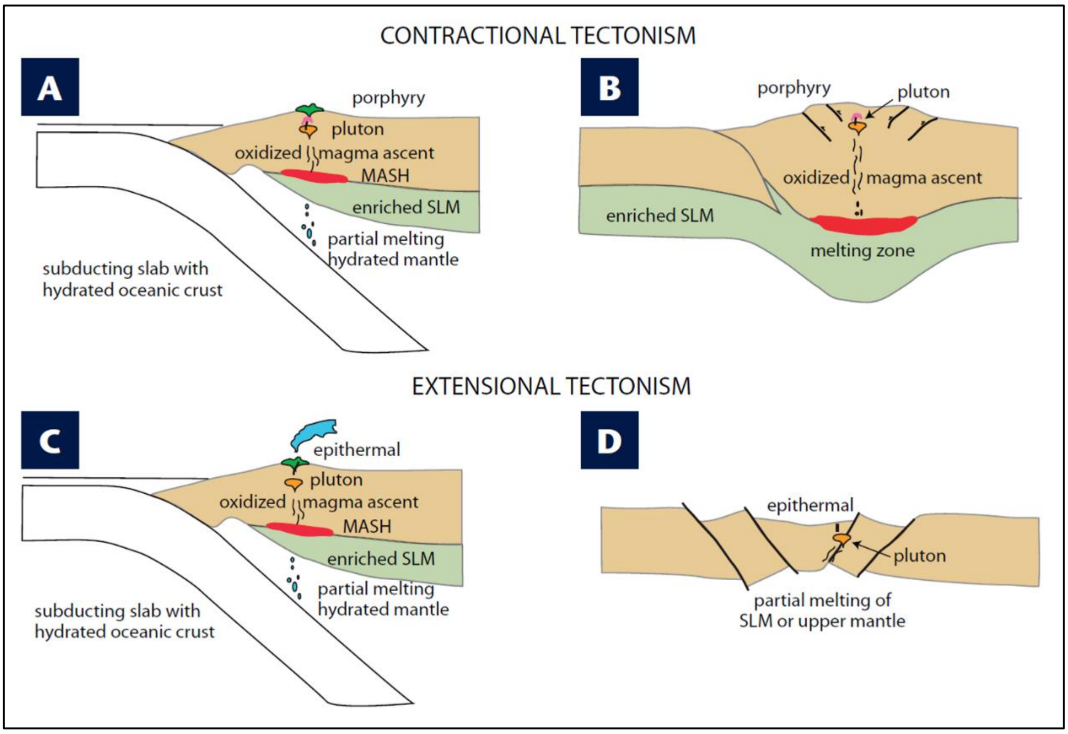

Figure 2.2: Tectonic setting of porphyry Cu and epithermal deposits. Porphyry Cu–Au deposits form at the end of magmatic episodes during contraction, dominantly in a convergent plate margin undergoing collision (A) or soon after collision (B). In contrast, epithermal deposits are associated with extension at the convergent plate margin (C) or (D) in a rift zone. MASH: zone of crustal melting and assimilation, magma storage, and homogenization. SLM: sub-lithospheric mantle (Tosdal, et al., 2009).

Varied relationships between porphyry-epithermal systems and precursor plutons were identified by many workers. Sillitoe (2010) noted that most of them are typically multiphased, equigranular and commonly of batholithic dimensions with dioritic to granitic compositions. He also explained that precursor plutons could be an actor of single deposit, as at Mount Polley, British Columbia or clusters of two or more discrete deposits, as in the El Abra intrusive complex, northern Chile.

2.2.1. Porphyry Deposits

Porphyry deposits currently maintain almost three-quarters of the world's Cu, half the Mo, perhaps one-fifth of the Au, most of the Re, and minor amounts of other metals like Ag, Pd, Te, Se, Bi, Zn, and Pb (Sillitoe, 2010). Porphyry deposits are magmatic-hydrothermal deposits in which sulfide and oxide ore minerals are precipitated from aqueous solution at elevated temperatures (Seedorff, et al., 2005). Porphyry-type systems are spatially and genetically associated with porphyritic intrusions and the stocks are of calc-alkaline to alkaline in composition and oxidized (Tosdal, et al., 2009). Tosdal et al., (2009) and many other workers (Richards, 2003; Simmons, et al., 2005; Seedorff, et al., 2005; Sillitoe, 2010; Sun, et al., 2015) explained occurrence stages of porphyry deposit formation as follows:

- Convecting magma reaches saturation in the lower-pressure parts of the magma chamber, thus top of the magma chamber become water saturated, forming a bubble-rich froth.
- Rise of fluids fractures hydraulically the overlying rock, allowing magma to rise as narrow plugs and dikes. Magma rising is accompanied by a pressure drop, vapor loss and pressure-quenching, thus forming the characteristic aplitic groundmass of the porphyry intrusions.
- Massive hydrofracturing of wall rocks and stocks creates the pathways for ascent of magmatic fluids from the cupola.
- The exsolved, water-rich volatile phase condensed at the top of the magma chamber comprising a range of water-soluble volatile components, such as Cl and S species.

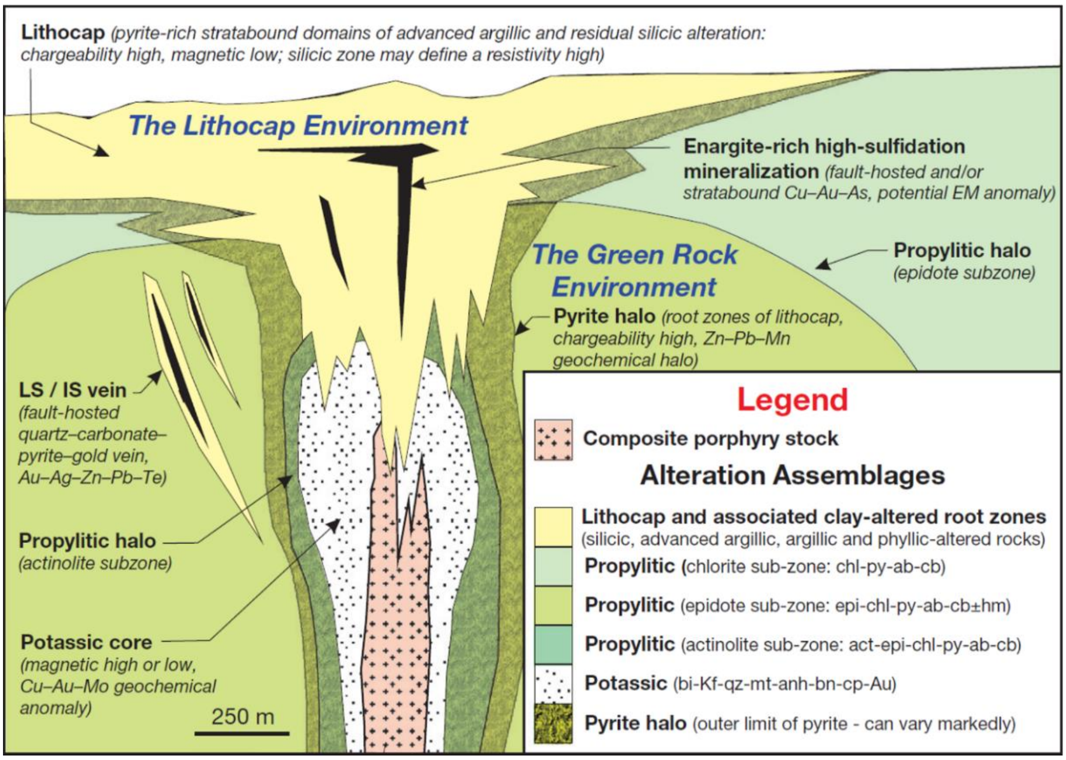

Figure 2.3: Schematic illustration of alteration zoning and overprinting relationships in a porphyry system and other epithermal systems, taken from (Cooke, et al., 2014) and references there in (ab, albite; act, actinolite; anh, anhydrite; Au, gold; bi, biotite; bn, bornite; cb, carbonate; chl, chlorite; cp, chalcopyrite; epi, epidote; gt, garnet; hm, hematite; Kf, K-feldspar; mt, magnetite; py, pyrite; qz, quartz).

At these stages; gold transported predominantly as $AuCl_2^-$ at high temperature (Williams-Jones, et al., 2009), which is around 400°C for the porphyry environment (Hemley & Hunt, 1992). Gold-bearing sulfide minerals are deposited with the potassic alteration assemblages (Figure 2.3) in association with chalcopyrite and bornite as disseminations in wavy or ductilely deformed, straight-walled, quartz-rich or sulfide-only veins (Tosdal, et al., 2009). In the porphyry environment, mineralization occurs in potassically altered intrusions and adjacent wall rocks (Tosdal, et al., 2009). The high-temperature fluid alters the rock to mineral assemblages, potassic alteration, consisting of quartz, K-feldspar, biotite, anhydrite and magnetite (Figure 2.3 & Figure 2.4) (Hemley & Hunt, 1992).

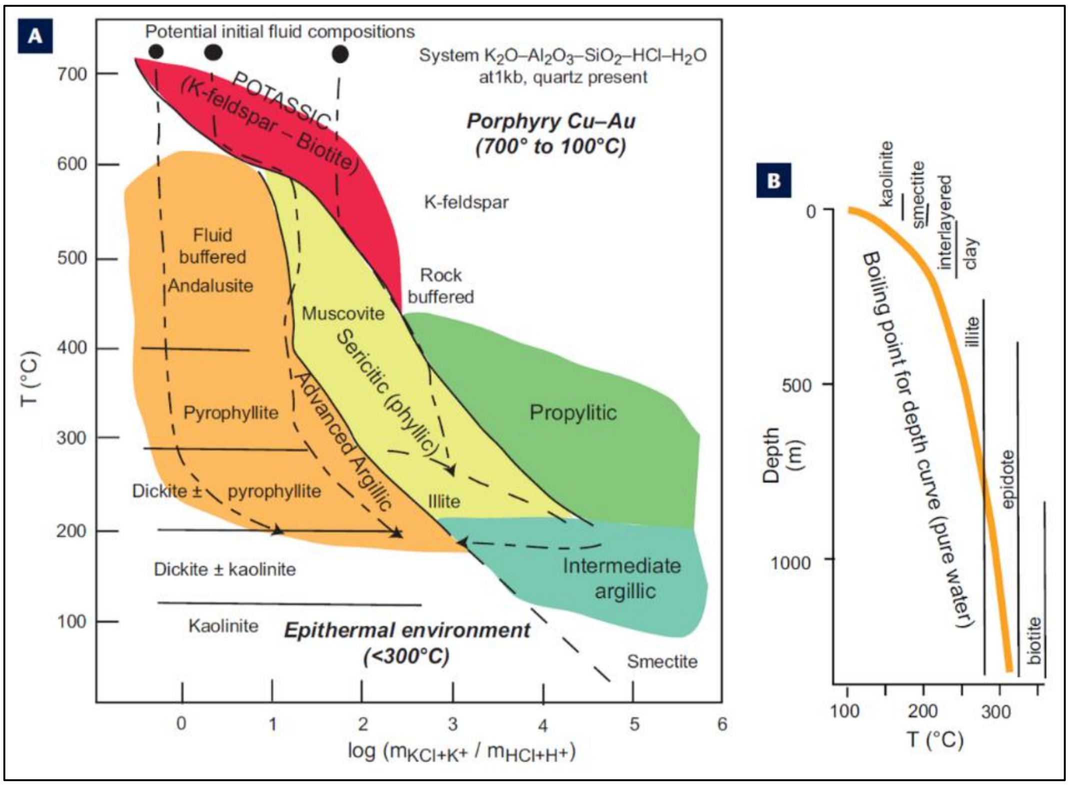

Figure 2.4: (A) Phase diagram for the system K2O–Al_2O_3–SiO_2–H_2O–KCl–HCl at PH_2O = 1 kbar, showing possible paths of fluid evolution (dashed lines) depending upon starting fluid composition. The diagram is shown in terms of temperature and the molal (m) composition of the fluid. The path at left represents a fluid-dominant alteration sequence, whereas the other two illustrate rock-buffered alterations. Different paths demonstrate the importance of the starting fluid composition on the sequence of alteration, which is in part due to different magma compositions. Late influx of external fluid into the porphyry environment forms the widespread rock-buffered intermediate argillic alteration (B) Boiling point for depth curve for epithermal deposits showing the vertical distribution of minerals in a boiling upflow zone (from Tosdal, et al., 2009 and references therein).

However, on the alkaline porphyry systems, the typical potassic alteration is characterized by Ca-bearing minerals such as garnet, diopside and actinolite (Lang, et al., 1995). Likewise Yerrington Porphyry Deposits (Nevada-USA), there is Na-Ca alteration minerals in the core, representing the influx of external non-magmatic fluids into the magma-derived hydrothermal systems (Dilles, et al., 2000). Three propylitic alteration subfacies (actinolite, epidote, and chlorite zones) can occur around the potassic- altered rocks (Cooke, et al., 2014). In Figure 2.3, the porphyry has been partially overprinted by a lithocap (silicic and advanced argillic alteration assemblages) that contains a domain of high-sulfidation epithermal mineralization and the roots of the lithocap lie within the pyrite halo to the porphyry system. Cooke et al (2014) also noted that the degree of superposition of the lithocap into the porphyry system is contingent on uplift and erosion rates at the time of mineralization. Alteration assemblages reflecting the gradual cooling of the exsolved magmatic-hydrothermal plume are stacked vertically. Mineral assemblages also depend on physicochemical changes in the fluid during the buoyant rise to shallow depths and circulating ground waters driven by thermal energy from the underlying pluton to form the propylitic alteration assemblage (Tosdal, et al., 2009).

2.2.2. Epithermal Deposits

Mined epithermal deposits provide world's 6 percent of Au and about 16 percent of Ag (Singer, 1995). Moreover, epithermal deposits have been still mined for its base metal contents; including Hg, Sb, Te, and Se (Lingren, 1933). In epithermal deposits, ore minerals' precipitation temperatures are range from ~150° to ~300°C and the depths are ranging from ~50 to ~1500 m below the water table (Simmons, et al., 2005).

There are numerous classifications of epithermal systems, and most of them are based on the characteristic hypogene mineral assembledges; they point two end member types (Figure 2.5) (White & Hedenquist, 1995; Simmons, et al., 2005):

- quartz ± calcite ± adularia ± illite (known as Low-Sulfidation)
- quartz + alunite ± pyrophyllite ±
- dickite ± kaolinite (known as High-Sulfidation)

Low-sulfidation forms in neutral pH environments (Sillitoe & Hedenquist, 2003) whereas High-sulfidation forms in acidic environments (White & Hedenquist, 1995).

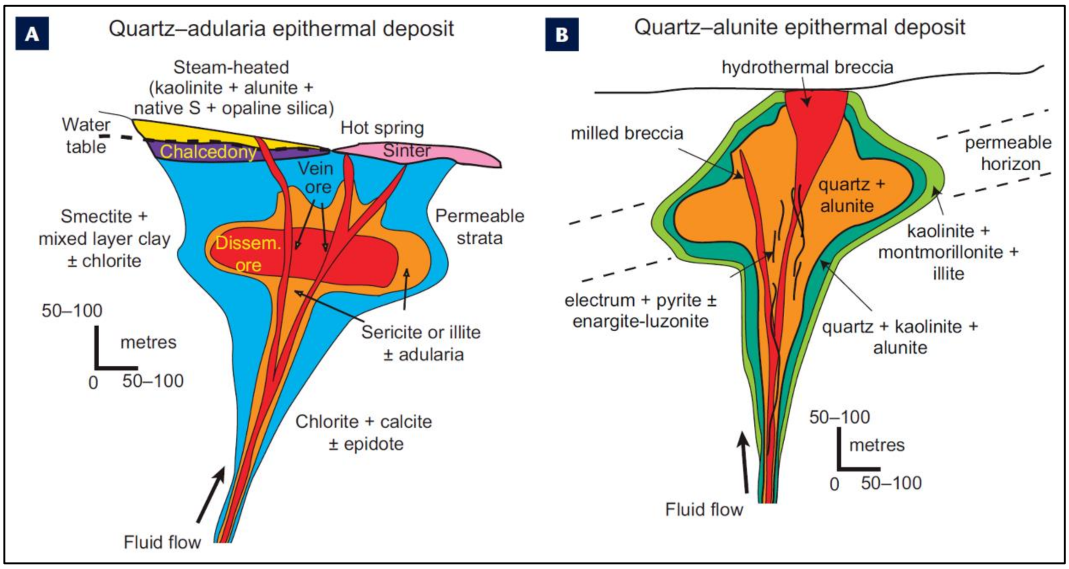

Figure 2.5: (A) Idealized cross section of a quartz–adularia epithermal deposit showing distribution of alteration assemblages. (B) Idealized cross section of a quartz–alunite epithermal deposit (from Tosdal, et al., 2009 and references therein).

Low-sulfidation epithermal deposits form due to the deep circulation of meteoric water driven principally by a shallow intrusion (Tosdal, et al., 2009). At depth, the chloride-dominated waters are near neutral pH, and contain reduced S species and dissolved CO_2; additionally the H_2S provides an important ligand for the transport of Au as a bisulfide complex (Tosdal, et al., 2009; Williams-Jones, et al., 2009). Tosdal et al., (2009) and many other workers (White & Hedenquist, 1995; Sillitoe & Hedenquist, 2003; Simmons, et al., 2005; Simmons & Brown, 2006) explained occurrence stages of low-sulfidation deposits as follows:

- The hydrothermal fluids contain small amounts of magmatic fluid, which is considered to be the source of metal precipitated in the epithermal deposits.
  - The fluid is generally in equilibrium with the host rocks and is thus rock buffered.
  - Boiling in the central up flowing fluid, the primary mechanism for sulfide deposition, is controlled by the ambient near-

hydrostatic pressure and temperature conditions, and quartz, adularia and platey calcite are deposited.

- The chloride-dominated fluid may rise to the surface and discharge, depositing sinter, or be dispersed laterally through an outflow zone, producing extensive zones of alteration and replacement.
- During boiling of the ascending fluid, dissolved CO_2 and H_2S are partitioned into the vapour, which rises to the surface and condenses into the local cool ground water, forming CO_2-rich or H_2S-rich steam-heated water.
  - The CO_2-rich ground water is concentrated along the shallow margins of the upflow zones, where a carbonate mineral–rich assemblage forms. The H_2S-rich ground water enters the vadose (unsaturated) zone, and H_2S reacts with the atmosphere and is oxidized to H_2SO_4.
- This results in steam-heated zones of alteration, in which a low-pH (<2) fluid high in dissolved sulfate alters the rocks to an advanced argillic mineral assemblage consisting of opal (cristobalite), alunite, kaolinite and pyrite as the fluid becomes neutralized near the water table.

High-sulfidation systems and its mineral assemblages are associated with acidic and oxidized fluids formed in the magmatic-hydrothermal environment adjacent to young volcanoes (Hedenquist & Lowenstern, 1994). At initial stage, these systems are facing extensive leaching of the host rocks by pH<2 fluids and characterized by magmatic vapours like H- and O- isotopic compositions (Roger, 1987). Intense silica residue (>95 wt% SiO_2) and ore mineral formation (Au bearing Cu and Fe sulphides) is the result of leaching on high-sulfidation epithermal deposits (Hedenquist & Lowenstern, 1994). Fluid–rock interactions form cations and neutralization the acidic fluid and lead to the precipitation of alunite, pyrophyllite, dickite, quartz, anhydrite, diaspore, topaz, kaolinite and illite (Tosdal, et al., 2009).

Hemley & Hunt (1992) and many other researchers have discerned stable-isotope and mineralogical similarities between high-sulphidation deposits and advanced argilic zone cap of pophyry deposits and nowadays it has also been widely proved that there is a close spatial relationship of high-sulfidation and porphyry deposits. Hedenquist & Lowenstern (1994) was further studied the similarities of these deposits and made a conclusion in the sense of conditions on decreasing salinity and temperature along the way from porphyry to high-sulfidation epithermal systems.

2.2.3. Geothermal Systems

Alternative energy sources demand created predisposition towards geothermal exploration and so drilling and development especially in New Zealand, Japan, Philippines, United States, etc… (Simmons, et al., 2005). During 1980s, some pressure-temperature similarities was figured out at the epithermal deposits then, precious and base metals deposition were found in springs, wells, and surface pipes of geothermal sites, e.g. Broadlands, New Zealand or Lihir Island, Papua New Guinea (Hedenquist & Henley, 1985).

To make conception and classification of epithermal deposits, active epithermal environments in geothermal and magmatic hydrothermal systems (Figure 2.6) were important (Lingren, 1933). Figure 2.6-A represents the epithermal environment forms in a magmatic-hydrothermal system, which is dominated by acid hydrothermal fluids, where there is a strong flux of magmatic liquid and vapor, containing H_2O, CO_2, HCl, H_2S, and SO_2, with variable input from local meteoric water. Figure 2.6-B demonstrates the epithermal environment in a geothermal energy systems dominated by neutral pH chloride waters, deeply circulated water and mostly of meteoric origin, having CO_2, NaCl, and H_2S. The location of magma chambers in both A and B on Figure 2.6 are described to show long-way paths of fluid circulation before facing the ore forming environment. The travel distance of fluid will directly affect the duration of water-rock interaction.

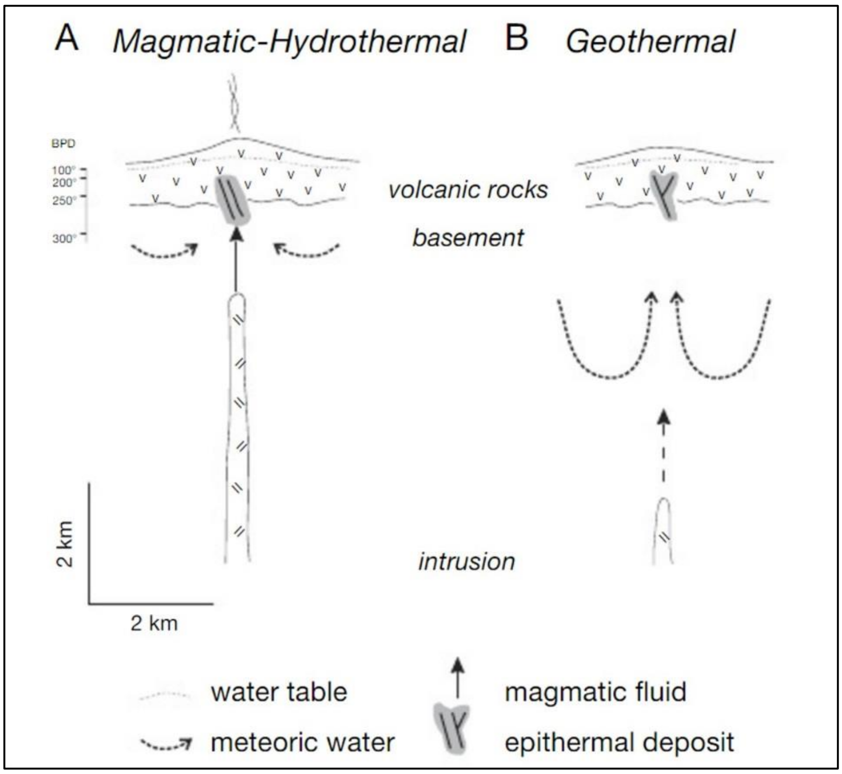

Figure 2.6: Simplified conceptual models of high-temperature hydrothermal systems, showing the relationship between epithermal environments, magmatic intrusions, fluid circulation paths and volcanic and basement host rocks (BPD-boiling point for depth) (from Simmons, et al., 2005 and references therein).

2.2.4. Duration of Deposit Formation

Time duration for formation of ore deposits is another critical phenomenon for porphyry and epithermal deposits. According to geochronological studies on porphyry or epithermal systems, the deposit form in geologically instant to wide frame with a different variety of gold flux through the time. For example, Ladolam epithermal deposit in Papua New Guinea (~46 Moz Au) could have been precipitated just in 55,000 years (Simmons & Brown, 2006). However, Tosdal, et al. (2009) mentioned the importance of considering the magmatic-hydrothermal systems, particularly a porphyry deposit, which is an integral part of a long-lived and evolving magmatic complex. A deep magma chamber, numerous intrusive events and overlapping hydrothermal systems creates this complexity as formed, cooled and been overprinted or moved to a different location by a younger hydrothermal system (Figure 2.7) (Gustafson & Hunt, 1975; Sillitoe, 2010).

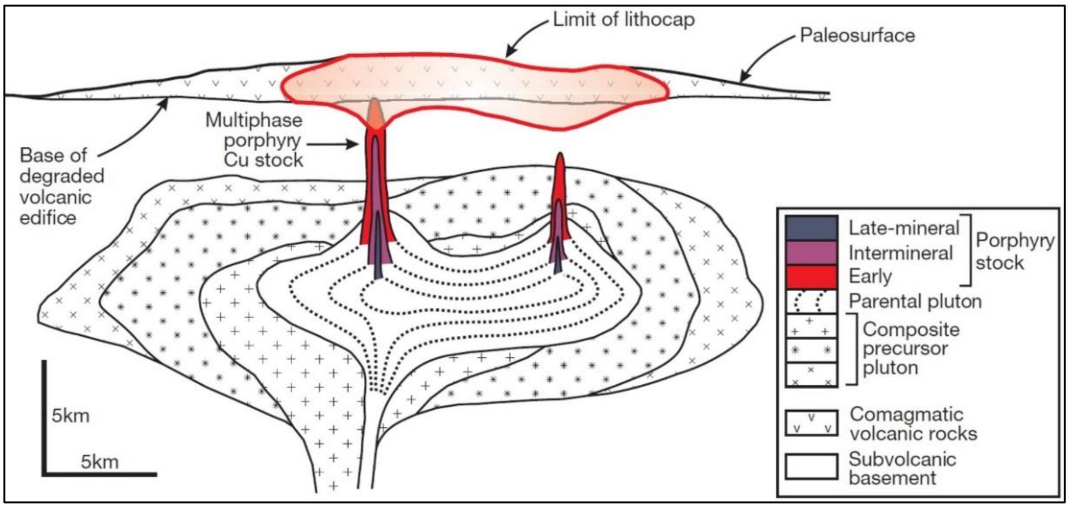

Figure 2.7: Spatial relationships between porphyry Cu stocks, underlying pluton, overlying comagmatic volcanic rocks, and the lithocap. The precursor pluton is multiphase, whereas the parental pluton is shown as a single body in which the concentric dotted lines mark its progressive inward consolidation (Sillitoe, 2010).

Moreover, Tosdal, et al. (2009) explained the duration of metal precipitation as follows:

> "Due to the rapid cooling of epithermal environment, geochronology generally classifies the multiple events. Conversely, the long-term perturbation of the thermal profile by multiple porphyry intrusions and their related hydrothermal systems, as well as by the underlying cooling batholith, may blur temporal distinctions between discrete spatially related porphyry systems, potentially detectable using modern geochronology tools. The result is an apparently long-lived and continuously operating porphyry hydrothermal system, rather than one characterized by superposed systems that may have acted episodically over a protracted period of time."

Heat transport bounds the duration of individual porphyry-related magmatic centers (Barton & John, 2010) and is the mostly used explanatory approach for duration of mineralization. The basic principle for conduction heat in solid and time range for cooling of a hot body tells the cooling time increase with half of unit distance increase (Carslaw & Jaeger, 1959). Barton & John (2010) explained the proposed relation for geological materials in porphyry systems as follows;

- Time (in years) is about $A^2/30$
    - where A is the characteristic distance in meters (half distance)
    - Example 1: 200 m wide dike, A= 100 m, cools to its original temperature in about 300 years
    - Example 2: 10 km diameter pluton, A= 5 km, cools in about 1 m.y. and reach its solidus in considerably less time.

The above-mentioned approach are similar to concluded time for the magmatic evolution of porphyry related magma chambers of Yerington batholith, USA (Dilles & Wright, 1988), Chuquicamata-El Abra Porphyry Copper Belt of northern Chile (Campbell, et al., 2006) and some other sites in the literature.

2.2.5. Structural Controls of Porphyry and Epithermal Deposits

In this section, localization of porphyry and epithermal deposits in a structural sense will be covered by the present literature knowledge. The perspective for this issue starts thinking about occurrence of linear tendency, orogeny-parallel belts, on porphyry and epithermal deposits (Richards, 2013; Sillitoe, 2010 and references therein). Moreover, Richard (2013) noted the today's well explored metallogenic belts are corresponding to whether past or present magmatic arcs and related mechanisms. Therefore, the timing of mineralization is closely linked to an equivalent magmatic event (Sillitoe, 2010). During the mineralization, the area was subjected to a spectrum of regional-scale stress regimes, ranging from moderately extensional through oblique slip to contractional, where changes in crustal stress regime are favorable times for porphyry Cu and high-sulfidation epithermal Au deposit generation (Sillitoe, 2010; Tosdal and Richards, 2001).

To some extent, the faults and/or intersections are involved in formation of mineralization sites and geometries (Sillitoe, 2010). That is why intra-arc fault systems are important localizers since they are active before and during magmatism and porphyry and epithermal mineralization. Domeyko fault system in northern Chile was active during middle Eocene to early Oligocene and forms a good example of a mineralizing fault system (Sillitoe & Parello, 2005). Moreover, some researchers emphasize the significance of conjugation of large-scale transverse fault zones or lineaments and arc-parallel structures for mineralization, as the Archibarca and Calama-El Toro lineaments of northern Chile (Figure 2.8) (Richards, et al., 2001). On the other hand, others claim that many large porphyry Cu-Au deposits are linked to adakitic rocks, which is closely associated with ridge subduction (Figure 2.8) (WeiDong, et al., 2010).

Forming a structural-tectonic model patterns emplacement mechanisms of granitoid stocks and possible ways of mineralizing hydrothermal fluids flows where there is a conjugations and duplexes of a fault systems (Drew, 2005). Overlayering the site geology and known deposits with structural-tectonic model would forecast probable area of new deposits. Tosdal and Richards (2001) comments on conditions for porphyry and epithermal deposit formation and proposes convergent margin settings (ranging from orthogonal compression to extension) and the more common intermediate stress conditions of transpression to transtension. Moreover, they explained the favorable conditions in certain ranges or phases on transpressional to transtensional settings, which are local relaxation of compressive stresses allowing for magmatic stock emplacement. Drew (2005) and many others studies have shown that fault jogs (Figure 2.9) may generate areas of extension, which are optimum localities for magma rise and potential mineralization.

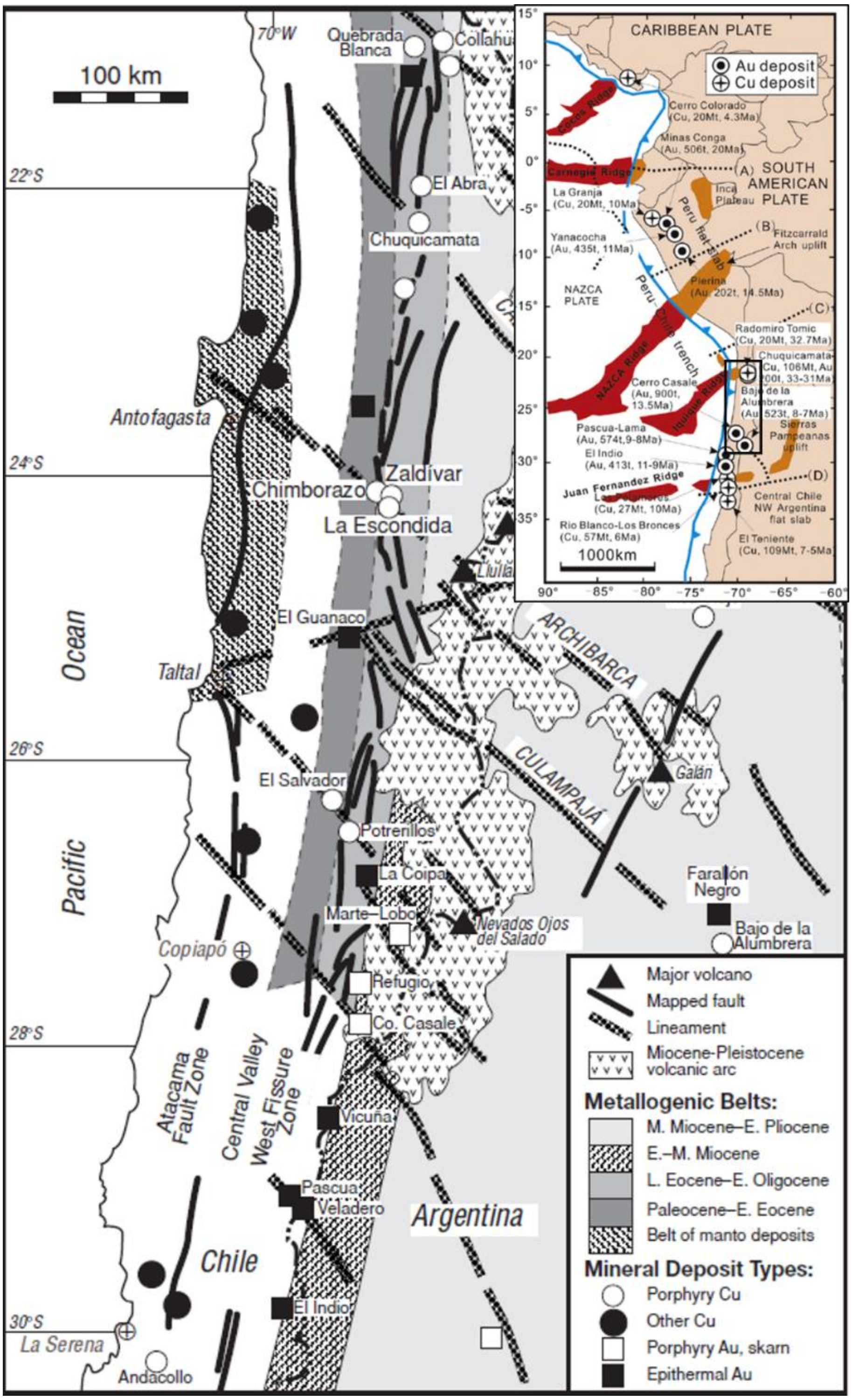

Figure 2.8: Ridge subduction and lineament relationships for localization of Porphyry and Epithermal deposits on Chile (from Richards, et al., 2001 and WeiDong, et al., 2010).

Due to the progressive stress accumulation, strike-slip fault system forms and evolves with wide variety of strain features (Figure 2.10) that are necessary channel ways for magma (dikes, stocks) (Drew, 2005) and hydrothermal activities (fluid accumulations).

According to model of Segall and Pollard (1980), zones of tensional fracturing, areas without shear, are formed at the fault tips in compressional and extensional duplexes (Figure 2.11). Deposition of porphyry mineralization requires local areas of extension without shear. The deposition of polymetallic veins, however, requires active shear and tensional fracturing in an extensional-shear mesh (Figure 2.12) (Drew, 2005).

The role of extensional-shear mesh for hosting mineralization was emphasized by Sibson (1987) as exemplified in vein- and porphyry-type deposits. Chuquicamata Cu porphyry deposit in Chile (Figure 2.13A) is a typical example of filling the entire fault duplex. It is explained as conjugate fractures (an extensional-shear mesh) between major strike-slip faults that had controlled the emplacement of the porphyry stock and the hydrothermal deposition of quartz and sulfides. Martha lode system, Waihi, New Zealand form a good example of a vein-type mineralization as explained by Sibson (1987). It is an extensional-shear mesh hosts gold-bearing veins system (Figure 2.13B). The ore trapped in tensional segments of the extensional-shear mesh observed in plan and cross sectional views of the mine.

One of the proposed tectono-structural model was proposed by Drew (2005); he worked on the Late Cretaceous porphyry copper and polymetallic vein deposits in the Srednogorie region of Bulgaria. On this area, porphyry copper deposits are most commonly localized at the corners, and occasionally along the edges, of strike-slip fault duplexes. Moreover, some vein-type deposits were also identified at interior sites of the duplexes (Figure 2.14).

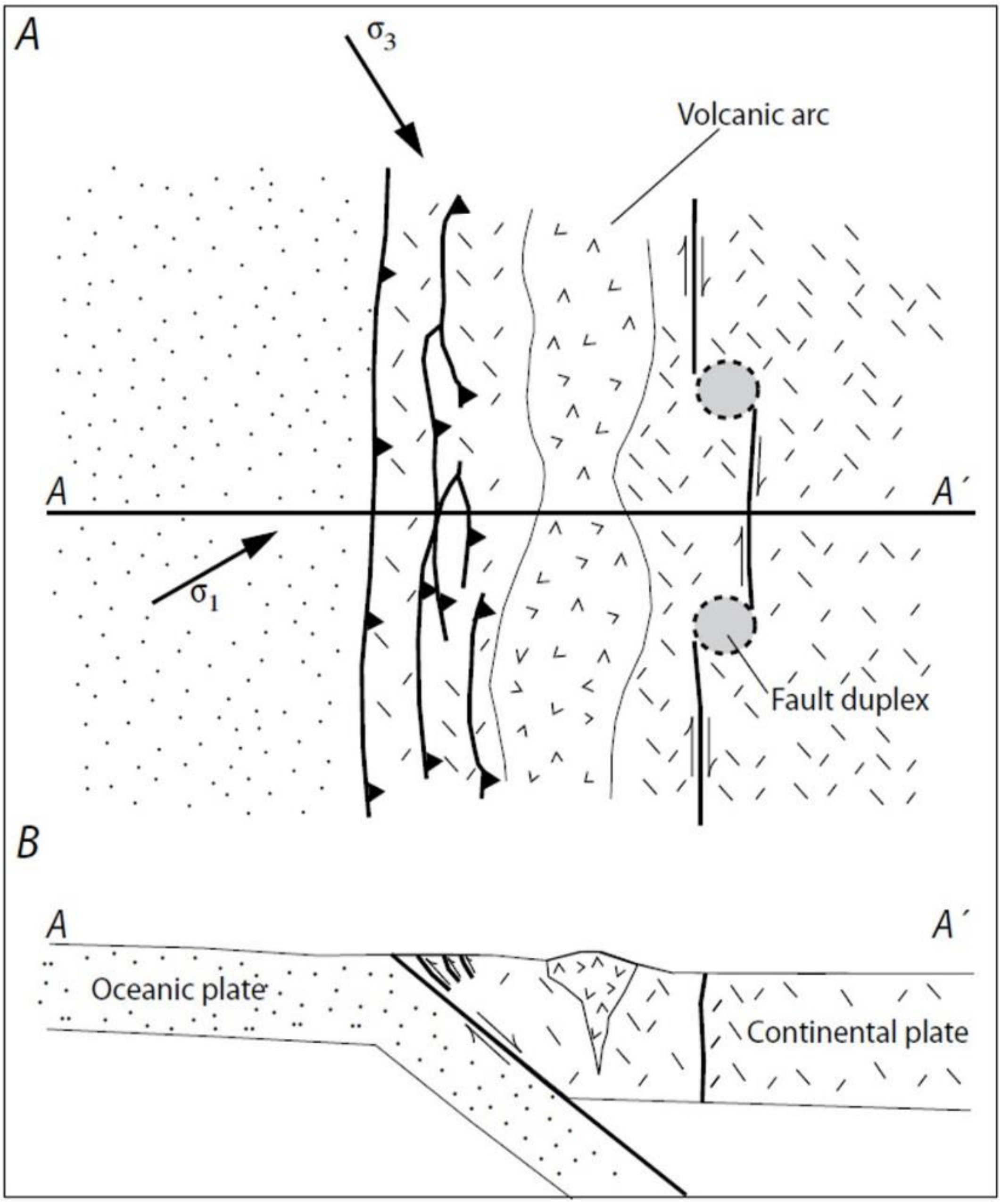

Figure 2.9: Location of strike-slip fault duplex structures along an active tectonic-plate margin. Strike-slip fault is right-lateral and has left and right stepovers. A, Map view; B, Cross section. (σ_1, maximum principal stress; σ_3, minimum principal stress) (from Drew (2005) and references therein).

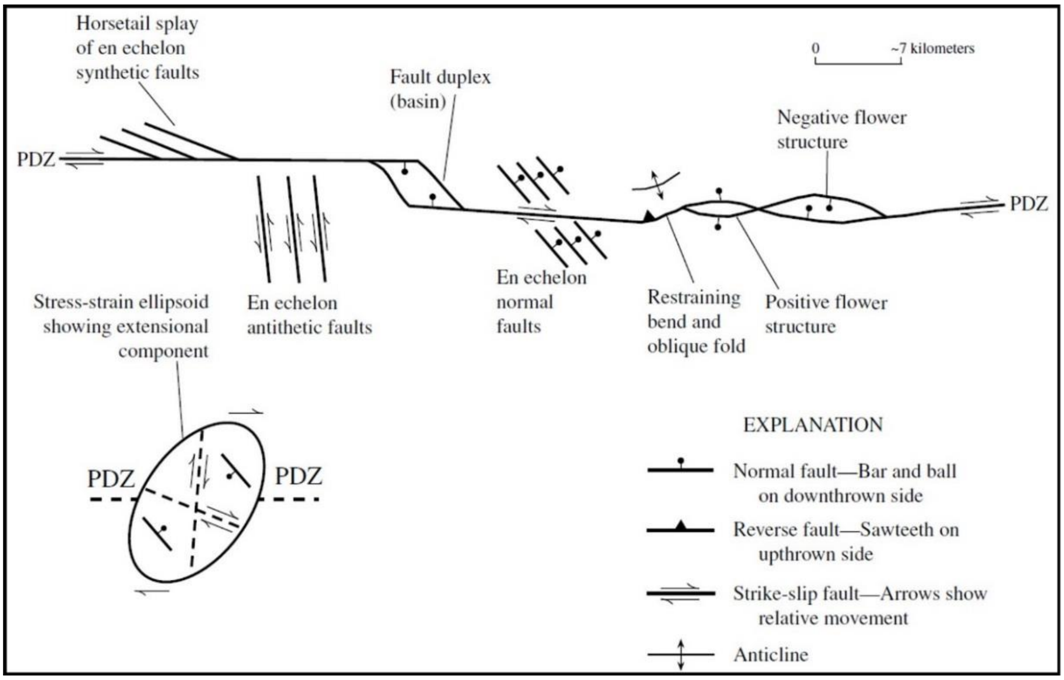

Figure 2.10: Some of the strain features developed in the principal deformation zone of a strike-slip fault system (Taken from Drew (2005) and references there in).

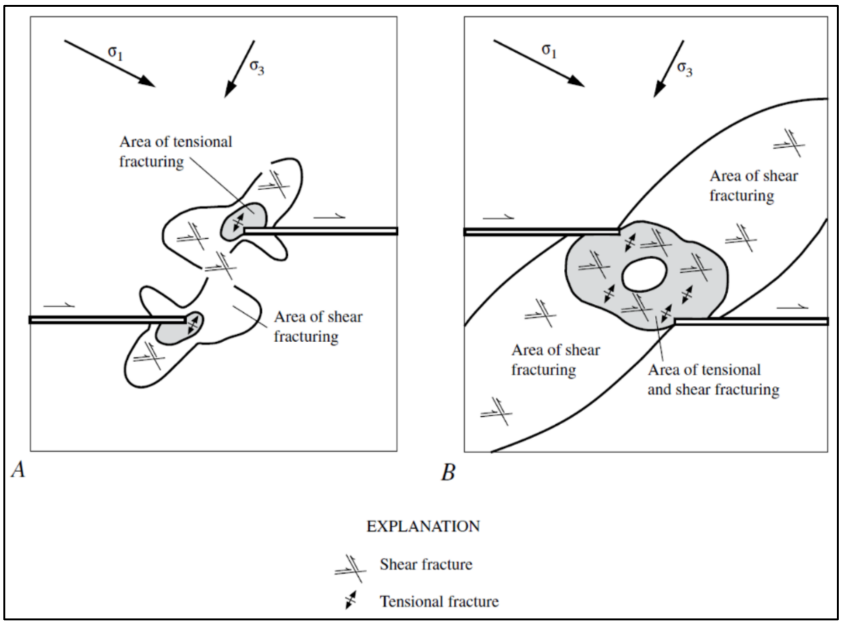

Figure 2.11: Areas of tensional and shear fracturing between the tips of two interacting master strike-slip faults in a right-lateral system. A, Compressional duplex; B, Extensional duplex (σ_1, maximum principal stress; σ_3, minimum principal stress) (from Drew 2005 and references therein; Segall and Pollard 1980).

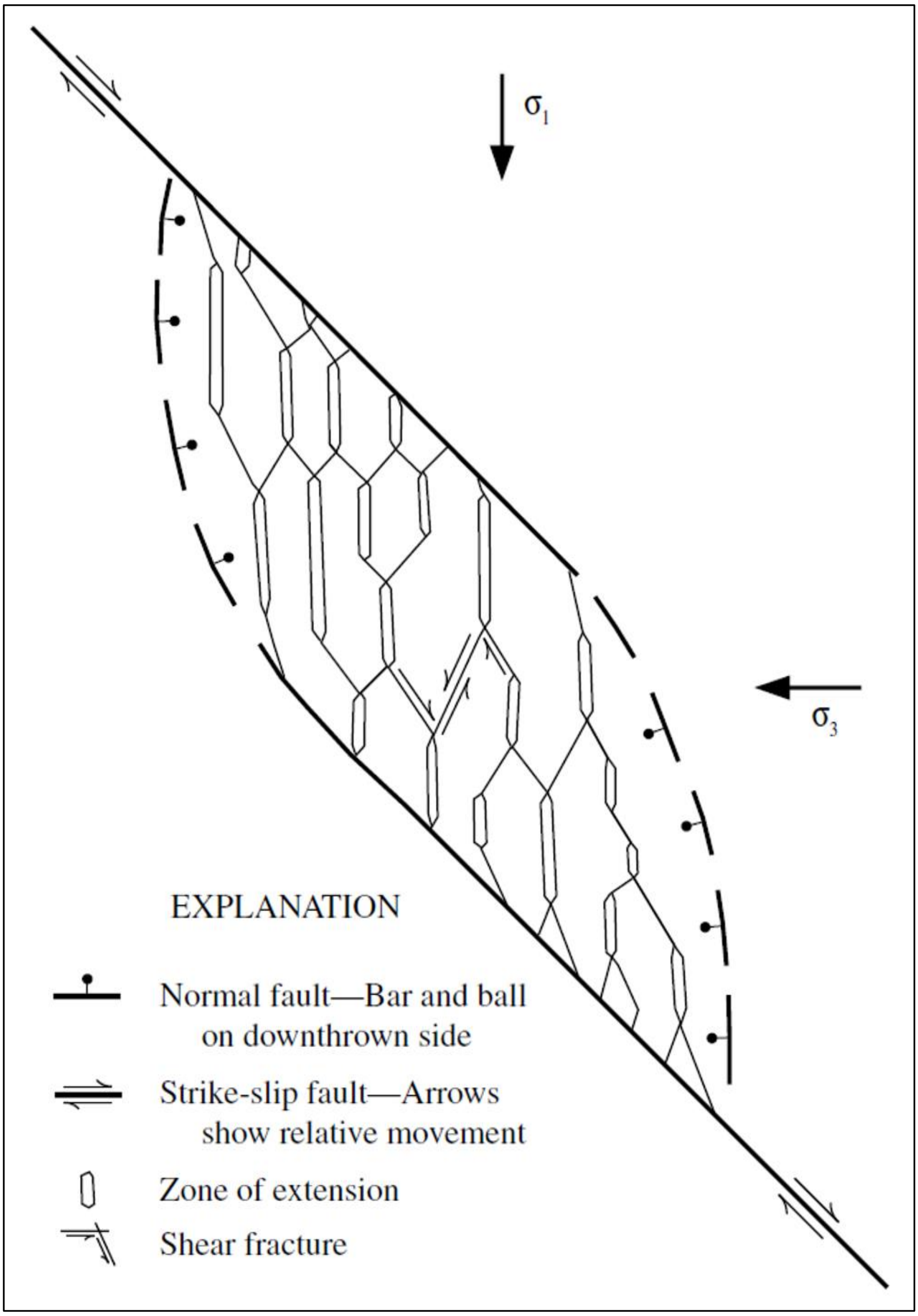

Figure 2.12: The extensional-shear mesh of a brittle fracture within a strike-slip duplex. Polymetallic veins are deposited along zones of extension connected by shear fractures (σ_1, maximum principal stress; σ_3, minimum principal stress) (from Drew 2005 and references therein; Sibson 1985).

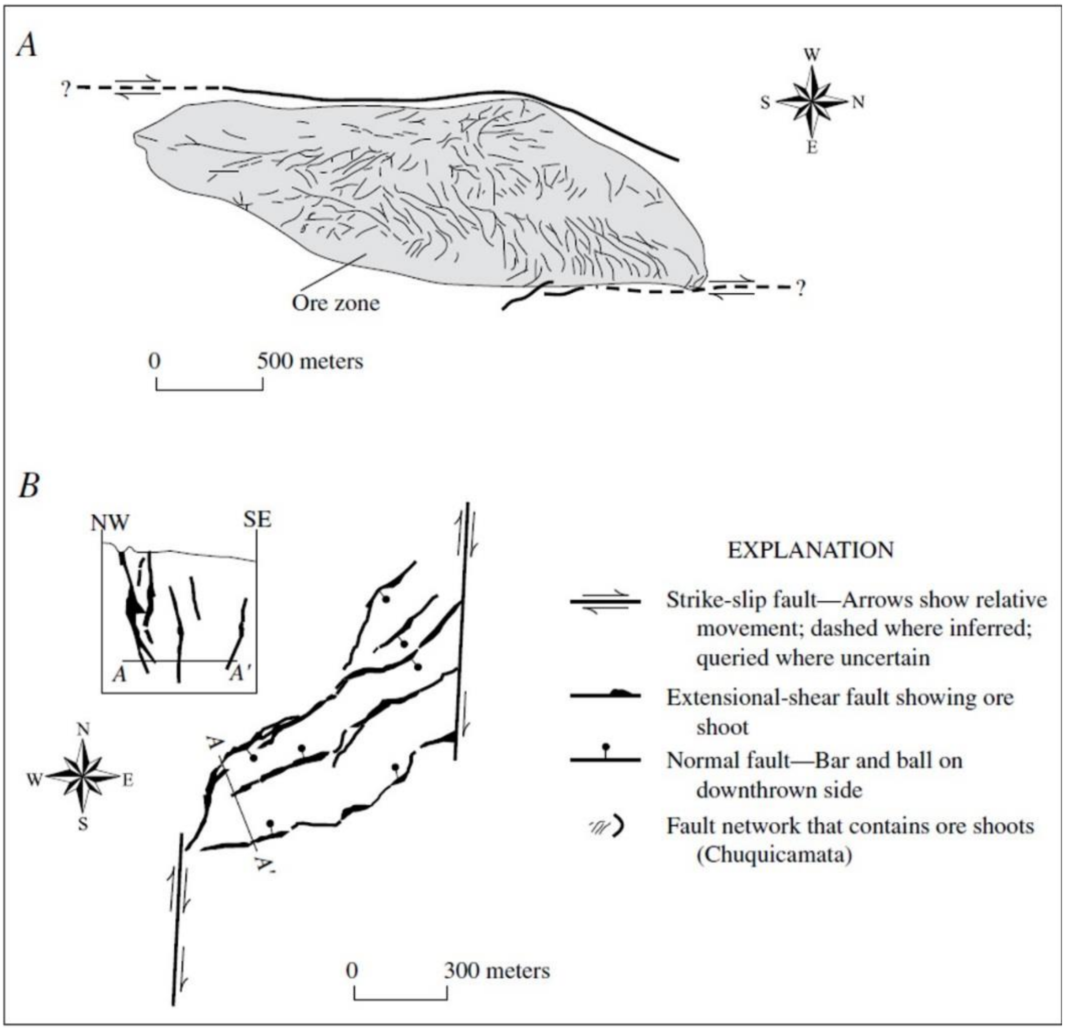

Figure 2.13: Examples of mineralized strike-slip fault duplexes. A, Map view of Chuquicamata, Chile; B, Martha lode system on the #9 level, Waihi, New Zealand (from Drew 2005 and references therein; Sibson 1987).

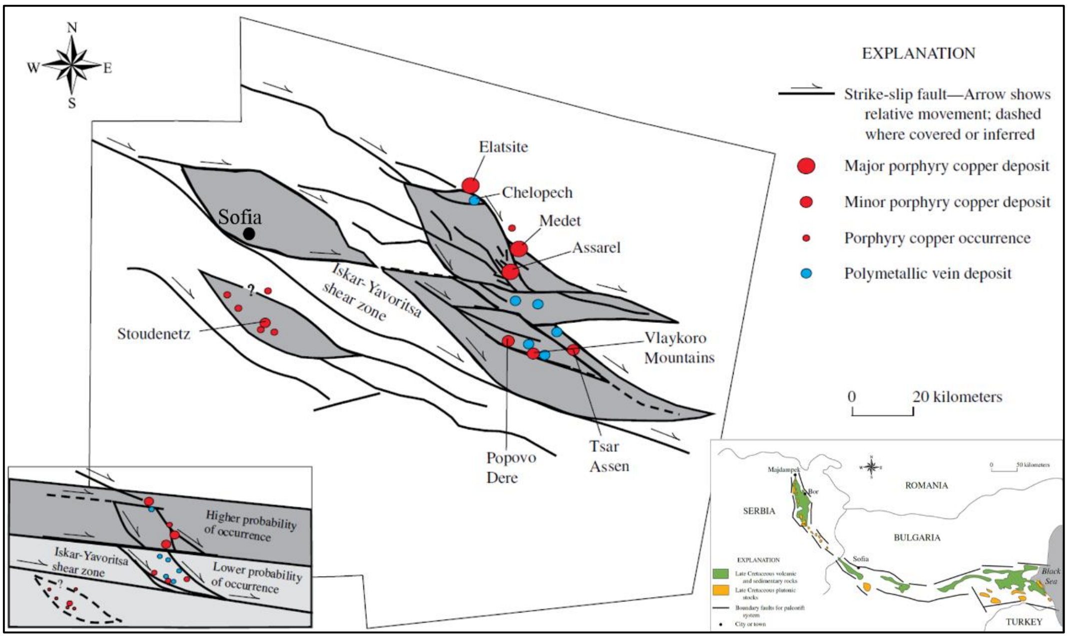

Figure 2.14: Map showing relations between porphyry copper deposits and their hosting strike-slip fault duplexes (shaded gray) in the west-central Srednogorie region, Bulgaria. Interpretation of additional faults based on geologic data from maps and satellite images. The numbered duplexes are discussed in text. Inset map shows interpretation of strike-slip duplex formation and the relative probabilities of occurrence of porphyry copper and polymetallic vein deposits relative to the location of the Iskar-Yavoritsa shear zone (Drew, 2005).

2.3. Geological overview of Biga Peninsula

Anatolia is located on the eastern Mediterranean region (Figure 2.15). It is formed by amalgamation of several tectonic fragments that are separated by suture zones marking the closure of branches of Tethyean oceanic basins (Paleotethys and Neotethys), which partly overlap in time (Şengör, 1979; Şengör and Yılmaz, 1981). Paleotethys was essentially a Paleozoic-Early Mesozoic ocean and Neotethys, Mesozoic-Early Tertiary ocean (Bozkurt and Mittwede 2001). There is no agreement on their definitions and paleogeographic locations. Considering the time range of rock units and geological processes discussed in this thesis, an overview about the closure of Neotethys and its corresponding magmatism, and post-orogenic processes will be given below.

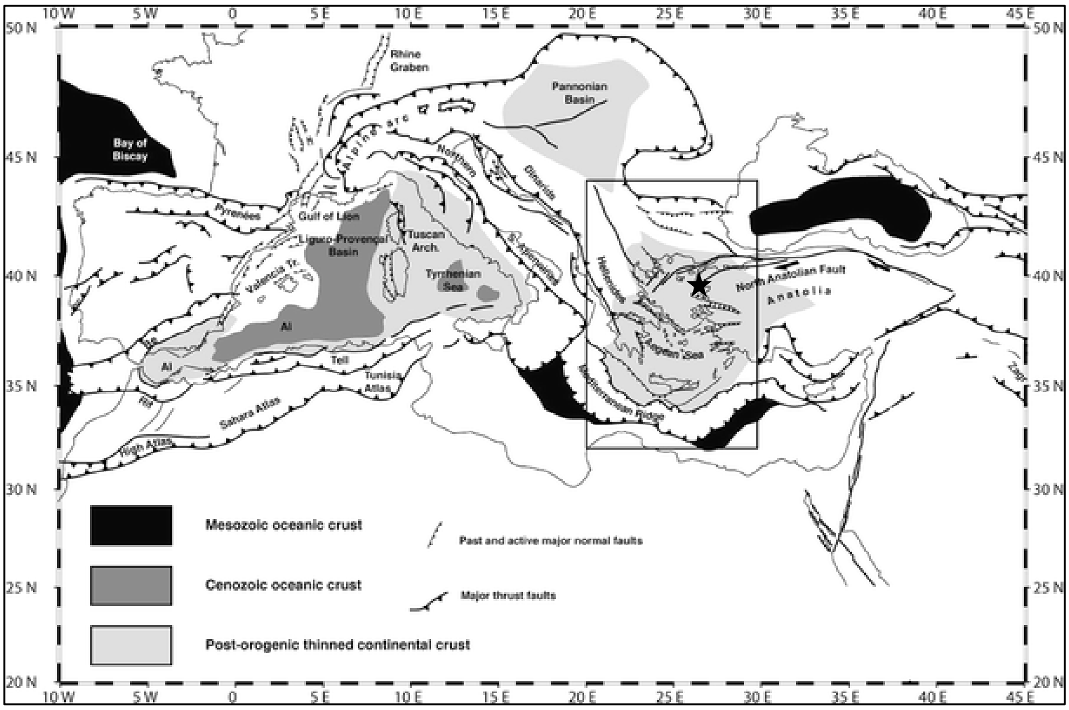

Figure 2.15: Tectonic map of the Mediterranean region and the location of the studied area. The main compressional and strike-slip features are highlighted as well as the major extensional basins, see Figure 2.16 for rectangle area (Jolivet and Brun, 2010). Black star is showing the location of Biga Peninsula.

Turkey’s major Neotethyan suture zones, from north to south, are İzmir-Ankara-Erzincan, Intra-Pontide, Inner-Tauride, Antalya amd Southeast Anatolian; they are marked by complete or partial ophiolite complexes and ophiolitic mélanges (e.g., Şengör and Yılmaz, 1981; Okay and Tüysüz, 1999). Northward subduction of northern branches of Neotethyan Ocean beneath the Sakarya Continent during late Cretaceous has resulted in collision of Anatolide-Tauride continental fragments with Pontides (Şengör and Yılmaz, 1981). According to the literature, pre-middle Eocene has been pointed for the timing of this collision (Okay and Tüysüz, 1999).

Today, Aegean-Cyprian (Figure 2.16) subduction zone, located between Hellenides-Anatolia and Africa, is the ongoing subduction of the remaining Neotethys Ocean (Şengör and Yılmaz, 1981). Le Pichon and Angelier (1979) has stated the slab retreat of the African Plate and southward migration of associated magmatism as the main cause and triggering mechanism of Aegean extension. Brun and Sokoutis (2010) claimed that Aegean back-arc extension driven by slab roll-back commenced around 45 Ma ago, then there are stages of acceleration of roll-back processes (see Jolivet et al., 2015 and references therein). Additionally, Jolivet and Brun (2010) measured the accommodated trench retreat as approximately 700 km.

Post-collisional extension emerged the core complexes all along the Aegean region. Those are Menderes Massif as the largest one, Rhodope, Kazdağ, Cyclades and Crete massifs (e.g., Buick, 1991; Dinter and Royden, 1993; Bozkurt and Park, 1994; Gautier and Brun, 1994; Vandenberg and Lister, 1996; Okay and Satır, 2000). In addition to exhumation of metamorphic assemblages, Western Turkey is also characterized by widespread coeval occurrences of volcanic rocks (lava flows and pyroclastic materials) and genetically associated hypabyssal rocks, and granitoid bodies (Bozkurt and Mittwede, 2005). According to many previous workers, Western Turkey's magmatism evolved at three distinct and continuous geochemical phases has occurred as follows (Aldanmaz, 2002; Ersoy and Palmer, 2013):

- Late Eocene–Middle Miocene phase with orogenic character; calc-alkaline to dominant high-K calc-alkaline to shoshonites;
- Late Miocene–Early Pliocene alkaline phase;
- Pliocene–Quaternary phase, characterized by Na-enriched alkali basalts with an oceanic island basalt (OIB) signature.

Due to the current back-arc environment with marine condition of the subduction in the Aegean, understanding of the geology of Biga Peninsula is significant owing to its broad exposures of igneous and metamorphic assemblages and major structures that enlist the dynamics of Aegean extension, exhumation and extrusion (Black et al., 2013).

Recent improvements in understanding deformation processes in the Aegean have led us to review the initiation age of extension and evolution. Philippon et al. (2014) stated that it is appropriate to describe Aegean extension as a two-stage process.

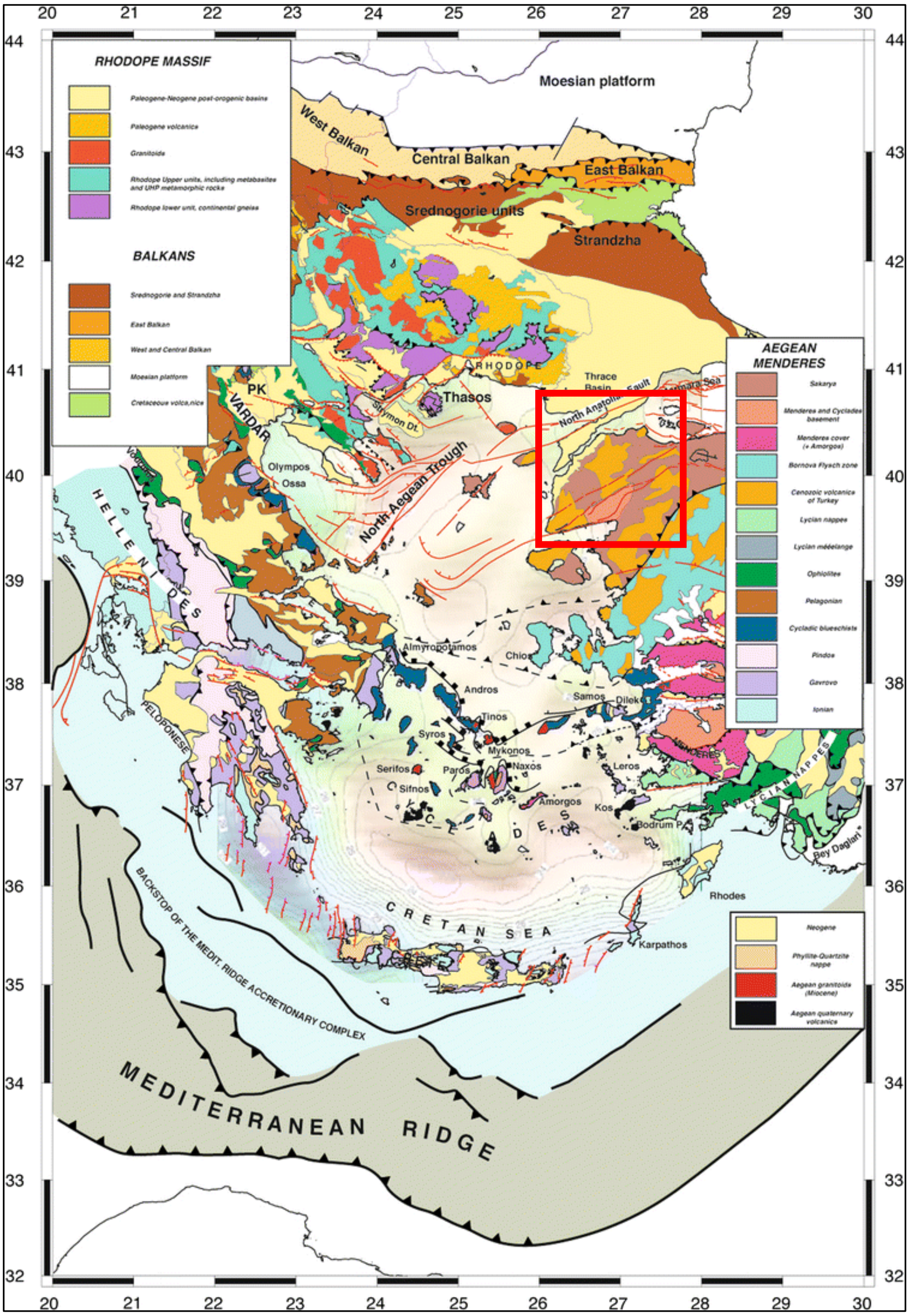

Figure 2.16: Compiled tectonic map of Jolivet and Brun (2010) and references there in for the Aegean region, Menderes massif, Rhodope massif and the Balkan. Reddish rectangle is showing the location of Biga Peninsula.

The first stage is starting from mid-Eocene (45 Ma) to middle Miocene (13 Ma). Brun and Sokoutis (2010) stated that trench retreat velocity was presumably lower than 1.0 cm $.y^{-1}$ and extension was mostly compensated by the exhumation of metamorphic rocks (Bozkurt, 2000) during this first stage. From middle Miocene to present is the second stage and characterized by increasing trench retreat velocity as 3.3 $cm \cdot y^{-1}$ (McClusky et al., 2000), causing to the development of extensional basins within a horst and graben structure (Mascle and Martin, 1990). During this second stage of Aegean extension, metamorphic core complexes was segmented, which were exhumed during the first stage. Philippon et al., (2014) model the Aegean region to understand mechanical meaning of the present day displacement fields. Figure 2.17 summarize the model according to the above-mentioned two stage extension-retreat relations, providing a simple scenario for the history of interaction between trench retreat and Anatolia escape since middle Miocene.

Geology of the Biga Peninsula (Figure 2.18) is characterized by the distributed occurrence of metamorphic-ophiolithic basement rocks (Okay & Satır, 2000), plutonic and associated volcanic and volcano-sedimentary rocks, related to the transition from a collisional to an extensional tectonic regime during the Cenozoic (Yılmaz et al., 2001).

The metamorphic and ophiolithic units of Biga Peninsula are named as Çamlıca metamorphics, Ezine Grup, Denizgören Ophiolites, Çetmi Mélange and Kazdağ Massif.

- Çamlıca metamorphics were undergone metamorphism under eclogite facies conditions during the Maastrichtian, 65-69Ma (Okay & Satır 2000)
    - Exposed on the western most part of the Biga Peninsula.
    - Tectonically separated from the Denizgören ophiolite in the west by the 33-km-long Ovacık fault.
    - Şengün, et al. (2011) stated that Çamlıca metamorphics contain high-pressure metamorphic slices (eclogite/blueschist) that formed in a subduction-accretionary complex in contrast to previous interpretations as whole high pressure metamorphism.

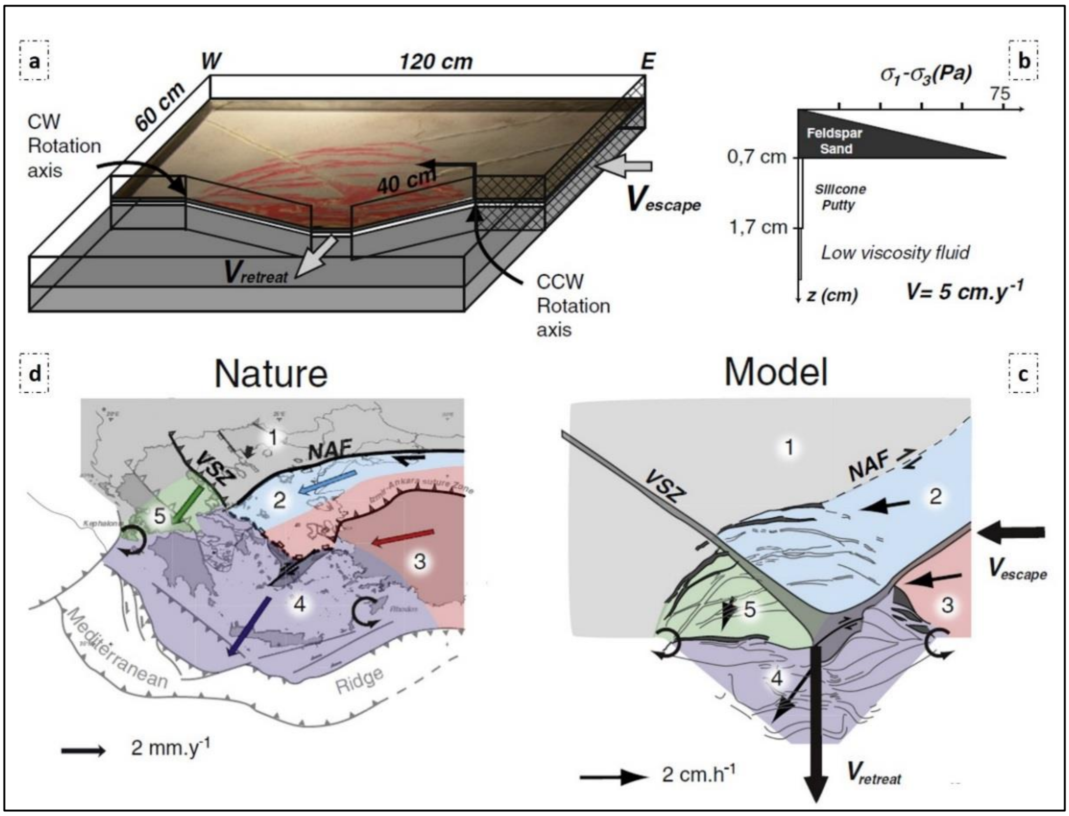

Figure 2.17: Comparison study of Philippon et al. (2014) and the velocity domains in the Aegean (a). (b). 3D sketch of experimental setting and strength profile of the analogue lithosphere used to run experiments with various input parameters (c). domains after two staged retreat in model (d). The model fairly replicates the five velocity domains of the Aegean defined by Nyst and Thatcher (2004): 1) Eurasia (fixed), 2) South Marmara, 3) Anatolia, 4) Aegean and 5) Greece, as a result of the interplay of trench retreat, Anatolia escape and suture reactivation since 15 Ma (NAF: North Anatolian Fault, VSZ: Vardar Suture Zone).

- Denizgören ophiolite and its sedimentary substratum, the Ezine Group, are located north of Ezine in the western part of the Biga Peninsula.
    - Beccaletto & Jenny (2004) subdivided three conformable formations
        - Geyikli Formation, slight terrigeneous detrital nature, Middle-Late Permian, transgressive subsidence
        - Karadağ Formation, platform-type sedimentation with local detrital input, Late Permian, transgressive subsidence

        - Çamköy Formation, carbonate detrital nature, Spathian to Carnian. syn-rift sequence
    - Ezine Group represents a fragment of the Rhodopian passive margin, consequence of the Permo-Triassic rifting of the future Maliac/Meliata Ocean (Beccaletto & Jenny, 2004).
- The Çetmi accretionary mélange is cropping out in western site of Kazdağ Massif and around town Biga. Beccaletto, et al. (2005) reviewed Çetmi as follows:
    - Light grey limestone blocks are a characteristic feature of the Çetmi mélange.
    - The youngest lithology of the mélange is the matrix (greywacke–shale association), Early to Middle Albian in age.
    - At a regional scale, the Çetmi mélange has little in common with the mélanges from the İzmir–Ankara and Intra–Pontide sutures of northwestern Turkey.
    - Another view says that Çetmi mélange shares many characteristics with the mélange units of the eastern Rhodope Zone, Bulgaria and Greece.
- Metamorphism dated from gneisses and yield Mid-Carboniferous ages on Pb-Pb/Zircon, 308 ± 16 Ma (Okay et al. 1996). Whereas the biotite and muscovite Rb-Sr and KAr ages are Oligo-Miocene, 19-22 Ma, (Okay & Satır 2000).
    - Interpreted as indicating two periods of high-grade metamorphism.
    - Post-metamorphic evolution of Kazdağ encompasses two stages (Cavazza, et al., (2009) and references therein);

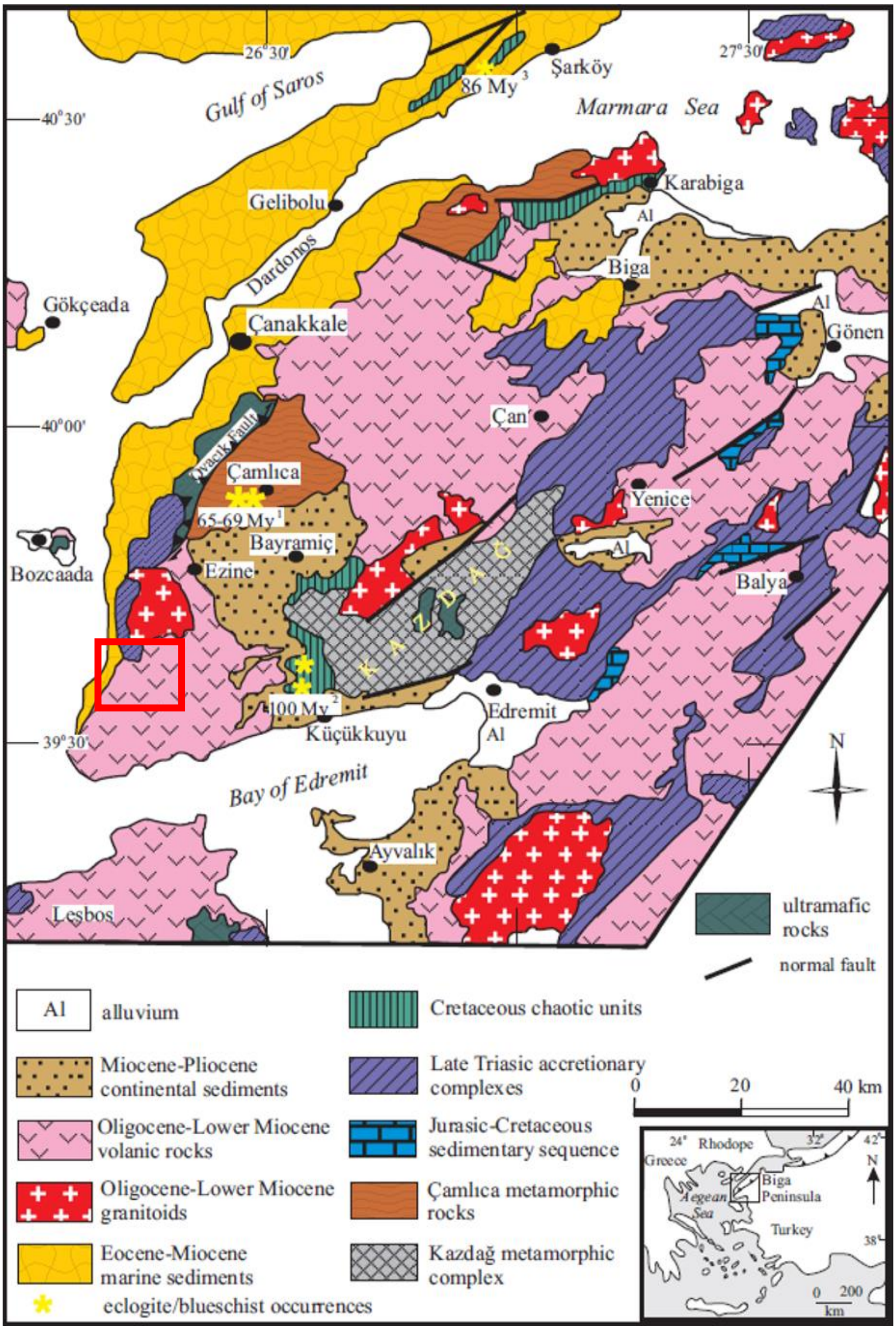

Figure 2.18: Generalized geological map of the Biga Peninsula (Şengün, et al., 2011). Inset map shows location of the Biga Peninsula. (*: location of the isotopic ages of eclogite/blueschist bearing metamorphic rocks). Reddish rectangle is showing the location of study area and near surrounding.

- The first stage comprises late Oligocene-early Miocene low-angle detachment faulting and early Miocene development of small supradetachment grabens.
    - During this phase much of the rapid thermal evolution of the massif occurred, including the emplacement of a suite of granitoid stocks with cooling ages around 21 Ma.
- The second stage comprises Plio-Quaternary strike-slip faulting related to the westward propagation of the North Anatolian fault system.

According to the recent review works (Aysal, 2015), the timing of emplacement vary from ~18 to 31 Ma for all of granitoids in Biga Peninsula implying that crystallization of the plutons began around 31 Ma and completed around 18 Ma. However, the new geochronological data vary only from 20.5 ± 0.5 to 27.89 ± 0.17 Ma (Aysal, 2015). During Late Oligocene-Early Miocene, calc-alkaline magmatism (Figure 2.18) in Biga Peninsula have been explained by the space problem of N-S crustal extending and following exhumation of Kazdağ Massif (Okay & Satır 2000) under extensional tectonic settings (Seyitoğlu & Scott, 1992), that was NE–SW extension during latest Oligocene (Bonev, et al., 2009).

Aysal, (2015) also summarized the petrogenesis and emplacement depth of NW Anatolian plutons as follows:

- Oligo-Miocene granitoids in Biga Peninsula contain mafic–intermediate (silicic plutons) and felsic (leucogranites and vein rocks) assemblages.
- Based on chemistry, temperature and pressure data, the plutons were emplaced into a shallow level magma chamber

A detailed geochemistry, temperature and pressure analysis work around Kazdağ Massif was carried out by Aysal (2015). According to his results, the plutons around the Kazdağ massif (Eybek, Yenice-Gönen, Evciler) giving critical informations for understanding the NW Anatolian plutons. Those are;

- Water content of melt ranges from 1.63% to 6.79% (mean = 4.15%), showing high water and volatile contents and stating that parent magmas of these plutons was emplaced at shallow crustal levels.
- The clinopyroxene and amphibole temperatures range between 823– 910 ± 45 C and 707–926 ^{0}C (mean = 798 ± 45 ^{0}C), respectively. Therefore, the crystallization depths are estimated to be in the interval of 1.02–10.2 km.

Altunkaynak & Genç (2008) studied rocks of the Cenozoic period in the Biga Peninsula and stated, based on their age and geochemical characteristics, that post collisional magmatism occurred in two distinct stages. Those are:

- Post-collisional magmatism's first product are the Middle Eocene magmatic rocks, represented by plutonic (45.3±0.9–38.1±1.8 Ma) and volcanic suites (37.3±0.9 Ma) with basalt to dacite compositions.
    - High level (epizonal) plutons and sub-volcanic associations (Genç and Yılmaz, 1997).
    - Volcanic products (lavas and ignimbrite, pyroclastics) and their sedimentary intercalations were formed in a marine environment.
- Post-collisional magmatism's second product are the Oligo-Miocene widespread emplacement of granitic plutons (granodiorite, quartz diorite and monzonitic) and volcanic rocks (basalt/trachy basalt to dacite with dominantly andesites and trachyandesites; partially coeval with plutonism).
    - Volcanism in the Biga Peninsula waned during 15–11 Ma, but it was subsequently rejuvenated in the Late Miocene with Basaltic composition of strongly alkaline distinct signature.

2.4. Previous Studies on the Study Area and Surroundings

The study area is located south of the Kestanbol Pluton exactly on the transitional zone of the crystalline to volcano sedimentary rock units. One of the first milestone work in this area was carried out by Karacık & Yılmaz (1998). The tectonostratigraphy of the rock units (Figure 2.19) is described as: (1) Basement metamorphic rocks (Karadağ metamorphic assemblage and Denizgören ophiolite), (2) Plutonic assemblage (Kestanbol granite), (3) Hypabyssal association (Poruklu formation), (4) Acidic and intermediate volcanic assemblages (Ayvacık and Balabanlı volcanics).

It is noted that the pluton was emplaced into the regionally metamorphosed basement rocks and develop a contact metamorphic aureole (e.g. Aladağ Skarn) (Karacık, 1995). Furthermore, Karacık & Yılmaz (1998) noted that along its eastern border, plutons passes gradually into fine-textured porphyritic rocks to rhyodacite and dacite. This transitional contact implies that the Kestanbol Granite was emplaced into its own volcanic ejecta (Karacık & Yılmaz, 1998). On the western part of the pluton, the contact corresponds to a deeper level of emplacement since there is a mylonilitic zone (Karacık & Yılmaz, 1998).

The dominant lithologies of the pluton are quartz-monzonite and granite with sets of aplite, pegmatite, lamprphyre and latite porphyry dykes (Karacık & Yılmaz, 1998). Moreover, Kestanbol plutons contains mafic microgranular enclaves and mafic vein rocks showing mixing and mingling relationships with the monzonitic to granodioritic magma (Yılmaz-Şahin et al., 2010). Black et al. (2013) describe Kestanbol Granite as Volcanic Arc Granite with a mostly magnesian, alkali-calcic, and metaluminous affinity. Yılmaz-Şahin et al. (2010) describe these plutons as post-collisional, subalkaline, metaluminous and high-K calc-alkaline, I-type. Kestanbol Plutons was dated by many scientists (Table 2.1).

Altunkaynak et al. (2012) interpreted Ar-Ar hornblende and biotite ages as crystallization and cooling of the pluton. Akal (2013) dated shoshonitic-ultrapotassic tephriphonolite dykes emplaced into Kestanbol Plutons; new data is intepreted to imply coeveal occurrence.

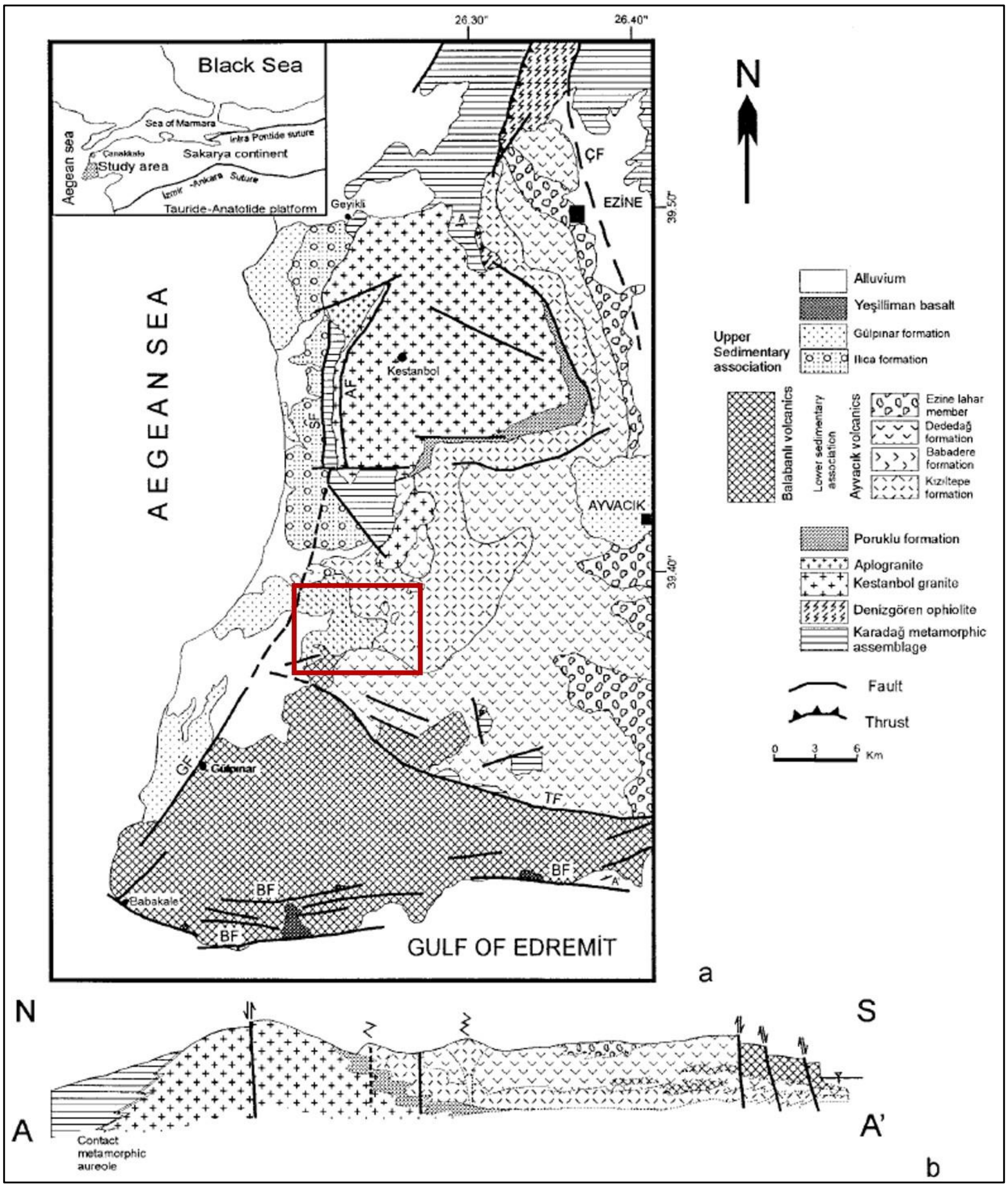

Figure 2.19: (a, b) Geology map and the associated cross section of the Ezine-Ayvacık region. Red rectangle shows location of the study area. (AF: Alemgah fault, SF: Sazaktepe fault, CF: Çamlıca fault, GF: Gülpınar fault, TF: Tuzla fault, BF: Behram fault) (Karacık & Yılmaz, 1998).

Table 2.1: Age data from the Kestanbol Granite.

Method	Mineral	Age (Ma)	Reference
K-Ar	Whole rock	28.0±0.88	**Fytikas et al. (1976)**
Ar-Ar	Biotite	21.5±1.6	**Birkle & Satır (1995)**
K-Ar	hornblende	20.5±0.6	**Delaloye & Bingöl (2000)**
Ar-Ar	hornblende	22.8±0.2	**Altunkaynak et al. (2012)**
	biotite	22.3±0.2	
U-Pb	zircon	20.8±0.5, 23.0±0.9 and 23.1±0.5	**Black et al. (2013)**
Ar-Ar	biotite	21.22±0.09	**Akal (2013)**
	Leucite	22.21±0.07	

Around the study area, the dominant volcanic units are named as Ayvacık and Balabanlı volcanics. Among them, Ayvacık volcanics crop out dominantly within the study area. Thus Balabanlı volcanics will not be overviewed in detail. The first volcanic products erupted in the northern areas are felsic lavas of the Kızıltepe formation; they are composed of rhyolite, rhyodacite and dacite lavas and the associated flow breccias (Karacık & Yılmaz, 1998). The Kızıltepe formation is overlain by the Babadere formation, which is composed of alternating lavas and pyroclastic rocks with well-bedded pyroclastic fallout deposits (Karacık & Yılmaz, 1998). The extrusion of the predominantly rhyolitic and dacitic volcanic ejecta is followed by andesitic and trachyandesitic lavas and flow-breccias, named as the Dededağ formation (Karacık & Yılmaz, 1998). Small domes were formed locally as the latest products of volcanic activity and named as the Tuzla and Ortatepe rhyolites (Karacık & Yılmaz, 1998). The Ayvacık volcanic association is unconformably overlain by two major sedimentary rock units (Karacık, 1995). Continental detrital rocks of the Ilıca formation occur at the bottom, and shallow-marine carbonates of the Gülpınar formation lies at the top (Karacık & Yılmaz, 1998). The further details are as follows:

- "The Ilıca formation begins with a coarse-grained and internally chaotic sedimentary assemblage, which passes upward into conglomerates with fragments of metamorphic and plutonic rocks. The internally chaotic sedimentary rocks were formed as scree deposits, derived from an adjacent fault block (Ezine-Şarköy Fault). The coarse clastics pass upward into carbonates of the Gülpınar formation.”

- “The Gülpınar formation is composed of fossiliferous, micritic, white limestones. The fossil assemblage yields a late Miocene-early Pliocene age (Karacık, 1995). This puts a time limit to the development of the Balabanlı and Ayvacık volcanics, which is clearly pre-Late Miocene in age.”

There are some geochronological works to determine age of volcanic rock units as well (Table 2.2):

Table 2.2: Age data from the Ayvacık volcanics.

Method	Mineral	Age (Ma)	Rock Unit	Location	Reference
K-Ar	biotite	21.5	lava dome	Ayvacık	**Borsi et al. (1972)**
	biotite	19.5	dyke	Baba Burnu	
	groundmass	17.1	ignimbrite	Tamos	
	K-feldspar	16.8	lava dome	Ezine	
	whole rock	9.7	alkali basalt	Ezine	
K-Ar	whole rock	21.3±0.3	trachyandesite (Kızıltepe unit)	Ezine	**Aldanmaz et al. (2000)**
		20.5±0.5 Ma	rhyolite (Koyunevi ignimbrite)	Ayvacık	
		20.3±0.6	trachyandesite- (Behram andesite)	Asos	
		19.7±0.3	basaltic trachyandesite- (Kovacıklı dyke swarms)	Ayvacık	
		8.32±0.19	basanite (Ayvacık volcanics)	Ayvacık	
K-Ar	whole rock	18.5±0.4	rhyolite (Koyunevi ignimbrite)	Ayvacık	**Ercan et al. (1995)**
		15.3±0.3	Bergas ignimbrite	Ayvacık	

Approximately N-S-trending Gülpınar-Kestanbol Fault of Siyako et al. (1989) or Gülpınar Fault Zone of Karacık & Yılmaz (1998) or Ezine-Şarköy Fault of Elmas & Meriç (1998) was named for the western lineaments. Among other researchers, Elmas & Meriç (1998) explained this fault in detail by documenting its properties. A late middle Miocene fault, Ezine-Şarköy fault, controlled the geometry of the basin from the eastern shoulder of the Biga Peninsula. It was reactivated as a right-lateral strike-slip fault during the late early Pliocene (Elmas & Meriç, 1998). Karacık & Yılmaz (1998) explained another critical fault in a way that after the cessation of the Early Miocene magmatic activity the Tuzla Fault was formed and triggered uplift of the northern part of the study area with respect to the southern area. Therefore, the magmatic successions have been obliterated in the northern region by the erosion, down to the pluton (Karacık & Yılmaz, 1998). Moreover, geothermal exploration mapping was carried out by Bozkurtoğlu et al. (2006), who propose that conjugate structural relations was present (NW-SE and NE-SW). Yaltırak et al. (2012) investigate the Tuzla and Baba Burun offshore by the help of deep seismic sections. He noted the occurrence of pull-apart basins and a series of E-W trending normal faults.

Despite the geological complexity of the study area, Tuzla town is now facing geothermal exploration and exploitation. Baba, et al. (2015) detected PbS (galena) and $CaCO_3$ (aragonite or calcite) in the down-hole and the surface pipeline of 174 °C reservoir of Tuzla. One of the exploration well has shown that at argillic, sericitic, skarn altered horizons starting from ~100 m depth to ~800 m depth, including 250 m thick chalcophyrite, pyrite rich zone (Şener & Gevrek, 2000) (Figure 2.20).

2.5. Summary

Although Turkey was one of the ancient places of mining, the metal endowment of the country has been taken into consideration after late 90s (Yiğit, 2009). Late Cretaceous to Cenozoic volcano plutonic rocks are the major fertile rock units of

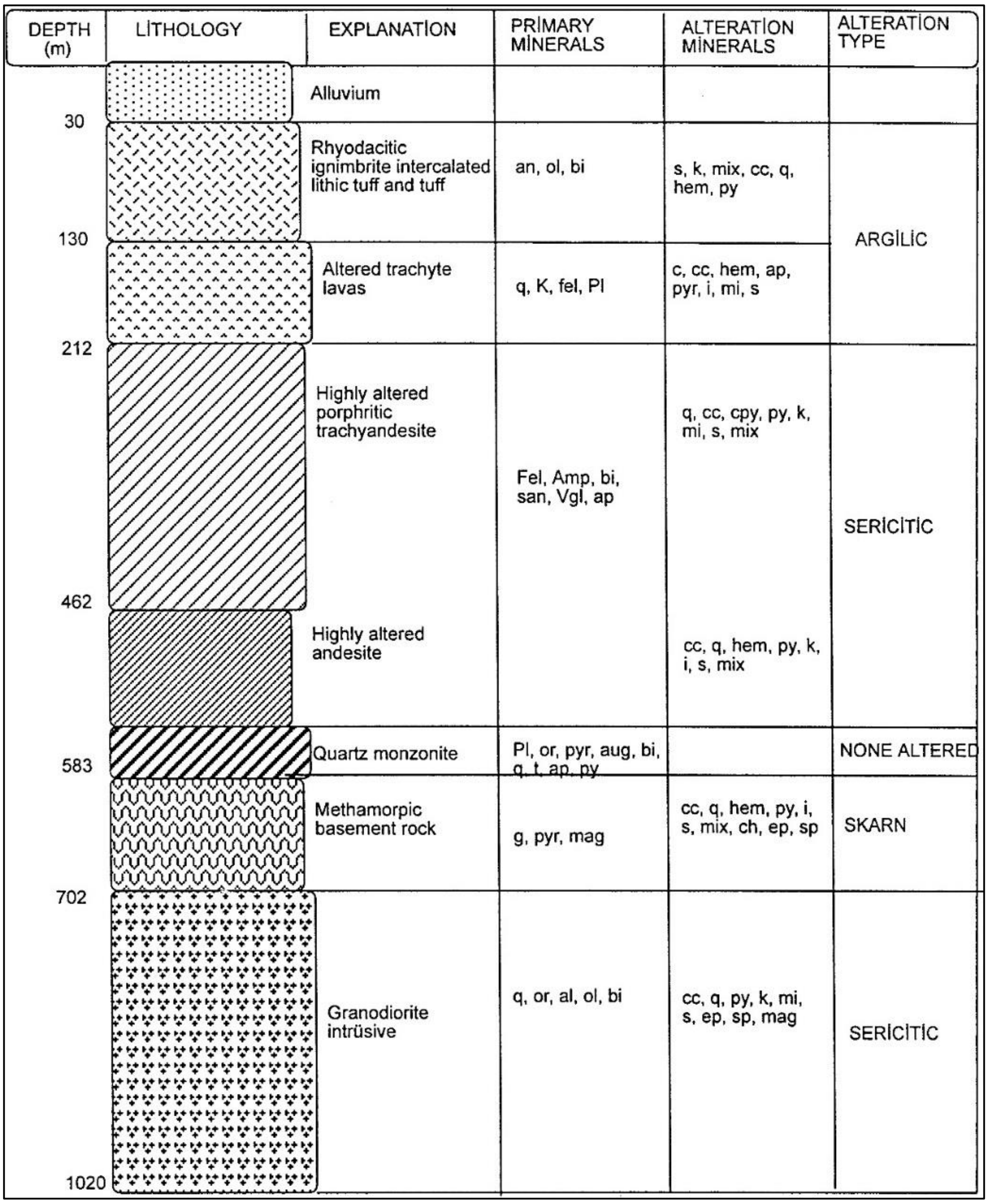

Figure 2.20: Vertical distribution of lithology, primary and alteration minerals and alteration types of T2 well (Şener & Gevrek, 2000). (al: albite; an: andesine; ap: apatite; amp: amphibolite; aug: augite; bi: biotite; c: clay; cc: calcite; ch: chlorite; cpy: calcopyrite; ep: epidote; fel: feldspar; hem: hematite; i: illite; k: kaolinite; K-fel: K-feldspar; mag: magnetite; mi: mica; mix: mixed layer clay minerals; ol: oligoclase; or: ortoclase; pl: plagioclase; py: pyrite; q: quartz; s: smectite; san: sanidine; sp: sphene; Vgl: volcanic glass).

Turkish gold (Yiğit, 2012), which is located in Tethyan metallogeny. In Turkey, formation and distribution of the majority of the gold occurrences (see Figure 2.21) shaped by tectonic stories of subduction, collision, postcollision, and rifting processes (Yiğit, 2009).

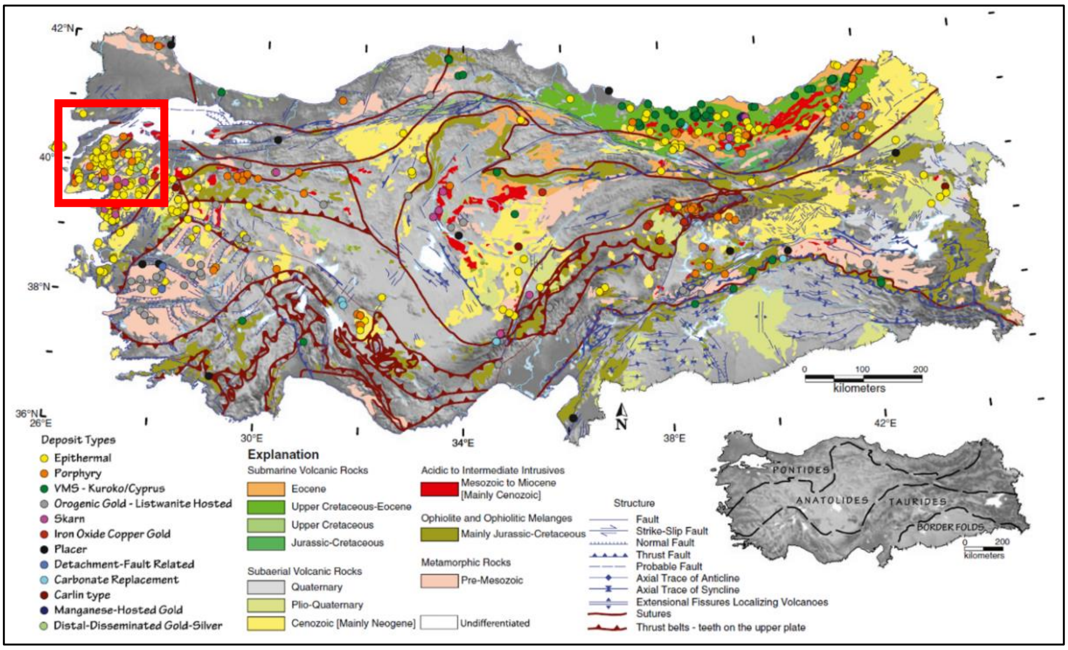

Figure 2.21: Classification and distribution of the gold deposits and prospects of Turkey with emphasis on host–rock lithologies and tectonic setting (Yiğit, 2009). Reddish rectangle is showing the location of Biga Peninsula.

Untill now, numerous mineral deposits was discovered in Turkey, most of them are of modest size by world standards (Yiğit, 2012). To increase discoveries or size of deposits, it is necessary to focus on the conditions that these deposits have evolved. Richards (2013) has listed conditions of characteristics for porphyry and epithermal deposits for mineralizing a standard or giant deposits (Table 2.3). From this point of view, Biga Peninsula is a prospective sector in the Tethyan Metallogenic Belt and fertile gold district for Turkey since it fits with most of the characteristics for standard and giant deposit.

Table 2.3: Characteristics of some giant porphyry Cu±Mo±Au and epithermal Au–Ag deposits compared with ‘standard’ systems (Richards, 2013).

Characteristic	‘Standard’ deposits	Giant deposits
	Porphyry Cu±Mo±Au deposits	
Tectonig setting	Volcanic arc above subduction zone	Similar, or shallow subduction, back-arc, collisional or post-subduction
Magmatic association	Calc-alkaline to mildly alkaline	Similar
Metal content of Magma	Typically <100 ppm Cu	Similar; enriched in some cases? (up to 125 ppm Cu)
Duration of hydrothermal activity	Typically ≤0.1 Myr for a single ore-forming event	Up to 0.7 Myr in multiple ore-forming events
Host rocks	Volcanic and clastic sedimentary rocks	Similar, ± chemically reactive mafic igneous rocks, carbonate rocks
Hydrothermal fluids	700-300^{o} C saline aqueous fluids of magmatic origin	Similar; unusually metalliferous in some cases?
Hydrothermal fluid flow	Focused above shallow pluton	Highly focused in structural corridors
	Epithermal Au-Ag Deposits	
Tectonic setting	HS-IS: Volcanic arc above subduction zone. LS/alkali: Extensional or back-arc settings.	HS-IS: Transitional island arc, shallow subduction. LS/alkali: Continental rifting: post-collisional back-arc transtension.
Magmatic association	HS-IS: Calc-alkaline. LS: Bimodal (felsic + mafic) or no association. Alkalic: Alkaline.	Similar
Host rocks	Volcanic and clastic sedimentary rocks	Similar, ± carbonaceous volcano-sedimentary rocks, carbonate rocks
Source of hydrothermal fluids	HS-IS: Magmatic fluid. LS: Dominantly groundwater. Alkalic: Possibly magmatic fluid.	Similar
Nature of hydrothermal fluids	HS-IS: Magmatic fluid. LS: Dominantly groundwater. Alkalic: Possibly magmatic fluid.	Similar
Hydrothermal fluid flow	Structurally focused	High degree of structural focusing: seismic trigerring of fluid flow
Ore depositional processes	HS-IS: Fluid mixing, boiling. LS: Boiling. Alkalic: H_2O-CO_2 phase separation.	Similar, but unusual efficiency of processes, especially flash-boiling induced by seismicity

CHAPTER 3

GEOLOGY OF THE STUDY AREA

3.1. Introduction

The rock units exposed in the study area are mostly made up of Oligo-Miocene arc volcanics, which are widely exposed in the western end of Biga Peninsula. They are represented by a sequence of crystalline, hypabyssal and extrusive rocks. Pre-Cenozoic metamorphic rocks form the basement, exposed about 20 km north of the study area in western and northern site of the Kestanbol Pluton. Miocene-Pliocene continental to submarine sedimentary rocks cover the basement and volcanic rocks. The rock units are bounded by the Aegean Sea in the west and Ezine-Şarköy Fault in the east, defining N-S-trending ribbon-like geometry along the western end of Biga Peninsula (Figure 2.19). The rock units exposed in and around the study area share a complex geological history and have experienced a multi-phase deformation and associated metamorphism, magmatic-hydrothermal and geothermal activities. In this chapter, the rock units is going to be introduced, structural ground truth data will cartographically be demonstrated (read following chapters for details) and alteration patterns will basically be stated in order to describe temporal relations of the rock units and its mineralization potential. The macroscopic description and detailed petrography of rock units (Table 3.1) will also be presented.

3.2. Lithology

Eleven different rock units are distinguished within the study area (Figures 3.1 - 3.2). These are, from oldest to youngest according to predominant field relations; basement unit, megacrystic monzonite, latite porphyry, andesite, dacitic lapilli tuff, rhyolithic crystal tuff, quartz monzodiorite, diorite porphyry, rhyodacite, conglomerate and alluvium (Figure 3.2). On the following sections, each rock unit will be described by their macro and micro-scale distinguishing properties (such as color, crystallinity, granularity, fabric, mineral assemblages, etc).

Table 3.1: List of samples for lithologic, petrographic, and alteration description.

#	Rock Unit	Investigations	
		Macro-scaled	**Micro-scaled**
1	**Basement**	4	4
2	**Megacrystic Monzonite**	4	5
3	**Latite Porphyry**	6	6
4	**Andesite**	11	11
5	**Dacitic Lapilli Tuff**	8	8
6	**Rhyolitic Crystal Tuff**	4	5
7	**Quartz Monzodiorite**	5	6
8	**Diorite Porphyry**	2	2
9	**Rhyodacite**	2	2
10	**Conglomerate**	1	0
11	**Alluvium**	0	0
	TOTAL	47	50

3.2.1. Basement

Basement rocks are whitish, creamy yellowish white, light brown and light greenish brown in color and generally distinguished by the resistant, spheroidal and locally foliated or earthy appearance (see Figure 3.3). This rock unit include marble and dolomite rich zones, where all of those cross cut by manganese, carbonate, silica and younger carbonate veins. They are mostly observed at the northeastern part of the study area as lenses or small (with dimensions not larger than a few meters) xenolithic remnants within both megacrystic monzonite and latite porphyry-andesite complexes (Figure 3.4). They also include small (unmappable) lenses of serpentinized ophiolitic (possibly remnants of Denizgören ophiolite of Okay et al., 1991) and cataclastic rocks. They are dissected by several faults.

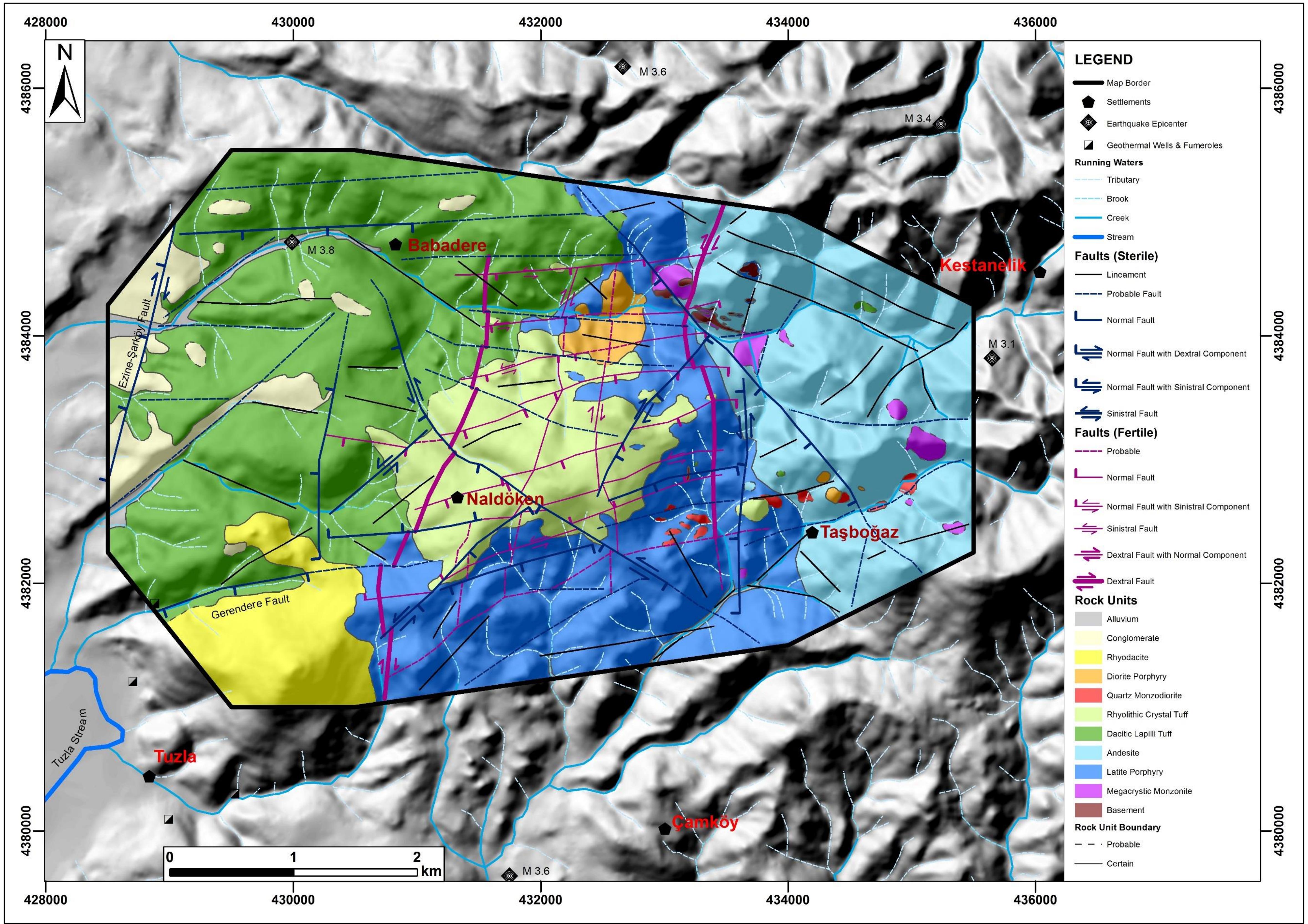

Figure 3.1: Lithology and structure map of the study area.

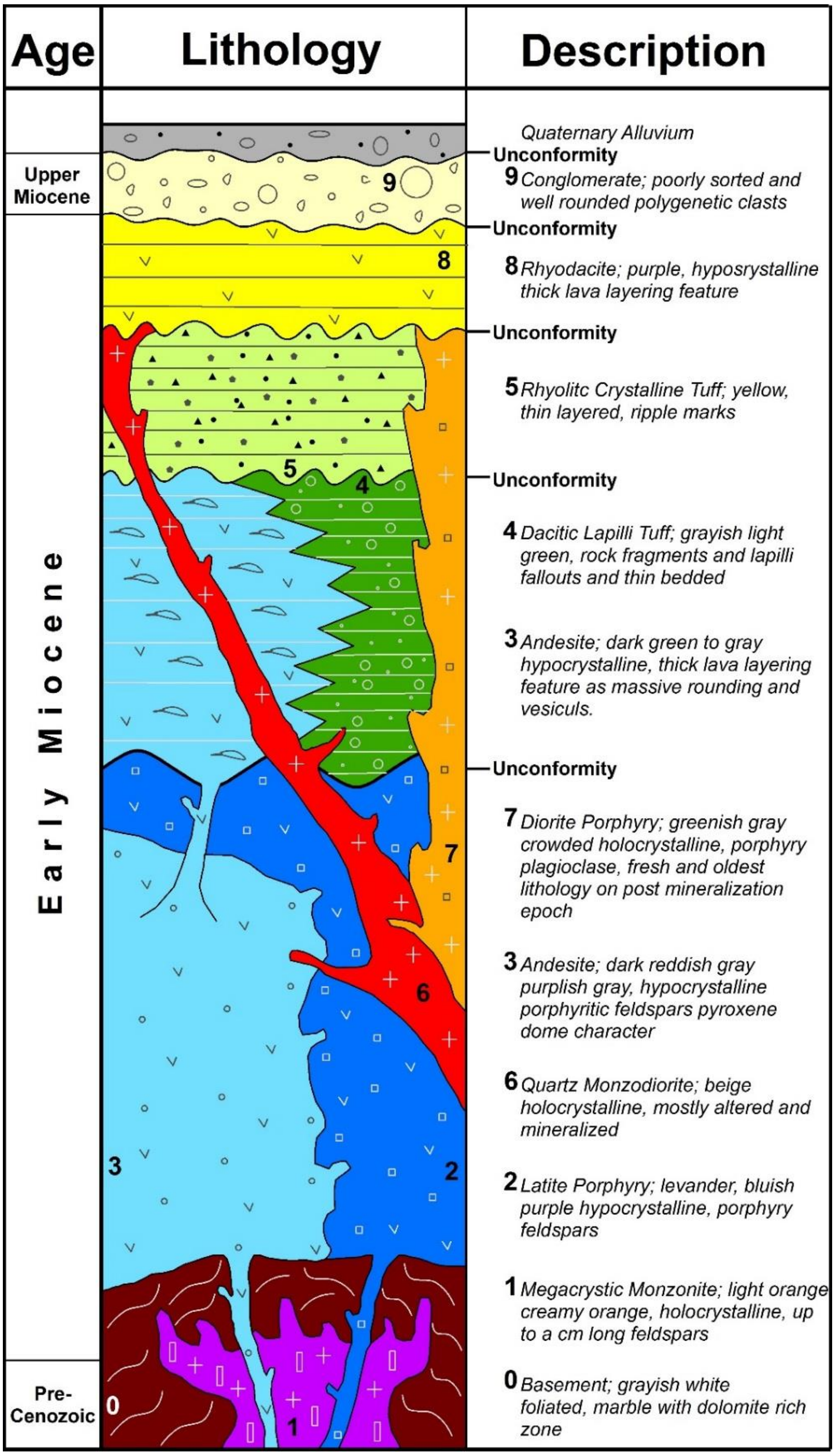

Figure 3.2: Generalized stratigraphic column of the study area.

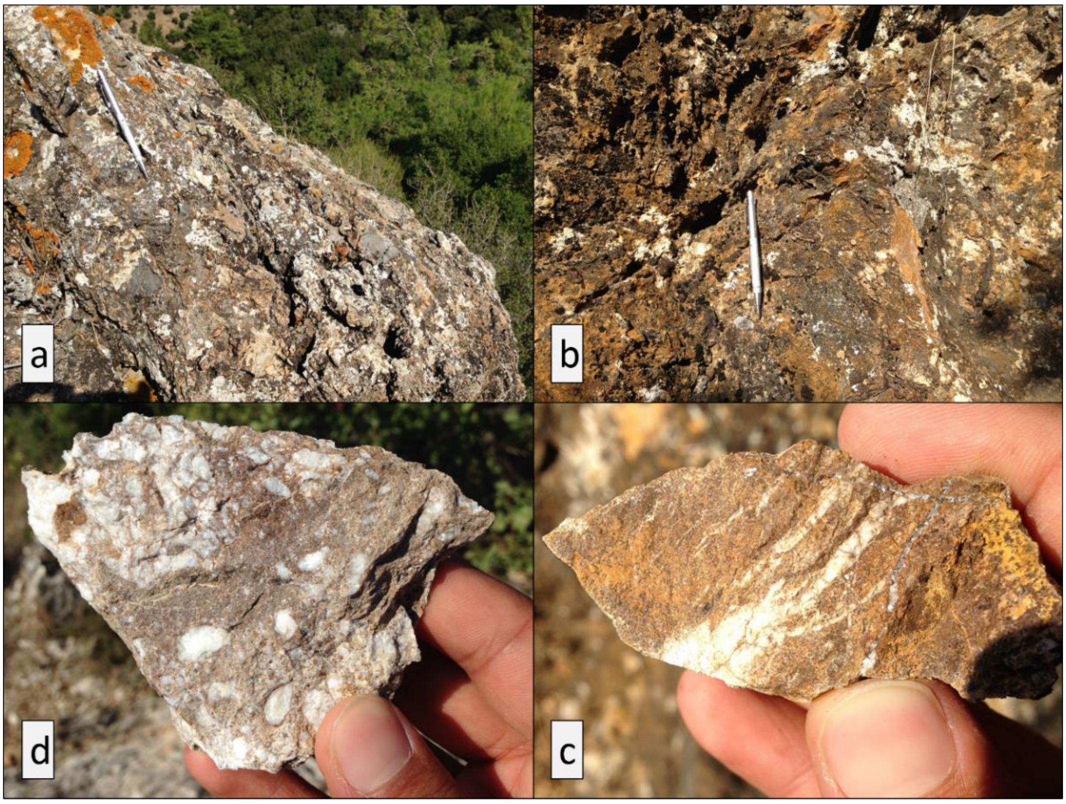

Figure 3.3: Field views from the basement rock units (a) general view of spheroidally weathered and foliated outcrop; (b) clay and dolomite rich chaotic ground; (c) carbonate and silica veining d) marble breccia cemented by carbonate/clay rich matrix. Scriber is ~12 cm long and thumb, ~3 cm.

Along the contact zone with basements and younger intrusions, well developed metamorphic aurole was developed and it can be exactly seen on the contact of megacrystic monzonite (Figure 3.5).

Marginal parts of the marble are characterized by manganese veining, which could be a possible source for dolomitization. The presence of disseminated silica grains on elongated silica zones are attributed to possible previous silicification process. Epidote, chlorite and very fine garnet crystals occur within the latest silica veins, that is probably retrograde phase of the skarn processes. Additionally, some of the disseminated silica grains in marble display deformation bands (Figure 3.5).

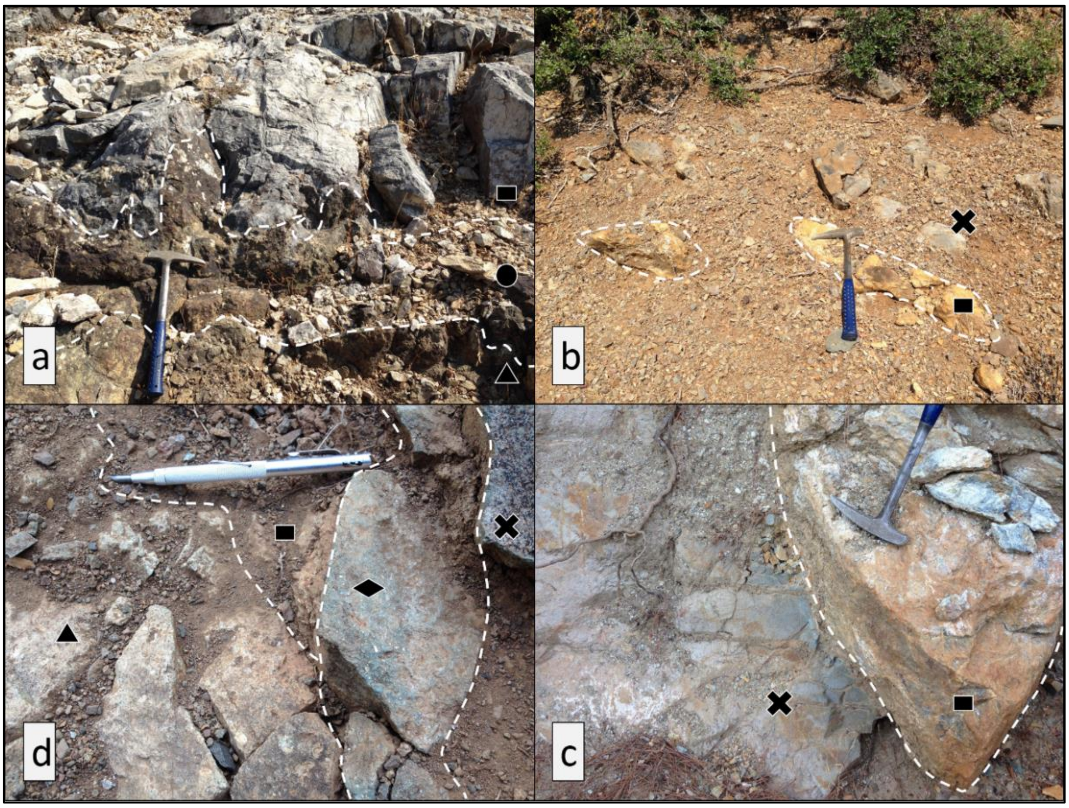

Figure 3.4: Cross-cutting relationships of three different intrusions (triangle for megacrystic monzonite, diamond for latite porphyry, and saltire for andesite) and basement (black square). (a) Metamorphic aurole (indicated by circle and dashed line) on the contact of massive marble and megacrystic monzonite; (b) basement lenses in andesitic rock unit; (c) serpentine-rich basements within andesites; (d) summary figure for three-phased intrusions with their cross-cutting relationships as basement are intruded by megacrystic monzonite, latite porphyry and andesite, respectively. Scriber is ~12 cm long and hammer, ~42 cm.

The field relations clearly indicate that these are the oldest rock units in the study area. They are described as Karadağ Metamorphics (Okay et al., 1991) but later renamed Geyikli formation of Ezine group (Beccaletto & Jenny, 2004).

Ezine Group is represented by a more than three-km-thick sequence, characterized by intercalation of basement rocks metamorphosed at greenschist facies conditions (Beccaletto & Jenny, 2004). It is subdivided into three formations:

- the Geyikli formation, transgressive terrigeneous detrital sediments of (Middle)-Late Permian age;

- the Karadağ formation, platform-type sediments, with local detrital input, of Late Permian (Djulfian) age;
- the Çamköy formation, carbonate detritals as part of a syn-rift sequence, (Early)-Late Triassic (Spathian to Carnian) in age.

The Ezine Group is tectonically overlain by early Cretaceous Denizgören ophiolite (Beccaletto and Jenny, 2004) and intruded by Kestanbol Pluton (Birkle and Satır, 1995).

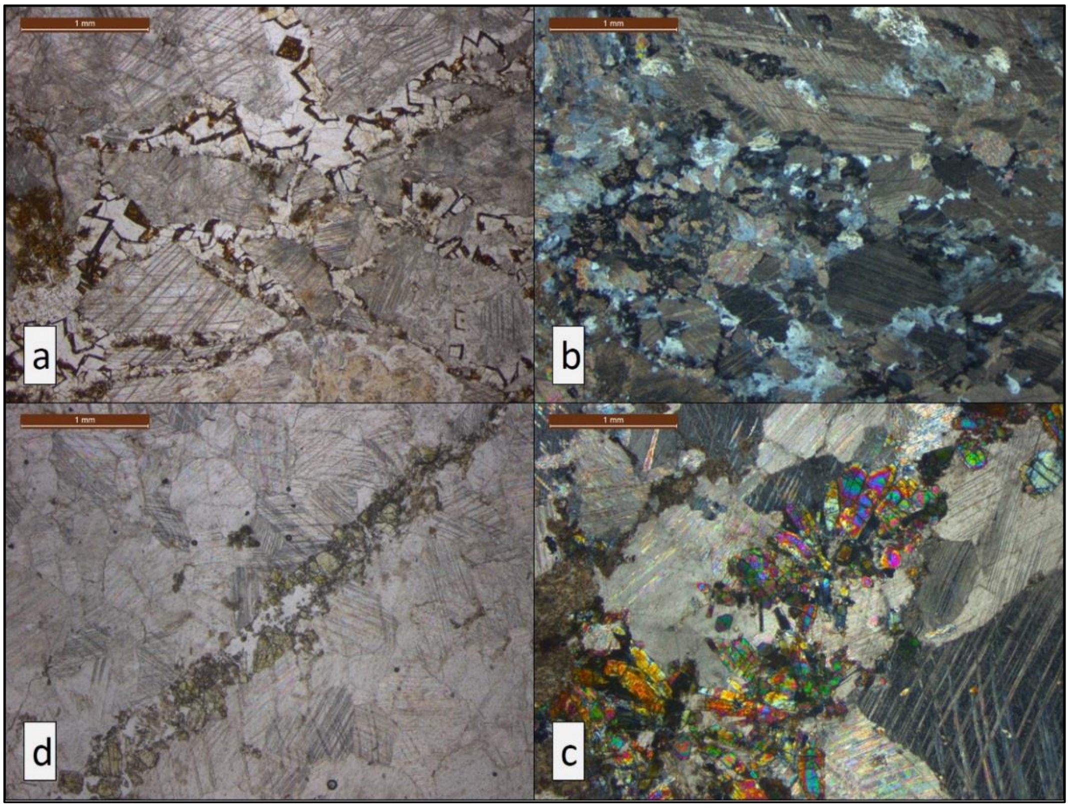

Figure 3.5: Photomicrographs of basement rock units: (a) a view from adolomitic zone; (b) disseminated and/or veined silica; (d) silica, epidote carbonate veining; (c) epidote, chlorite retrograde and garnet, diopside as prograde phase assemblages.

3.2.2. Megacrystic Monzonite

Megacrystic monzonites are pinkish white, light orange brown, creamy white in color (Figure 3.6), holocrystalline rocks with a crystalline groundmass; they are generally distinguished by the resistant to erosive and phanerithic, especially megacrystic, appereance with spheroidal and jointed geometry. Most outcrops are dissected by faults of pre-syn-post mineralization activities. In the study area, it shows partially altered to fresh patchy outcrops whereas one of the large outcrops, located on the junction of north-south flowing Acı D. creek and Babadere-Kestanelik road, is unaltered. The rock unit is mostly distributed on the eastern side of the study area and bounded mostly andesite and latite porphyry (Figure 3.1).

Megacrystic monzonite is composed of anhedral quartz crystals, up to a few mm in size (about 5-10%), (up to 8 mm) mostly twinned euhedral plagioclase phenocrysts (about %35), euhedral orthoclase mega-crystals larger than 10 mm (about %30) and euhedral biotite (up to 4 mm) with minor small hornblende and pyroxene crystals (about %35). Some of the ferromagnesian minerals occur as inclusions within feldspar phenocrysts. A mm-sized euhedral muscovite occurs sporadically, up to %2. The megacrystic monzonite is moderately magnetic.

Figure 3.6: Views from hand-specimens of megacrystic monzonite: (a) altered (chlorite-clay-jarosite) and (b) unaltered. The size of thumb is ~3 cm.

Thin section studies show presence of non-pervasive carbonate and clay-chlorite alteration due to supergene activities. The rock is characterized by orthoclase mega-crystals with Carlsbad twinning and equigranular plagioclase crystals (Figure 3.7). According to above-mentioned field observations and petrographic characteristics, this unit can be named as megacrystic quartz monzonite or megacrystic monzonite. Hereafter, it is named as megacrystic monzonite.

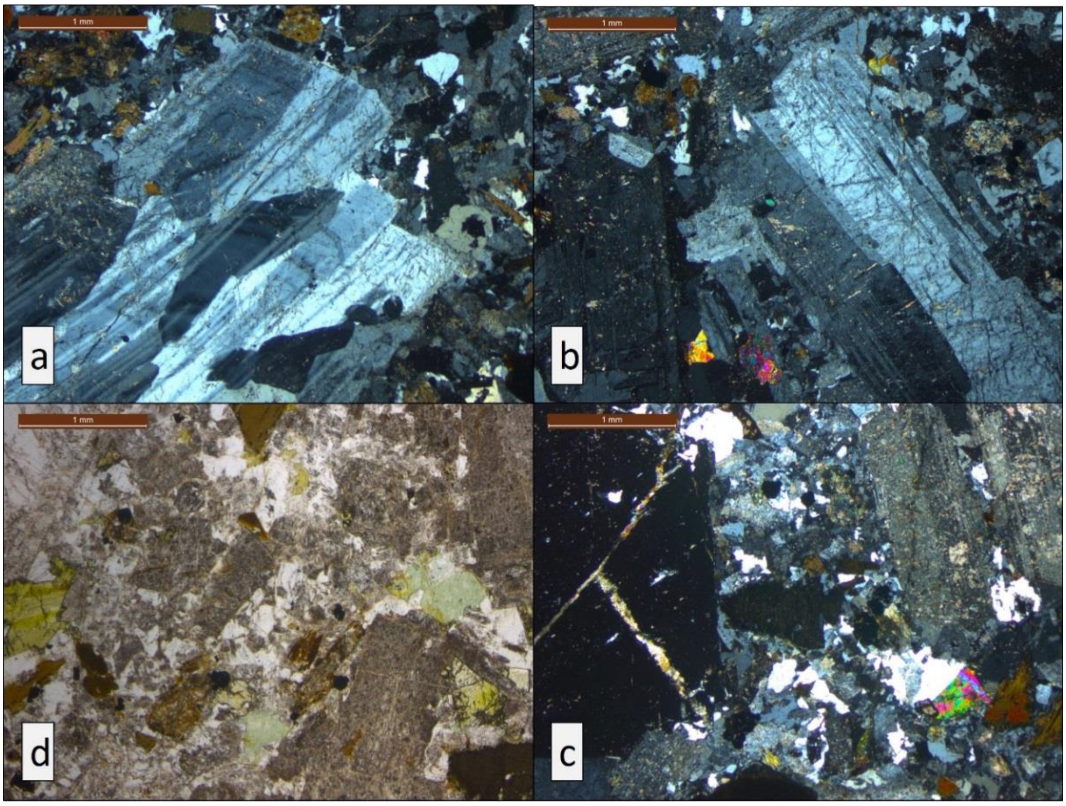

Figure 3.7: Photomicrographs of megacrystic monzonite: (a) mechanically twinned euhedral orthoclase megacrysts and crystalline groundmass; (b) zircon-bearing plagioclase orthoclase phenocrysts within a crystalline groundmass; (c) orthoclase megacrystals with carbonate veining and altered perthitic feldspars and biotites within a titanite-bearing partially felsic groundmass; (d) plane polarized view of megacrystic monzonite, showing amphiboles and chlorite with altered feldspars.

According to cross-cutting relationships, the megacrystic monzonite is the second oldest rock unit of the study area (Figure 3.3). It is one of peripheral small intrusions of the Kestanbol Granitoid and mapped, for the first time, by Karacık and Yılmaz (1998). Kestanbol pluton was studied by many workers and dated by different dating methods along different part of the pluton. The available ages range from 20.5 to 28.0 Ma and is mainly constrained around 23.0 Ma. However, the exposures of the megacrystic monzonite within the study area are not dated.

3.2.3. Latite Porphyry

Latite porphyry is light grayish to lavender, dark grayish green in color (Figure 3.8). It is typical porphyritic rock with feldspar megacrysts within an aphanitic groundmass. The rock generally distinguished by its sub-resistant appearance and spheroidal geometry.

The rock unit is exposed in central and southern parts of the study area and form altered to fresh outcrops. Petrographically, the rock is composed euhedral feldspar megacrystals, up to 7 mm (about %40), euhedral biotite + hornblende, up to 2 mm (about 20%) and small quartz crystals (about 5%). It is non-magnetic. The megacrystals are embedded within an aphanitic to very fine crystalline matrix, made up of equally weighted feldspars and limited quartz crystals; magmatic corrosion during quartz crystal growth is evident (Figure 3.9). According to field observations and petrographic characteristics, this unit can be named as latite porphyry or latite-andesite porphyry. In this study, latite porphyry is preferred.

The latite porphyry is bounded by later andesitic emplacement on eastern side (Figures 3.10). It is overlain unconformably by dacitic lapilli tuff and rhyolitic crystal unit. Intrusion of quartz monzodiorite, diorite porphyry and occurence of rhyodacite had taken place after its intrusion. It is also deformed by several fertile or sterile structural activities. According to cross-cutting relationships, the latite porphyry is the third oldest rock unit of the study area. It is mapped as rock unit in lava and subvolcanic character (Karacık and Yılmaz, 1998).

Figure 3.8: Field views from the latite porphyry: (a) moderately weathered feldspar megacrystic latite porphyry; (b) appearance of the rock on a cut fresh surface. Note evident porphyritic texture with large megacrystals embedded within a fine-grained matrix; (c) preferred alignment of feldspar megacrysts oriented in ~030^{o}/90^{o}; (d) altered latite porphyry with iron oxides (jarosite-hematite). The size of the thumb is ~3 cm and hammer, ~20 cm long.

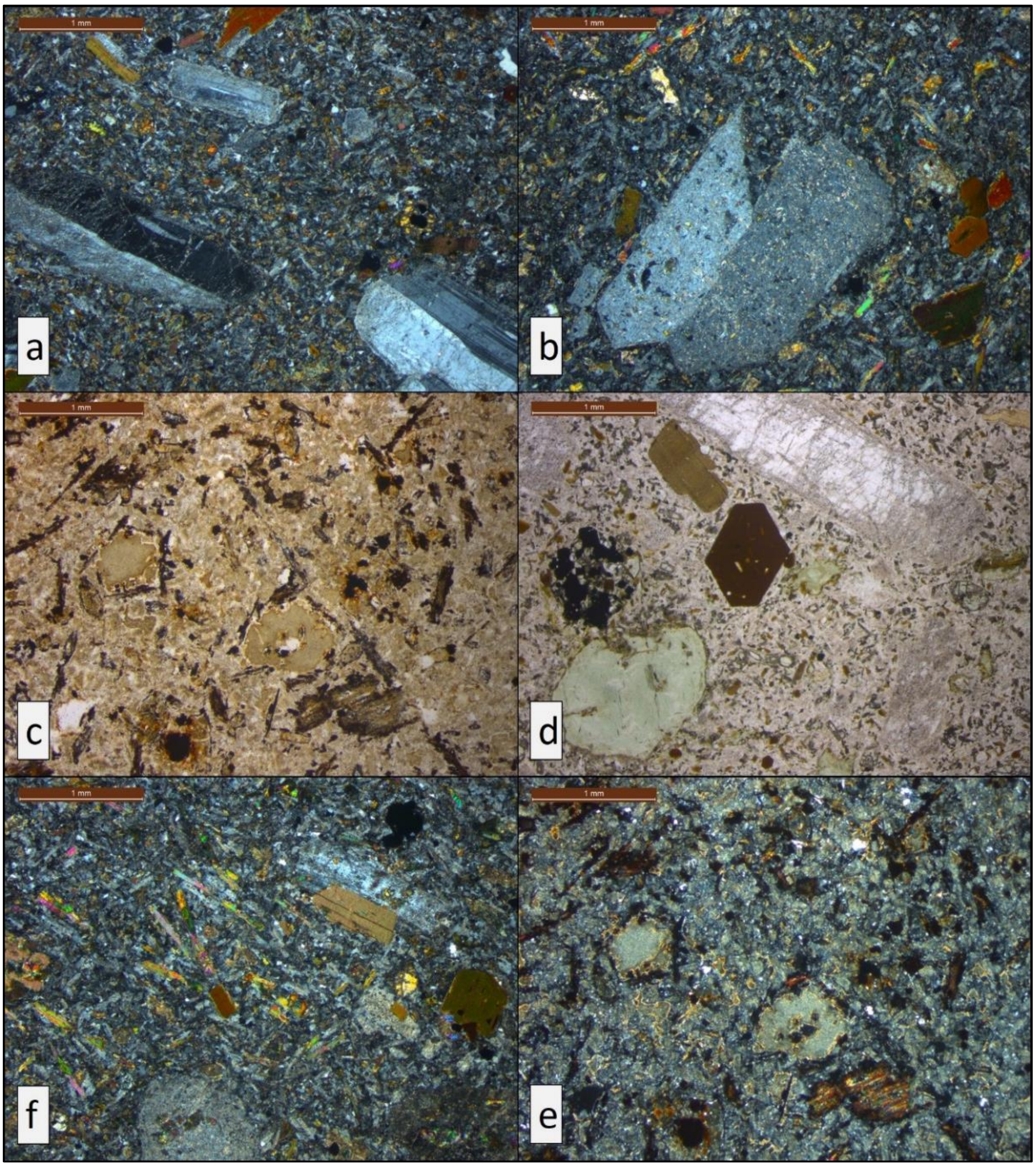

Figure 3.9: Photomicrographs of latite porphyry rock units a) very fine biotite, feldspar rich glassy matrix having megacrystals of orthoclase and plagioclase (same as 'b' and 'f') c) analyzer out view of altered biotite and ground mass d) selectively pervasive chlorite alteration and euhedral biotite and clay altered porphyritic feldspar e) analyzer in view of screenshot 'c'.

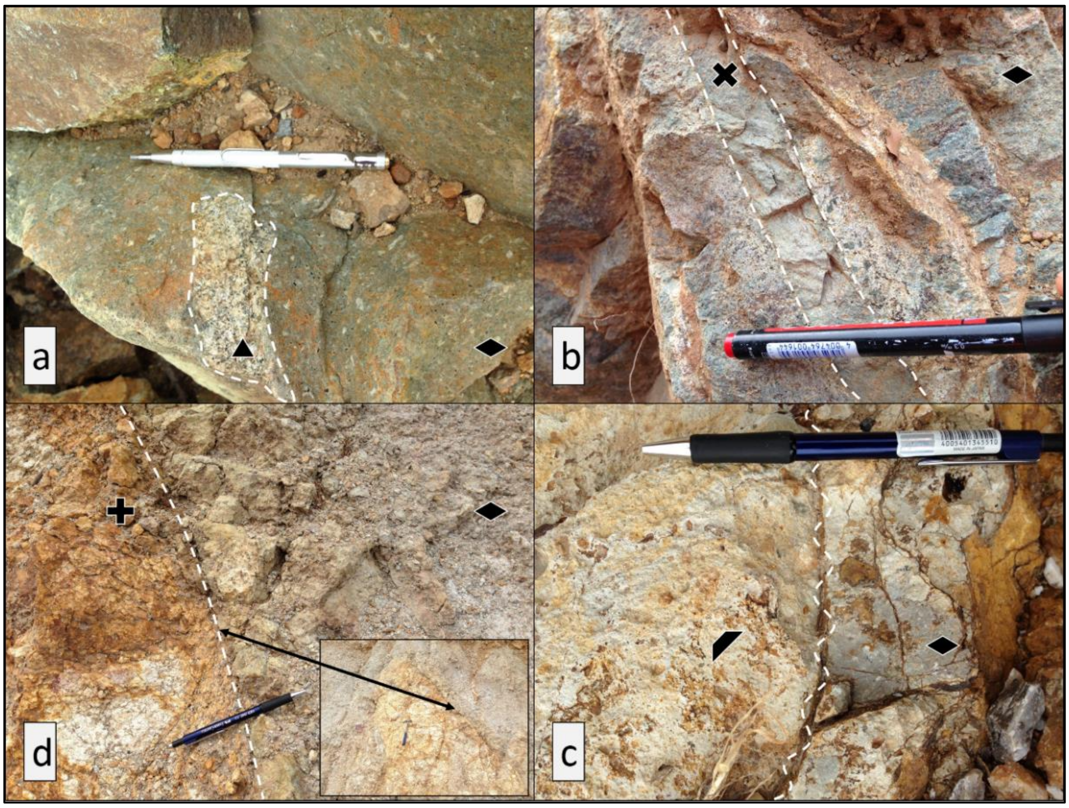

Figure 3.10: Field views illustration field relations of latite porphyry (a) megacrystic monzonite xenolith in latite porphyry; (b) latite porphyry cross-cut by an andesite dike; (c) unconformity surface between latite porphyry below and tuff unit above; (d) altered quartz monzodiorite emplaced into the latite porphyry. Scriber or pens are ~12 cm long. Triangles for megacrystic monzonite, diamonds for latite porphyry, saltires for andesite, diagonal stripes for tuff unit, and crosses for quartz monzodiorite.

3.2.4. Andesite

Andesite is dark grayish black, dark reddish brown, dark blackish green in color (see Figure 3.11). It is a hypocrystalline rock with larger phenocrysts within an aphanitic groundmass. The unit is generally distinguished by resistant, dark and rounded to boxy appearance. Andesite forms large fresh-altered exposures in the eastern part of the study; north-south flowing Acı D. creek forms its western boundary (Figure 3.1), along which breccia zones are evident. Andesite unit has both hypabyssal and lava flow character (Figure 3.12).

Figure 3.11: Macroscopic views from the andesite unit: (a) iron oxide and chlorite rich andesite layering; (b) andesite dome rich in feldspar phenocrysts; (c) selectively pervasive clay and silica altered andesite; (d) hand specimen of a fresh andesite. The size of thumb is ~3 cm and hammer, ~42 cm long.

Petrographically, andesite has generally no quartz crystals or if present, quartz is not more than 5%. It is composed of euhedral plagioclase (up to 4 mm, about %40) and euhedral biotite + hornblende crystals (up to 2 mm, about 20%). It is moderately magnetic. In thin sections, plagioclase phenocryts, euhedral pyroxene and biotites form essential minerals with limited corrosive quartz. The groundmass is mostly glassy but plagioclase microlites are also present (Figure 3.13). Evidence for mineralization and supergene alteration is common both in outcrops and thin sections. Field observations and petrographical characteristics are consistent with andesite terminology. According to cross-cutting relationships, it is designated as the fourth oldest unit of the study area. The andesite unit is considered within the Dededağ formation (and questionably Kızıltepe formation?) (Karacık and Yılmaz, 1998) or Hallaçlar volcanics (Dönmez et al., 2005). The lava features are observed around north of Taşboğaz village and may correspond to upper levels of the volcanic sequence. At lower elevations, cross-cutting relationships with older units and dome-like geometries are reported (Borsi et al., 1972); there, the unit is dated at 21.5 Ma.

Figure 3.12: Field view from extrusive (lava) andesite, showing flow layering.

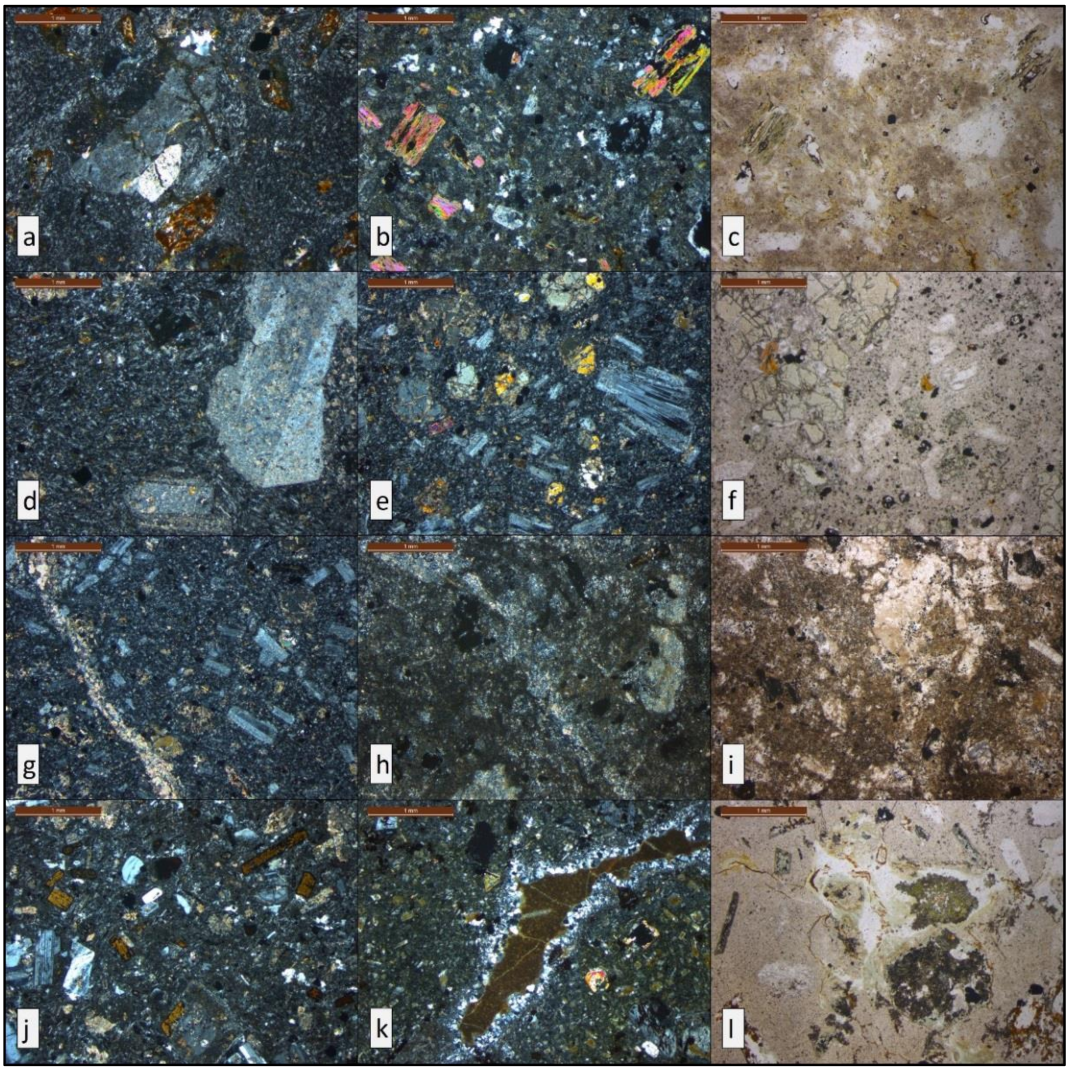

Figure 3.13: Photomicrographs from the andesite unit: (a, b, d, e, j) anhedral plagioclase phenocrysts and biotite crystals within a glassy ground with feldspar microlites (b) non-pervasively altered (chlorite, epidote, clay, carbonate) andesite; (c) plane polarized view of screenshot in ‘b’; (f) plane polarized view of screenshot in ‘e’, showing high relief pyroxene and black opaque minerals; (g) silica carbonate vein; (h) andesite totally altered to clay and carbonates; (i) plane polarized view of screenshot in ‘h’; (k) silica vein and silicification overprinted by intense carbonate veins; (l) (i) plane polarized view of screenshot in ‘k’.

3.2.5. Dacitic Lapilli Tuff

Dacitic lapilli tuff is light grayish, grayish light green, dark to light grayish purple and light reddish in color (Figure 3.14). It is a rock fragment-bearing pyroclastic rock, generally distinguished by the erosive and layered appearance. It is mostly tilted westward by about 60^o along a north-south-trending zone. Exposures are common in the central and western parts of the study area (Figure 3.2).

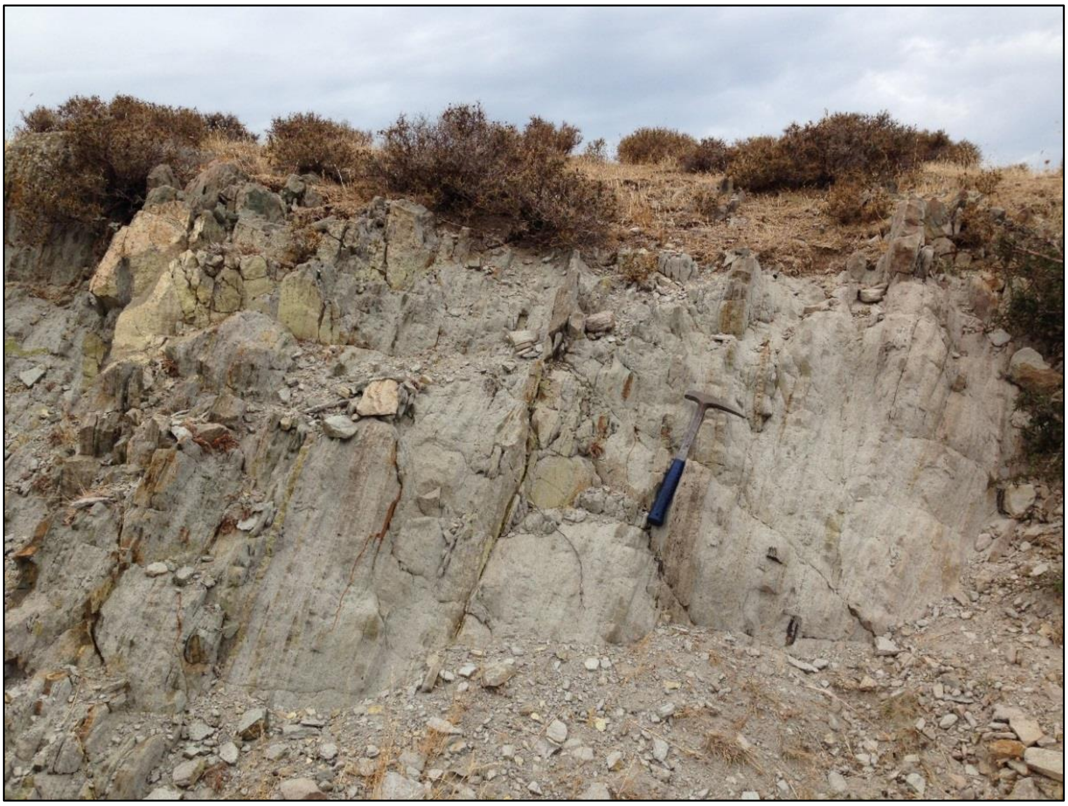

Figure 3.14: Road-cut view of dacitic lapilli tuff. Hammer is ~42 cm long, and faces towards north.

Dacitic lapilli tuff has rock fragments and mineral overgrowths, ranging from a few mm to ~50 mm in size (dominantly 2-4 mm crystals and/or fragments) and display slightly different compositional alternations. It is composed of euhedral quartz crystals up to 4mm and/or fragments (about %20) and anhedral plagioclase crystals and/or fragments up to 3 mm (about %20) and euhedral mafic crystals and/or fragments as 2 mm (about %20). It is non-magnetic and show typical fiamme texture in white-green color, defined by banded silica- and carbonate-rich layers (Figures 3.15 and 3.16). Thin section appearance of the tuffs is consistent with field observations and supports existence of compositional layering in a fiamme-type alignment of different particles. Non-pervasive carbonate and clay alteration with iron-oxide occurrences are present. Vitric ground and broken crystalline are settled together with volcanic rock fragments. Some of the crystals have experienced magmatic corrosion. Dacitic lapilli tuff show a volcano-clastic texture and is named, based on field observations and petrographic characteristics (Figure 3.17), as lapilli tuff with dacitic composition.

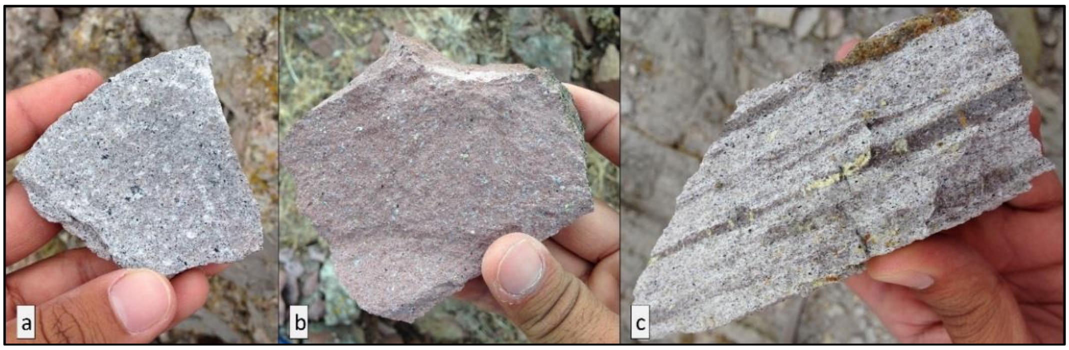

Figure 3.15: Handspecimen views of dacitic lapilli tuff: (a) equigranular texture; (b) quartz phenocrysts within a fine-grained matrix; (c) fiamme texture. The size of the thumb is ~3 cm.

Dacitic lapilli tuff unconformably overlies basements, megacrystic monzonite, latite porphyry and interdigitized with andesite unit of having lava flow texture and is unconformably overlain by rhyolitic crystal tuff, rhyodacite and conglomerates (Figure 3.2). Moreover it is cross cut by the quartz monzodiorite and diorite porphyry units.

It is known as Babadere formation (Karacık and Yılmaz, 1998) or Babadere dacite (Dönmez et al., 2005). There is no report of age data. Karacık & Yılmaz (1998) described this unit as well-bedded pyroclastic fallout deposits (pyroclastic rocks), made up of volcanic rock fragments, crystal pumice tuffs, and local ballistic bombs. The base of this unit is observed in the eastern end of the study area where latite-andesitic compositional affinities and lithic characteristics with fiamme texture are characteristic.

Figure 3.16: A view from a fiamme texture in lapilli tuff, lying above the latite porphyry. Pen is ~11 cm long.

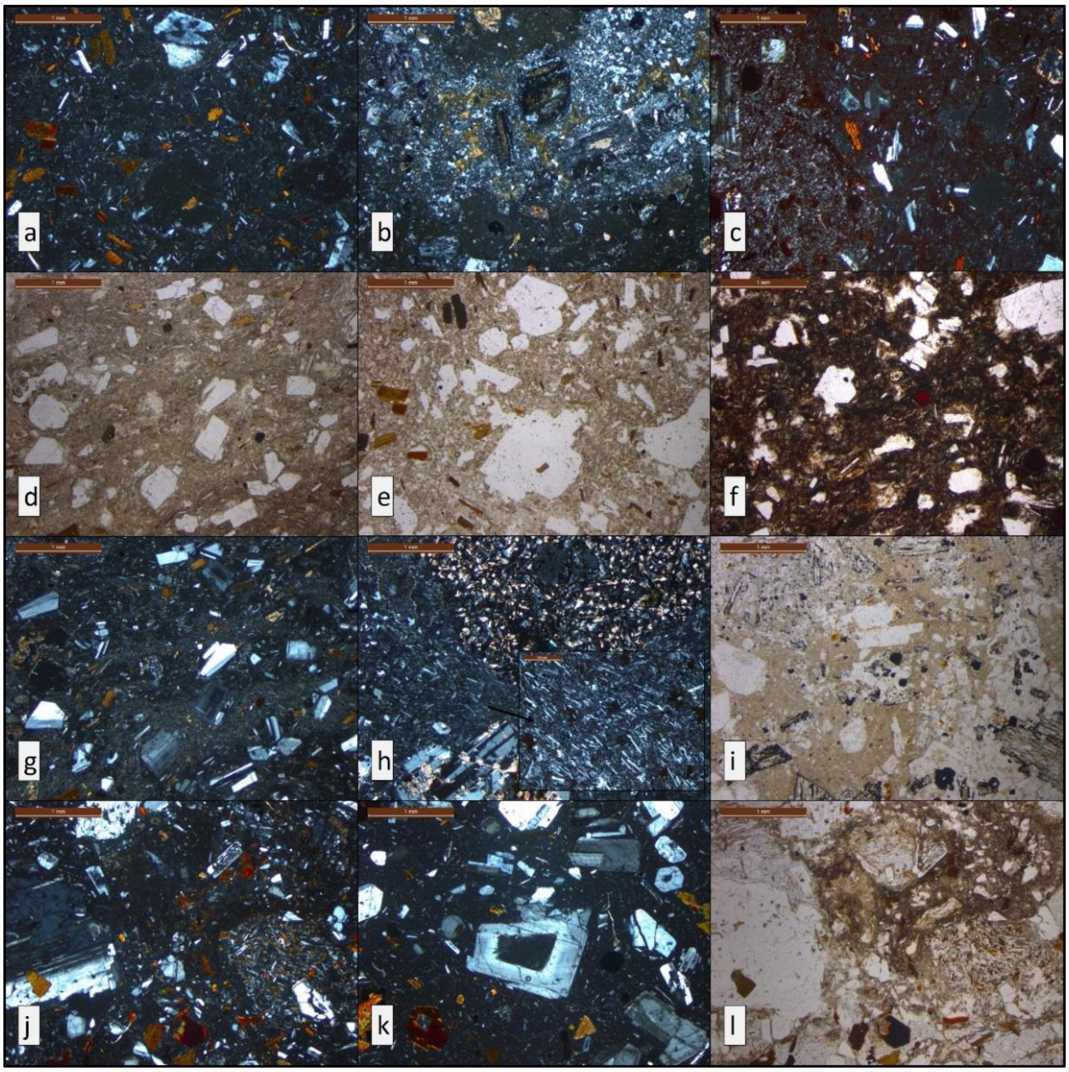

Figure 3.17: Photomicrographs of dacitic lapilli tuff unit: (a-d) glassy matrix and broken biotite feldspar phenocrysts; (b-e) fiamme texture of different compositional phases; (c-f) iron-oxide-rich groundmass; (g) fiamme texture, defined by glassy and carbonate-rich volcanic micro facies; (h-i) elongate minerals, broken crystals and a few-mm-thick rock fragments; (j) a characteristic view of the dacitic lapilli tuff unit (k-l) glassy matrix with rapid cooled broken feldspar crystals and partially corroded anhedral quartz crystals.

3.2.6. Rhyolitic Crystal Tuff

Rhyolitic Crystal Tuff is light yellowish white, light grayish yellow in color (Figure 3.18). It is composed of very fine rock fragments and generally distinguished by its thin layering or flaky and crunchy appearance.

It is mostly exposed in the center of the study area (Figure 3.1) and overlies dacitic lapilli tuff and latite porphyry (Figure 3.2). The boundary between those tuff units is transitional whereas latite porphyry contact is an unconformity surface (Figure 3.2). The unit shows a fining-upward sequence commenced by basal conglomerate and agglomerates where grain size ranges from volcanic bombs to tuff sized particles. Petrographically, it has very fine, less than 2 mm, equigranular rock fragments. It is non-magnetic and has very low specific gravity compared to other lithologies of the study area. On the thin sections (Figure 3.19), it shows a non-pervasive clay alteration of mostly orthoclase crystals. Magmatic corrosion and, broken feldspars and biotite crystals are present. The groundmass is dominated by volcanic glass and very thin compositional variation (carbonate-glass) as seen in fiamme textures.

Figure 3.18: Cut surface of a fresh Rhyolitic Crystal Tuff hand specimen. The size of the thumb is ~3 cm.

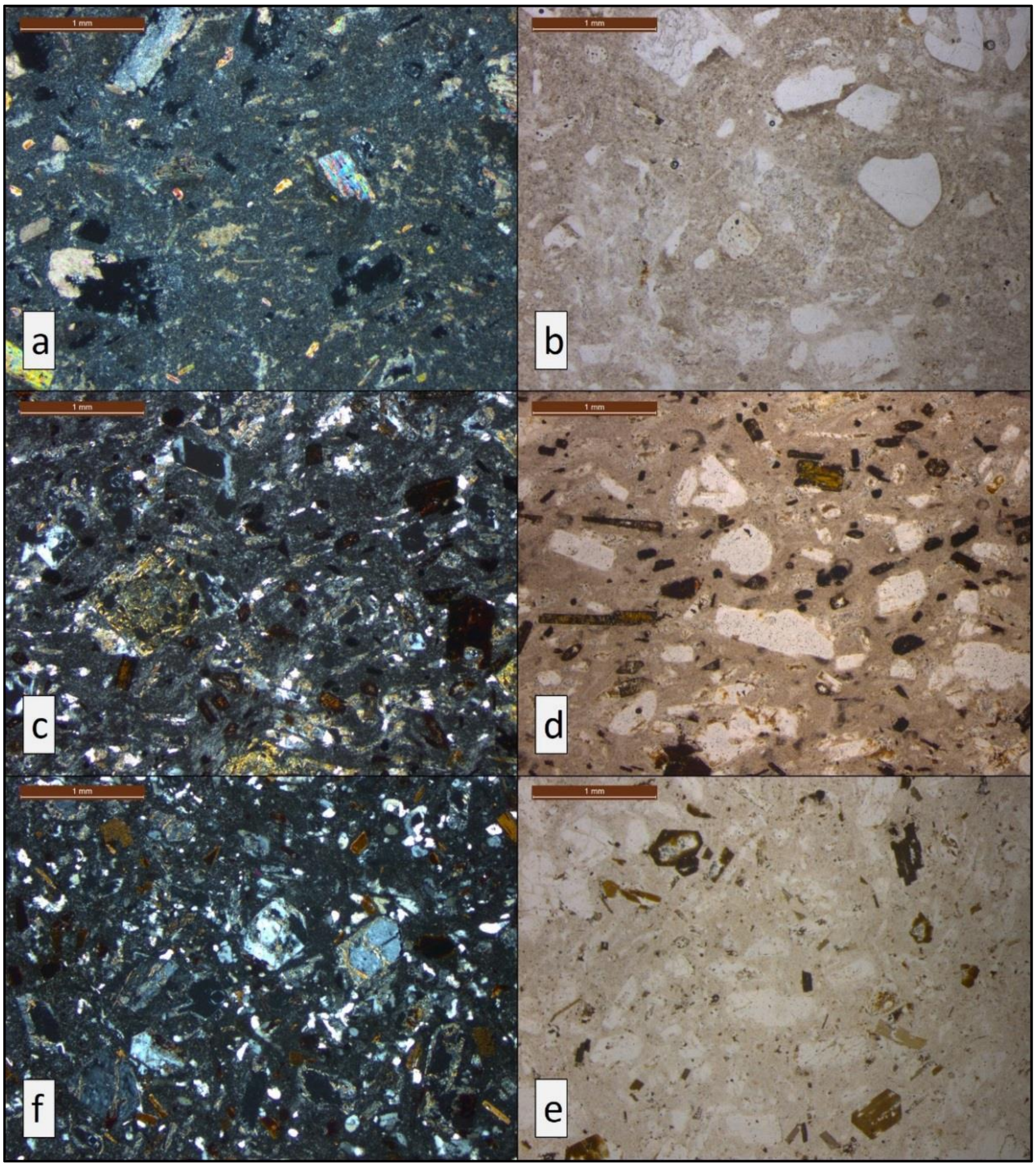

Figure 3.19: Some of the photo micrographs of rhyolitic crystal tuff units showing fiamme and broken crystal pieces with very fine groundmass. (d) elongated biotite crystals can be traced.

The unit is a crystal tuff with rhyolitic composition and forms a part of the Babadere formation of Karacık & Yılmaz (1998) or Babadere dacite of Dönmez et al. (2005). Likewise dacitic lapilli tuff unit, there is no absolute age data in the literature for Rhyolitic Crystal Tuff. Moreover, primary structures like ripple marks (Figure 3.19) and peperites (Figure 3.33.d) are observed, both of which indicates an underwater depositional environment.

Figure 3.20: Ripple marks between Rhyolitic Crystal Tuff layers. Hammer is ~16 cm long.

3.2.7. Quartz Monzodiorite

Monzodiorite is greenish brown cream, grayish light green in color, hypocrystalline; it is a holocrystalline, rarely porphyritic rock (Figure 3.21). Erosive and phanerithic appearance is characteristic. In the study area most of the outcrops are pervasively altered and weathered. It has patchy and limited outcrop distribution in the eastern side of the study area (Figure 3.1). Most exposures show evidence for later deformation, as joints. Petrograhically, the rock is composed of subhedral quartz crystals (about 10%), subhedral plagioclase up to 7 mm (about %30), subhedral biotite up to 2 mm (about 20%) with undifferentiated hornblende, euhedral muscovite (half mm in size; about %1) (Figure 3.22). It is moderately magnetic. Pervasive carbonate and clay alteration are characteristic.

Figure 3.21: Least altered monzodiorite hand specimen cut face for. The size of the thumb is ~3 cm.

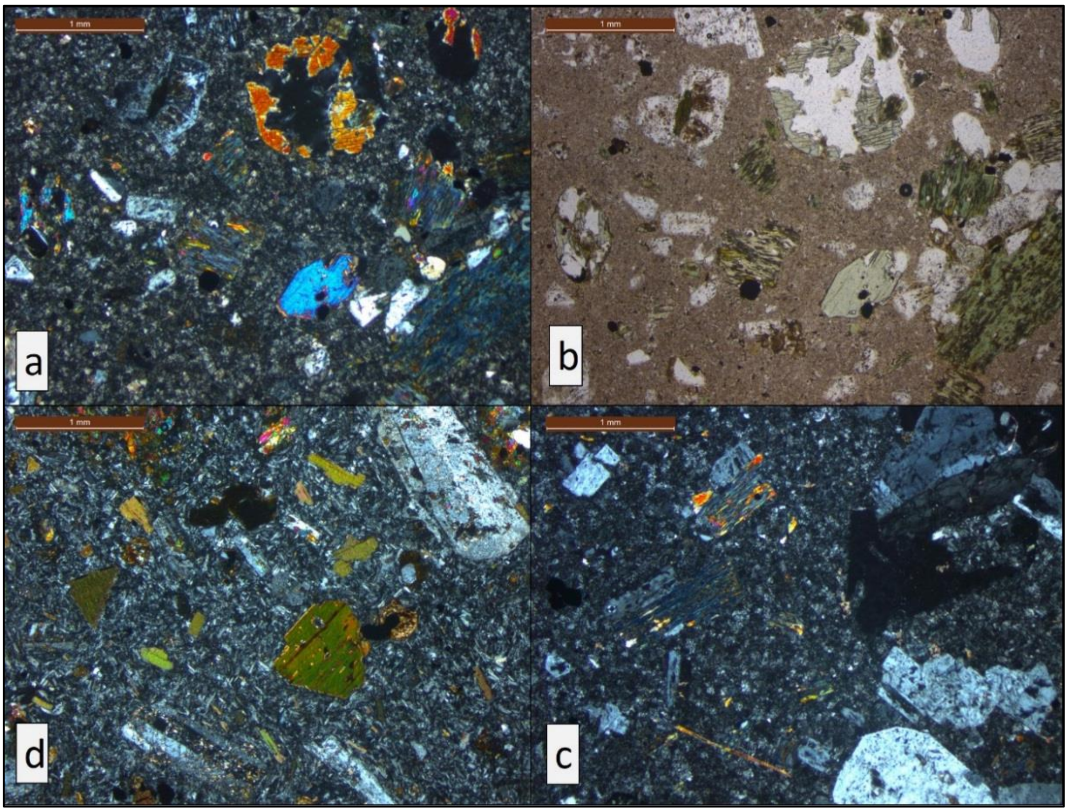

Figure 3.22: Photomicrographs of quartz monzodiorite unit: (a, c) chlorite, clay alteration; (b) plane polarized view of screenshot in ‘a’; (d) biotite and feldspars phenocrysts within a crowded groundmass.

According to field observations and petrographic characteristics, the rock can be named as quartz monzodiorite. Field observations suggest that emplacement of quartz monzonite gave birth to mineralization and related alteration; quartz monzodiorite is emplaced through latite porphyry and produced alteration zones within it. The same alteration has also developed within the andesite unit. Moreover, the mineralization has also affected the upper volcano clastic units. The age of the quartz monzodiorite and related mineralization must be younger than those units but older than lately emplaced bodies and clastic associations. In the literature, there is no overwhelming evidence about the age of emplacement and its causative alteration fertility.

3.2.8. Diorite Porphyry

Diorite porphyry is greenish gray, brownish green, gray in color (Figure 3.24). It is a holocrystalline rock with crystal size is in the order of a few mm’s (Figure 3.24). The unit is generally distinguished by resistant to erosive appearance and by a very fine to porphyritic texture. Most outcrops are patchily distributed and emplaced throughout the altered zone. It has fresh outcrops but locally exposed to weathering processes. Petrographically, the rock consists of quartz crystals (about 5%), subhedral plagioclase phenocrysts up to 8 mm (about %45), euhedral biotite up to 2 mm (about 20%) with macroscopically undifferentiated hornblende (Figure 3.26). It is moderately magnetic. Non-pervasive clay alteration of feldspars is evident in thin sections. Moreover, magmatic corrosion and plagioclase phenocrysts within a micro- crystalline groundmass is also observed (Figure 3.26). The field observations and petrographic characteristics are consistent with diorite porphyry terminology.

Figure 3.23: Road-cut view of diorite porphyry (scaled by hammer as ~42 cm)

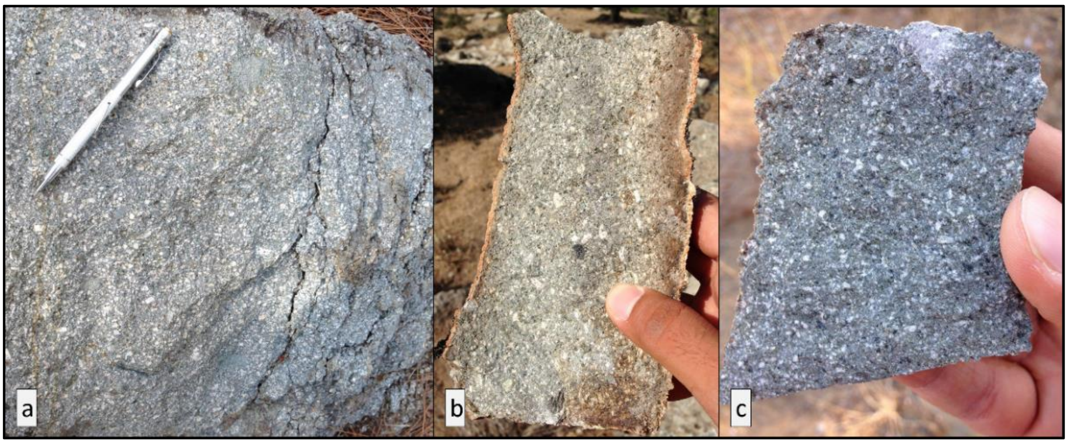

Figure 3.24: Macroscale view of diorite porphyry hand samples (scaled by scriber as ~12cm and thumb as ~3cm). a) up to a cm sized porphyry plagioclase within crowded ground b) holocrystalline texture c) micro crystalline crowded textured diorite porphyry

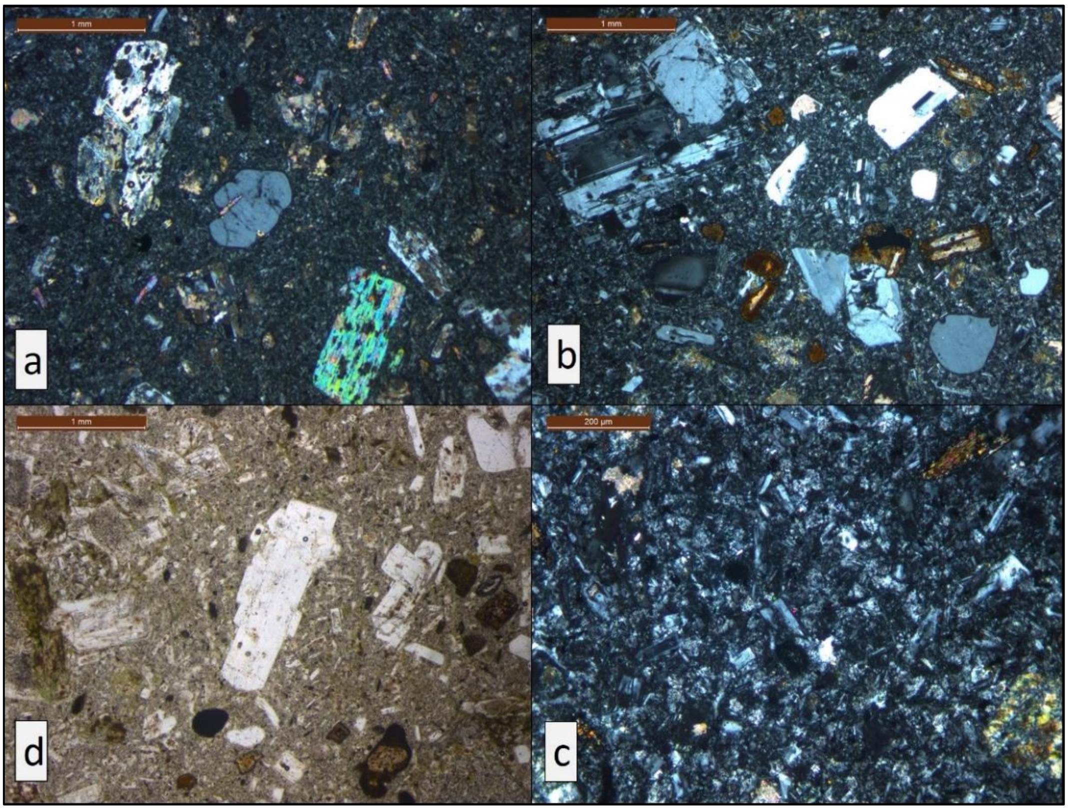

Figure 3.25: Photomicrographs of diorite porphyry showing crowded groundmass with porphyritic feldspars.

The contact relationship between the diorite porphyry and dacitic lapilli tuff (Figure 3.26) illustrates that the former is one of the latest intrusions. Diorite porphyry has experienced post-mineralization deformations, such as joints.

Figure 3.26: Cross-cutting relationship between the diorite porphyry (pie symbol) and the dacitic lapilli tuff unit (hexagonal symbol). Baked zone and chilled margins along the contact (dashed line) are characteristic. Hammer tip is ~16 cm long.

3.2.9. Rhyodacite

Rhyodacite is a purple, hypocrystalline, very fine to porphyritic rock (Figure 3.27). It is generally distinguished by its color and resistant to erosive appearance. It is widely exposed on Tuzla Hill, close to Tuzla Village. It has fresh to altered outcrops and show evidence for partial weathering effects. Petrographically, the rock is composed quartz crystals (more than 10%), euhedral plagioclase crystals up to 2 mm (about %30), euhedral mafic minerals as up to 3 mm (about %20), small (a few mm) euhedral muscovite crystals (about %2). It has low magnetic property. Thin section investigation also proves presence of smectite and chlorite type of alteration, which can be attributed to effect of either weathering or close geothermal association (Figure 3.28).

Figure 3.27: A view from a rhyodacite handspecimen from Tuzla-Ortaoba formation, southwest of study area. The size of the thumb is ~3 cm.

Field observations and petrographic characteristics are consistent with a rhyodacite terminology. The contact relations of the rhyodacite unit are not easy to map in the study area because most of the land is highly cultivated. In its the most characteristic outcrop (may be type locality), rhyodacite forms a small and stout-like dome in Tuzla Tepe, which is interpreted as latest products of regional volcanism in the

Biga Peninsula (Karacık & Yılmaz, 1998). The age of the unit is interpreted as late Miocene (Akal, 2013). Others included this rock unit within rhyodasitic volcanic rocks of the Tuzla and Ortatepe formations that overlie the Ayvacık and Balabanlı volcanic rocks (Bozkurtoğlu et al., 2006).

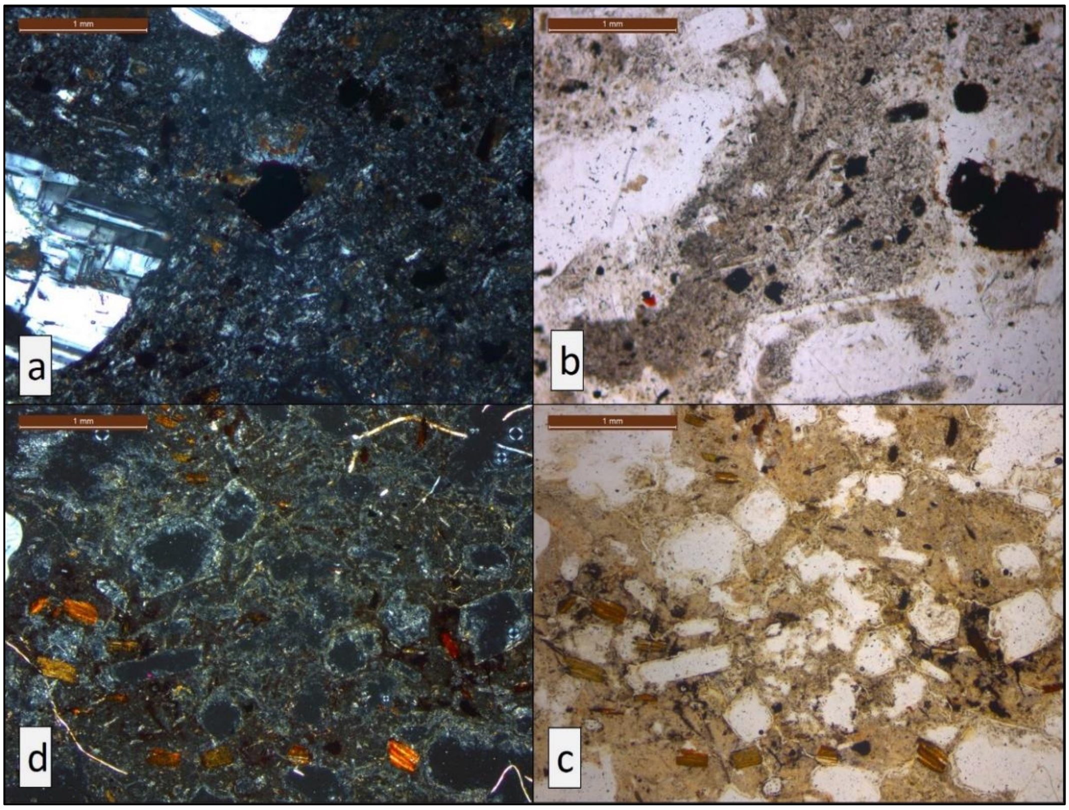

Figure 3.28: Photomicrographs of rhyodacite unit: (a, b) porphyritic texture, from Ortaoba hill (out of the study area); (d-c) equagranular texture, from Tuzla hill.

3.2.10. Conglomerate

Conglomerate is poorly sorted, yellowish white, brownish gray rock, composed rounded and gravel sized clastic rock (Figure 3.29). The fragments are derived mostly from marble, schist, plutonic and dominantly volcanic rocks and lie within a carbonatic matrix. Conglomerate unconformably covers all of the rock units in the western end of the study area (Figure 3.1). The deposition of conglomerates is attributed to activation of north-south-trending Ezine-Şarköy Fault (Elmas and

Meriç, 1998). It is named as Bayramiç formation (Siyako et al., 1989) or Ilıca formation (Karacık and Yılmaz, 1998). Both schools suggested an alluvial and/or fluvial depositional environment and late moiocene early Pliocene age for these conglomerates.

Figure 3.29: A view from the conglomerate unit. Pen is ~1 cm thick.

3.2.11. Alluvium

Alluvium represents the youngest unit of the study area and occurs in river beds.

3.3. Alteration and Mineralization

Alteration and mineralization in the study area are controlled mainly by geologic structures and plutonic emplacement. According to: (i) the timing of pluton emplacement, magmatic-hydrothermal and (present) geothermal activity, (ii) age of the rock units, (iii) the presence and/or absence of and (iv) number of alteration and mineralization events in different rock units (they differ from one rock unit to other), the alteration-mineralization events are going to be introduced as their compositional and their causative process relations.

3.3.1. Skarn Zone

Skarn zone occurred in relation to the emplacement of megacrystic monzonite into the basement rock units. A 2-3-meter-wide metamorphic aureole formed within the basements as illustrated by a range of contact metasomatic mineral assemblages formed at pyroxene-hornfels P/T conditions (Figure 3.30), which are quartz + diopsite + epidote + garnet showing along the contact zone (Figure 3.31).

Figure 3.30: Views from the skarn zone: (a) marble with epidote, garnet vein fillings; (b) garnet-bearing hand specimen; (c) diopside-bearing handspecimen; (d) diopside-rich carbonate/silica vein and sulfide-bearing skarn sample. The size of the thumb is ~3 cm.

Skarn zone, therefore, characterizes the earliest mineralization and alteration event in the study area and it is observed within a small outcrop. Considering the basement outcrop extent and average contact aureole width, it is hard to interpret this event as a sizable mineralization within the study area. As a note, contact metasomatic zone bears some silica sulfide veins. Chalcopyrite is mostly observed together with silica veins. Disseminated galena and pyrite also occur around the sulfide-bearing silica veins, where it crops out as few m lenses in the andesite unit. Sulfides show mostly supergene alteration products, like malachite or iron-oxide minerals.

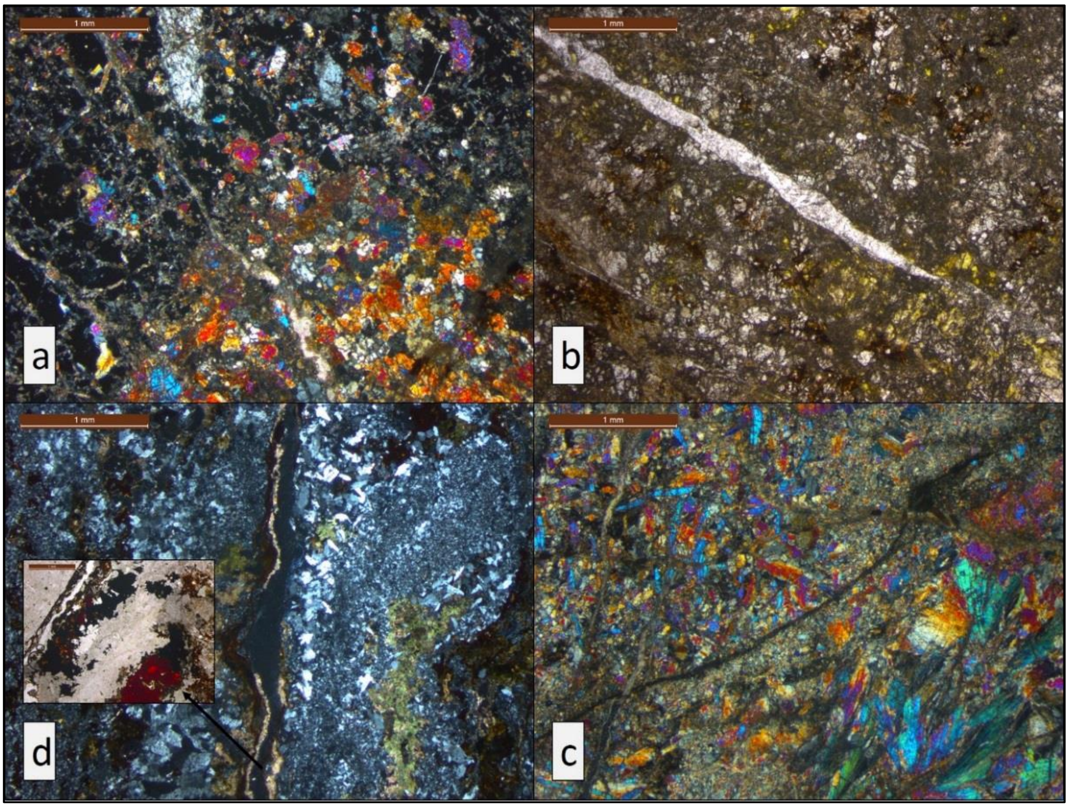

Figure 3.31: Photomicrographw of rhyodacite showing (a, b, d) quartz-diopside-epidote-garnet- carbonate-silica vein assembledges and (d) opaque minerals, chalcopyrite, galena, and pyrite.

3.3.2. Veining, Silicification and Clay Alteration Assemblages

Another mineralization and alteration activities are characteristically dominated by elongated and patchy distributed zones of selectively pervasive clay and silica alteration; some vein and breccia formation are also encountered (Figure 3.32). The formation of approximately east-west-trending silica veins and sparsely distributed breccia zones are also main characteristics of mineralization in the study area. Massive and chalcedonic silica constitute most of the vein fillings (Figure 3.33). What's more, comb, cockade, lattice bladed and druzy are locally seen silica textures.

Even in the silica textures, the time relations are clearly observed such that massive silica is overprinted by chalcedonic silica. Field relations among silica textures and clay alterations are also double checked during thin section investigation. To sum up, clear alteration and mineralization zonation of silica to low temperature clay, chlorite alteration pattern are observed (Figure 3.34) on the both tuff units.

Breccia zones are sparsely distributed and generally located at the conjunction of some faults and/or discontinuities like ruptures zones and vein fillings. The fragmentation can also be driven by hydrothermal-related explosive activities if the hydrothermal water reach to cold water reservoir and/or water table; this causes an increase in volatile- and vapor-phased explosions in a diatreme pipe, as explained in Sillitoe (1985). Here, occurrence of the both tuff and latite particles within bilithic breccia zone attest absence of diatreme pipe since tuff unit already has underwater conditions.

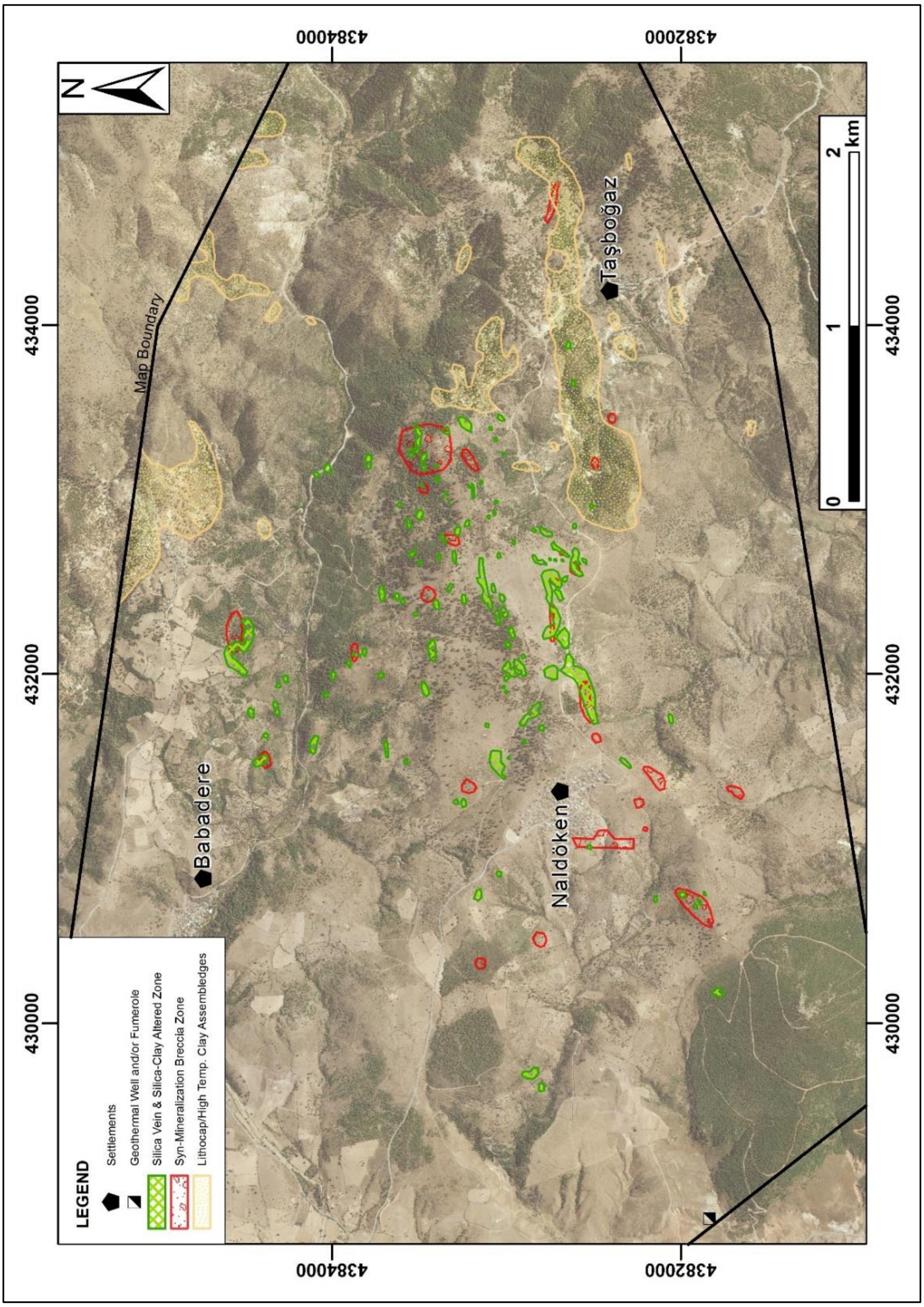

Figure 3.32: Alteration map of the study area with Bing maps overlay.

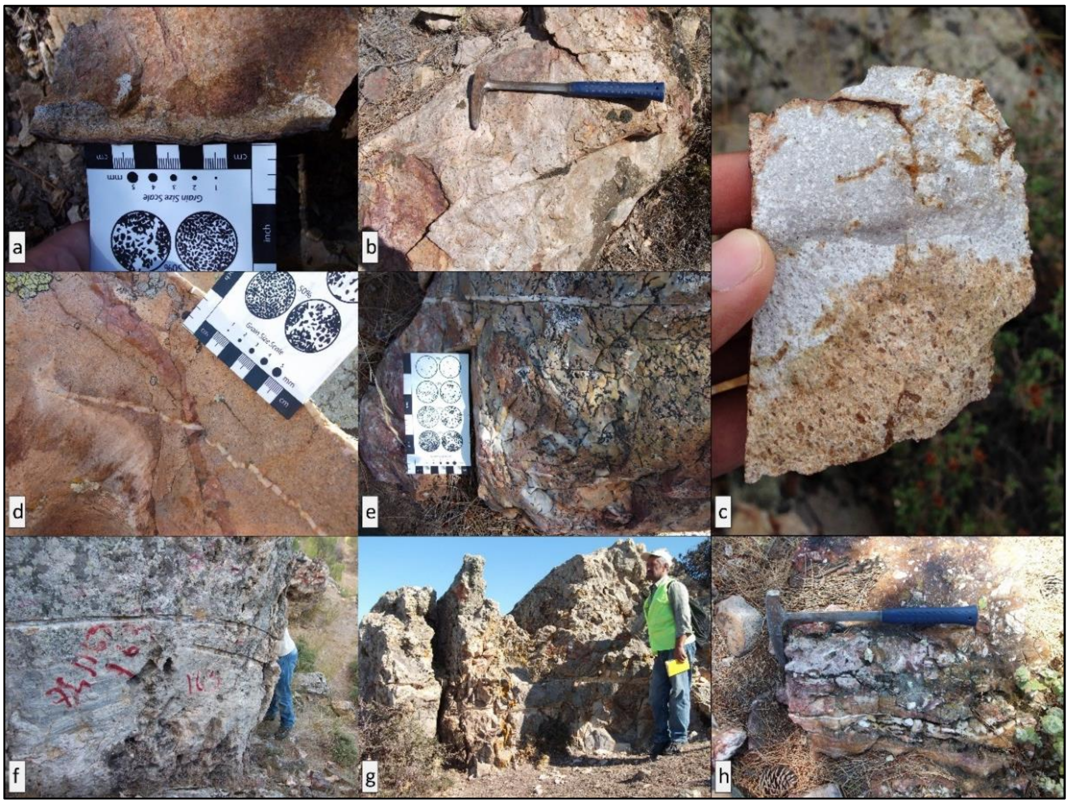

Figure 3.33: Field views of rhyolitic crystal tuff with syn-mineralization activities: (a) comb texture in a few mm thick quartz vein, corresponding silicification and clay alteration halo; (b) massive silica vein; (c) tuff with gradually changing silica dominant to clay pervasive alterations; (d) peperite texture and milky chalcedonic vein having cross-cutting relationships; (e) massive-brecciated silica cross cut by milky chalcedonic silica; (f) possibly sinter-like layered silica formation; (g) brecciated and silicified outcrop; (h) synthetic chalcedonic vein with early brecciated quartz.

To sum up, alteration patterns of these activities in the study area are generally overlapping (except high temperature clay-bearing zones) with silica veins and breccia zones. Selectively pervasive clay and non-pervasive silica alteration form examples of main alterations around them. The clays are generally low temperature products, such as smectite, kaolinite, and chlorite. Considering quartz textures and mineralization temperature, it is also possible to observe adularia, sericite or illite kind of clay minerals. Considering the host rock lithology of the veins and breccias, alteration mostly occurs in tuff and latite units (Figure 3.35). As a key note for precious metal content (possibly gold and silver), there are many old working activities, like trenches, galleries and collection sites in the study area where there are breccias and some veins.

In addition to low temperature alteration and quartz-breccia mineralization features, there are also high temperature (alunite, dickite, sericite) alteration assemblages in the southeastern part of the study area (Figure 3.32). The high temperature products are overlapping with patchily distributed quartz monzodiorite emplacements. Around the emplaced stocks, pervasive clay alteration, associated with hypogene and supergene activities, are present. The relevant alteration is quite extensive pulsing through most of the proximal area and older rock units, such as latite porphyry (Figure 3.36), andesite and dacitic lapilli tuff. Latite porphyry shows lithocap-like alteration assemblages whereas andesite unit (including dome and extrusive phase) has broad range of alteration products, from argillic to prophylitic mineralogy (Figures 3.37 and 3.38). Same alteration mineralogy occurs in the dacitic lapilli tuff unit, in especially those exposed in the area between dome and extrusive andesite unit. The corresponding high temperature and low pH alteration also points out potassic alteration or mineralization in the quartz monzodiorite. In the study area, quartz magnetite veining ± sulfide overpinting potassic altered zone (Figures 3.37-3.39) are identified in the southern and northeastern part of the study area (Figure 3.32).

According to the thin section studies, early veins in potassic altered zone are quartz and sulfide free veinlets, and contains actinolite, magnetite ± biotite with no alteration halo. Then, it is cross cut by the sulfide-bearing granular quartz dominated veinlets and partially recognizable alteration selvages. Quartz veins with sulfides are also present. These observations are consistent with those of Sillitoe (2010) and are illustrated in Figure 3.41. The first and second phase of the veins, however, show complex cross-cutting relationships as different sets of veinlets with same compositions even in single thin section. To sum up, it is important to mention that different sets of veins, that cross cuts each other, show repetition of metal-rich vein formation since a great rate of metal in porphyry deposits is contained in the quartz-dominated veinlets (cf. Sillitoe, 2010). Additionally, Sillitoe (2000) mentioned the strong correlation between quartz veinlets' intensity and metal content of Au-rich porphyry deposits.

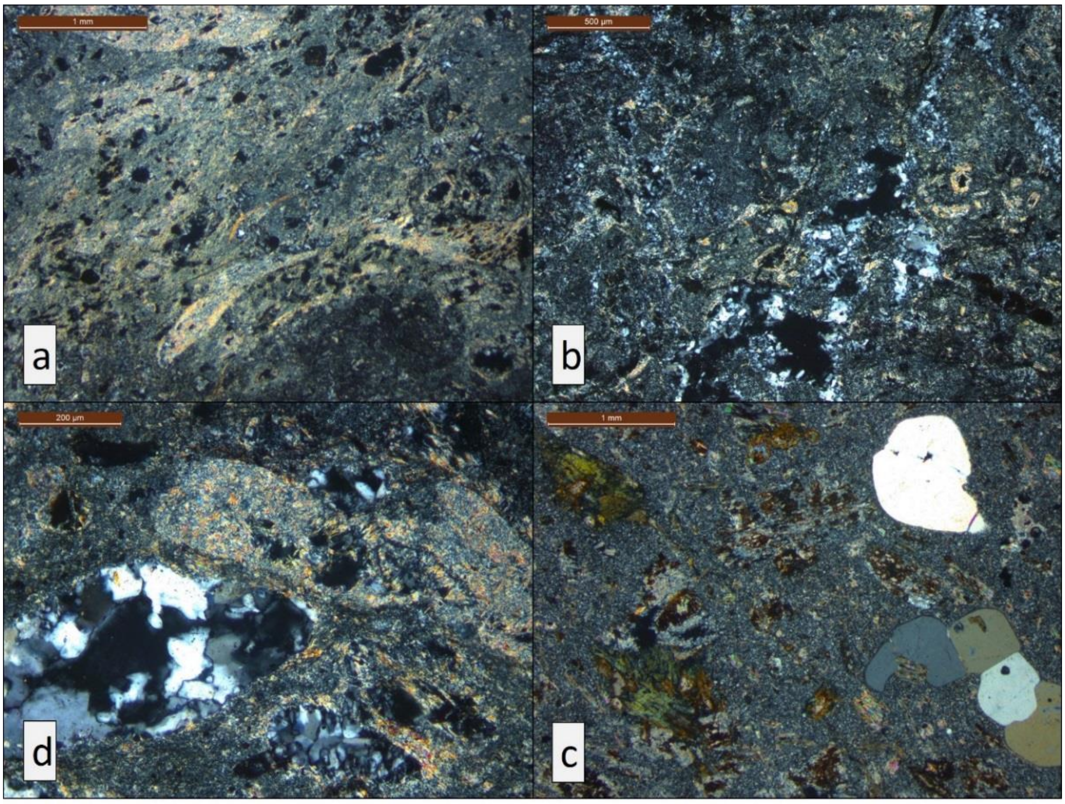

Figure 3.34: Photomicrographs of clay and silica altered rhyolitic lapilli tuff: (a) preferred alteration pattern on fiamme texture, showing clay mineral assemblages; (b) pervasive silicification and euhedral quartz mineral geode like growth; (c) chlorite altered tuff; (d) summary view for replaced quartz and clay alteration over possibly feldspars.

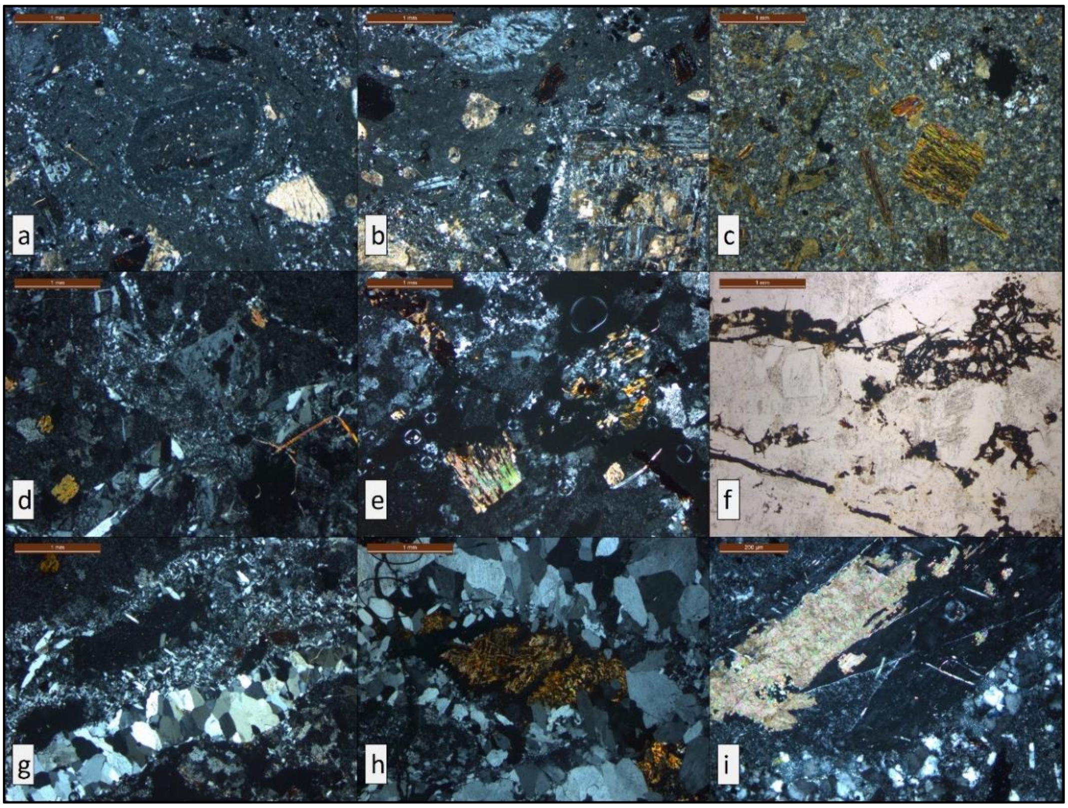

Figure 3.35: Photomicrographs of altered and mineralized latite porphyry: (a, b) selectively pervasive silica and clay alteration; (c) chlorite, carbonate, clay and silica alteration; (d) latite breccia porphyry, showing silica dominant cement; (e, f) euhedral quartz growth with some iron oxide and silica cement in between latite clasts; (g) pervasive silica alteration with quartz veining; (h) low to high temperature clay-bearing clasts in-between silicified and silica vein zone; (i) carbonate displacement on feldspars and lateral non-pervasive silicification.

Figure 3.36: Field view of hypogene and supergene alteration in the latite porphyry. Scriber is ~11 cm long.

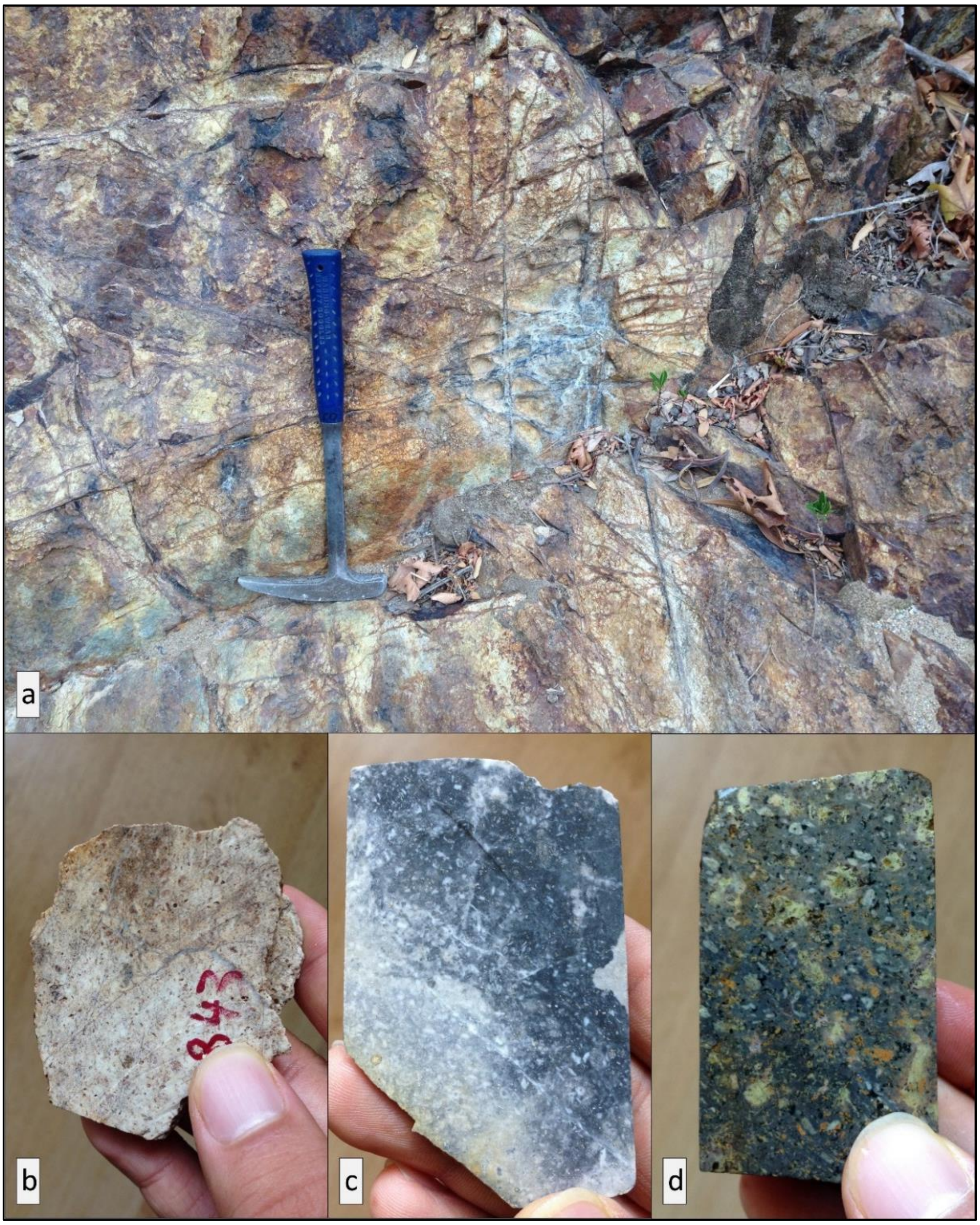

Figure 3.37: Views of central to proximal alteration patterns of andesite unit and porphyry stock (quartz monzodiorite): (a) quartz-magnetite veining in potassic altered zone of the porphyry; (b) pervasive clay alteration in quartz veinlets in root zone samples; (c) gradually decreasing alteration as seen in ‘b’; (d) prophylitic alteration assembledges; chlorite and epidote.

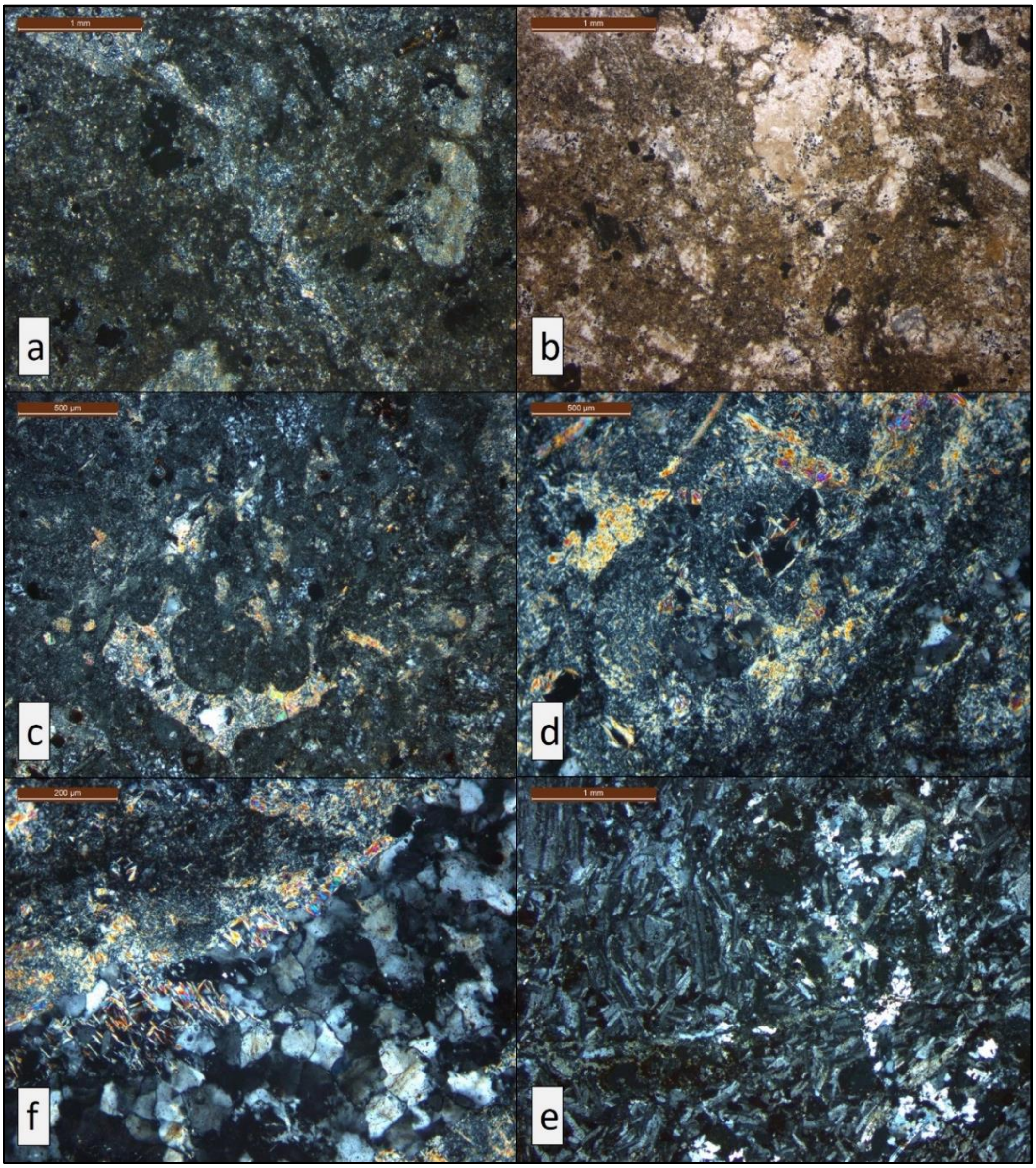

Figure 3.38: Photomicrographs of altered andesite unit: (a, b) pervasive clay and selectively pervasive silica altered (veined); (c) alunite-bearing silicified screenshot; (d) euhedral elongated alunite occurrences; (e) alunite with ore zone or (f) silicified vein.

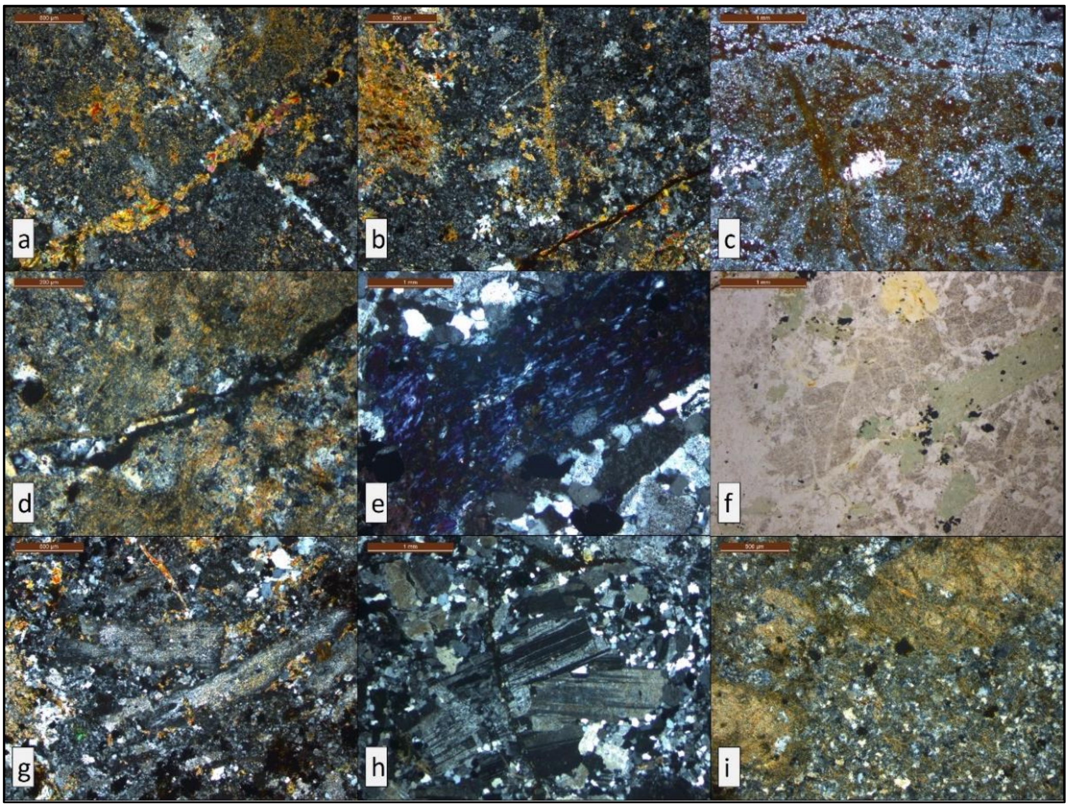

Figure 3.39: Photomicrographs of pervasively altered quartz monzodiorite porphyry stock: (a) pervasively biotite-actinolite quartz sulfide vein cut by biotite?-actinolite vein; (b) late sulfide rich vein; (c) different sets of veining with different compositions; (d) magnetite-quartz veining; (e) chlorite halo-bearing quartz veining; (f) green actinolites; (g) alunite- and anhydrite-bearing pervasive potassic alteration; (h) pervasive silica and k-feldspar alteration; (i) pervasive replacement of feldspars after clay minerals.

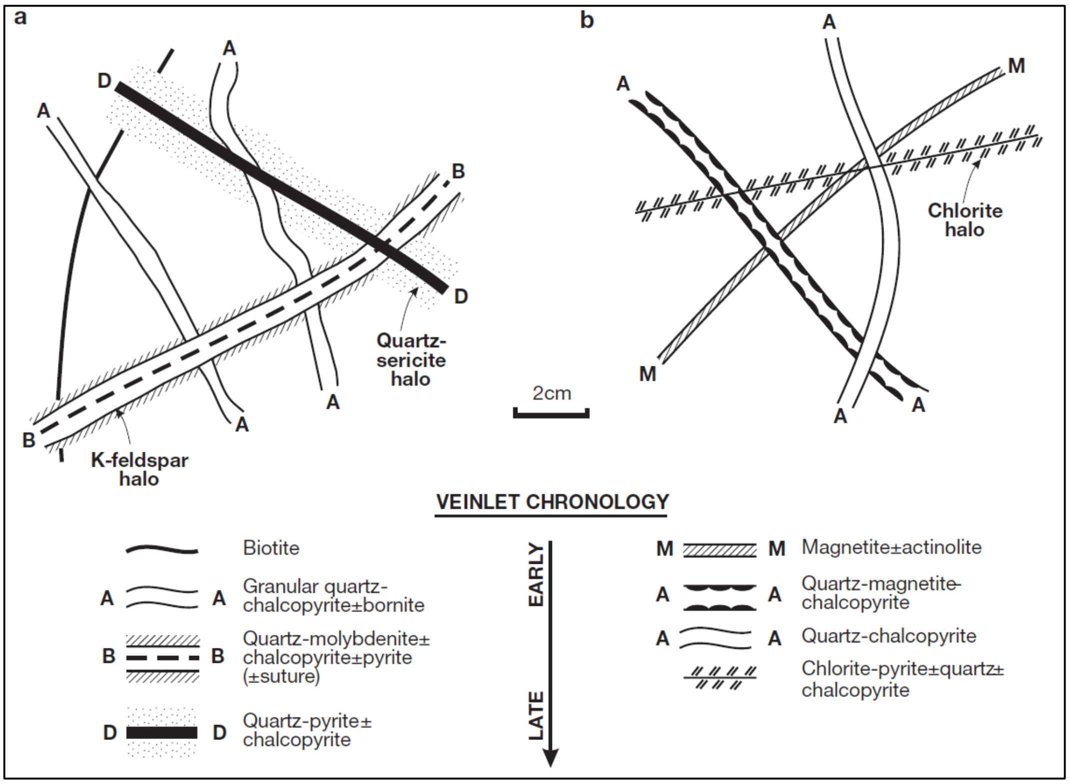

Figure 3.40: Schematic chronology of typical veinlet sequences in (a) porphyry Cu-Mo deposits and (b) porphyry Cu-Au deposits associated with calc-alkaline intrusions (porphyry Cu-Au deposits hosted by alkaline intrusions are typically veinlet poor). Background alteration between veinlets is mainly potassic (taken from Sillitoe 2010 and references therein).

3.3.3. Weathering and Present Geothermal Occurrence Effect

Weathering has occurred due to atmospheric activities, collectively resulting supergene assemblages. Supergene activity can initiate low temperature alteration during which, depending of created pH value, a broad range of clay minerals may form (Corbett & Leach 1998). The alteration products may be illite, halloysite, kaolinite, chlorite, smectite, carbonate, calcite and etc… Moreover, some iron-oxides, like hematite, jarosite, goethite, may also also form during supergene activities (Figure 3.41). In some cases, iron-oxide leakeage and corresponding acidity may result in ferrocrete formation where low pH iron oxide-rich solution meets with the running waters (Figure 3.42). In addition to the weathering, the proximity of Tuzla Geothermal field is critical and continuously causing alteration around geothermal fumaroles, that is a few km southwest of the study area; it is quite significant because it may produce a low temperature extensive halo with overprinting alteration assemblages, like smectite, chlorite, carbonate and calcite. Along pathways of fumaroles or geothermal waters, talc or serpentine occurrences are common. Rhyodacite and some portion of the latite porphyry exposed in the southwestern part of the study area show evidence of geothermal causative non-pervasive clay-carbonate alterations. These alteration products get selectively pervasive around some faults in sterile occasion. The products are generally identified as carbonate, smectite, kaolinite and chlorite assemblages with rare jarosite occurrences. Microscopically, alteration are common around feldspars and some mafic minerals, biotite.

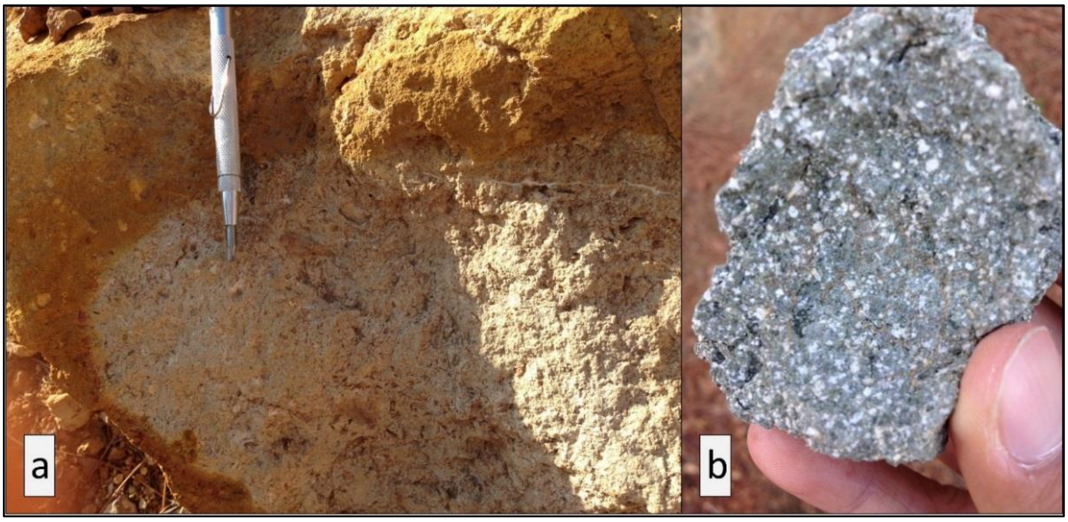

Figure 3.43: Views from weathering effects: (a) altered andesite, overprinted by dissolution of sulfide and occurrence of jarosite; (b) chlorite alteration on highly weathered diorite porphyry sample.

Figure 3.44: Field view of hanging/elevated ferrocrete formations.

3.4. Discussion

A detailed account of eleven different rock units and three-staged mineralization events are given in the preceding sections; temporal and spatial relationships among rock types and different process are discussed. The basement and megacrystic monzonite share earliest mineralization related history according to the cross cutting relationships of these rock units. There is no evidence of later mineralization activities except weathering products affected these rock units because they are not located in a suitable proximity for provoking alteration agents. The emplacement of latite porphyry is the first hypabyssal product in the study area. Literature knowledge about emplacement depth is worth remembering at this point: Akal (2015) claimed that Kestanbol granite is emplaced at shallow crustal levels in the range of about 1-10 km. considering average erosional rates as 1 km Ma-1 (Ring et al., 1999), the unconformable boundary between latite porphyry and extrusive volcanic rocks can be explained by erosional activities. At this time span, second hypabyssal andesitic emplacement into the latite porphyry occurred, and then followed by andesite lava flows unconformably above the latite porphyry (Figure 3.3). Extrusive andesite is interdigitated with dacitic lapilli tuff unit. The carbonate vesicule-fillings (amygloidals) of extrusive andesite suggest underwater environment. The lateral equivalent, dacitic lapilli tuff unit may therefore be formed under water conditions since it has carbonate-rich fiamme textures. Consequently, extrusive andesite and dacitic lapilli tuff will be considered as deposited under water conditions; there is, however, more evidence is needed to support this assertion. The unconformable (or questionably transitional) rhyolitic crystal tuff unit is also deposited under water conditions since it has primary depositional features like ripple marks or peperite textures. All of the rock units, except basements and megacrystic monzonite, are altered and mineralized subsequent to the emplacement of quartz monzodiorite. Its cross-cutting relationships with the extrusive volcanic rocks are not observed because of agricultural activities and limited exposures. But, occurrence of adjoining high-temperature mineralization and alteration associated with quartz monzodiorite and low temperature alteration and mineralization in distal sites (Figures 3.2 and 3.32), extrusive volcanic rocks, constrain the age relations of quartz monzodiorite. After main mineralization event, diorite porphyry was emplaced into the high temperature alteration zones and tuff units but its relation to the rhyodacite and conglomerate units is not well explained. The rhyodacite unit is represented by thick lavas and considered as early products of early Miocene volcanic activity (Karacık and Yılmaz, 1998; Bozkurtoğlu et al., 2006; Akal, 2015). The conglomerate unit is the product of the latest alluvial-fluvial deposition of the study area under the control of north-south-trending Ezine-Şarköy Fault.

High temperature alteration and mineralization products explain porphyry-type mineralization at the bottom and at the top of the rock sequence, whereas low temperature alteration and mineralization demonstrate the presence of low sulfidation type mineralization. The cross-cutting silica viens (± breccias) with different textures in the high temperature and low temperature zones favors structural active mechanisms during mineralization. Underwater conditions of the host rock units explain low temperature silica formation, chalcedonic, and limited quartz crystalline textures. Moreover, silica sinter formations are also present around the fault conjugations and then they are all sealed by volcano-sedimentary sequence. High temperature quartz sulfide veinlets show banded and synthetic fillings on thin sections and this is ascribed to the shallowness of porphyry formation (<1 km) (cf. Sillitoe 2010 and references therein).

According to the geothermal exploration well-loggings and thermal spring occurrences, the study area may have been affected by active mineralization at a depth of about 1 km, which may overprint current alteration products of prophylitic (chlorite dominant) assemblage. This post-mineralization activity is commented as ongoing mineralization at depth. It is interesting to see same rock units also in the geothermal cores as addressing same source-host relations.

Due to the fault activities, the western side of the study area is less prone to mineralization with respect to the eastern side of the area; that is why western site appears to be sterile. Additionally, the temperature relations of both alteration and mineralization show gradual zonation from east (high temperature) to west (low temperature). Fertilization on eastern side is therefore attained to the out cropping and erosional mechanisms triggered by fault activities.

CHAPTER 4

STRUCTURAL GEOLOGY

"Among all geologic techniques, the mapping of structures and their analysis nonetheless remain a key guide to ore."

(Simmons, et al., 2005)

The importance of geologic structures for ore formation is incontestable truth since it directly effects the ore genesis by controlling and contributing permeability and fluid flow, transport and transfer processes, pressure gradients and water rock reaction and depositional process. Additionally magma localization and its fertility are also quite dependent on regional tectonism and structural factors. In the absence of structural studies, modelling the mineralization will be a trivet without a pillar.

4.1. Introduction

The structures exposed in the study area are both mineralization affected (fertile) and mineralization sterile features, those features include quartz veins, faults, breccia zones, joints and beddings. To understand the spatial and temporal variations and relationships among these structures, a totally of 456 different structures was measured (Figure 4.1). Despite of spatially homogeneous descriptive data collection, data processing was also carried out before kinematic investigation run. Those are data validation, sorting, summarization and classification stages. After all, dip and strike measurements of planar features and direction, plunge and course of motion data of linear features were analyzed on computer software program to describe the geometrical characteristics of features.

Consequently a proposed structural model for occurrence of mineralization related structures and its relation with other structural features will be the outcome of this chapter.

4.2. Geological Structures

There are four different structural features are mapped in the study area; beds, joints, veins and faults. The veins are directly related with the mineralization activity. Moreover, the faults are noted for its mineralization relationships in order to correlate its importance for localization of mineralization. In addition to these structural elements, the study area also consists of five different nearly planar hiatus between rock units and breccia zones, which are formed by the activity of faulting. Unconformities are briefly explained in the previous chapter and the other structural features will be described and investigated in the following sections.

4.2.1. Beds

Beddings are well developed in the extrusive volcanic rocks. They are thin to thick bedded (a few cm to m thick) features and locally bear some primary structures (Figure 4.2).

Due to the extensive coverage of bedded rock units within the study area, it is preferred to get focused on bedding around mineralization area, particularly the rhyolitic crystal/lithic tuff unit. They display well-developed bedding planes with dips ranging between 08° and 73°. According to strike and dip measurements of 23 homogenously distributed bedding planes, the dominant set trends in northwest direction (Figure 4.3).

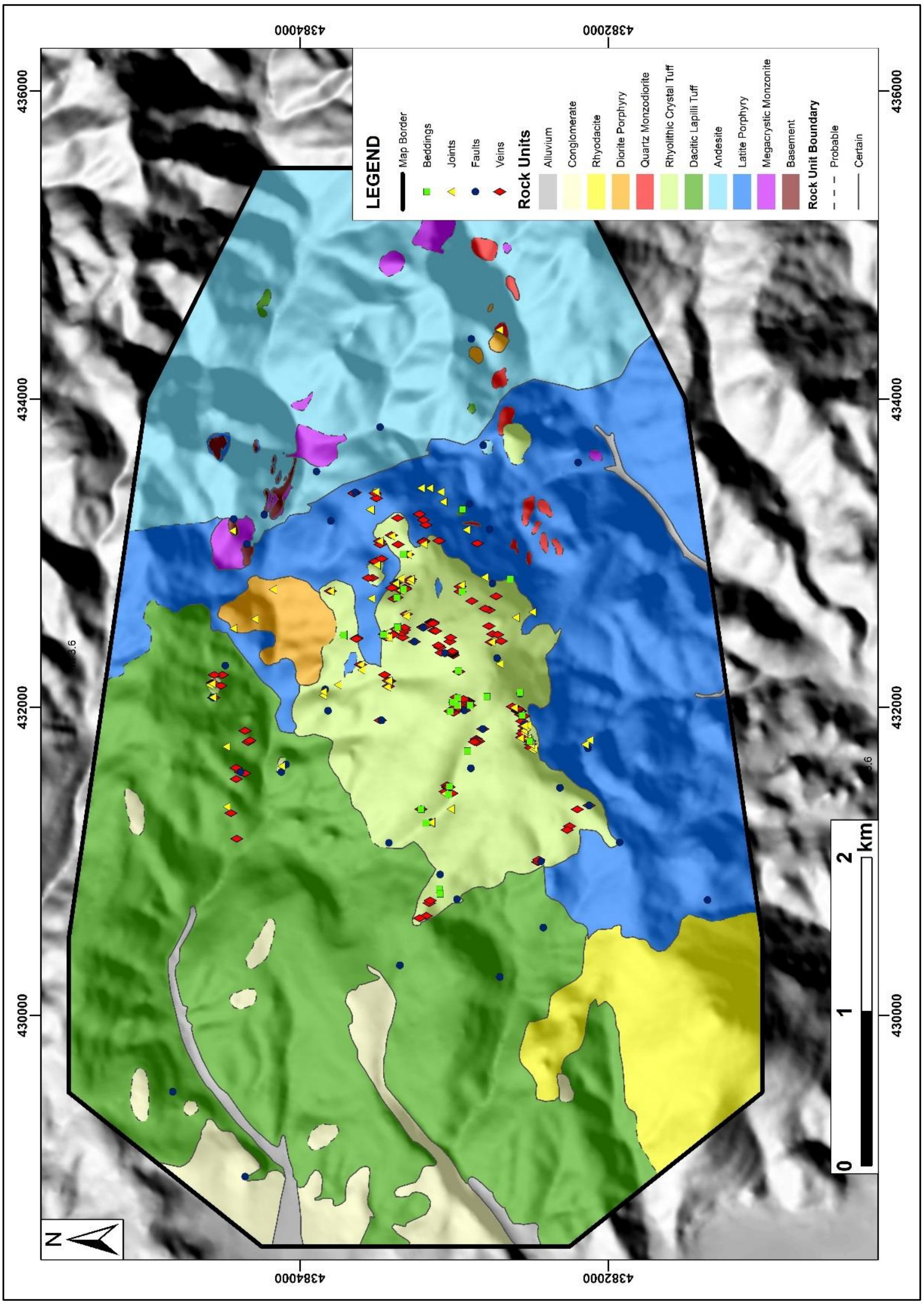

Figure 4.1: Locations of structural measurements.

Figure 4.2: A view from thin-bedded rhyolitic crystal/lithic tuff.

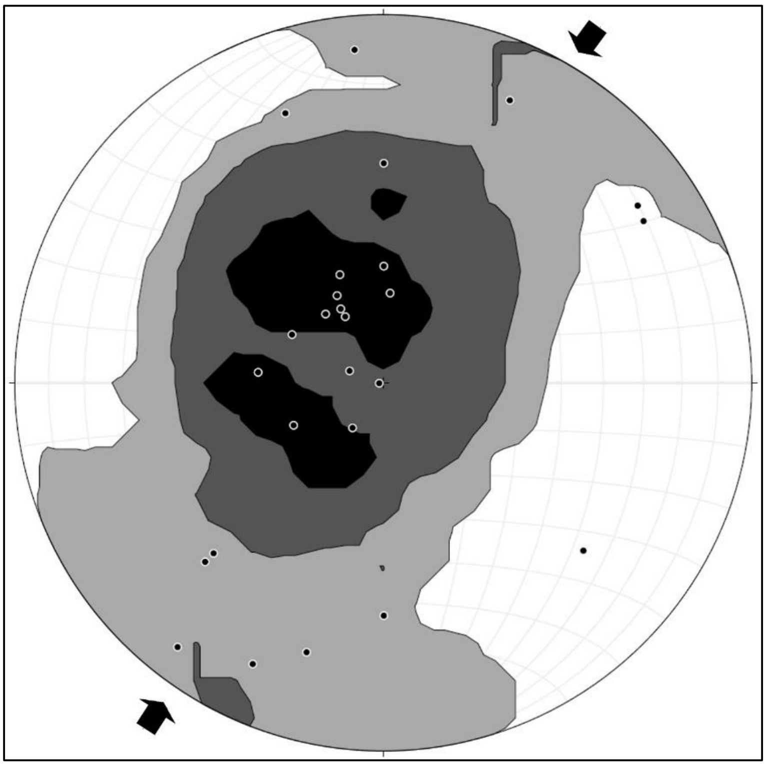

Figure 4.3: Poles to bedding planes on the Schmidt's lower hemisphere net. Large arrows show the proposed shortening direction of the deformation phase that might have deformed the rhyodacitic crystal tuff unit.

4.2.2. Joints

Joints are well developed in the hypabyssal and extrusive rock units. Due to the extensive jointing in different rock units, it is preferred to get focused on mineralization-bearing area and near surroundings for joint analyses. Dips of joint planes ranges from a few degrees to vertical. According to strike and dip measurements of 116 homogenously distributed joint planes, the dominant interpreted trends (Figure 4.4) are;

- Set 1: ESE-WNW trending joints
- Set 2: NW-SE trending joints
- Set 3: NE-SW trending joints
- Set 4: NNE-SSW trending joints.

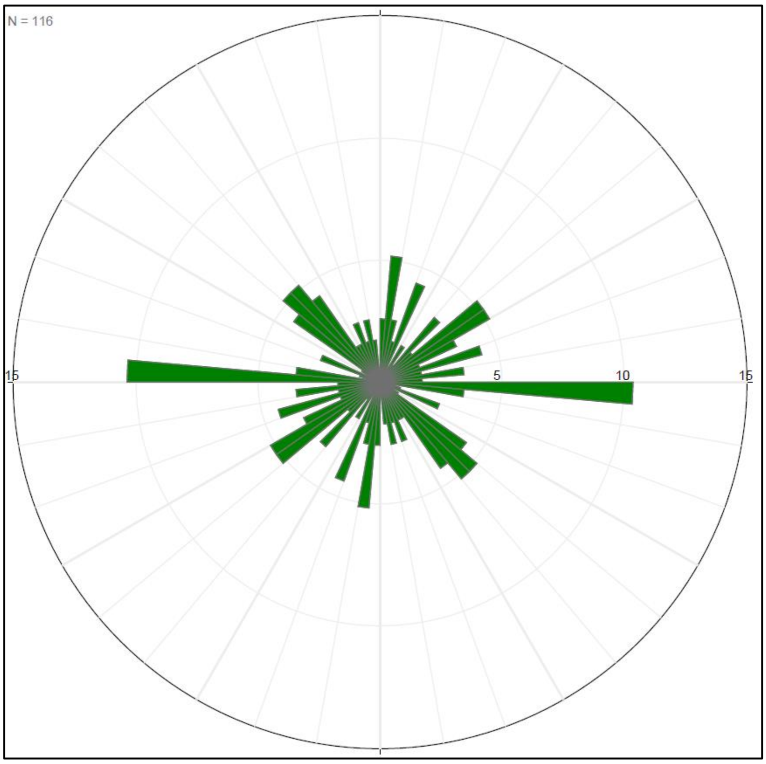

Figure 4.4: Trend-weighted rose diagram, showing four dominant orientations.

Joints generally show conjugate geometry; each unit is general deformed by two to four different sets of jointing. Older hypabyssal, crystalline and basement rock units show relatively more joint sets than extrusive volcanic rocks. All measurements are taken from mineralization free areas. There is always a possibility that overlapping trends with mineralization features. The same trends of quartz veins and isolated conditioned joints can be commented as portioning of flow among elements of a fracture (cf. Cox & Knackstedt, 1999; Figure 4.5).

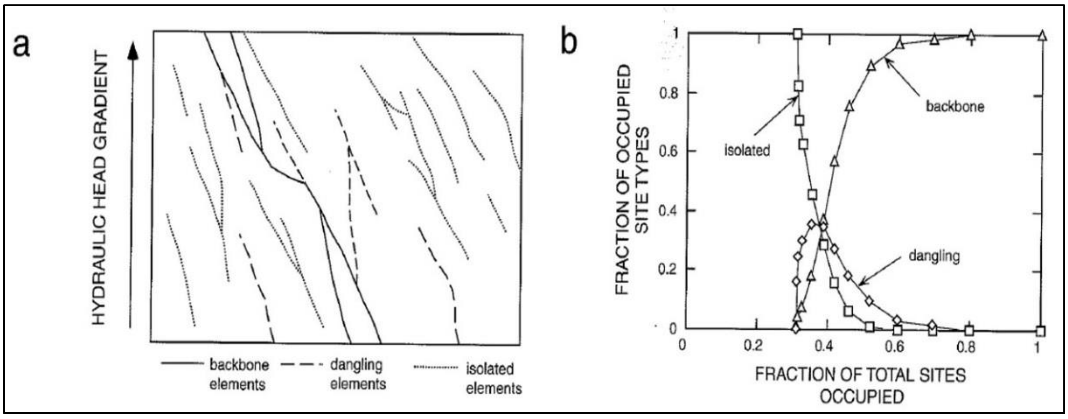

Figure 4.5: (a) Schematic two dimensional representation of a fault/fracture network consisting of isolated elements, dangling elements and the backbone structure. Most flow is localized along the flow backbone. Dangling elements in the upstream (lower) part of the system feed fluid to the backbone of the system, whereas dangling elements of the network in the downstream (upper) part of the system act as fluid discharge sites. (b) Fraction of isolated, dangling and backbone sites as a function of total number of sites for the three-dimensional case of conjugate fractures or faults inclined at 45^{o} to the bulk flow direction. (Cox & Knackstedt, 1999).

4.2.3. Veins

Veins are definitely formed during along structural features, with thickness ranging from a few cm to a few meter, well-crustiform to cross-cutting banded, single phased, brecciated and cemented or all at once (Figure 4.6). They mostly extends several meters and show linear patchy trends (Figure 4.7). Veins can be used to determine major extension directions. 184 vein data are therefore analyzed in order to demonstrate stress configurations of the region during vein formation. In Figure 4.7, a stereographic rose and rose trend plot of the veins and their pole are given, using a contour diagram. Consequently analysis shows the attitude of best fit great circle ($\sigma 1$ and $\sigma 2$ on it, $\sigma 3$ perpendicular; seen as yellow box) as 086^{o} $/09^{o}$ (strike/dip; right hand rule). The dominant pole position corresponds $183^{o}/58^{o}$, $\sigma 3$ (seen as black box). The orientations of principal stresses are as follows; $\sigma 1$: 356^{o} $/82^{o}$. $\sigma 2$: $178^{o}/08^{o}$, and $\sigma 3$: 088^{o} $/01^{o}$ (Figure 4.8).

Figure 4.6: Massive silica vein, later fault brecciated and cemented by translucent quartz.

Figure 4.7: Chalcedonic quartz crustiform vein with brecciated central zone.

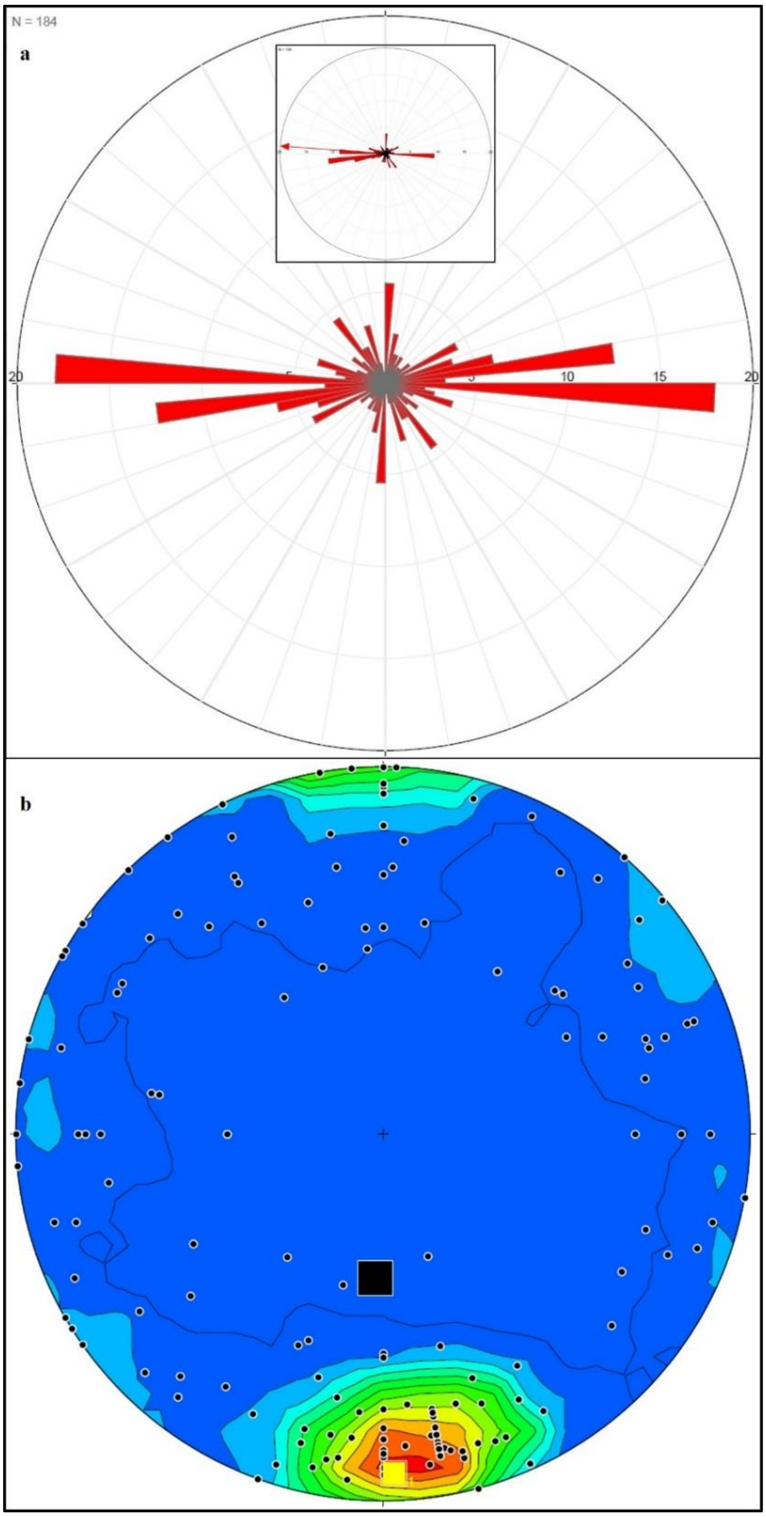

Figure 4.8: (a) Trend-weighted rose diagram, showing two dominant trends. (b) Contour diagram of the veins based on their poles and orientation of the best fit plane, and direction of stress, NNW-SSE (squares; yellow-best fit great circle, black-poles)

Some veins were mined during ancient times, during which the promising part of the veins – mostly brecciated centers or crystalline quartz-rich zones are taken (Figure 4.9).

Figure 4.9: ENE-WSW-trending old working site on a few tens of meter thick quartz vein About 1.5 meter thick central zone of the vein was mined.

4.2.4. Faults

Major structures that shaped the study area are normal and strike-slip faults; they differentiated according to their relation to mineralization fertility and/or occurrence of silicification with clay alteration halo (Figure 4.10). Accordingly, they are considered as fertile or sterile structures or fault related features. Sterile faults occur in some of the brecciated zones with loose, fragile and unpacked appearance. The breccia clasts get smaller and smaller towards the area of maximum displacements. Fertile faults occur mostly along with the quartz veins or quartz and/or quartz iron-oxide, cemented breccia zones. The kinematic indicators are observed along quartz vein zones where silicification is critical for preservation of coeval plane of motion. The breccia zones having same orientation with fault planes are assumed to be marking extend of fault planes. Moreover, geomorphological features like running water course, abrupt change in slope and elongated hills and terraces are all considered with confidence on defining the fault extends, lineaments and probable faults.

4.2.4.1. Mineralization Sterile Faults

Thirteen different sterile faults are identified, mapped and labeled with letters A to K (Figure 4.11). As a note, there is no field and/or seismic evidence, these structures may well be active. According to the USGS earthquake catalog, the seismic activities in the Biga Peninsula are frequent, where magnitudes of earthquakes are lower than 4 and focal depths are shallower than 10 km.

Rose diagrams for sterile faults are prepared in order to determine the general trends. To see the picture better, an average of 1km long fault was identified and some of the longer fault planes were cut into a km long features. Four main sets of orientation are determined, trending in ENE-WSW, NE-SW, NW-SE and NNE-SSW (Figure 4.11a-d). The linear structural features are also investigated in terms of their attributes as; lineaments, probable faults and faults. According to the trend-based stereonet plotting, the following trends are identified;

- Lineaments (manually drawn); NE-SW and NW-SE
- Probable faults; ENE-WSW
- Faults; NNE-SSW, ENE-WSW and NW-SE

Figure 4.10: Field views of sterile and fertile faulting. Upper photo, blue arrow shows location of sterile fault; lower photo, purple half arrows shows motion sense along mineralization bearing fault (fertile) where fault zone is marked by extensive mineralization.

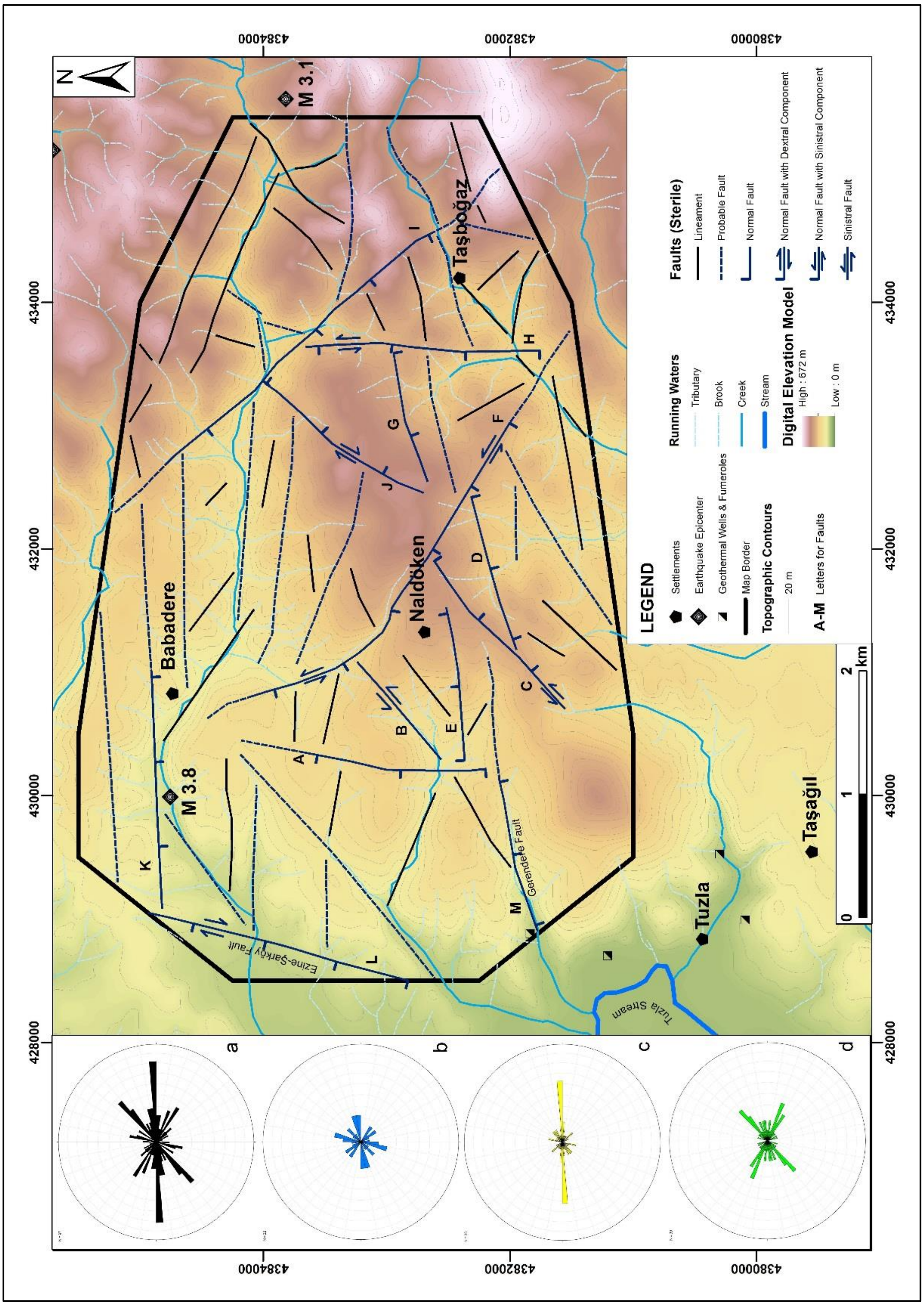

Figure 4.11: Map of the sterile faults in the study area and trend-weighted rose diagrams: (a) all post structures plotted, (b) post faults, (c) probable faults, and (d) lineaments.

Kocayatak (letter F in Figure 4.11), Karakaşçamı (I) and Çardak (H) faults are distinctly characterized by their up to tens of meter wide deformation zones; intense fracturing and brecciation (Figure 4.12).

The study area experiences intense and conjugate faulting with normal and oblique-slip normal components, suggesting an extensional stress regime. Considering the proximity of study area to the main fault zones, like Çan-Etili-Bigadiç and Edremit Graben faults, the nature of these faults seem to consistent with regional structures. The Ezine-Şarköy fault and Gerendere fault have already been mapped and reported in the literature; the remaining eleven faults are mapped in this study. For the kinematic analysis and fault regime, see the discussions section of this chapter.

Figure 4.12: Post-mineralized deformation-damaged zones a) Karakaşçamı Fault, b) Kocayatak Fault c) Çardak Fault (pervasively altered zone also faced damaging after formation of alteration).

4.2.4.2. Mineralization Fertile Faults

Eleven different fertile fault trends are identified, mapped and labeled as W1 to W4 and N1 to N7 (Figure 4.13). Due to occurrence of mineralization along the fault zone, those faults are interpreted to be present at the time of mineralization process.

Rose diagram for mineralization bearing faults are prepared; for understanding the general trends of faults. To see the picture better, an average of 450m long fault was identified and some of the longer fault planes were cut into a half km long features. According to the whole linear feature rose diagram, two main sets are observed: ENE-WSW and NNE-SSW trending faults ((Figure 4.13a-e).

In the regional scale, Karacık and Yılmaz (1998), the emplacement of Kestanbol pluton was preferentially localized along a NE-SW trend, possibly related to an extensional regime. Moreover, according to recent studies, the Kazdağ Massif exhumed in the footwall of low-angle detachment faults/shear zones during late Oligocene and early Miocene time interval; and it is attributed to an approximately N-S extension (Okay and Satır, 2000; Cavazza et al., 2009 and i.e.…)

The linear structural features are also investigated in terms of their attributes as probable and other fault types. According to the trend based stereonet plotting, the following trends are identified;

- Probable Faults; ENE-WSW and NNE-SSW
- Normal Faults; ENE-WSW
- Normal faults with oblique slip-sinistral component; ENE-WSW
- Sinistral Faults; ENE-WSW
- Dextral Faults; N-S and NNE-SSW

According to the field observations, dextral faults W1 and W4 are interpreted as major controlling agents for producing other fertile faults (Figure 4.13). W1 fault is characterized by brecciation and quartz cementing. On the other hand, W4 is characterized by its older lithological offsets and bimictic silicified breccia content with selectively and extensively pervasive clay alteration assemblages (Figures 4.14 and 4.15).

Most of the fertile structures are latter cut and displaced by mineralization sterile structural features. Most importantly, the identified lately forming faults played an important role for juxtaposition of structural features and also rock units. The field relations illustrate that some sterile faults cut and displace the fertile structures (Figure 4.13). The amounts of displacements are mostly in the order of a few meters and recorded as patchy outcrops of mineralization. Consequently, conjugation of fertile features or veins with sterile and probable faults is more likely aimed to show attributive representations.

Additionally, the study area is very close to intense clay alteration zones along its eastern, northern and northeastern sides. There is therefore a possibility that similar structural orientations may have localized mineralization in those areas. For the kinematic analysis and fault regime, see the discussions section of this chapter.

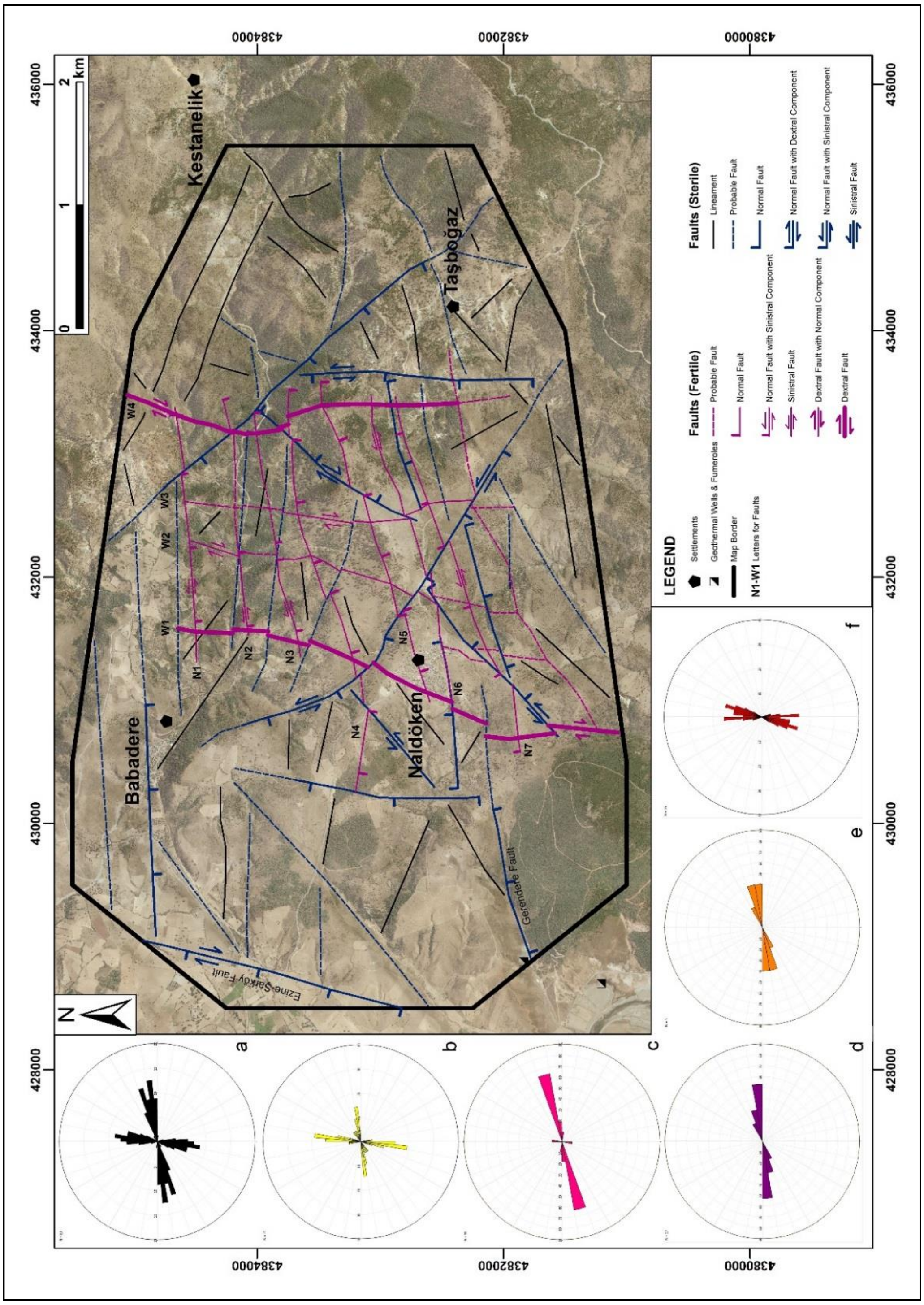

Figure 4.13: Map of fertile faults in the study area and their trend-weighted rose diagrams for related structures: (a) all fertile structures plotted, (b) probable faults, (c) normal faults, (d) oblique-slip normal faults with sinistral component, (e) sinistral faults, (f) dextral faults.

Figure 4.14: Field views of fertile structural features: (a) blossoming fault geometry as marked by purple dashed lines; (b) growth patterns and centers of a quartz vein; (c) taken from on the top of blossoming, and brecciated thick silicified zone. Note roundness of the clasts; (d) different sized and rounded rhyolitic crystal tuff breccia.

Figure 4.15: a and d) rhyolitic crystal tuff breccia showing well rounding and molithic and abrasive feature b) dacitic lapilli tuff breccia showing well rounded and equally sized breccia clats with some quartz crystal bearing drussy cavities c) bilithic, well rounded and abraded breccia on the contact zone of latite porphyry and tuff unit.

4.3. Results and Discussion

On the following sections, paleostress analyses of faults and silicified brecciation mechanisms is going to be discussed.

4.3.1. Kinematic Analysis

Paleostress analyses of faults will be presented in the following paragraphs. The paleostress configurations are reconstructed by using software T-TECTO (Zalohar and Vrabec, 2007; Zalohar and Vrabec, 2008) that analyzes fault-slip data collected from exposed fault planes (Figures 4.16 and 4.17). This program "…enables classical and micropolar (Cosserat) analysis of heterogeneous and homogeneous fault-slip data using several different numerical methods including the Gauss method. The program is based on the classical philosophy of fault-slip data inversion which involves the concept of the best-fitting stress and strain tensors...” (Zalohar and Vrabec, 2008).

Fault attitudes, sense of block motions and slip data are used to infer principal stresses (σ1: maximum, σ2: intermediate and σ3: minimum). From 26 sites, 68 fault-slip measurements, including direction and sense of relative movements, are collected. Paleostress inversion of the data is carried out on each fault separately. Thirteen stress configurations are constructed for post-mineralized faults (Figures 4.18 and 4.19; Table 4.1). From 23 sites, 54 fault-slip measurements are collected for paleostress inversion of the eleven different mineralization bering faults; eleven different stress configurations are constructed (Figures 4.20 and 4.21; Table 4.1).

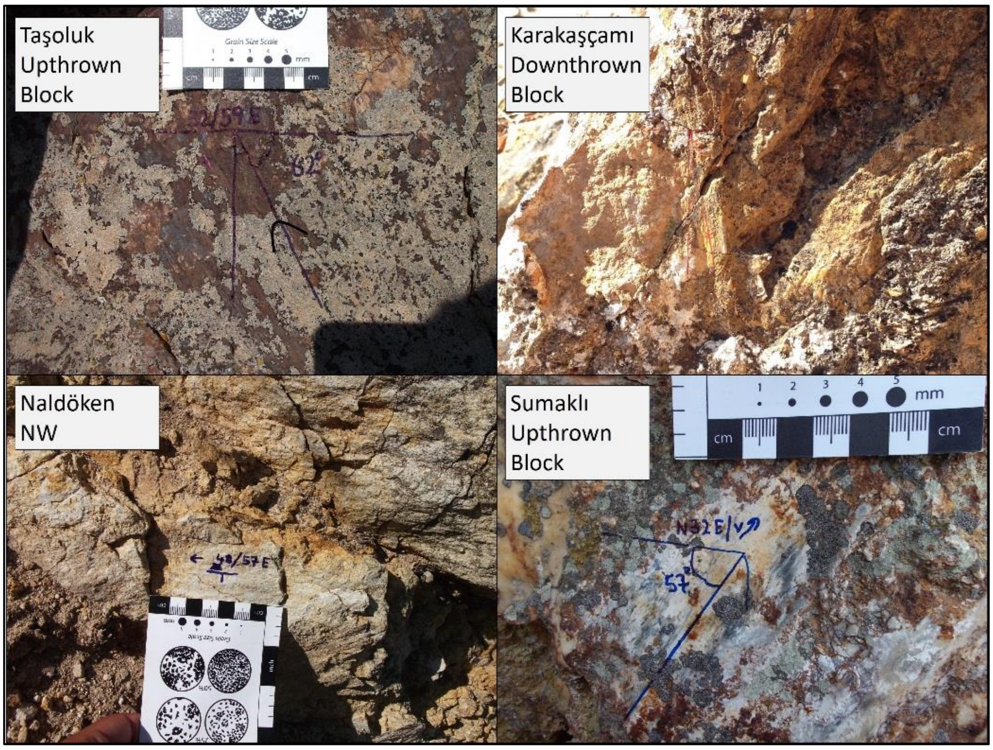

Figure 4.16: Views form the mineralization sterile fault planes.

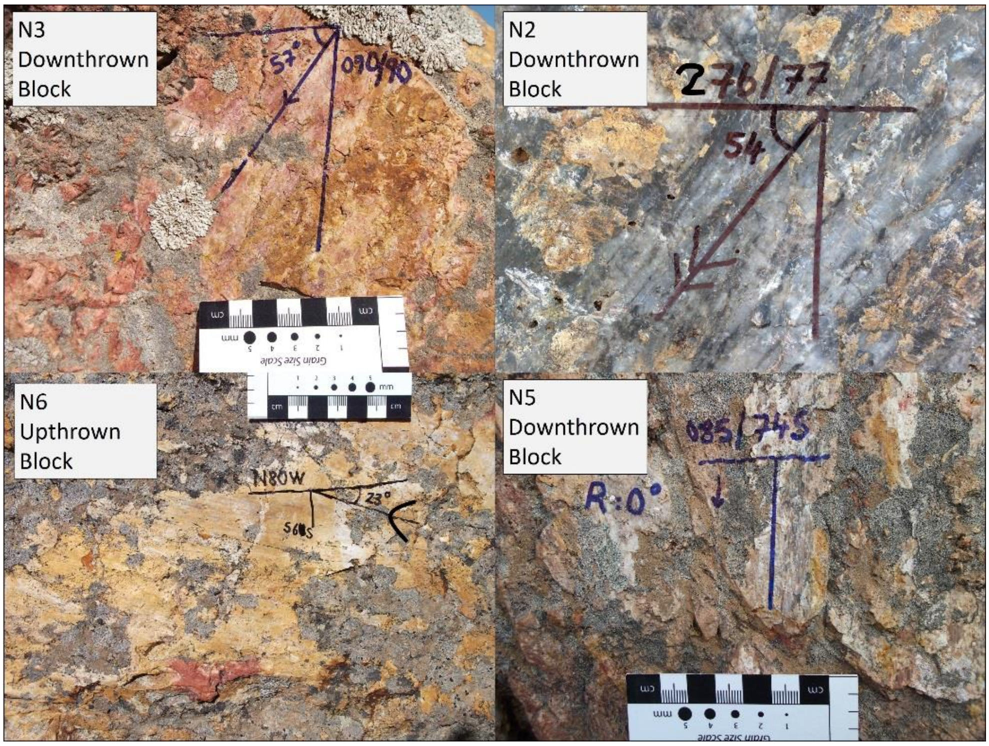

Figure 4.17: Views form mineralization bearing fault planes.

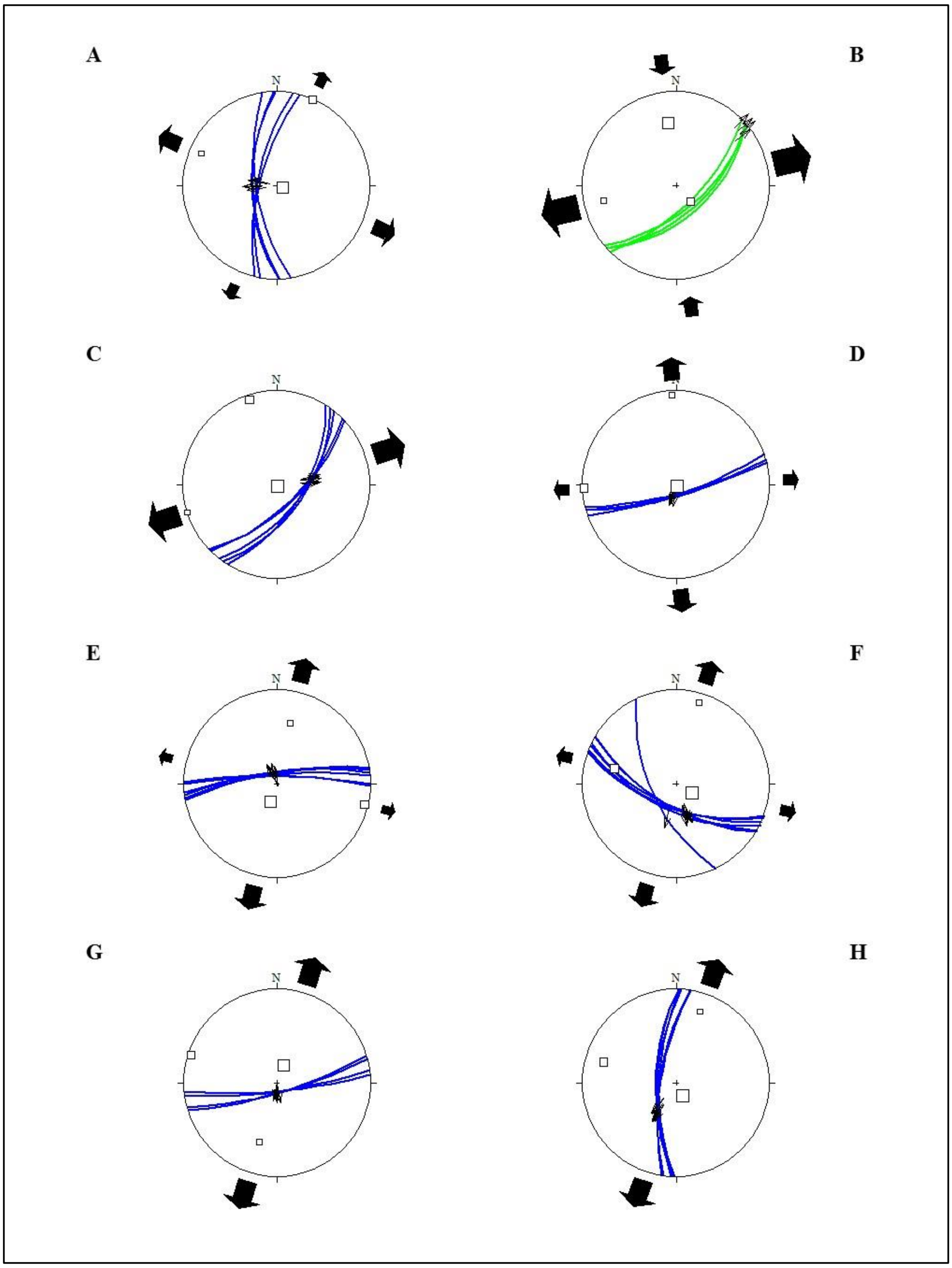

Figure 4.18: Stereoplots showing constructed paleostress for first 8 sterile fault orientations, fault planes and slip lineations (lower hemisphere equal area projection). See Table 4.1 for fault identification letters and Figure 4.19 for legend.

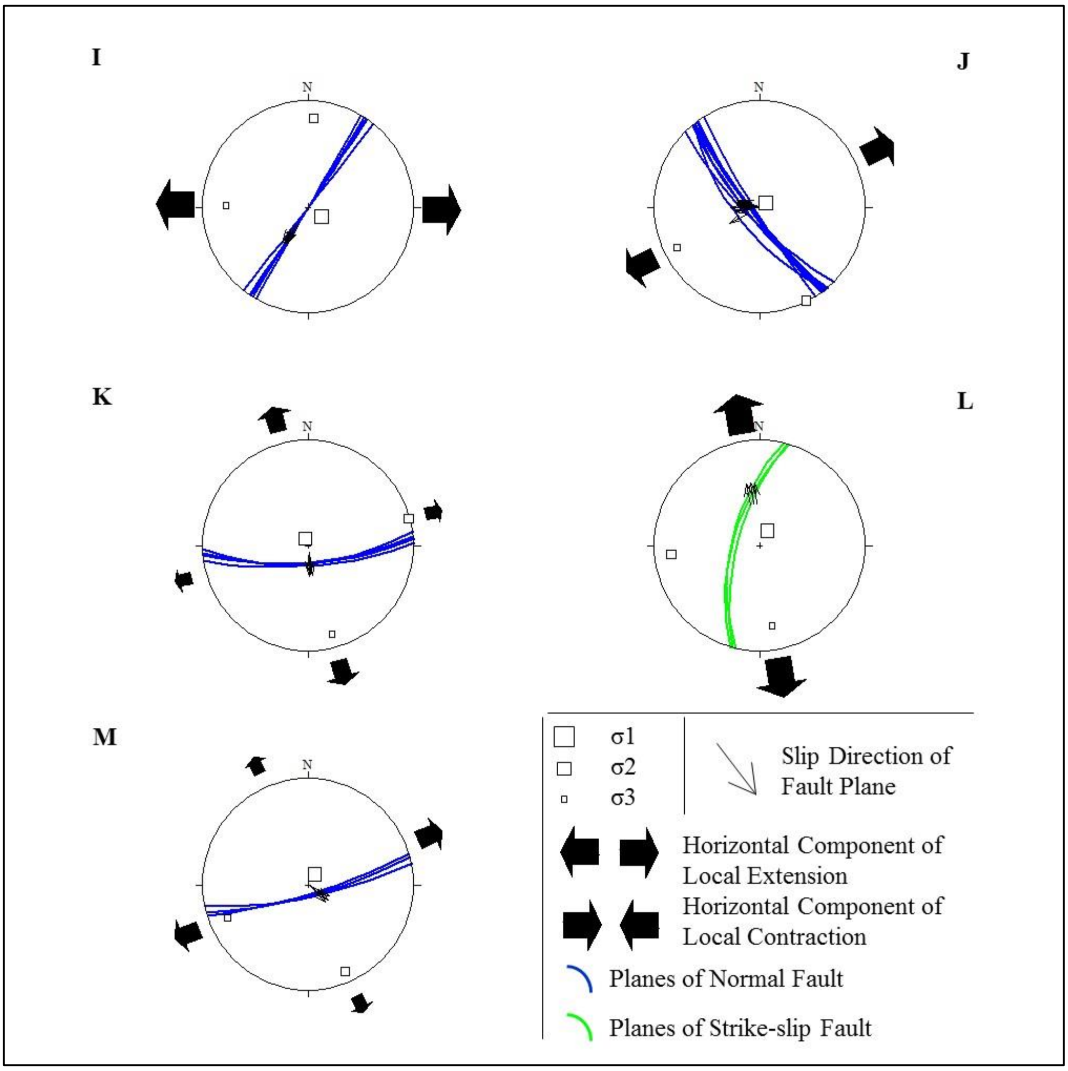

Figure 4.19: continuation of Figure 4.18.

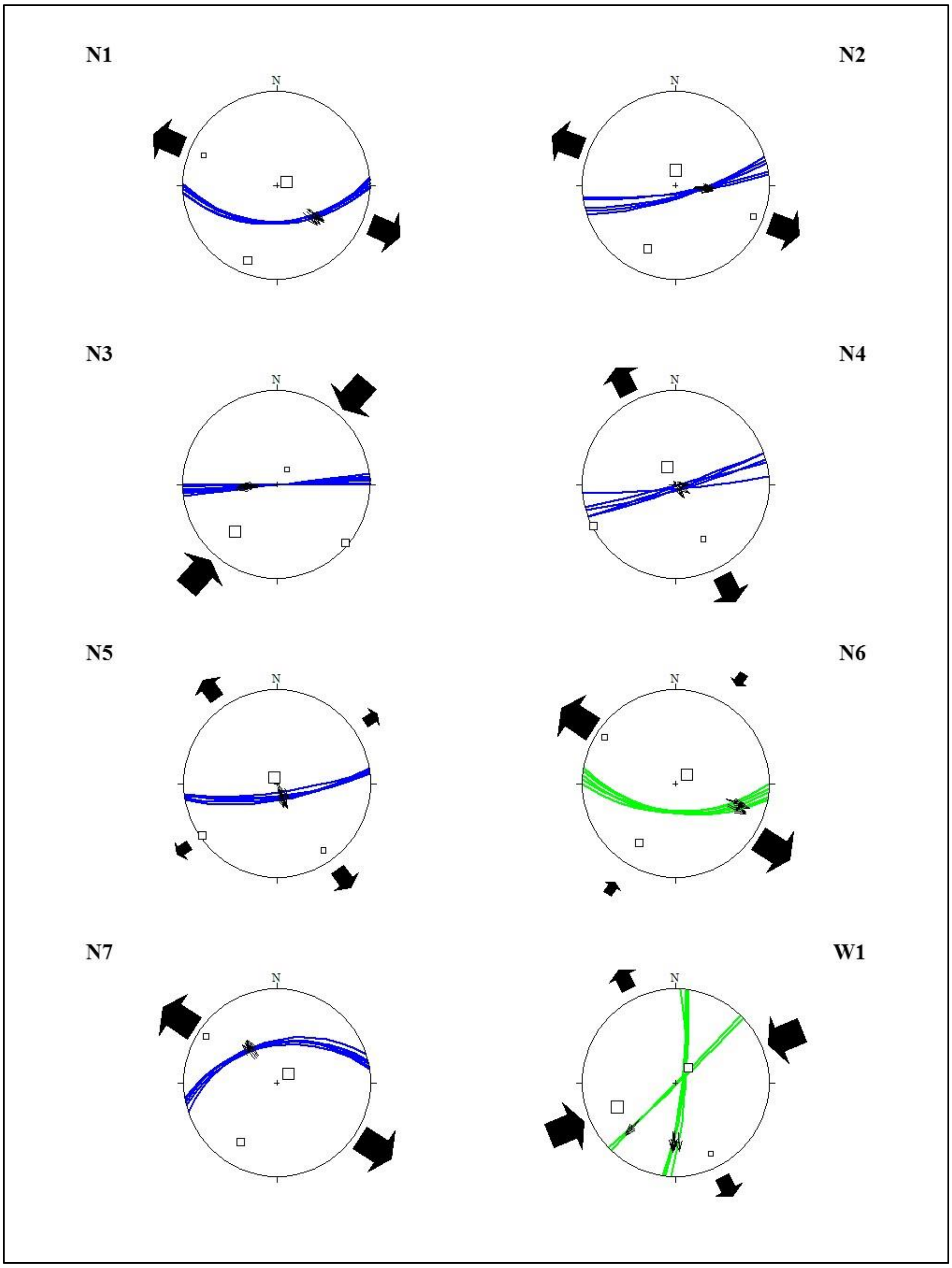

Figure 4.20: Stereoplots showing constructed paleostress for first 8 fertile fault orientations, fault planes and slip lineations (lower hemisphere equal area projection). See Figure 4.21 for the legend.

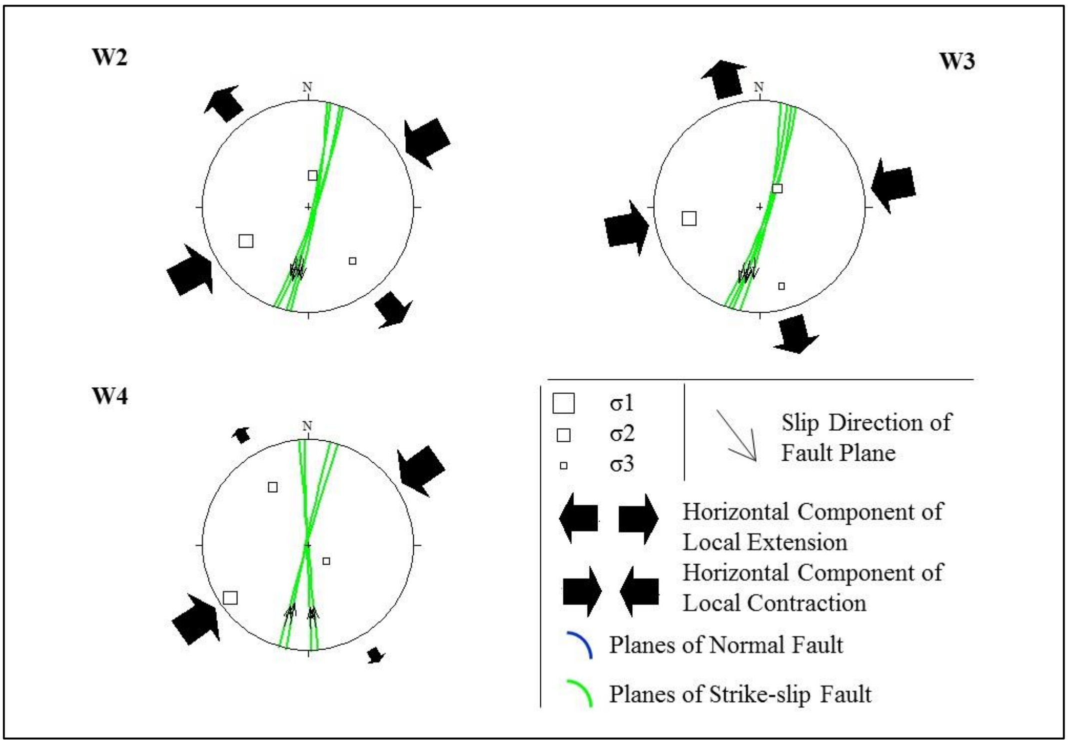

Figure 4.21: continuation of Figure 4.20.

Constructed paleostress orientations for whole faults are analyzed for their regional consistency. Table 4.1 shows that σ_1 is generally oriented sub-vertical on both episodes, whereas σ_2 and σ_3 show variable orientations. This phenomenon is explained by uniaxial stress conditions, which result in stress permutation-substitution in the study area.

Mineralization sterile deformational features are extensional, as indicated by the vertical σ_1, which is consistent with normal faulting in the study area. Faults with strike-slip behavior are attributed to either probable stress permutations to accommodate local space problems or to regional-scale transfer faults. In contrast to N-S to NE-SW extension on sterile faults, mineralization related faults' paleostress solution demonstrates a transtensional (right-dextral shear) zone, causing local extension and spaces for vein formation. The direction of stress accumulation during mineralization coeval deformation occurred in NE-SW

Table 4.1: Faults, surface lengths and paleostress orientations.

#	Letter	Fault Name	Length (m)	σ1 (D/P)	σ2 (D/P)	σ3 (D/P)
		Faults (Sterile)				
1	A	Düzveren	1520	115/82	023/00	293/08
2	B	Naldöken NW	1050	353/22	138/64	258/14
3	C	Taşoluk	1600	153/87	343/03	252/01
4	D	Güngörmez	1300	153/88	267/01	358/03
5	E	Naldöken S	1250	198/67	104/02	013/23
6	F	Kocayatak	3200	120/67	284/22	016/06
7	G	Gökçe	1100	022/67	287/02	197/23
8	H	Çardak	1950	153/72	286/13	019/13
9	I	Sumaklı	1550	128/72	004/10	271/15
10	J	Karakaşçamlığı	2850	059/82	154/01	244/08
11	K	Babadere	1900	340/82	075/01	165/08
12	L	Ezine-Şarköy	2200	027/72	264/10	171/15
13	M	Gerendere	1300	037/77	156/06	248/11
		Faults (Fertile)				
14	-	N1	2000	072/77	201/08	292/10
15	-	N2	1300	003/72	203/17	112/06
16	-	N3	1350	221/22	130/02	036/68
17	-	N4	3150	335/67	243/01	153/23
18	-	N5	2750	340/82	235/02	145/08
19	-	N6	2600	053/72	212/17	303/06
20	-	N7	3050	053/72	212/17	303/06
21	-	W1	3750	247/22	42/66	154/09
22	-	W2	2050	241/22	010/57	141/23
23	-	W3	1550	262/22	045/64	165/14
24	-	W4	2750	236/07	329/25	131/64

orientation. Its paleostress solutions with extensional state of strain might have been caused by releasing or dilatant bends along NNE-SSW-trending dextral faulting.

4.3.2. Fault Intersections and Brecciation

Intense mineralization related faulting caused a pathway for the flow of silica-rich fluids. Hence, fault conjugations form suitable locations for percolating ore-bearing fluids. In the study area, silica-rich fluids are condensed around fertile fault conjugation areas, which are characterized by fault-driven cemented breccias (Figure 4.22). The brecciation is important as described by Laznica (1989); he noted that brecciation is significant since it has close relations with metallic ore deposition and its grade.

In the study area, the breccias show crackle, mosaic, rubble to mélange-milled (monolithic-bilithic) textures, indicating tectonic comminuting-fault activities. Most breccias show volume expansion and display fragmented to rounded appearance. They partially contain iron-oxide and silica cement with different textural styles. Some matrix have druzy cavities, whereas others are filled totally with silica (crackle-mosaic-rubble) with a mechanical to abrasive rounding appearance (named as mélange-milled breccia). Some silica and iron-oxide cement only hold the tip points of the fragments as in the case of rubble breccia but these breccias are mostly observed at the higher elevation with respect to totally quartz cemented breccia. As whole, mechanical formation with partially fluid assisted brecciation, volume expansion and stress-related corrosion are dominant breccia characters in the study area.

Figure 4.22: A view from conjugation of iron-oxide-rich silica veins and rounded and abraded breccia clasts.

4.3.3. Mineralization and Geologic Structures

Paleostress solutions and field observations are modeled a dextral transtensional stress conditions. Dextral strike-slip faulting with an extensional overstepping or local extensional features showing these conditions are the main controlling feature during mineralization. Field distribution of quartz veins, alteration extends and silica cemented breccia localities fit well with a dextral transtensional conditions. Additionally, the quartz veins and stress solutions of its corresponding faults demonstrate that mineralization are localized along T and R’ components in a strike-slip fault system (Figures 4.23 and 4.24).

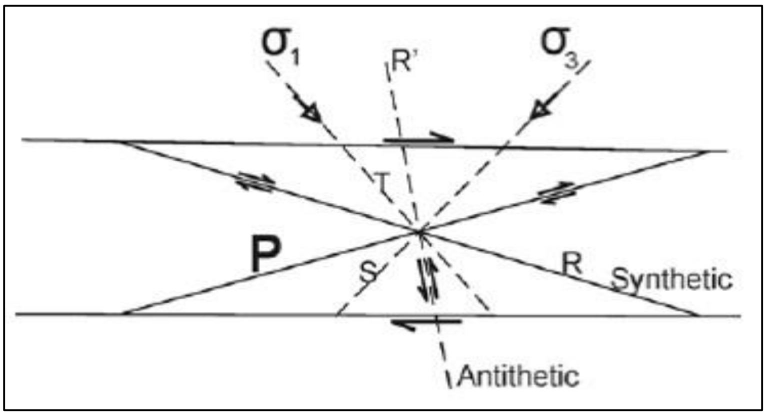

Figure 4.23: Reidel shears in a dextral strike-slip system. Tension fractures (T), cleavage (S), synthetic shears (R), antithetic shears (R') and P-shears (P). (URL-2).

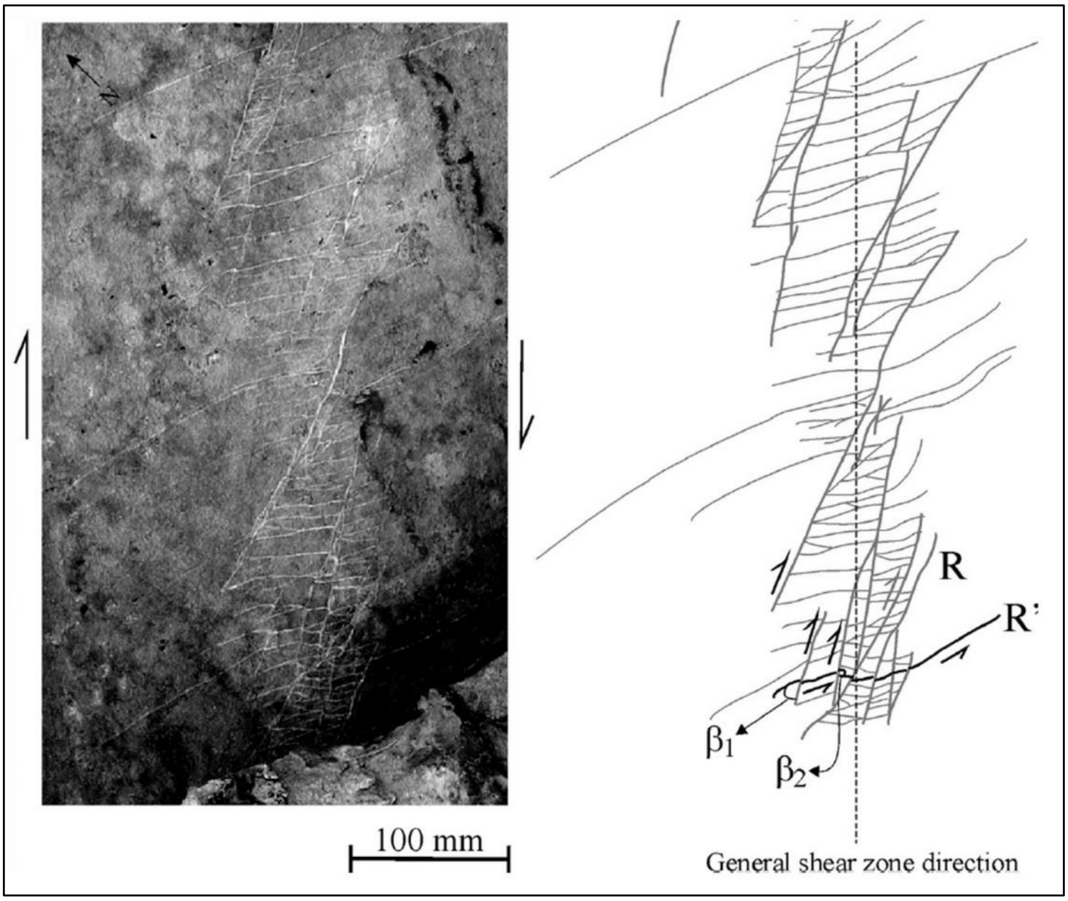

Figure 4.24: Riedel shear structures within NE-trending dextral shear zone (Katz et al., 2004).

This model can also be used to explain NE-SW-trending bedding planes in the study area. Moreover, parallel to sub parallel elongation of N-S-trending quartz veins might have formed along jogs or local openings on R-P shears of the system (Figure 4.24).

Considering intense fault activity and suitable conditions for fault conjugations, it is reasonable to produce fault breccia and its' sealing with quartz and/or quartz iron-oxide fluids. Breccia-rich areas in the study area are therefore considered as marking location of mineralization fertile faults. Breccia textures are consistent with a structural control (Figure 4.25). And, later extensional regime induced structures partially cut and displace the fertile faults and quartz veins (Figure 4.26).

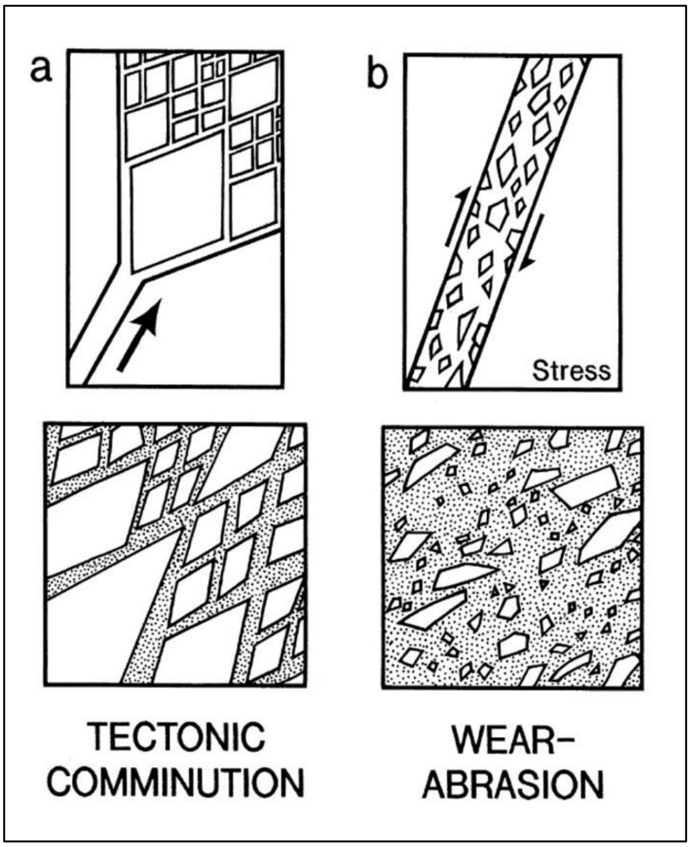

Figure 4.25: Schematic illustration of the brecciation mechanisms in hydrothermal vein deposits, and resulting geometry of the breccias (Jebrak, 1997).

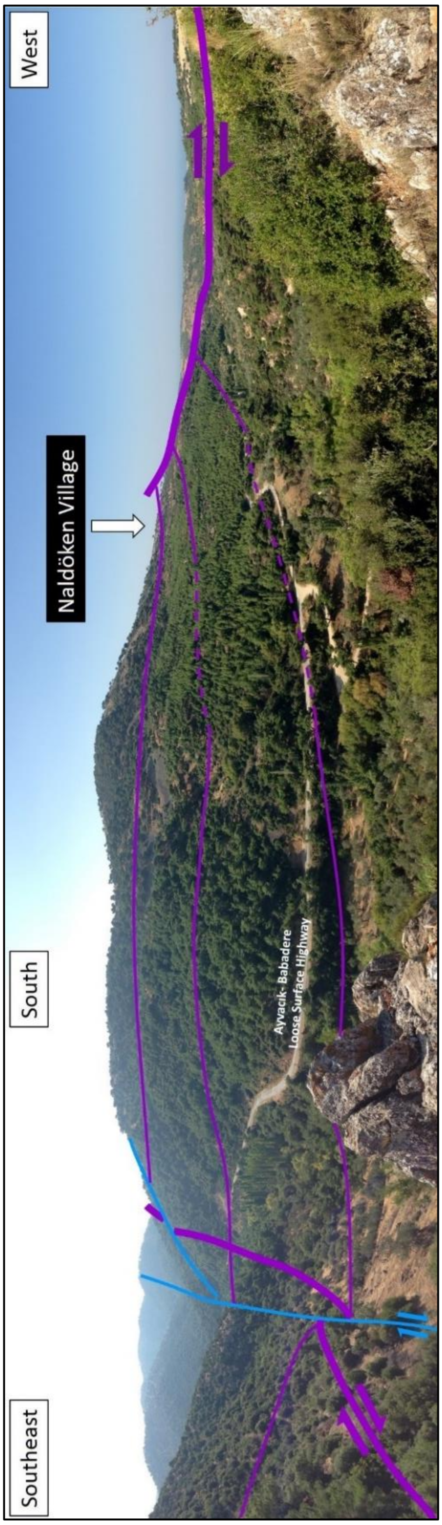

Figure 4.4.26: Field view of some faults on the study area. Note some of the N-S-trending (fault W2-W3) fertile faults are not shown on purpose.

126

CHAPTER 5

U-Pb AND Ar-Ar GEOCHRONOLOGY

5.1. Introduction

In this study, U-Pb and Ar-Ar isotopic systems are utilized to constrain the age of rock units and mineralization. Intrusive and extrusive rocks in the study area and near surrounding are sampled. Combination of U-Pb dating techniques on zircons and Ar-Ar technique on biotite, K-feldpars, hornblende and altered and fresh whole rocks contributed to constrain the mineralization age.

5.1.1. Material and Sample Collection

Twenty rock samples were collected during 2014 summer season. Despite the goal of dating was to learn age of eight igneous rock units, the number of samples was extended due to geological complexities. Alteration and geographic location of rock units form main complexities of geochronological sampling (Table 5.1). Some suitable localities like road-cuts or outcrops are identified for sample locations. Additionally, two samples are taken from the available cores.

5.1.2. Mineral Separation

During zircon separation, all samples were crushed, then run through Wilfley table, followed by magnetic separation using Frantz magnetic separator, separation via heavy liquids and finally zircons are hand-picked.

Table 5.1: Detailed geochronological samples list (*: target minerals are not separated during enrichment).

#	ID	Lithology	U-Pb System		Ar-Ar Method		Alteration
			Result	Target	Result	Target	
1	GBP-21	**Latite porphyry**	Not achieved*	Zircon	Not achieved	Whole Rock	Altered
2	GBP-22	**Rhyolitic Crystal Tuff**	Achieved	Zircon	Achieved	Biotite	Unaltered
3	GBP-23	**Latite porphyry**	Achieved	Zircon	Achieved	Biotite & K-feldspar	Unaltered
4	GBP-24	**Diorite porphyry**	Achieved	Zircon	Achieved	Whole Rock & Biotite	Unaltered
5	GBP-25	**Dacitic Lapilli Tuff**	Not achieved*	Zircon	Achieved	Biotite	Unaltered
6	GBP-26	**Megacrystic Monzonite**	Achieved	Zircon	Achieved	Biotite	Unaltered
7	GBP-27	**Dacitic Lapilli Tuff**	Achieved	Zircon	Achieved	Biotite	Unaltered
8	GBP-28	**Rhyodacite**	Achieved	Zircon	Achieved	Biotite	Unaltered
9	GBP-29	**Latite porphyry**	Achieved	Zircon	Not achieved	Whole Rock & Sericite	Altered
10	GBP-30	**Quartz Monzodiorite**	Not achieved*	Zircon	Achieved	Whole Rock	Altered
11	GBP-31	**Andesite**	Not achieved*	Zircon	Not achieved	Whole Rock & Sericite	Altered
12	GBP-32	**Quartz Monzodiorite**	Not achieved*	Zircon	Achieved	Whole Rock	Altered
13	GBP-33	**Quartz Monzodiorite**	Achieved	Zircon	Not achieved	Whole Rock & Sericite	Altered
14	GBP-34	**Dacitic Lapilli Tuff**	Not achieved*	Zircon	Not achieved	Whole Rock & Sericite	Altered
15	GBP-35	**Quartz Monzodiorite**	Achieved	Zircon	Not achieved	Altered Whole Rock	Altered
16	GBP-36	**Andesite**	Achieved	Zircon	Achieved	Biotite	Unaltered
17	GBP-37	**Megacrystic Monzonite**	Achieved	Zircon	Achieved	Biotite	Unaltered
18	GBP-38	**Latite porphyry**	Achieved	Zircon	Achieved	Biotite	Unaltered
19	GBP-39	**Quartz Monzodiorite**	Achieved	Zircon	Achieved	Biotite	Unaltered
20	GBP-40	**Andesite**	Not achieved*	Zircon	Achieved	Altered Whole Rock	Altered

Futher laboratory procedures and U-Pb analysis was performed in Geochronology and Radiogenic Isotope Laboratory, Institute of Geoscience, Göethe University of Frankfurt. In Frankfurt, zircon grains were faced following procedures; epoxy, polishing and cathodoluminescence imaging (here after; CL imaging).

For Ar-Ar techniques, samples containing large, unaltered biotite and K-felspar crystals were selected for mineral dating. Samples are crushed into 0.3-2 mm fraction and appropriate mineral grains were picked out of the bulk fraction. Following analysis procedure and data gathering was done in Geosciences Rennes (University of Rennes, France). In France, samples wrapped in A1 foil to form packets (11 mm 11 mm 0.5 mm) to make further data gathering process in nuclear reactor.

These separation steps are followed by mass-spectrometer phase of analysis procedure (see the relevant isotopic systems for mass-spectrometer stage).

5.2. U-Pb Zircon Geochronology

Zircon ($ZrSiO_4$) is zirconium orthosilicate and common accessory mineral of sedimentary, igneous and metamorphic rocks. It is proven that zircon consists of trace amounts of P, U and Th and rare-earth elements and uranium is more compatible than lead meaning that amount of non-radiogenic Pb is less in zircon which makes it as a datable and easily processable minerals in U-Pb isotopic sytems. In addition to chemical features of zircon, closure temperatures are critical factors to target mineral for measuring. As a note: closure temperature is critical temperature for each mineral that starts to be a crystal while mass is still an open system. The closure temperature of zircon is more than 850° C (Davis et al., 2003); and it close itself at the beginning of magma process or recrystallized under high-grade metamorphism. Additionally, later thermal events may abrade and/or surround the zircons as seen by overgrowing rims as traced by abrasional, resorptional and corrosive boundaries or truncations around inherited cores and/or previous rims. These boundaries and growth stages of zircons can be seen on their zoned textures under CL imaging. Detrital zircons can be used to discuss age and provinance sedimentary rocks. During metamorphism, at suitable temperature and compositional fluids, overgrowths as rims around older zircon may form. It is therefore critical to define the zircon growth episodes for statistically condensed and meaningful output. Moreover, during deciding the location of measurement on zircon grain, the micro inclusions, microcracks and voids may also dilute the data for who works on rim overgrowth timing. To make all these judgment, the importance of CL imaging are indispensable (Figure 5.1).

5.2.1. Analytical Procedure

In Frankfurt, detrital zircons are analyzed by laser ablation induced couple mass spectrometry method (LA-ICPMS) since it is suitable for even collecting low amount of U-Pb concentration; young and tight episodic events. Ablating the mineral with laser beam takes 53 seconds per spot and the error range is less than many other methods. Ablation analyses were performed with ThermoScientific Element 2 ICP-MS coupled to a Resolution M-50 (producing 30-50 micrometer crater; Figure 5.1) excimer laser system. Due to the quality control and quality assurance was also taken into consideration as controlling after each 30 spots, standarts GJ-1 (606 Ma), Felix (500 Ma), Plesovice (350 Ma) and 91500 (1050 Ma) were measured to check the calibration of the machine and determine constant values for data processing. Processing the raw data was done by using MS Excel macro program of Gerdes and Zen (2006, 2009); Millonig et al. (2012). Data is plotted on concordia diagrams by Isoplot 3.71 of Ludwig (1990).

During deciding the ablation location on a zircon, micro observational studies was carried out by capturing three different CL images (Figure 5.1). Various types of zonation; oscillatory, sectored, convolute and crystal shapes; idiomorphic and xenomorphic grains can be easily seen on CL images. By the help of CL images, a possible micro cracks, voids, resorption boundaries, inclusions, truncations can also be surveyed and ablation location was defined accordingly. Those features are helpful to detect the overgrowth stages of zircons and pathfinders for thermal and compositional episodes. However, some of the episodes have overgrowth less than ablation crater size so some spot on zircons can be mixed staged zircon episode. Moreover, it is also necessary to consider that crater depth may crop out the unwanted staged zircon overgrowth that also results in statistically decreasing the age contrast among whole data. Morevoer, the microcracks or inclusions and micro voids in the zircon grains create the fitting age on concordia with minor amount of bias (radiogenic lead loss). In such a geologically complex environment (structurally and magmatically), it is also reasonable to have some plots that did not fit on the concordia. To overcome this complexity result, it is applied to use zircon age data in a statistically validation manner like ablation many zircons and many overgrowth zones.

5.2.2. Results

Thirteen zircon enriched samples from different rock units were analyzed; the ages are constrained between 19 Ma and 21 Ma. The probability/density plots and concordia diagrams with best fit intercepts are shown in Figures 5.2 to 5.14.

Several zircon grains are analyzed in Sample GBP-22; they yielded $^{206}Pb/^{238}U$ ages ranging between 21.97±0.29 Ma and 20.05±0.28 Ma. The peaks on probability/density plot gives ages of 20.65 Ma and 20.21 Ma. This yielded a wide spread of $^{206}Pb/^{238}U$ apparent ages along a poorly constrained discordia with a lower intercept of 20.01±0.69 Ma and a upper intercept of a meaningless age with a large error (Figure 5.2).

Sample GBP-23 yielded ages mostly ranging between 22.85±0.32 Ma and 18.70±0.33 Ma. Their distribution on a probability/density plot fall into two distinct peaks at 22.20 Ma and 20.11 Ma. Wide spread of $^{206}Pb/^{238}U$ apparent ages on a discordia diagram defines a lower intercept age of 20.47±0.32 Ma whereas upper intercept age appears to be meaningless (Figure 5.3).

Sample GBP-24 appears to be poor in zircon content; there are only 16 grains separated; their ages range between 22.32±0.36 Ma and 18.82±0.34 Ma.

Probability/density plot shows bimodal distribution with peaks at 22.17 Ma and 20.70 Ma. The data gives a concordant age of 20.63±0.17 Ma (Figure 5.4).

More than 60 zircon grains are analyzed in Sample GBP-26; they yielded $^{206}Pb/^{238}U$ ages ranging between 23.9±0.35 Ma and 19.7±0.26 Ma. Their distribution on a probability/density plot fall is constrained in ca. 20-21 Ma, with a peak at 20.81 Ma. This yielded a wide spread of $^{206}Pb/^{238}U$ apparent ages along a poorly constrained discordia with a lower intercept of 20.02±0.66 Ma and a upper intercept of a meaningless age with a large error (Figure 5.5).

GBP-27 sample is also poor in zircon content, from which 16 grains are separated. The age of zircons falls into a wide range of 21.52±0.26 - 18.38±0.29 Ma, as illustrated in probability/density plot. The peak age is 20.70 Ma. The data gives a concordant age of 20.47 ±0.33 Ma (Figure 5.6).

Sample GBP-28 is very rich in zircon content; more than 60 grains are analyzed and they yielded ages ranging between and 22.54±0.38 Ma and 19.56±0.28 Ma. Their distribution on a probability/density plot is constrained in ca. 20-22 Ma, with a peak at 21.46 Ma. $^{206}Pb/^{238}U$ apparent ages on a poorly constrained discordia yield a lower intercept age of 20.90±0.62 Ma but upper intercept age is difficult interpret (Figure 5.7).

Several zircon grains are analyzed in Sample GBP-29; they yielded $^{206}Pb/^{238}U$ ages ranging between 21.98±0.38 Ma and 18.17±0.32 Ma. The peaks on probability/density plot gives ages of 21.72 Ma, 20.92 and 19.88 Ma. The data gives a concordant age of 21.04±0.14 Ma (Figure 5.8).

Several zircon grains are analyzed in Sample GBP-33; they yielded $^{206}Pb/^{238}U$ ages ranging between 23.04±0.46 Ma and 20.44±0.40 Ma. Their distribution on a probability/density plot is constrained in ca. 20.5-21.5 Ma, with a peak at 21.00 Ma. This yielded a wide spread of $^{206}Pb/^{238}U$ apparent ages along a poorly constrained discordia with a lower intercept of 20.62±0.27 Ma and a upper intercept of a meaningless age with a large error (Figure 5.9).

Sample GBP-35 is also rich in zircon; more than 60 grains are analyzed. They yielded $^{206}Pb/^{238}U$ ages ranging between 27.71±0.44 Ma and 18.13±0.28 Ma. Their distribution on a probability/density plot fall is constrained in ca. 20-21 Ma, with peaks at 20.77 Ma and 19.98 Ma. This yielded a wide spread of $^{206}Pb/^{238}U$ apparent ages along a poorly constrained discordia with a lower intercept of 19.98±0.59 Ma and a upper intercept of a meaningless age with a large error (Figure 5.10).

GBP-36 sample is rich in zircon content, from which more than 50 grains are separated. The age of zircons falls into a wide range of 27.62±0.40 - 18.76±0.25 Ma, as illustrated in probability/density plot. The peak age is 19.93 Ma. The data gives a concordant age of 20.47 ±0.33 Ma (Figure 5.6). This yielded a wide spread of $^{206}Pb/^{238}U$ apparent ages along a poorly constrained discordia with a lower intercept of 20.00±0.40 Ma and a upper intercept of a meaningless age with a large error (Figure 5.11).

Several zircon grains are analyzed in Sample GBP-3; they yielded 206Pb/238U ages ranging between 22.90±0.40 Ma and 19.43±0.36 Ma. The peaks on probability/density plot gives ages of 21.30 Ma and 20.34 Ma. The data gives a concordant age of 21.47±0.13 Ma (Figure 5.12).

From sample GBP-38, more than 40 zircon grains are analyzed and they yielded ages ranging between and 21.72±0.29 Ma and 19.14±0.28 Ma. Their distribution on a probability/density plot is constrained in ca. 19.5-21.0 Ma, with two peaks at 20.44 Ma and 19.9 Ma. 206Pb/238U apparent ages on a poorly constrained discordia yield a lower intercept age of 19.98±0.36 Ma but upper intercept age is difficult interpret (Figure 5.13).

Sample GBP-39 yielded ages mostly ranging between 2222.87±0.38 Ma and 18.82±0.61 Ma. Their distribution on a probability/density plot falls into a peak at 20.95 Ma. Wide spread of 206Pb/238U apparent ages on a discordia diagram defines a lower intercept age of 20.20±0.78 Ma whereas upper intercept age appears to be meaningless (Figure 5.14).

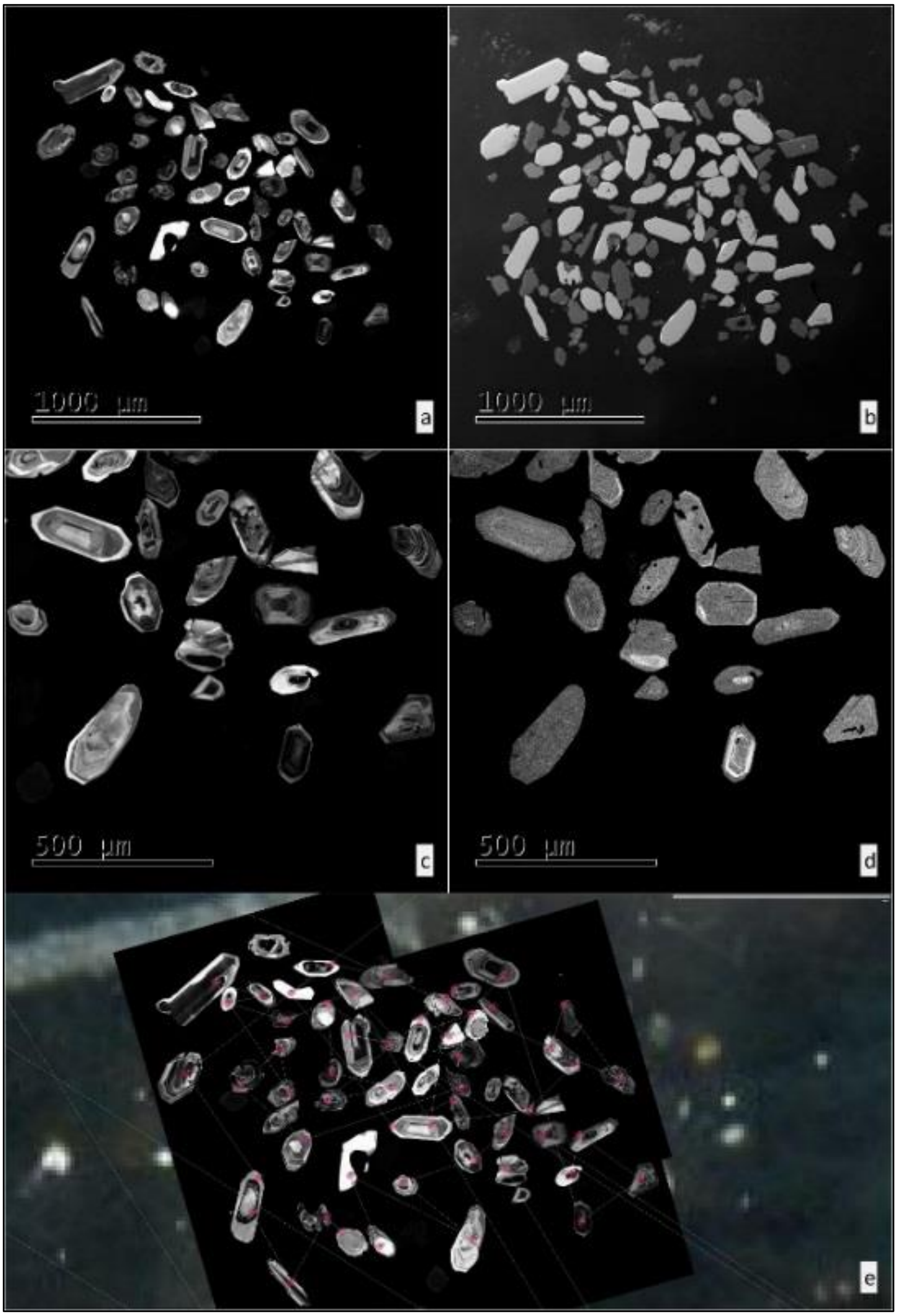

Figure 5.1: Example for CL imaging of zircon grains (of GBP-22) and defined laser ablation locations.

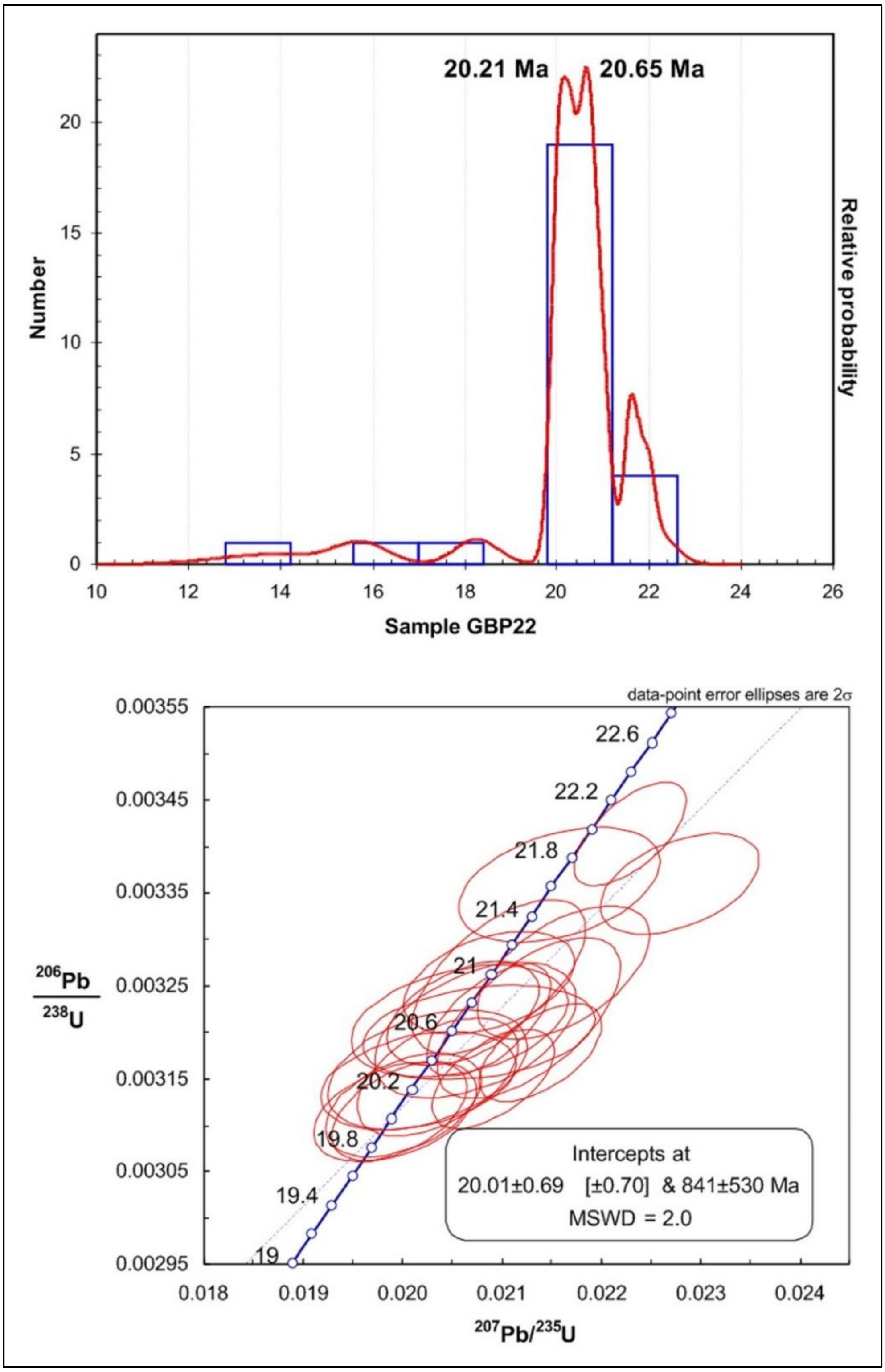

Figure 5.2: U-Pb results of Sample GBP-22 on probability/density plot and concordia diagram.

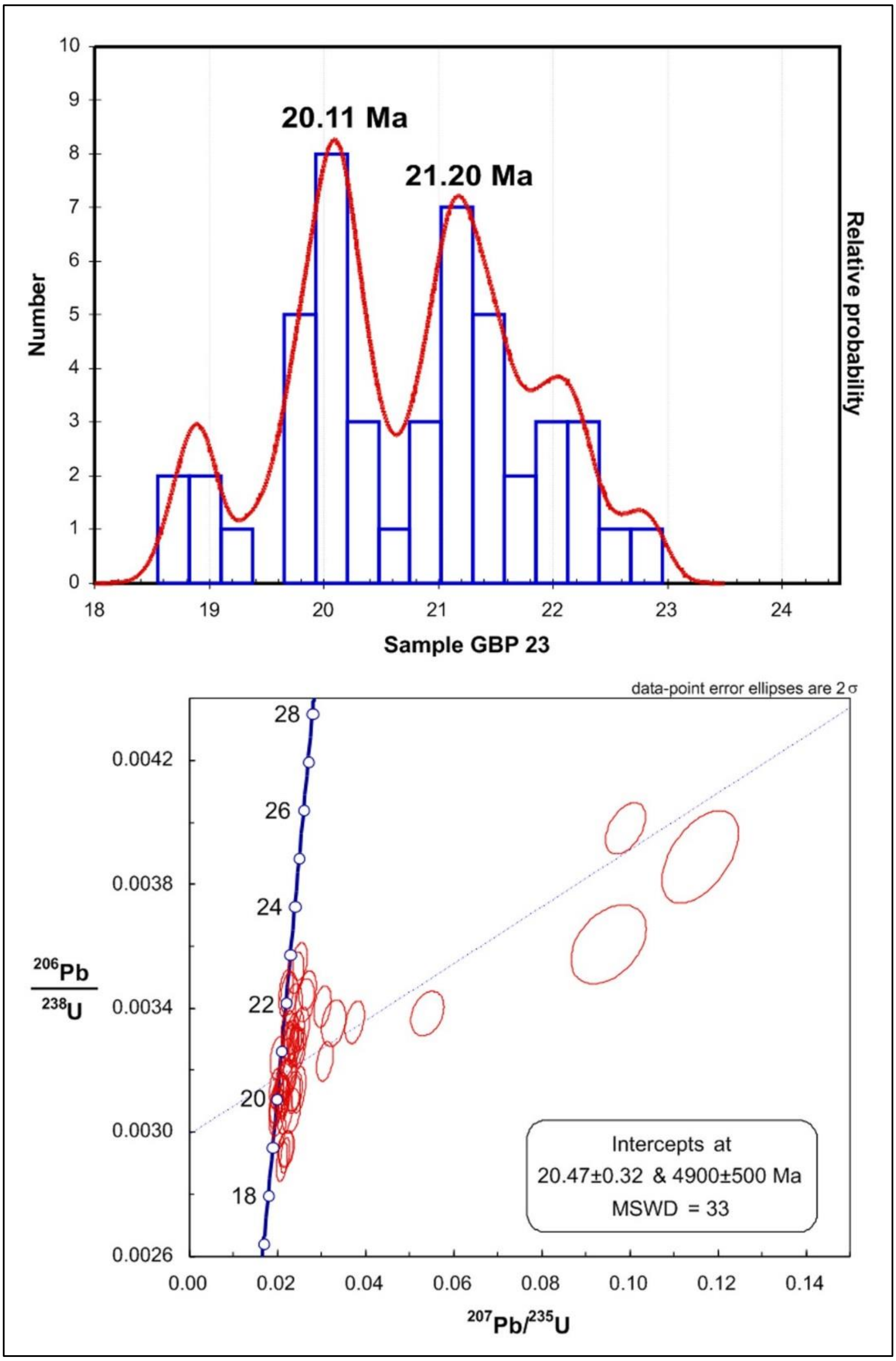

Figure 5.3: U-Pb results of Sample GBP-23 on probability/density plot and concordia diagram.

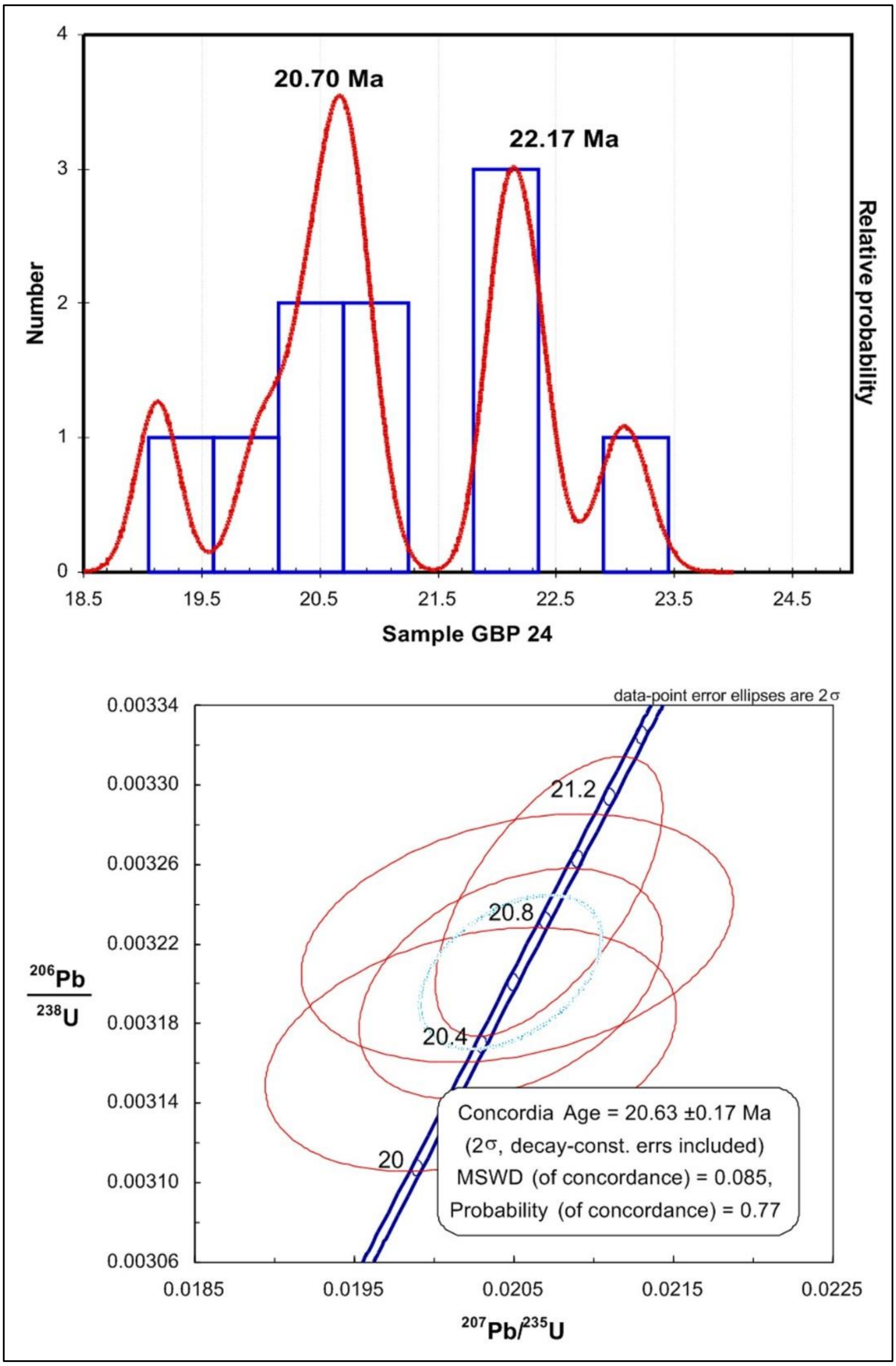

Figure 5.4: U-Pb results of Sample GBP-24 on probability/density plot and concordia diagram.

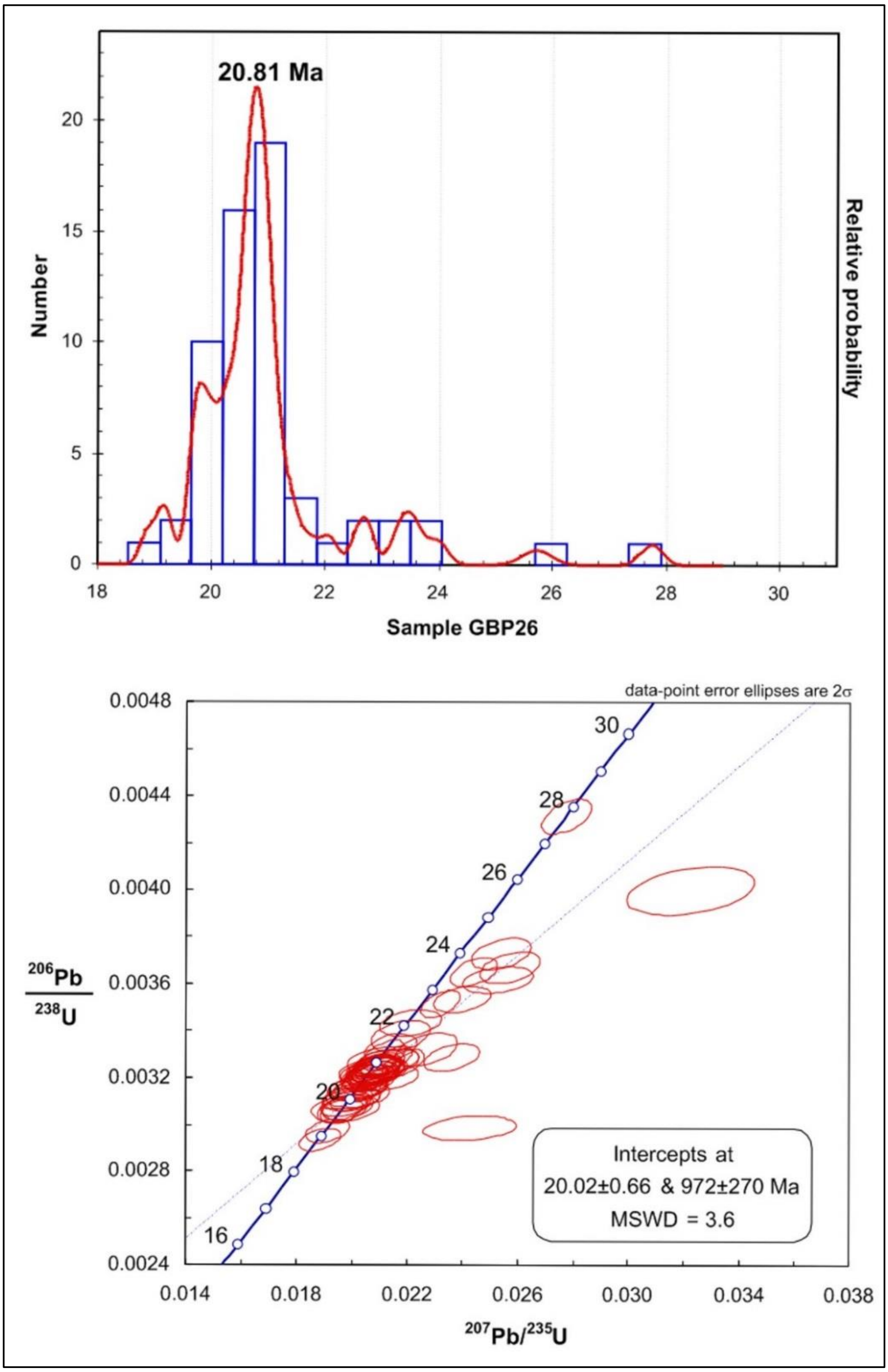

Figure 5.5: U-Pb results of Sample GBP-26 on probability/density plot and concordia diagram.

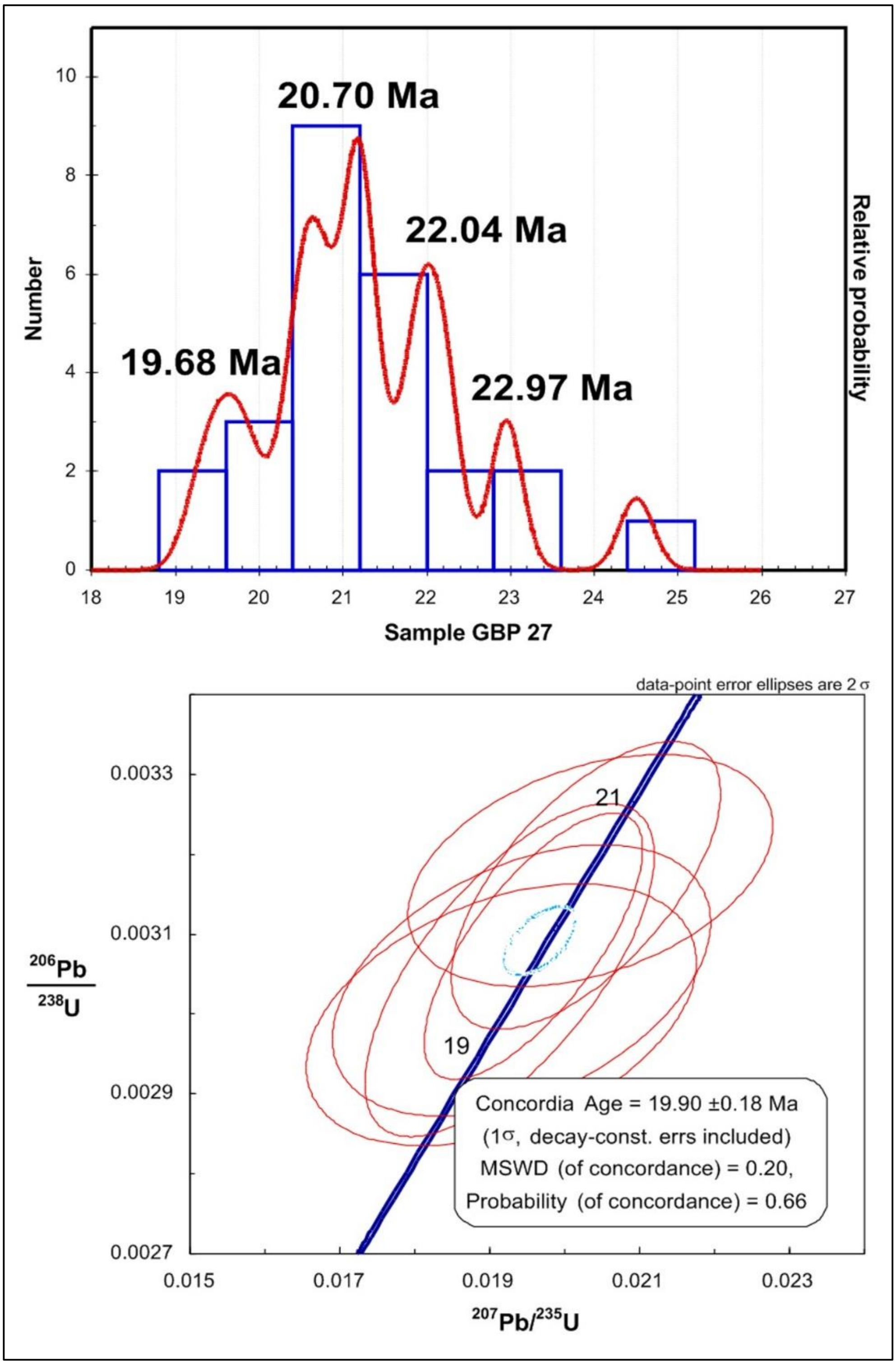

Figure 5.6: U-Pb results of Sample GBP-27 on probability/density plot and concordia diagram.

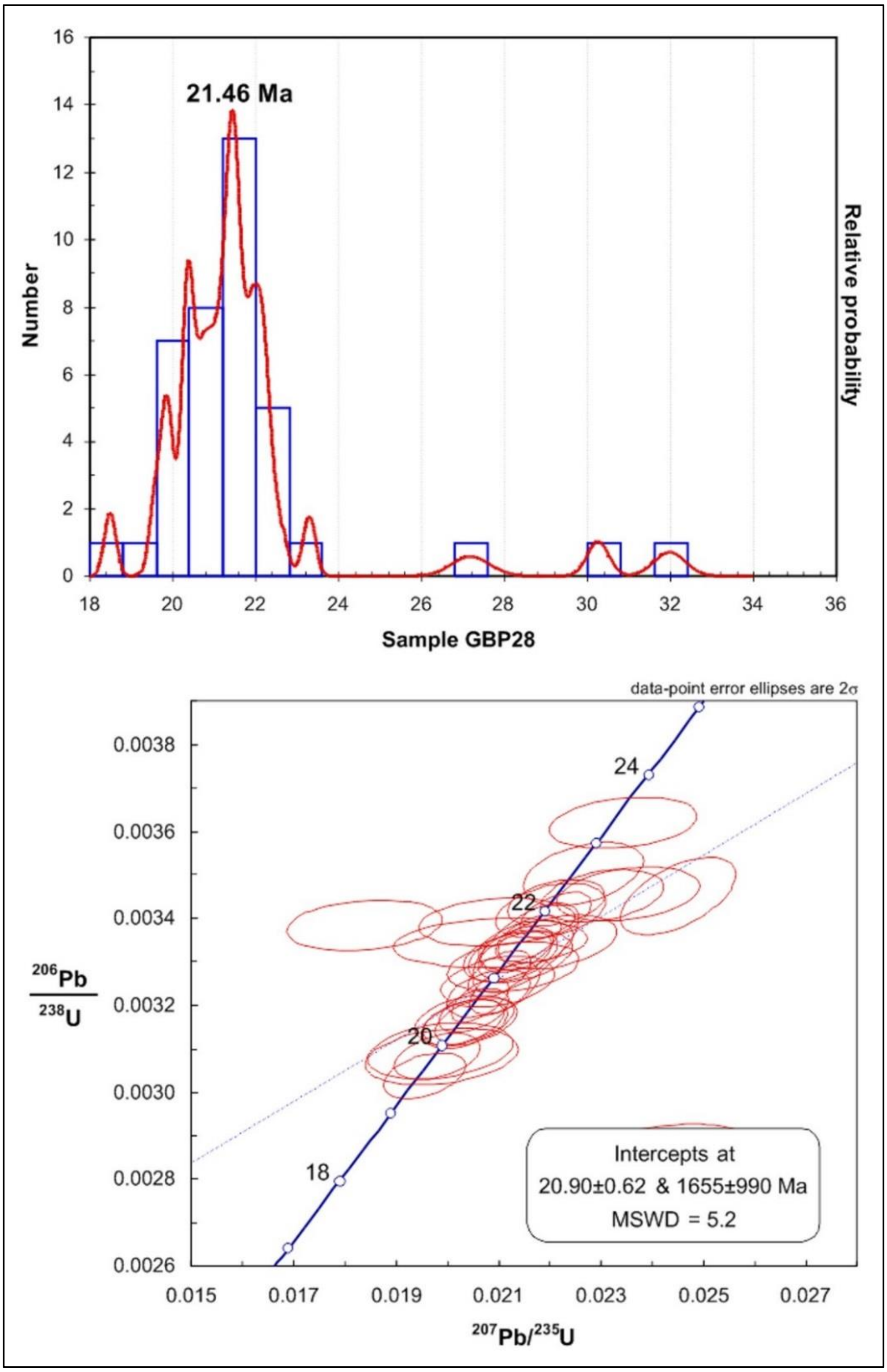

Figure 5.7: U-Pb results of Sample GBP-28 on probability/density plot and concordia diagram.

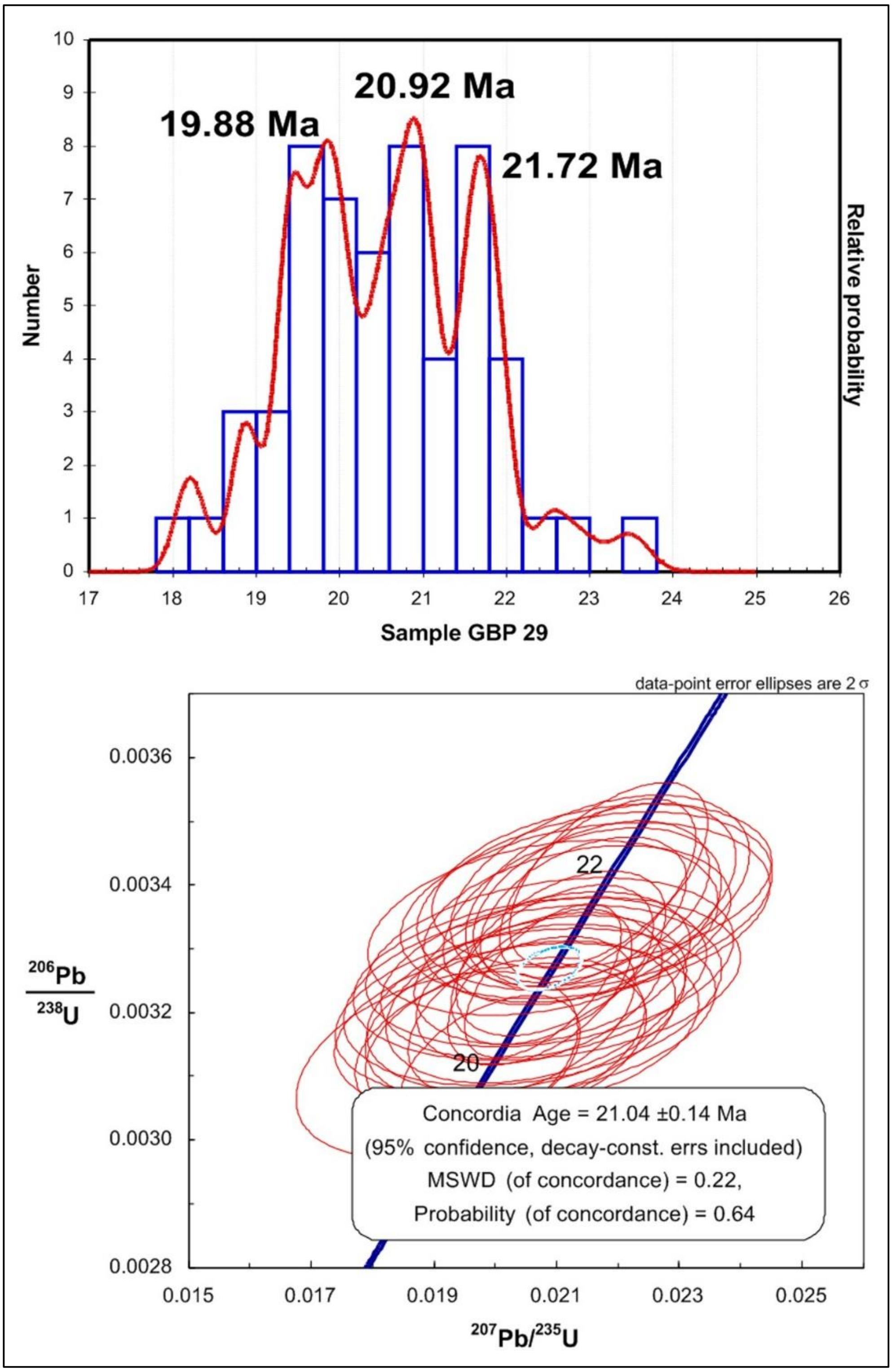

Figure 5.8: U-Pb results of Sample GBP-29 on probability/density plot and concordia diagram

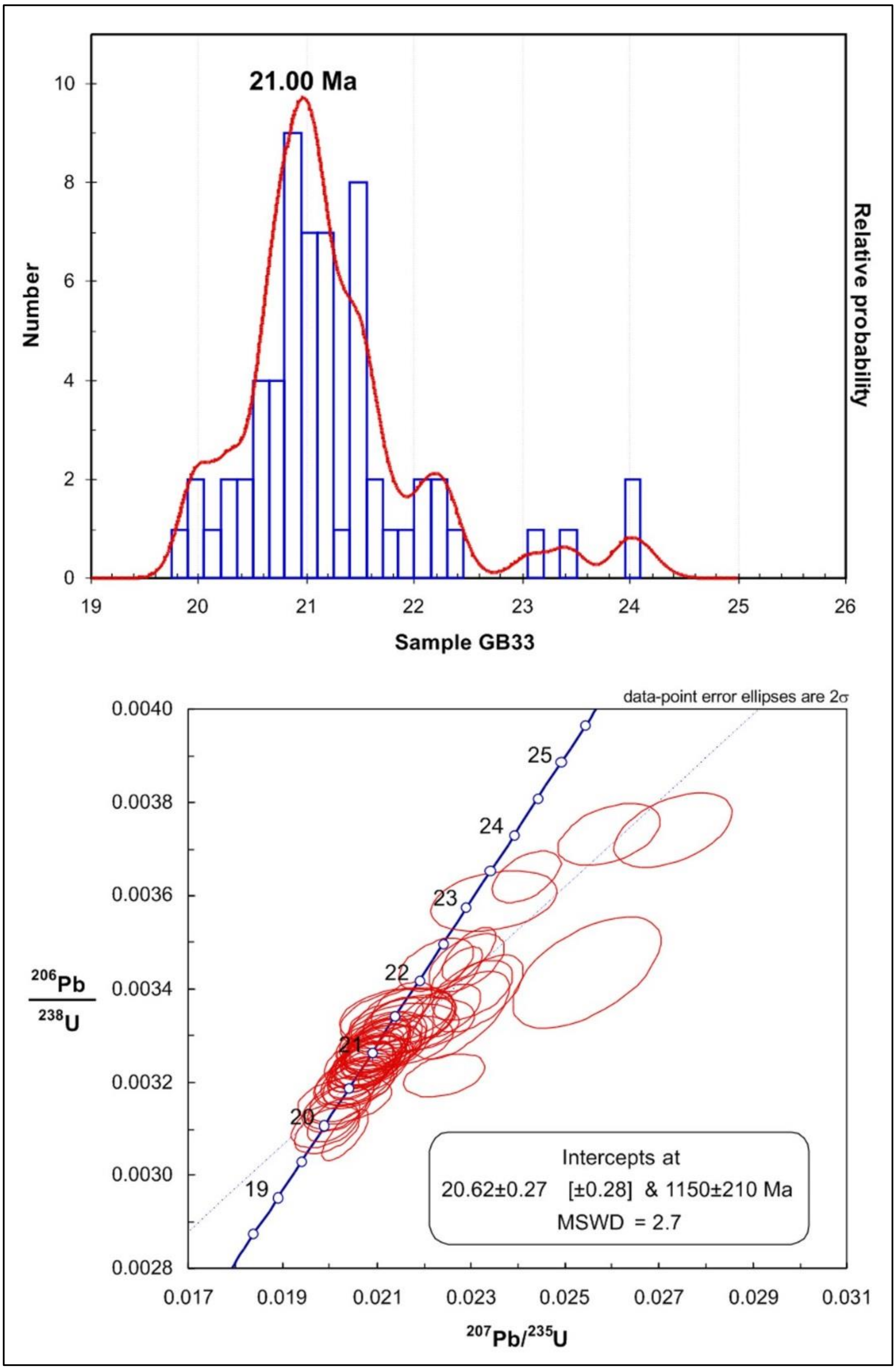

Figure 5.9: U-Pb results of Sample GBP-33 on probability/density plot and concordia diagram.

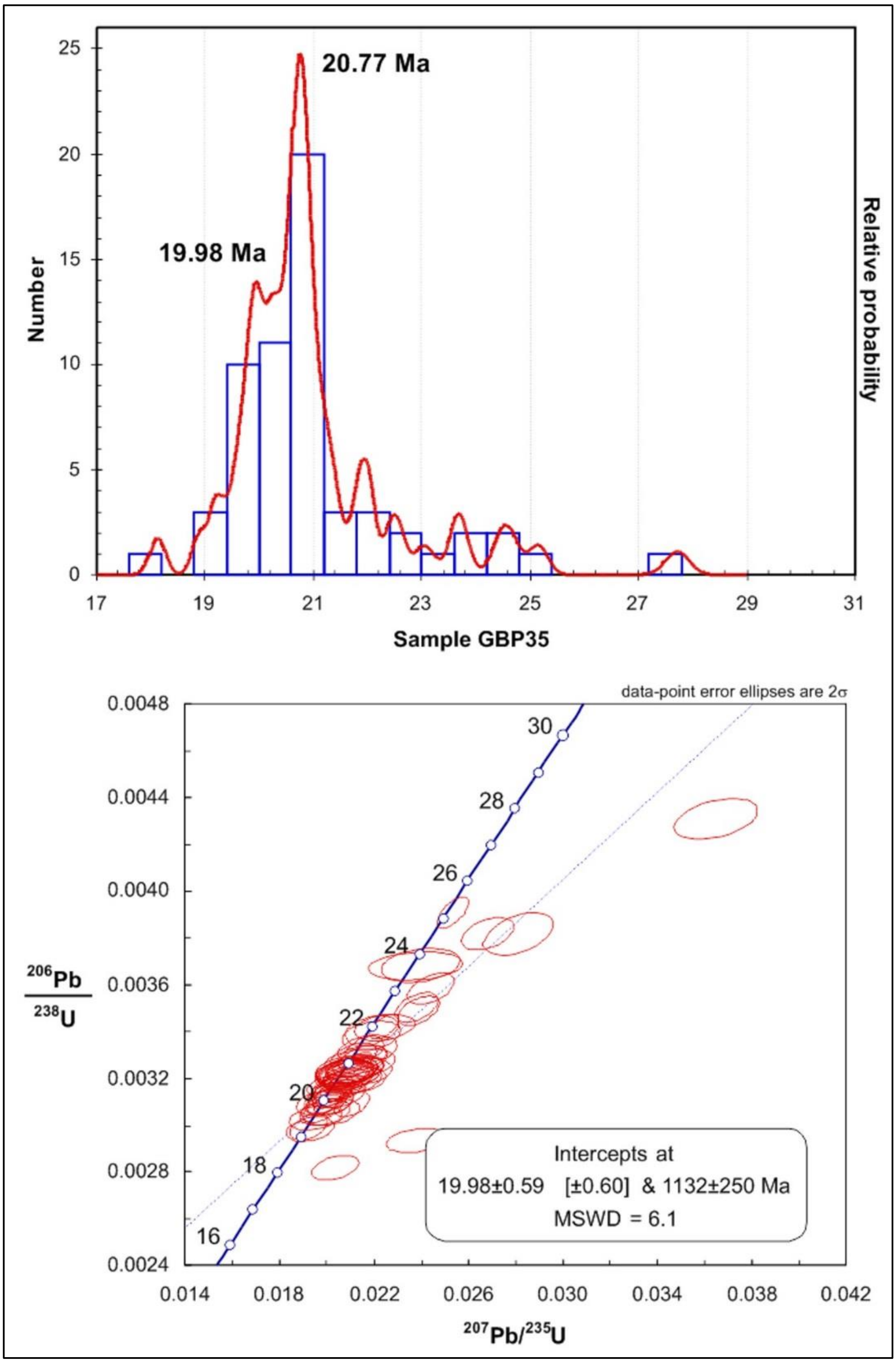

Figure 5.10: U-Pb results of Sample GBP-35 on probability/density plot and concordia diagram.

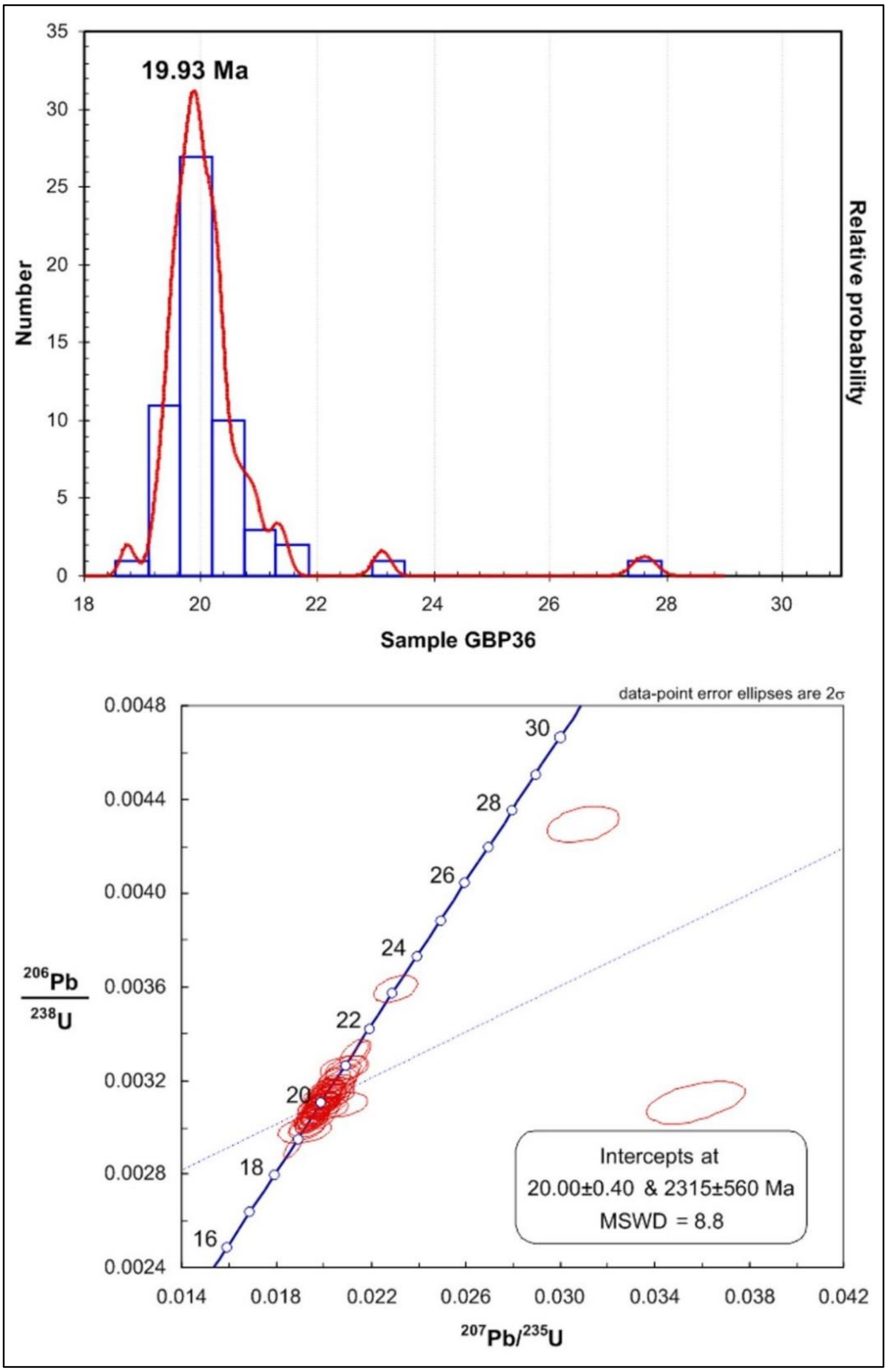

Figure 5.11: U-Pb results of Sample GBP-36 on probability/density plot and concordia diagram.

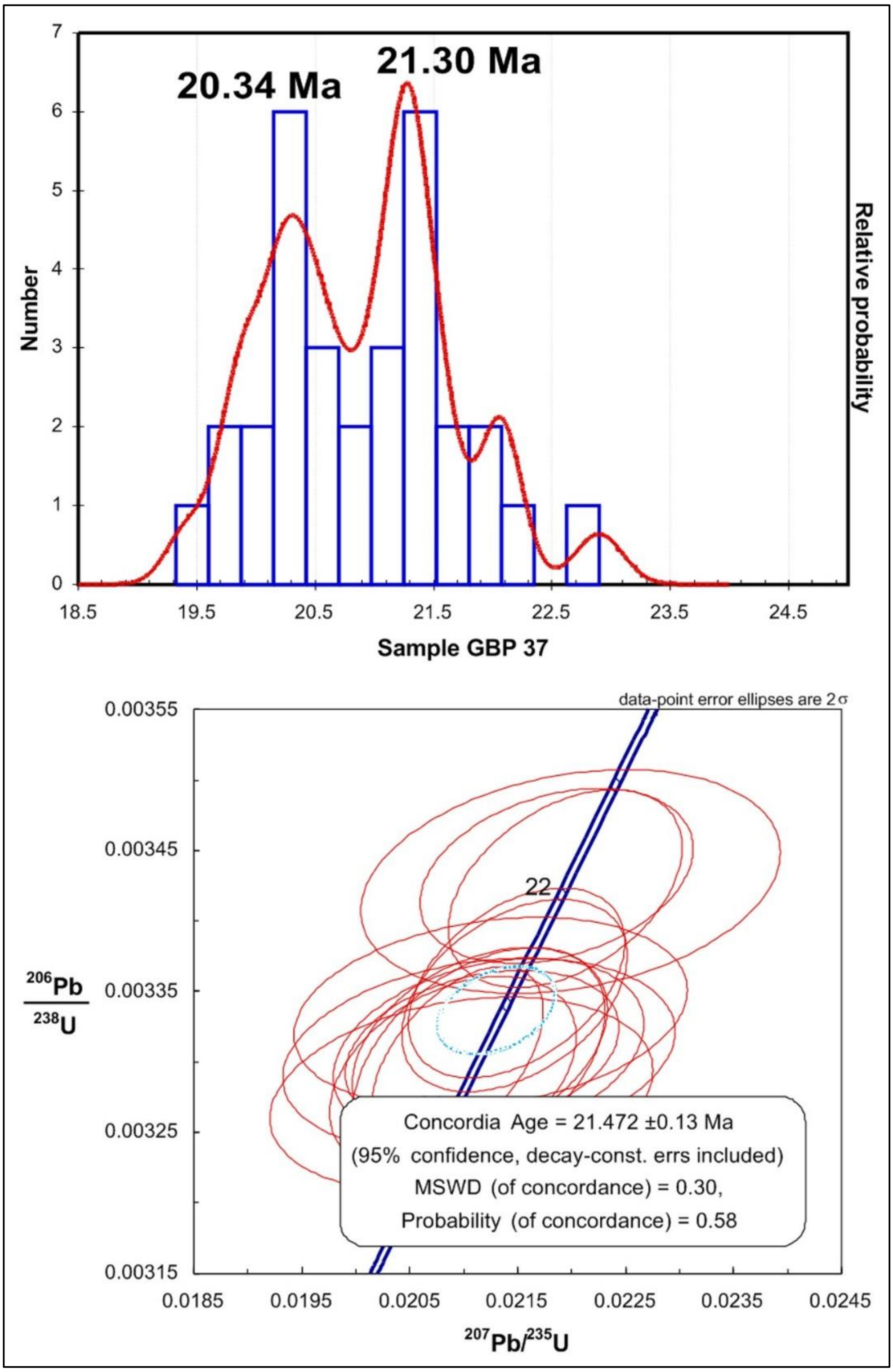

Figure 5.12: U-Pb results of Sample GBP-37 on probability/density plot and concordia diagram.

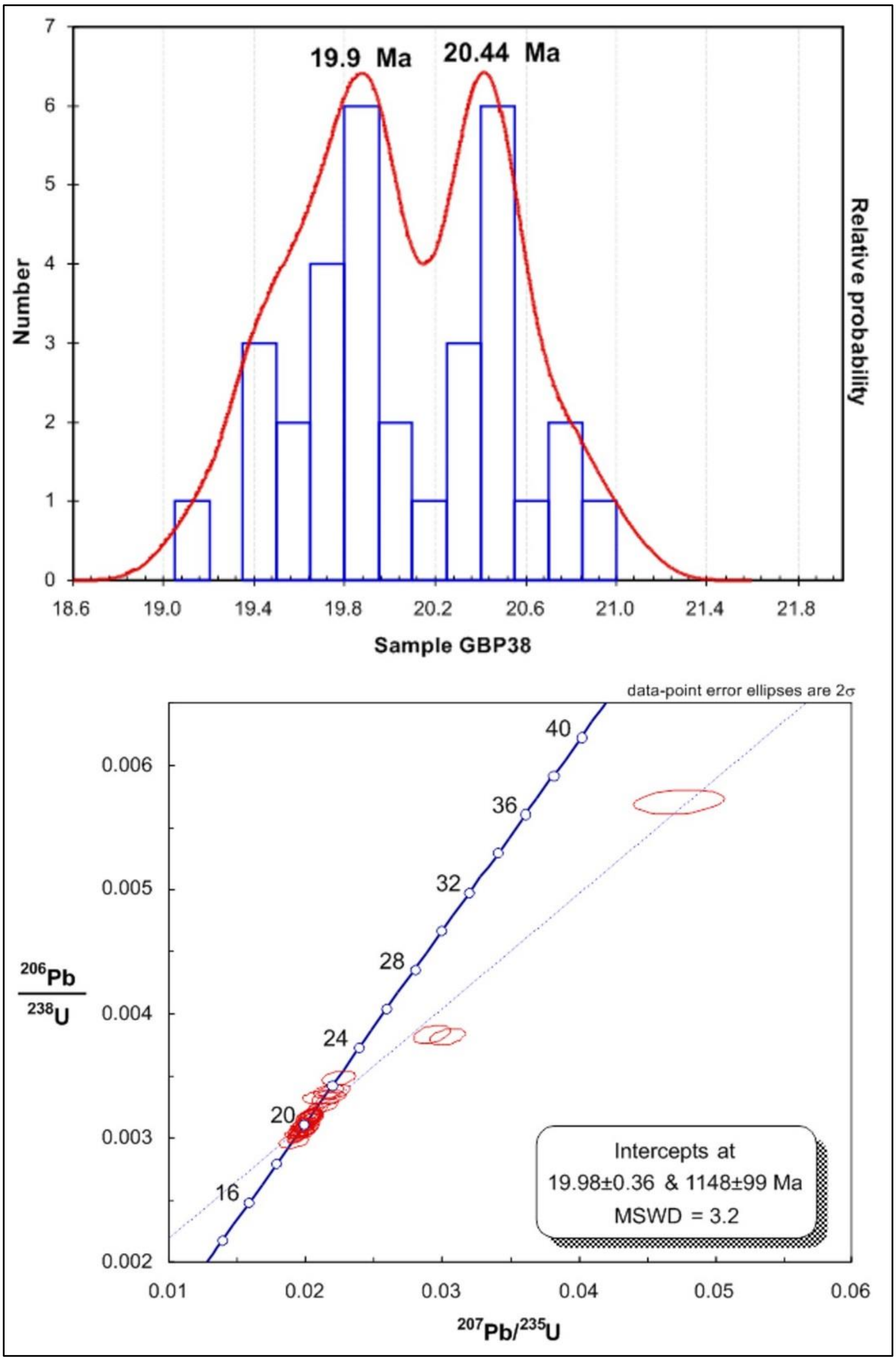

Figure 5.13: U-Pb results of Sample GBP-38 on probability/density plot and concordia diagram.

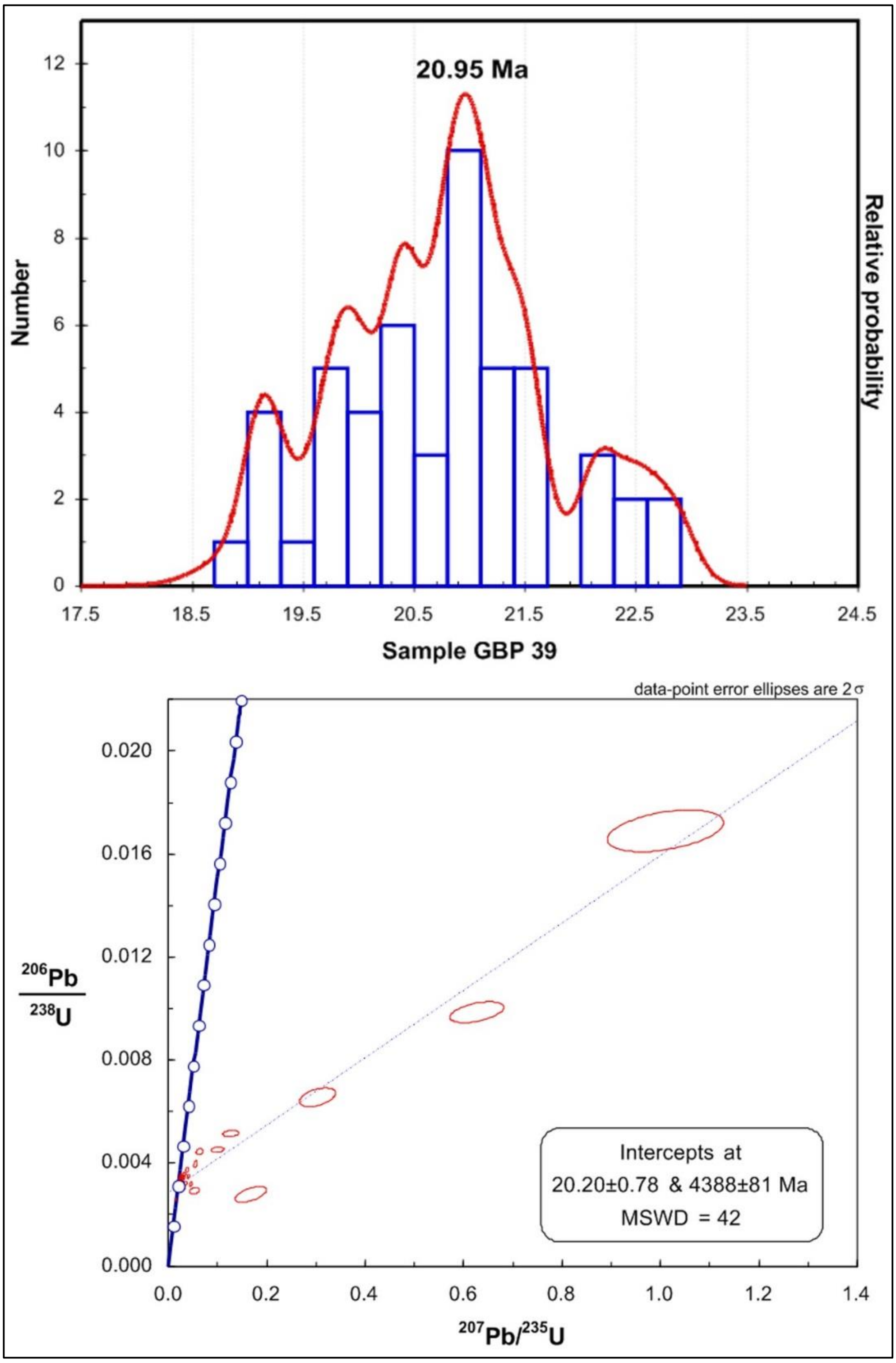

Figure 5.14: U-Pb results of Sample GBP-39 on probability/density plot and concordia diagram.

5.3. Ar-Ar Geochronology

$^{40}Ar/^{39}Ar$ geochronology is an experimentally robust and versatile method for constraining the age and thermal history of rocks (USGS $^{40}Ar/^{39}Ar$ Geochronology Labaratory n.d.). Defining the age and thermal history is quite valuable for understanding a variety of geological processes including the formation of ore deposits, mountain building and history of volcanic events, paleo-seismic events, and paleo-climate. The $^{40}Ar/^{39}Ar$ isotopic dating method has evolved into the most commonly applied geochronological method, and can be applied to many geological problems that require precise and accurate time and temperature control (USGS $^{40}Ar/^{39}Ar$ Geochronology Labaratory n.d.). This method is derived from radioactive isotope of potassium, ^{40}K, which has a dual decay to ^{40}Ca and ^{40}Ar and a half-life of 1250 million years). In this way, radiogenic ^{40}Ar accumulates in a mineral over geologic time. The time since accumulation of ^{40}Ar began (age of the mineral or rock) can be determined by measuring the abundance of ^{40}K and radiogenic ^{40}Ar. In order to obtain quantitative data on the age of igneous activity, volcanism in the study area as well as the timing of the formation of the mineralization, it is conducted that biotite, K-feldspar, fresh and altered wholerock age determination was aimed. Biotite is often ascribed a nominal closure temperature for argon of ∼300 °C (Hodges, 1991), but Grove and Harrison (1996) suggest that the predicted com-positional variation can allow this parameter to range as high as 450 °C. K-feldspars is listed as its closure temperature was around less than 350 °C (Folland, 1994).

5.3.1. Analytical Procedure

Sample packets were irradiated for 16.7 hours at the McMaster reactor (Hamilton, Canada). Stepwise heating experimental procedure has been described in detail by Ruffet et al. (1995 and 1997). For the data quality, the blanks and standard samples was used. The irradiation standard was the sanidine TCR-2 (28.34 Ma according to Renne et al., 1998). Blanks are used on each first or third run. Analyses were performed on a Map215 mass spectrometry.

5.3.2. Results

Fourteen samples were analyzed by Ar-Ar isotopic methods and plateau ages are achieved for the relevant minerals or whole rock data. The age results generally constrained between 19 Ma and 22 Ma. The plateau plots for each samples are illustrated in Figures 5.15-5.17.

There are also multiple ages for the samples GBP-23 and 24 giving thermal history of rock units and its constituent minerals. K-feldspars and biotite crystals was tested on GBP-23 resulting nearly same age ~20.9 Ma. However, GBP-24's biotite and whole rock age are not well overlapping (19.68 Ma to 20 Ma) since it has different materials to be tested, which indicates the thermal history of GBP-24 sample.

5.4. Discussion

According to the dating results, the study area comprises mainly early Miocene (Aquitanian to Burdigalian; Figure 5. 18). Because of zircon overgrowth complexity and Ar-Ar analysis limitations, some of the ages are not easy to interpret. Most U-Pb zircon and Ar-Ar ages are consistent and suggest that both the rock-forming processes and mineralization has taken place during Aquitanian to Burdigalian period. Some Ar-Ar ages are older than the zircon ages from the same sample, suggesting that system became opened so that radiogenic Ar has lost. Additionally, Ar-Ar dating may also yield relatively much younger ages; this may be due to resetting of the Ar system because of several factors, like alteration, intense weathering.

U-Pb age ranges, the most feasible explanation for age range is that the zircon core-rim, collectively overgrowth, patterns and location of dated zone due to the instrument and mineral limitations may result in a comparably wide range of result. However, it is clear that the ages are mostly overlapping with the field observations and general geology of the area. Which is megacrystic monzonite is the oldest and andesite is the youngest emplaced bodies and dacitic lapilli tuff and rhyolitic crystal tuff formed according to time manner as early; dacitic and late; rhyolitic tuff units.

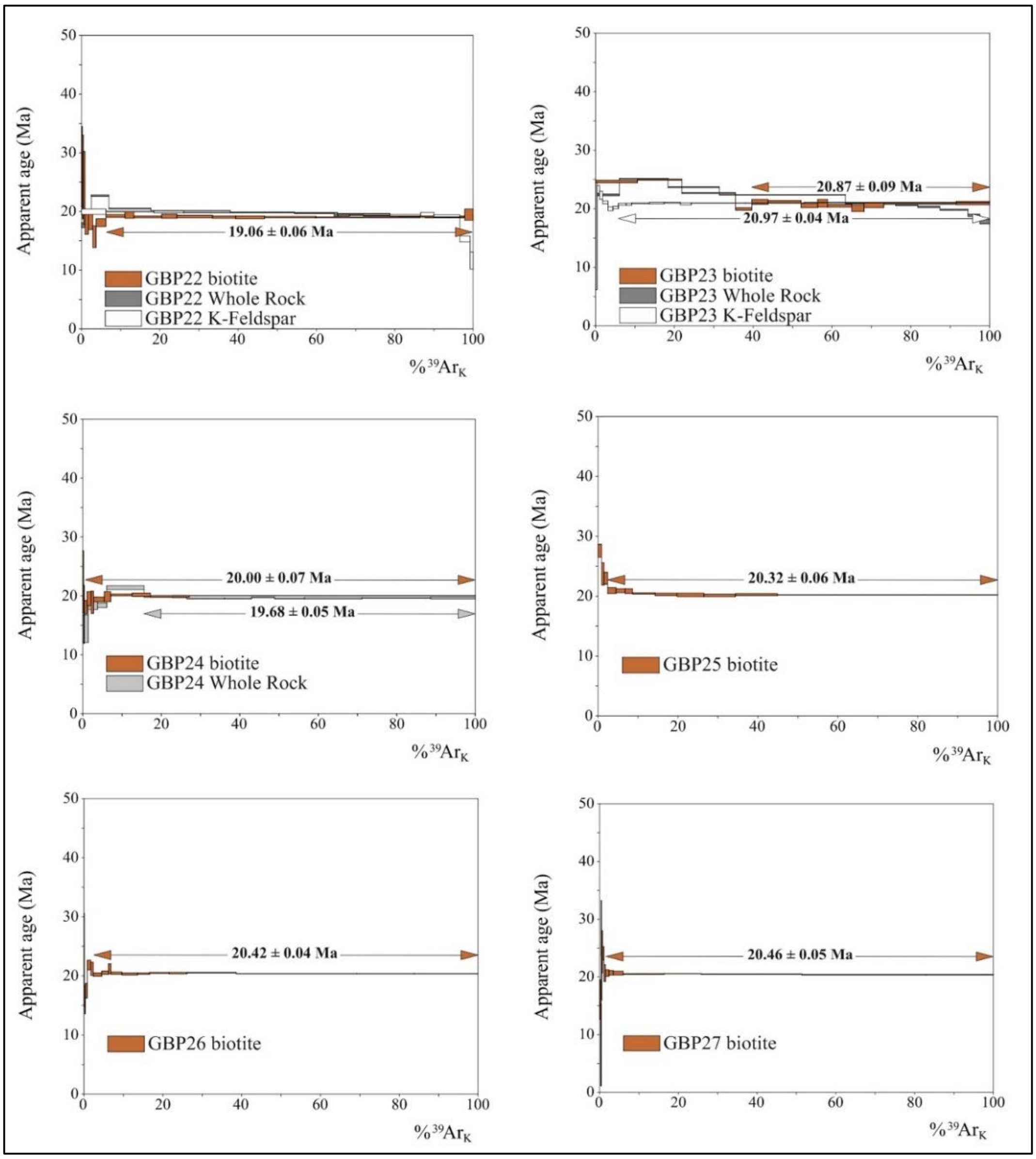

Figure 5.15: Ar-Ar plateau ages for GBP series of samples.

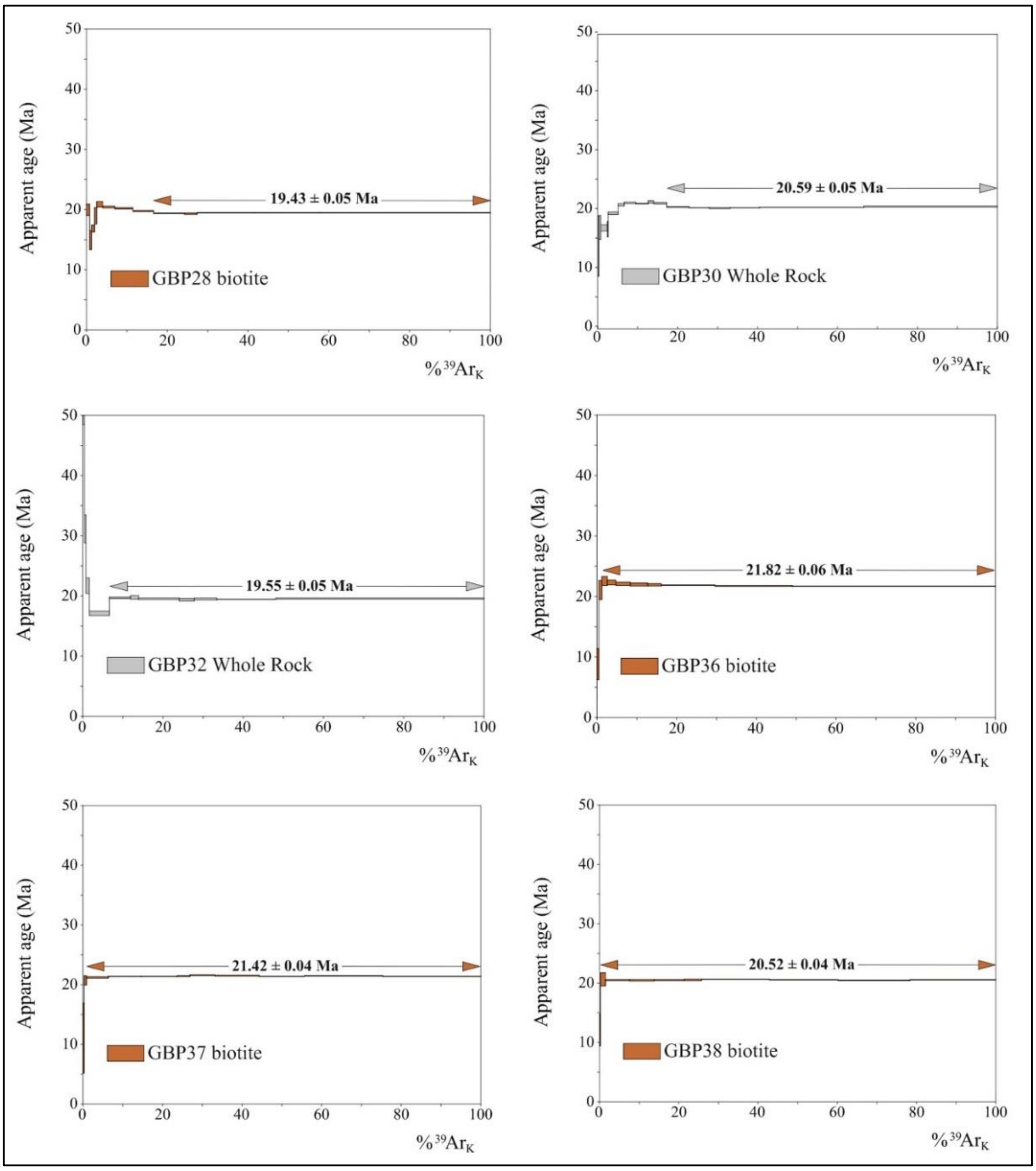

Figure 5.16: Ar-Ar plateau ages for GBP series of samples.

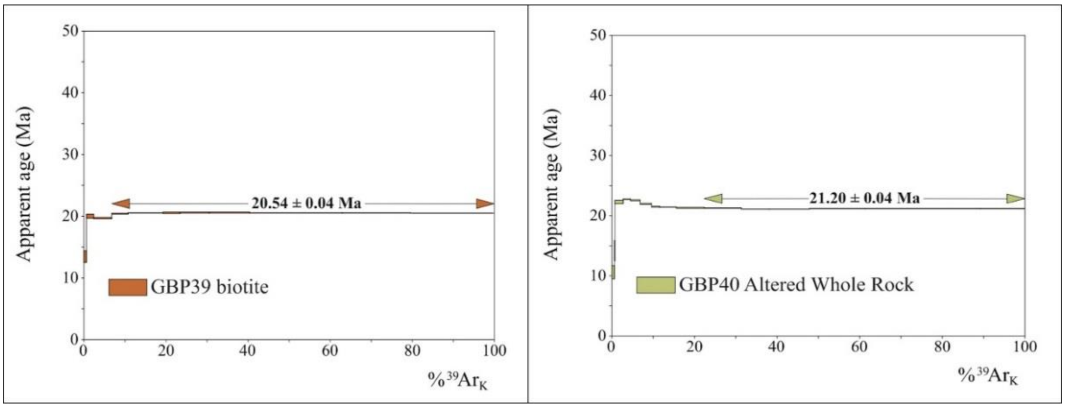

Figure 5.17: Ar-Ar plateau ages for GBP series of samples.

Morever the relations of alteration-giving emplacement (quartz monzodiorite) and alteration-eaten out (diorite porphyry) emplacement can be clearly seen. Finally the latest volcanic product, rhyodacite, was also seen on the area.

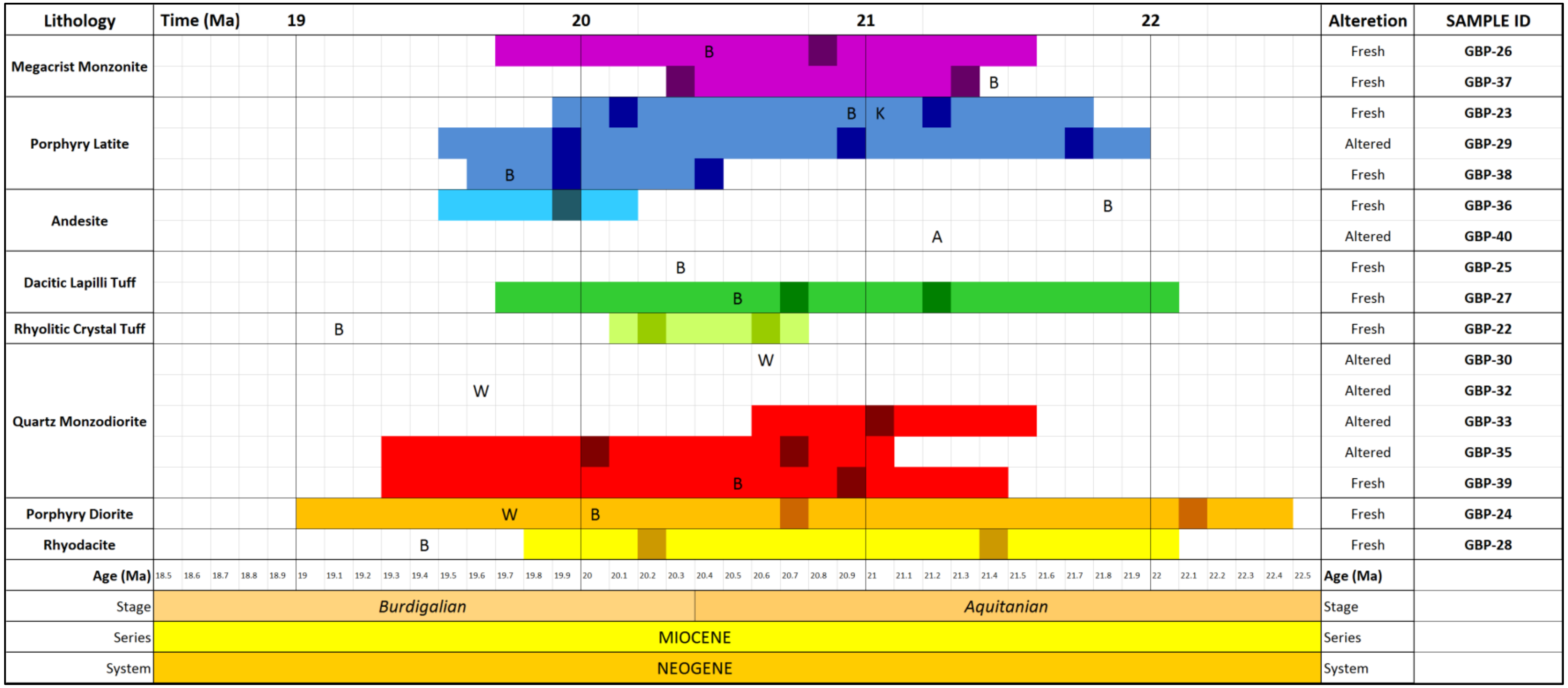

Figure 5.18: Summary diagram showing age ranges for different rock units exposed in the study area. Abbreviations for Ar-Ar plateu ages: B, biotite, A, altered whole rock, W, whole rock (fresh), K, alkali feldspar and Color bars for U-Pb histogram distributions and local maxima and/or intercept ages in darker color.

CHAPTER 6

GEOCHEMISTRY

6.1. Introduction

This chapter will investigate and give summary on geochemical signatures of the rock units in order to support field observations and results of petrographic studies. The results of geochemical analysis may be used to explore for source of magma and subsequent events. Major and trace element data will be used to determine rock types and their tectonic settings.

6.2. Analytical Methods

Geochemical analyses were carried out at Acme Analytical Laboratories in Canada. Trace and rare earth elements (here after REE) were determined by inductively coupled plasma-mass spectrometry (here after ICP-MS). The detection limits range for those investigations are as follows: 0.1 to 10 ppm for trace elements and 0.01 to 0.5 ppm for REE.

6.3. Whole Rock Geochemistry of Study Area

6.3.1. Rock Classification Diagrams

There are several investigation charts to determine geochemical affinity of magmatic rocks. Among them, Winchester and Floyd (1977) diagram is widely used for volcanic rock composition identification because it uses immobile elements. Element mobility are significant for areas where critical secondary activities, like hydrothermal alteration, metamorphism, weathering and diagenesis, may induce compositional changes. Additionally, for the plutonic rocks R1-R2 diagram of Roche et al. (1980) is considered as useful to determine geochemical affinity of rock units.

In R1 (…..) vs R2 (….) diagram of Roche et al. (1980), the plutonic rocks exposed in the study are are defined as monzonite, monzodiorite, tonalite, quartz monzonite, granodiorite, quartz syenite, granite, alkali granite (Figure 6.1a) whereas in Nb/Y vs Zr/TiO2 diagram of Winchester and Floyd (1977), they fall in rhyodacite/dacite and trachy andesite fields (Figure 6.1b).

6.3.2. Tectonic-Setting Discrimination Diagrams

For tectonic setting discrimination diagrams, it is also critical to used immobile elements; specific trace and rare-earth elements due to element mobility. Therefore, Pearce et al. (1984) and, Cabanis and Lecolle (1989) are used for tectonic discriminations. According to Y/15-La/15-Nb/8 ternary plot of Cabanis and Lecolle (1989), the analysed rocks units fall into arc calc-alkaline field (Figure 6.2a) whereas in Nb+Y vs Rb plot of Pearce et al. (1984), they are classified in syn-collisional and volcanic arc granite fields (Figure 6.2b).

6.4. Discussion

Studied volcanic and plutonic rock units' geochemical signature has proven that they have calc-alkaline composition with arc, volcanic arc character as also stated in the literature for Kestanbol Magmatism. The plots on syn-COLG represents volcanic originated samples. Additional comment, evolutionary pattern of latite porphyry both represent possibly partially altered samples or evolving of this unit during emplacement. Compositionally the studied rocks have showing felsic dominated composition as a whole, since most of the plutonic and volcanic units are located on felsic rock groups like; granite, monzonite, rhyolitic products.

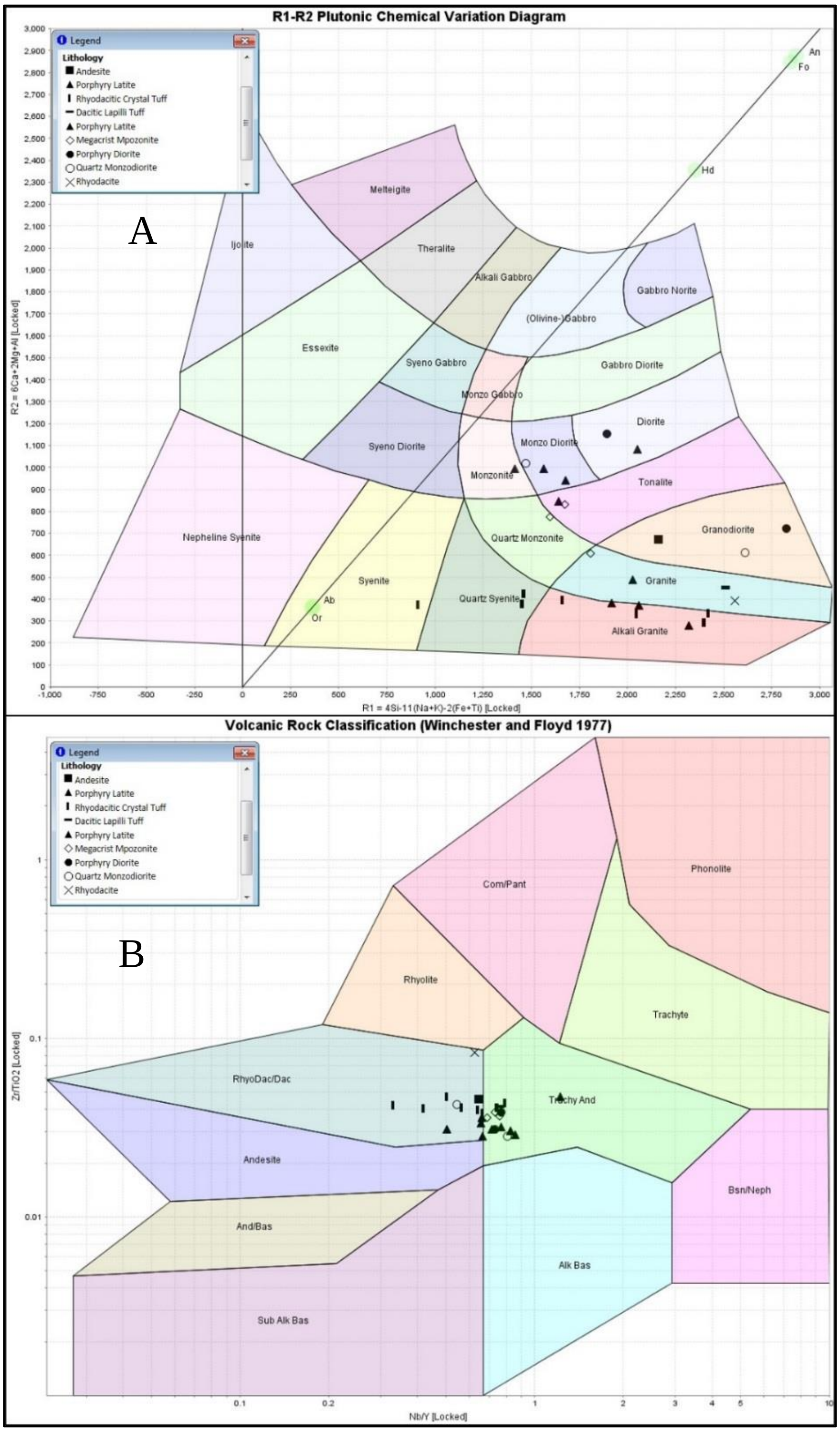

Figure 6.1: Classification of rock units on (a) R1-R2 diagram of Roche et al. (1980), and (b) Nb/Y vs Zr/TiO2 diagram of Winchester and Floyd (1977).

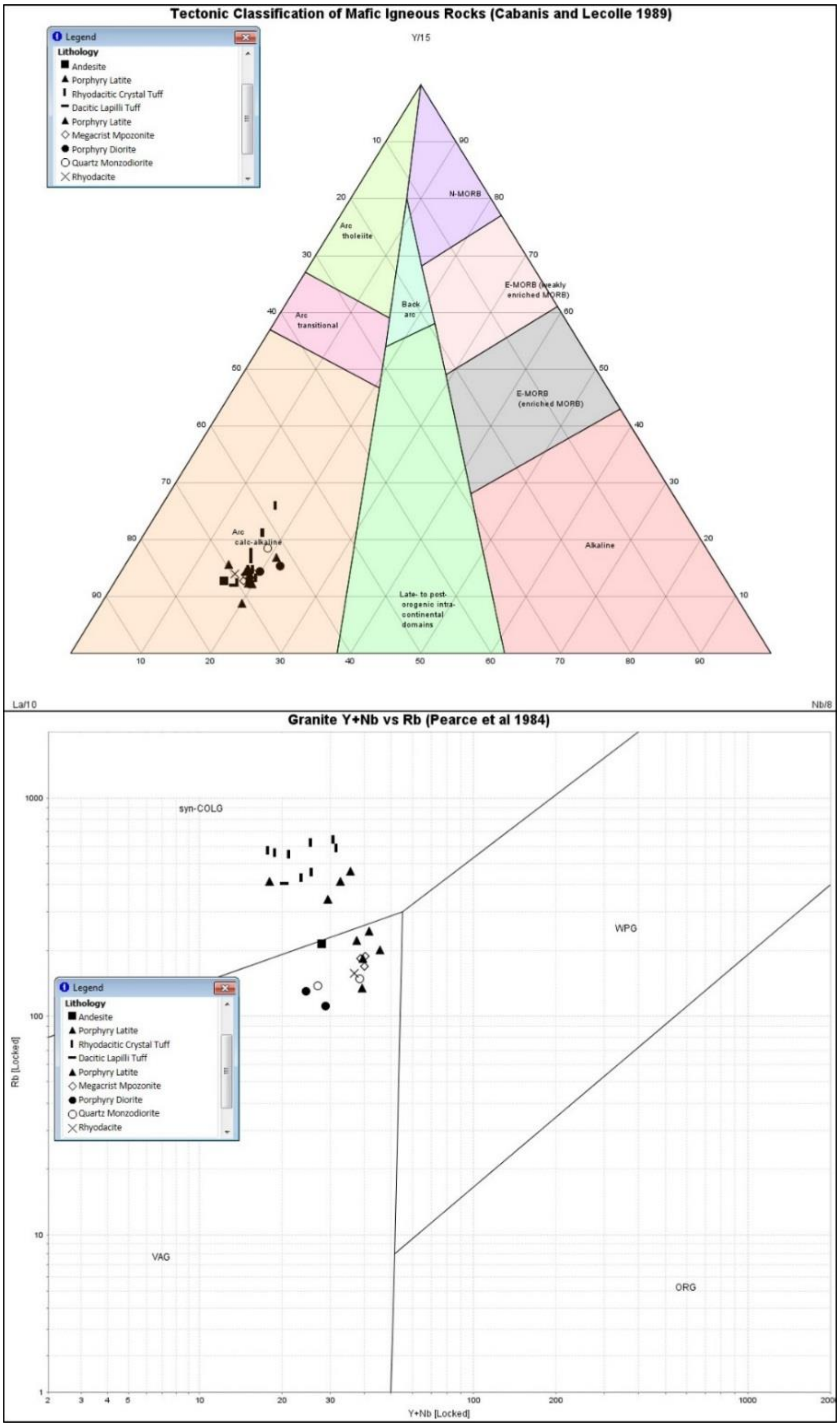

Figure 6.2: Tectonic setting of rock units exposed in the study area in (a) Y/15-La/15-Nb/8 ternary plot of Cabanis and Lecolle (1989) and (b) Nb+Y vs Rb plot of Pearce et al. (1984).

CHAPTER 7

DISCUSSION

7.1. Timing of Mineralization

According to the field observations and isotopic dating results, the mineralization is correlated with occurrence of quartz monzodiorite emplacement, whose age ranges between 21.3 to 19.4 Ma (early Miocene; Aquitanian to Burdigalian). This time interval corresponds to extensional tectonics and exhumation of metamorphic terranes in western Anatolia (Menderes Massif) and Biga Peninsula (Kazdağ Massif) (references: Bozkurt 1994; Bonev et al. 2009; e.g…). This time also corresponds to widespread magmatic activity (Karacık and Yılmaz, 1998; Altunkaynak and Genç, 2008; Aysal, 2015; e.g…). Volcanic, hypabyssal and shallow-intrusive rocks are all proven to be products of coeval events.

7.2. Structural Control on Mineralization

NE-SW-trending transtensional stress conditions along a dextral extensional overstepping are considered as the cause of extensional veining and coeval brecciation. Occurrence of breccia zones and rounded clast geometry along the structural trends and conjugations are explained by the intense structural activities during mineralization. Bimictic breccia zones are generally located at the boundary of two rock units so it is reasonable to see mixing patterns for a considerable thickness. Underwater conditions of tuff units was also critical for this study, because it rule outs the possibility that these breccia zones are related to a diatreme pipe of porphyry systems. Sillitoe (2010) suggested that diatreme pipe can occur when fluid reaches to cold water table; it results in an increase in volatile content and pressure, which then produces explosion features. Field observations, however, does not support a possible diatreme pipe model because of roundness of breccia fragments and underwater conditions of the host rocks. Explosive breccias are typical cracked breccias with angular fragments. Breccia zones show evidence for monomictic silicification and coeval slip history along faults. The mineralization around Naldöken village is attributed to a more structural control.

7.3. History of Mineralization

7.3.1. Skarn Zone

Earliest mineralization related activities are significantly observed along the boundary of basement with megacrystic monzonite; the contact zone is characterized by a mineralogical assemblages as pyroxene-hornfels suggesting elevated temperatures due to emplacement of the monzonitic rocks. Megacrystic monzonite show slow cooling processes. The emplacement of megacrystic monzonite is associated with Kestanbol Pluton.

7.3.2. Naldöken Mineralization

Main mineralization processes are related with the occurrence of quartz monzodiorite as seen around Naldöken village. The emplacement directly creates selectively pervasive and extensive clay alterations in rocks at proximal locations. Topographically distal locations, however, shows structurally-controlled vein-breccia-related mineralization. The veins in the potassic altered rock units show different veins sets like sinuous (old) and planar (young) veins with variety of compositions. The cross-cutting relationships and vein straightness are possibly related to the formation of sinuous veins under high-temperature, overall ductile conditions, whereas later veins are more planar and indicate more brittle and cooler conditions. The occurrence of silica veining and brecciation proves structural control in the area. Due to the cross-cutting relationships of emplaced bodies, the quartz monzonite altered and mineralized the older units.

7.3.3. Post-mineralization

Overprinting (later) and today's activities are listed as post-mineralization activities. In the study area, the occurrence of today's geothermal field in Tuzla village are critical since core log studies (Bozkurtoğlu et al., 2006; Baba et al., 2015) shows that galena-rich scaling is the dominant problem in geothermal reservoir. This also proves that ongoing mineralization may also prevail at deeper horizon. In the cores, 'highly altered' rocks and sulfide occurrences are also reported at shallower depths (~800 m).

7.4. Proposed Geological Model

Crystalline, hypabyssal, and extrusive rock units exposed in the study area must be originated from the same magma chamber, as stated by Karacık and Yılmaz (1998), who relates these units as magma chamber ejecting system to the volcanic center. These rock units do have different cross cutting relationships and unconformably overlying nested history. And, Naldöken area is one of the mineralization located on the south of this chamber, Kestanbol magmatism. The alteration and rock association are in the Naldöken area favors a porphyry type of mineralization potential with intense silica veining on upper and/or distal localities.

Mineralization in Naldöken area with commenced with the formation of structural features. These structures possibly created a water percolation mechanism for both meteoric-sea and connate waters through deeper parts. Approximately north-south-trending extensional overstepping feature forms the preferential localization sites for quartz veins. The overstepping extensional areas are best places for a change in pressure gradients and formation of mineralization (Figure 7.1). In our model, it fits with field distribution of quartz veins, coeval fault slip data. NE-SW-trending transtensional system is therefore considered as controlling mineralization in the Naldöken prospect.

Figure 7.1: A meso-scale example of a book-type, dextral transtensional overstepping characterized by vein formation (URL3).

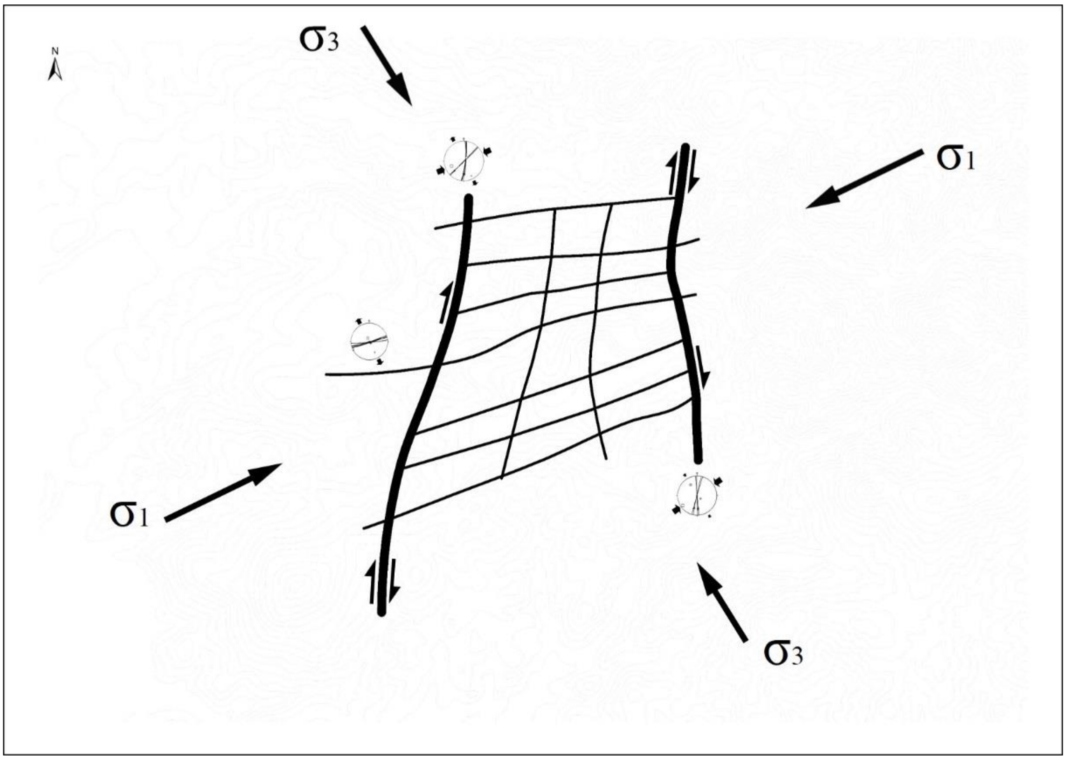

Figure 7.2: Proposed structural model for the study area.

CHAPTER 8

CONCLUSIONS

8.1. Overview

Major concluding outcomes of this thesis can be summarized as follows:

- Porphyry and epithermal mineralization has a magmatic-hydrothermal history that preferentially localized on structural conjugations and local extensional areas.
- Among eleven different rock units, quartz monzonodiorite is suggested as the main cause/source of mineralization and alteration.
- Geochemistry of rock units suggests that they are calc-alkaline rhyolitic, dacitic and andesitic, monzonitic and monzodioritic rocks emplaced within a syn-collisional and volcanic arc settings.
- Mineralization is controlled mainly by a transtensional stress regime along NE–SW-trending dextral strike-slip faults (extensional overstepping).
- Sterile structural features were resulted stress inversions as N–S and E–W extensions.
- U-Pb and Ar-Ar dating suggests that the rock formation and mineralization have taken place during early Miocene (ca. 22–19 Ma).
- The mineralization occurred at around 20.1 Ma by the emplacement of quartz monzodiorite.
- Geochronological studies also prove multi-staged complex magmatic history as observed by zircon overgrowths and some of the incompatible Ar-Ar ages due to the resetting, alteration and system and/or mineral closure complexity.

8.2. Recommendations for Future Work

Research conducted during the course of this research addressed closely mineralization related spatial and temporal issues. Like in all other academic work, this study also exposed topics worthy for further study. Here some of the eye catching further study suggestions are listed.

- Detailed mapping at 1/1000 k or larger scales in the study and near surroundings is critical for successfully understanding the evolution of the mineralization.
- Regional-scale reconnaissance work to be initiated in order to understand Kestanbol magmatism and its volcanic assemblages.
- Radiogenic (Sr, Nd, etc…) and stable (S, O, etc…) isotope analysis will be useful tools for discriminating different mineralization and magmatic sources. By this way the source of metals and transporting agent can be traced.
- Core logging, and geophysical survey can be useful to trace mineralization in new dimension.
- Fluid inclusion studies are recommended to determine temperature and salinities of mineralizing fluids.

REFERENCES

Agricola, G., 1556. *De Re Metallica.* s.l.:The Mining Magazine.

Altunkaynak, Ş. & Genç, Ş. C., 2008. Petrogenesis and time-progressive evolution of the Cenozoic continental volcanism in the Biga Peninsula, NW Anatolia (Turkey). *Lithos,* Volume 102, pp. 316-340.

Aysal, N., 2015. Mineral chemistry, crystallization conditions and geodynamic implications of the Oligo–Miocene granitoids in the Biga Peninsula, Northwest Turkey. *Journal of Asian Earth Sciences,* Volume 105, pp. 68-84.

Baba, A., Demir, M. M., Koç, G. A. & Tuğcu, C., 2015. Hydrogeological properties of hyper-saline geothermal brine and application of inhibiting siliceous scale via pH modification. *Geothermics,* Volume 53, pp. 406-412.

Barton, M. D. & John, D. A., 2010. *Porphyry Copper Deposit Model; Scientific Investigations Report 2010–5070–B,* s.l.: USGS.

Beccaletto, L. et al., 2005. Biostratigraphic data from the C¸ etmi Mélange, northwest Turkey: Palaeogeographic and tectonic implications. *Paleogeography, Paleoclimatology, Paleoecology,* Volume 221, pp. 215-244.

Beccaletto, L. & Jenny, C., 2004. Geology and Correlation of the Ezine Zone: A Rhodope Fragment in NW Turkey?. *Turkish Journal of Earth Sciences,* Volume 13, pp. 145-176.

Black, K. N., Catlos, E. J., Oyman, T. & Demirbilek, M., 2013. Timing Aegean extension: Evidence from in situ U–Pb geochronology and cathodoluminescence imaging of granitoids from NW Turkey. *Lithos,* Volume 180-181, pp. 92-108.

Blackwell, J. L., Cooke, D. R., Mcphine, J. & Simpson, K. A., 2014. Lithofacies Associations and Evolution of the Volcanic Host Succession to the Minifie Ore

Zone: Ladolam Gold Deposit, Lihir Island, Papua New Guinea. *Economic Geology,* Volume 109, pp. 1137-1160.

Bonev, N., Beccaletto, L., Robyr, M. & Monie, P., 2009. Metamorphic and age constraints on the Alakeçi shear zone: Implications for the extensional exhumation history of the northern Kazdağ Massif, NW Turkey. *Lithos,* Volume 113, pp. 331-345.

Bozkurt, E., and Mittwede, S. K., 2001, Introduction to the Geology of Turkey-A synthesis, International Geology Review, Volume 43, p. 578-594.

Bozkurtoğlu, E., Vardar, M., Suner, F. & Zambak, C., 2006. A new numerical approach to weathering and alteration in rock using a pilot area in the Tuzla geothermal area, Turkey. *Engineering Geology,* Volume 87, pp. 33-47.

Burchfiel, B. C. et al., 2008. Evolution and dynamics of the Cenozoic tectonics of the South Balkan extensional system. *Geosphere,* Volume 4(6), pp. 919-938.

Campbell, I. H. et al., 2006. U-Pb Zircon Geochronology of Granitic Rocks from the Chuquicamata-El Abra Porphyry Copper Belt of Northern Chile: Excimer Laser Ablation ICP-MS Analysis. *Economic Geology,* Volume 101(7), pp. 1327-1344.

Carslaw, H. S. & Jaeger, J. C., 1959. Conduction of Heat in Solids. In: 2nd ed. s.l.:OXFORD, p. 510.

Cavazza, W., Okay, A. I. & Zattin, M., 2009. Rapid early-middle Miocene exhumation of the Kazdağ Massif (western Anatolia). *International Journal of Earth Science,* Volume 98, pp. 1935-1947.

Cooke, D. R., Hollings, P. & Walshe, J. L., 2005. Giant Porphyry Deposits: Characteristics, Distribution, and Tectonic Controls. *Economic Geology,* Volume 100, pp. 801-818.

Cooke, D. R., Hollings, P., Wilkinson, J. J. & Tosdal, R. M., 2014. Geochemistry of Porphyry Deposits. In: K. Turekian & H. Holland, eds. *Treatise on Geochemistry.* 2nd ed. s.l.:Elsevier Ltd., pp. 357-381.

Cox, S. F. & Knackstedt, M. A., 1999. *Ore genesis in fracture-controlled hydrothermal systems: Percolation theory approaches.* Bali, Indonesia, PACRIM'99.

Davis D.W., Williams I.S., Krogh T.E., 2003. Historical development of zircon geochronology. In:Reviews in mineralogy and geochemistry (editors: Hanchar J.M., Hoskin P.W.O.). Mineralogical Society of America, 53: 145-181.

De la Roche, H., Leterrier, J., Granclaude, P. and Marchal, M., 1980. A classification of volcanic and plutonic rocks using RIR2-diagram and major-element analyses – Its relationships with current nomenclature. Chem. Geol., 29: 183—210.

Dilles, J. H., Einaudi, M. T., Proffett, J. & Barton, M. D., 2000. Overview of the Yerington Porphyry Copper District: Magmatic to Nonmagmatic Sources of Hydrothermal Fluids, Their Flow Paths, Alteration Affects on Rocks, and Cu-Mo-Fe-Au Ores. In: T. B. Thompson, ed. *GUIDEBOOK SERIES.* s.l.:Society of Economic Geologist, pp. 55-66.

Dilles, J. H. & Wright, J. E., 1988. The chronology of early Mesozoic arc magmatism in the Yerington district of western Nevada and its regional implications. *Geological Society of America Bulletin,* Volume 100, pp. 644-652.

Dönmez, M., Akçay, A. E., Genç, Ş. C. & Acar, Ş., 2005. Biga Yarimadasinda Orta-Üst Eosen Volkanizmasi ve Denizel İgnimbiritler. *MTA Dergisi,* Volume 131, pp. 49-61.

Drew, L. J., 2005. *A Tectonic Model for the Spatial Occurrence of Porphyry Copper and Polymetallic Vein Deposits—Applications to Central Europe: Scientific Investigations Report 2005–5272,* s.l.: USUS.

Foland KA (1983) 40Ar/39Ar incremental heating plateaus for biotites with excess argon. Isot Geosci 1:3–21.

Folland, K. A., 1994. Argon Diffusion in Feldspars. *Feldspars and Their Reactions,* 1(Parson), pp. 415-447.

Gerdes A., Zen A. 2006. Combined U–Pb and Hf isotope LA-ICP-MS analyses of detrital zircons: comparison with SHRIMP and new constrains for the provenance and age of an Armorican metasediment in Central Germany. Earth and Planetary Science Letters, 249: 47–61.

Gerdes, A., Zen, A., 2009. Zircon formation versus zircon alteration — New insights from combined U–Pb and Lu–Hf in-situ LA-ICP-MS analyses, and consequences for the interpretation of Archean zircon from the Central Zone of the Limpopo Belt. Chemical Geology, 261: 230-243.

Gregory, M. J., Lang, J. R., Gilbert, S. & Hoal, K. O., 2013. Geometallurgy of the Pebble Porphyry Copper-Gold-Molybdenum Deposits, Alaska: Implications for Gold Distribution and Paragenesis. *Economic Geology,* Volume 108, pp. 463-482.

Gustafson, L. B. & Hunt, J. P., 1975. The Porphyry Copper Deposits at El Salvador, Chile. *Economic Geology,* Volume 70, pp. 857-912.

Hedenquist, J. W. & Henley, R. W., 1985. Hydrothermal Eruptions in the Waiotapu Geothermal System, New Zealand: Their Origin, Associated Breccias, and Relation to Precious Metal Mineralization. *Economic Geology,* Volume 80, pp. 1640-1668.

Hedenquist, J. W. & Lowenstern, J. B., 1994. The role of magmas in the formation of hydrothermal ore deposits. *Nature,* Volume 370, pp. 519-527.

Hemley, J. J. & Hunt, J. P., 1992. Hydrothermal Ore-Forming Processes in the Light of Studies in Rock-Buffered Systems: II. Some General Geologic Applications. *Economic Geology,* Volume 87, pp. 23-43.

Jebrak, M., 1997. Hydrothermal breccias in vein-type ore deposits: A review of mechanisms, morphology and size distribution. *Ore Geology Reviews,* Volume 12, pp. 111-134.

Juras, S., Miller, R. & Skayman, P., 2010. *Technical Report for the Kışladağ Gold Mine, Turkey,* Turkey: Eldorado Gold Corporation.

Karacık, Z. & Yılmaz, Y., 1998. Geology of the ignimbrites and the associated volcano-plutonic complex of the Ezine area, northwestern Anatolia. *Journal of Volcanology and Geothermal Research,* Volume 251-264, p. 85.

Katz, Y., Weinberger, R. & Aydin, A., 2004. Geometry and kinematic evolution of Riedel shear structures, Capitol Reef National Park, Utah. *Journal of Structural Geology,* Volume 26, pp. 491-501.

Lang, J. R., Stanley, C. R., Thompson, J. F. & Dunne, K. P., 1995. Na-K-Ca Magmatic-Hydrothermal Alteration in Alkalic Porphyry Cu-Au Deposits, British Columbia. *From Magmas, Fluids and Ore Deposits,* 23(Short Course), pp. 339-366.

Laznica, P., 1989. Breccias And Ores. Part 1: History, Organization And Petrography Of Breccias. *Ore Geology Reviews,* Volume 4, pp. 315-344.

Lingren, W., 1933. *Mineral Deposits.* 4 ed. New York: McGraw-Hill.

Ludwig, K.R., 2003. Isoplot 3.00: A Geochronological Toolkit for Microsoft Excel. Berkeley Geochronology Center Special Publication 4, 70 p.

Millonig, L. J., Gerdes, A., and Groat, L. A. (2012). The effect of amphibolite facies metamorphism on the U – Th – Pb geochronology of accessory minerals from meta-carbonatites and associated meta-alkaline rocks. Chemical Geology, 1–11.

Okay, A. I., Siyako, M. & Bürkan, K. A., 1991. Geology and Tectonic Evolution of the Biga Peninsula, Northwest Turkey. *Bull. Tech. Univ. Istanbul,* Volume 44, pp. 191-256.

Okay, A. İ., Satır, M., Maluski, H., Siyako, M., Monie, P., Metzger, R. & Akyüz, S., 1996. Paleo- and Neo-Tethyan events in northwest Turkey: geological and geochronological constraints. In: YIN, A. & HARRISON, M. (eds), Tectonics of Asia. Cambridge University Press, pp. 420-441.

Okay, A. I. & Tüysüz, O., 1999, Tethyan sutures of northern Turkey. In: Durand, B., Jolivet, L., Horvath, F., and Seranne, M., (eds.), The Mediterranean Basins:

Tertiary Extension within the Alpine Orogen. Geological Society, London, Special Publications, 156, 475-515.

Okay, A. I. & Satır, M., 2000. Upper Cretaceous Eclogite-Facies Metamorphic Rocks from the Biga Peninsula, Northwest Turkey. *Turkish Journal of Earth Sciences,* Volume 9, pp. 47-56.

Philippon, M., Brun, J.-P., Gueydan, F. & Sokoutis, D., 2014. The interaction between Aegean back-arc extension and Anatolia escape since Middle Miocene. *Tectonophysics,* Volume 631, pp. 176-188.

Renne, P. R., Swisher, C. C., Deino, A. L., Karner, D. B., Owens, T. L. and DePaolo, D. J., 1998. Intercalibration of standards, absolute ages and uncertainties in 40Ar/39Ar dating. Chemical Geology 145, 117-152.

Richards, J. P., 2003. Tectono-Magmatic Precursors for Porphyry Cu-(Mo-Au) Deposit Formation. *Economic Geology,* Volume 98, pp. 1515-1533.

Richards, J. P., 2013. Giant ore deposits formed by optimal alignments and combinations of geological processes. *Nature Geoscience,* Volume 6, pp. 911-916.

Richards, J. P., Boyce, A. J. & Pringle, M. S., 2001. Geologic Evolution of the Escondida Area, Northern Chile: A Model for Spatial and Temporal Localization of Porphyry Cu Mineralization. *Economic Geology,* Volume 96, pp. 271-305.

Ring, U., Brandon, M. T., Lister, G. & Willett, S. D., 1999. *Exhumation Processes: Normal Faulting, Ductile Flow and Erosion.* 1st ed. London: The Geological Society of London.

Roger, S., 1987. Genesis of Acid-Sulfate Alteration and Au-Cu-Ag Mineralization at Summitville, Colorado. *Economic Geology,* Volume 82, pp. 1575-1591.

Ruffet, G., Féraud, G., Balèvre, M. and Kiénast, J.-R., 1995. Plateau ages and excess argon in phengites: an 40Ar-39Ar laser probe study of Alpine micas (Sesia Zone, Western Alps, northern Italy). Chemical Geology (Isotopic Geoscience Section) 121, 327-343.

Ruffet, G., Gruau, G., Ballèvre, M., Féraud, G. and Philippot, P., 1997. Rb-Sr and 40Ar-39Ar laser probe dating of high-pressure phengites from the Sesia zone (western Alps): underscoring of excess argon and new age constraints on the high-pressure metamorphism. Chemical Geology 141, 1-18.

Seedorff, E. et al., 2005. Porphyry Deposits: Characteristics and Origin of Hypogene Features. *Economic Geology,* Volume 100th Anniversary, pp. 251-298.

Segall, P. & Pollard, D. D., 1980. Mechanics of Discontinuous Faults. *Journal of Geophysical Research,* 85(B8), pp. 4337-4350.

Şener, M. & Gevrek, A. İ., 2000. Distribution and significance of hydrothermal alteration minerals in the Tuzla hydrothermal system, C¸anakkale, Turkey. *Journal of Volcanology and Geothermal Research,* Volume 96, pp. 215-228.

Şengün, F., Yiğitbaş, E. & Tunç, İ. O., 2011. Geology and Tectonic Emplacement of Eclogite and Blueschists, Biga Peninsula, Northwest Turkey. *Turkish Journal of Earth Sciences,* Volume 20, pp. 273-285.

Sibson, R. H., 1987. Earthquake rupturing as a mineralizing agent in hydrothermal systems. *Geology,* Volume 15, pp. 701-704.

Sillitoe, R. H., 2010. Porphyry Copper Systems. *Economic Geology,* Volume 105, pp. 3-41.

Sillitoe, R. H. & Hedenquist, J. W., 2003. Linkages between Volcanotectonic Settings, Ore-Fluid Compositions, and Epithermal Precious Metal Deposits. *Volcanotectonic Settings, Ore-Fluid Compositions, & Epithermal Precious Metal Deposits,* 10(Special Publication), pp. 315-343.

Sillitoe, R. H. & Parello, J., 2005. Andean copper province: Tectonomagmatic settings, deposit types, metallogeny, exploration, and discovery. *Economic Geology,* Volume 100th Anniversary, pp. 845-890.

Simmons, S. F. & Brown, K. L., 2006. Gold in Magmatic Hydrothermal Solutions and the Rapid Formation of a Gaint Ore Deposit. *Science,* Volume 314, pp. 288-291.

Simmons, S. F., White, N. C. & John, D. A., 2005. Geological Characteristics of Epithermal Precious and Base Metal Deposits. *Economic Geology,* Volume Economic Geology 100th Anniversary, pp. 485-522.

Singer, D. A., 1995. World Class Base and Precious Metal Deposits - A Quantitative Analysis. *Economic Geology,* Volume 90, pp. 88-104.

Slama, J., Kosler, J., Crowley, J. L., Gerdes, A., Hanchar, J., Horstwood, M., Morris, G., Nasdala, L., Norberg, N., Schaltegger, U., Tubrett, M., Whitehouse, M., 2007. Plešovice zircon – a new natural standard for U-Pb and Hf isotopic microanalysis. 17th Annual Goldschmidt conference, Cologne.

Sun, W. et al., 2015. Porphyry deposits and oxidized magmas. *Ore Geology Reviews,* Volume 65, pp. 97-131.

Şengör, A.M.C., 1979, Mid-Mesozoic closure of the Permo-Triassic Tethys and its implications, *Nature*, Volume 279, pp. 590-593.

Şengör, A. M. C., and Yılmaz, Y., 1981, Tethyan evolution of Turkey: A plate tectonic approach, *Tectonophysics*, Volume 75, p. 181-241.

Tosdal, R. M., Dilles, J. H. & Cooke, D. R., 2009. From Source to Sinks in Auriferous Magmatic-Hydrothermal Porphyry and Epithermal Deposits. *Elements,* Volume 5, pp. 289-295.

Tosdal, R. M. & Richards, J. P., 2001. Magmatic and structural controls on the development of porphyry Cu (Mo-Au) deposits. *Economic Geology,* Volume 14, pp. 157-181.

WeiDong, S. et al., 2010. Ridge subduction and porphyry copper-gold mineralization: An overview. *Science China: Earth Sciences,* Volume 53(4), pp. 475-484.

White, N. C. & Hedenquist, J. W., 1995. Epithermal Gold Deposits: Styles, Charecteristics and Exploration. *SEG Newsletter,* pp. 1-13.

Williams-Jones, A. E., Bowell, R. J. & Migdisov, A. A., 2009. Gold in Solution. *Elements,* Volume 5, pp. 281-287.

Yaltırak, C., İşler, E. B., Aksu, A. E. & Hiscott, R. H., 2012. Evolution of the Bababurnu Basin and shelf of the Biga Peninsula: Western extension of the middle strand of the North Anatolian Fault Zone, Northeast Aegean Sea, Turkey. *Journal of Asian Earth Scientists,* Volume 57, pp. 103-109.

Yiğit, Ö., 2009. Mineral Deposits of Turkey in Relation to Tethyan Metallogeny: Implications for Future Mineral Exploration. *Economic Geology,* Volume 104, pp. 19-51.

Yiğit, Ö., 2012. A Prospective sector in the Tethyean Metallogenic Belt: Geology and geochronology of mineral deposits in the Biga Peninsula, NW Turkey. *Ore Geology Reviews,* Volume 46, pp. 118-148.

Yiğit, Ö., 2012. Discovered and undiscovered gold endowment of Turkey: a quantitative mineral resource assessment using GIS and rank statistical analysis. *Miner Deposita,* Volume 47, pp. 521-534.

Yılmaz, Y., Genç, Ş. C., Karacık, Z. & Altunkaynak, Ş., 2001. Two contrasting magmatic associations of NW Anatolia and their tectonic significance. *Journal of Geodynamics,* Volume 31, pp. 243-271.

Zalohar, J. & Vrabec, M., 2007. Paleostress analysis of heterogeneous fault-slip data: the Gauss method. *Journal of Structural Geology,* Volume 29, pp. 1798-1810.

Zalohar, J. & Vrabec, M., 2008. Combined kinematic and paleostress analysis of fault-slip data: The Multiple-slip method. *Jeournal of Structural Geology,* Volume 30, pp. 1603-1613.

USGS 40Ar/39Ar Geochronology Laboratory n.d., Ar-Ar Introduction, Available from: < http://minerals.cr.usgs.gov/argon_lab/introduction.html>. [14 December 2015].

URL1-http://www.magnetic-declination.com/

URL2-
https://www.tcd.ie/Geology/staff/chewd/images/Misc.%20Structure/pull%20apart.JPG entered 5/12/2015

URL-3
http://legacy.virtualexplorer.com.au/special/meansvolume/contribs/bons/figures/bonsf4.jpg entered 5/12/2015